RAFAEL DE ANDRADE WATAI

A TIME-DOMAIN BOUNDARY ELEMENTS METHOD FOR THE SEAKEEPING ANALYSIS OF OFFSHORE SYSTEMS

SÃO PAULO
2015

RAFAEL DE ANDRADE WATAI

A TIME-DOMAIN BOUNDARY ELEMENTS METHOD FOR THE SEAKEEPING ANALYSIS OF OFFSHORE SYSTEMS

Thesis submitted to the Escola Politécnica da Universidade de São Paulo for the partial fulfilment of the requirements for the degree of Doctor of Science

SÃO PAULO
2015

RAFAEL DE ANDRADE WATAI

A TIME-DOMAIN BOUNDARY ELEMENTS METHOD FOR THE SEAKEEPING ANALYSIS OF OFFSHORE SYSTEMS

Thesis submitted to the Escola Politécnica da Universidade de São Paulo for the partial fulfilment of the requirements for the degree of Doctor of Science

Research Area:
Naval Architecture and Ocean Engineering

Supervisor: Prof. Alexandre Nicolaos Simos

SÃO PAULO
2015

Este exemplar foi revisado e corrigido em relação à versão original, sob responsabilidade única do autor e com a anuência de seu orientador.

São Paulo, 02 de Fevereiro de 2015.

Assinatura do autor _____

Assinatura do orientador _____

Catalogação-na-publicação

Watai, Rafael de Andrade

A time-domain boundary elements method for the seakeeping analysis of offshore systems / R.A. Watai. – versão corr. – São Paulo, 2015.

259 p.

Tese (Doutorado) – Escola Politécnica da Universidade de São Paulo. Departamento de Engenharia Naval e Oceânica.

1.Comportamento no mar 2.Método de elementos de contorno no domínio do tempo 3.Sistemas multi-corpos I.Universidade de São Paulo. Escola Politécnica. Departamento de Engenharia Naval e Oceânica II.t.

I dedicate this thesis to my parents Ariovaldo and Vania and my brother Felipe.

To the woman of my life Isadora, for her love, inspiration and patience.

ACKNOWLEDGMENTS

I would like to express my gratitude to my friend Prof. Alexandre Nicolaos Simos, who has been supervising my scientific activities since my graduation period. I really appreciate his dedication on following closely the development of this thesis, keeping me motivated and confident to conduct my studies during the last years.

I gratefully acknowledge Prof. Kazuo Nishimoto for giving me numerous opportunities and votes of confidence, which were positively decisive in my personal and professional development. I am also very thankful to Prof. Claudio Mueller Prado Sampaio, Prof. Eduardo Aoun Tannuri and Prof. André Luis Condino Fujarra of the laboratory TPN-USP[1]. The conditions offered me at TPN in terms of office space and resources were excellent, providing me an adequate environment to write this thesis.

I am also indebted to Prof. Mardel Bongiovanni de Conti for teaching me the first lessons on programming the boundary elements method and to Prof. Celso Pupo Pesce by the relevant advices and text corrections, which certainly contributed to the achievements reached in this work.

A special thank you goes to my colleagues Guilherme Rosetti, Felipe Ruggeri and Rodrigo Lavieri with whom I have been learning and sharing many experiences for the last years. It has been a real pleasure working with such a talented and successful team, in which I truly want to continue being part and contributing for the next years.

I appreciate the valuable discussions, studies and technical publications conducted together with Pasquale Dinoi and Prof. Antonio Souto-Iglesias from ETSIN-UPM[2], who also gave me the opportunity to conduct a set of experimental tests in their facilities, in Madrid, in Spain, from which I obtained results that significantly increased the quality of

[1] Tanque de Provas Numérico da Escola Politécnica da Universidade de São Paulo
[2] Escuela Técnica Superior de Ingenieros Navales de la Universidad Politécnica de Madrid

this thesis.

I also acknowledge the financial support of FAPESP [3] PhD grant (2010/08778-2).

I am grateful to my friends who have contributed directly or not to the development of this work: Pedro Cardozo de Mello and Oygres Siqueira for their support on the conduction and planning of the experimental tests; Fabio Tadao Matsumoto and Edgard Borges Malta for the technical discussions, which helped me on solving many obstacles along the way; To all my friends of TPN with whom I have been working with every day; To my dear friends Fabio Massatoshi, Guilherme Daker, Fernando Alvarez, Kin Honda, Dante Cirillo, Guilherme Teixeira, Lucas Pesinato, Rodrigo Seródio, Ricardo Bertoni, Daniel Soares, Mariana Rhein, Fabiola Alvarez, Paula Leardini, Ana Paula Medeiros, Érica Sundfeld, Débora Takemura and Carolina Oliveira by the entertaining and necessary rest times during the weekends; To Isabel, Flavio and Bernardo Hoffmann for making me feel like I have a second family.

I am very thankful to my wife Isadora for being always by my side, motivating and giving me love and care every day. Thank you very much for the infinite patience and for my undesirable delays in several evenings, which forced you to stay with me at work until very late hours. You can count on me for everything and forever.

Finally, I am most thankful to my brother Felipe and to my parents Ariovaldo and Vania for all the support, trust and love. Your dedication on ensuring me the best education as possible is the most valuable lesson that I have ever learned since I was born and I will certainly pass on this learning to your grandchildren.

[3] Fundação de Amparo à Pesquisa do Estado de São Paulo

RESUMO

Esta tese apresenta o desenvolvimento de um método de elementos de contorno (BEM) no domínio do tempo baseado em fontes de Rankine para análise linear de comportamento no mar de sistemas oceânicos. O método é formulado por dois problemas de valor inicial de contorno definidos para os potenciais de velocidade e aceleração, sendo este último utilizado para calcular de maneira acurada a derivada temporal do potencial de velocidades. Testes de verificação são realizados para a solução dos problemas de difração, radiação e de corpo livre para flutuar. Uma vez verificada, a ferramenta é aplicada em dois problemas multicorpos considerados no estado-da-arte em termos de modelagem hidrodinâmica utilizando BEM. O primeiro trata do problema envolvendo duas embarcações atracadas à contrabordo. Este é um caso no qual os códigos baseados na teoria de escoamento potencial são conhecidos por apresentarem dificuldades na determinação das soluções, tendendo a superestimar as elevações de onda no vão entre as embarcações e a apresentar problemas de convergência numérica associados a efeitos ressonantes de onda. O problema é tratado por meio do método de *damping lid* e a convergência das séries temporais é investigada avaliando diferentes níveis de amortecimento. Os resultados são comparados com dados experimentais. O segundo problema se refere à análise de sistemas multicorpos com grandes deslocamentos relativos. Neste problema, ferramentas no domínio da frequência não podem ser utilizadas, por considerarem apenas malhas fixas. Deste modo, o presente método é estendido para considerar um gerador de malhas de painéis e um algoritmo de interpolação de ordem alta no laço de tempo do código, possibilitando a mudança de posições relativas entre os corpos durante a simulação. Os resultados são comparados com dados de experimentos executados especificamente para fins de verificação do código, apresentando uma boa concordância. De acordo com o conhecimento do autor, esta é a primeira vez que certas questões relativas à modelagem numérica destes dois problemas multicorpos são relatadas na literatura especializada em hidrodinâmica computacional.

Palavras-chave: comportamento no mar, método de elementos de contorno no domínio do tempo, sistemas multicorpos

ABSTRACT

The development of a time domain boundary elements method (BEM) based on Rankine's sources for linear seakeeping analysis of offshore systems is here addressed. The method is formulated by means of two Initial Boundary Value Problems defined for the velocity and acceleration potentials, the latter being used to ensure an accurate calculation of the time derivatives of the velocity potential. Verification tests for solving the diffraction, radiation and free floating problems are presented. Once verified, the code is applied for two complex multi-body problems considered to be in the state-of-the-art for hydrodynamic modelling using BEM. The first is the seakeeping problem of two ships arranged in side-by-side, a problem in which all potential flow codes are known to have a poor performance, tending to provide unrealistic high wave elevations in the gap between the vessels and to present numerical convergence problems associated to resonant effects. The problem is here addressed by means of a damping lid method and the convergence of the time series with different damping levels is investigated. Results are compared to data measured in an experimental campaign. The second problem refers to the analysis of multi-body systems composed of bodies undergoing large relative displacements. This is a case that cannot be properly analyzed by frequency domain codes, since they only consider fixed meshes. For this application, the present numerical method is extended to consider a panel mesh generator in the time loop of the code, enabling the change of body relative positions during the computations. Furthermore, a higher order interpolation algorithm designed to recover the solutions of a previous time-step was also implemented, enabling the calculations to progress with reasonable accuracy in time. The numerical results are compared to data of experimental tests designed and executed for verification of the code, and presented a very good agreement. To the author's knowledge, this is the first time that certain issues concerning the numerical modelling of these two complex multi-body problems are reported in the literature specialized in hydrodynamic computations.

Keywords: seakeeping, time domain boundary elements method, multi-body systems

List of Figures

List of Tables

Contents

Chapter 1

Introduction

1.1 Motivation

Seakeeping analysis is a topic of great importance for the design of floating systems, such as ships and oil and gas production units. In fact, the design of several subsystems and consequently the costs associated to each one may be directly impacted by the level of the motions that the floating system may present in waves. For example, oil platform hulls, even with appropriate responses to the waves excitation that result in low vertical displacements may be critical for enabling the use of the so-called rigid risers, which if applied, might reduce the costs for this type of subsystem significantly.

Current practice in the area of ocean engineering, the conduction of experimental activities with scaled models have provided great knowledge and understanding of complex phenomena involving the interaction among floating structures and environmental agents, such as waves, wind and current. Through these tests, observations and measurements can be performed in a controlled manner, partially isolating the effects of distinct external sources present in real environments. Nevertheless, scaled model tests often present difficulties in relation to physical limitations of the basins, specially when modelling systems that operate in deep waters. Moreover, since the tests require high costs and considerable time for its conduction, presently they are preferred for final design verifications and not as a prediction tool for earlier stages of the design.

Another approach commonly adopted in engineering problems is the use of numerical methods to solve the equations that describe the dynamics of the phenomenon in study.

Mathematical models may be solved numerically, providing approximate solutions to very complex problems which, in most cases, are impossible to be treated analytically. Numerical approaches are becoming increasingly popular in the various stages of engineering designs, mainly due to the growth of computational power and development of new techniques for numerical processing. In the context of offshore system designs, nowadays, it is often possible to observe applications of numerical methods, reducing the demand of experimental tests between the stages of conception and final verification.

The development of numerical tools used for solving problems of real fluid flows is one of the major areas of research in hydrodynamics. Its application is necessary when the phenomena that is being studied requires the inclusion of viscous effects as, for example, the prediction of forward resistance of ships or in the design of bilge keels used to reduce the amplitude on the roll motions of the ship. However, in spite of its increasingly widespread use, this approach is still very unpractical for many applications, since it demands high computational efforts and processing time to tackle the sophisticated numerical methods that handle the Navier-Stokes equations.

Thus, for the evaluation of seakeeping problems of offshore systems, other types of methods are applied. Due to the relatively small (and, somehow, punctual) influence of viscous effects, the problem is commonly addressed with the use of the potential flow theory, which allows one to determine the solutions more simply and quickly in comparison to numerical methods that deal with real fluid flows. In this context, the use of numerical methods that deal with potential boundary value problems, such as the Boundary Elements Method (BEM), is widely applied throughout the different design stages for solving the hydrodynamic issues.

Presently, BEM is present in several computational tools used to solve problems related to the hydrodynamic interaction of floating bodies with waves. Among several different alternatives for its implementation, frequency domain and time domain approaches are two distinct large groups that may be analyzed separately. The former approach is always used for linear or weakly nonlinear wave theories in which the time dependence can be removed by assuming that the solution is harmonic in time and, therefore, only steady solutions are obtained. In this case, we may list some examples of well-known commercial softwares as, for example, WAMIT[1], AQWA[2] and WADAM[3]. However, if no assumption about the steadiness of the solution is established, a time domain approach has necessarily to be applied. Although less efficient for problems involving single harmonic waves, time domain codes may be extended for more generic cases in which the inclusion of nonlinear terms or

[1] http://www.wamit.com
[2] http://www.ansys.com/Products/Other+Products/ANSYS+Aqwa
[3] http://www.dnv.com/services/software/products/sesam/sesamhydrod/wadam.asp

external loads from different sources (e.g. mooring lines) is implemented straightforwardly. However, the availability of time domain codes is fairly scarce and although there are reports of codes, such as TIMIT (KORSMEYER; BINGHAM; NEWMAN, 1999) and SWAN ((NAKOS, 1990), (KRING, 1994) and (HUANG, 1997)), most of them are not commercialized and their applicability is restricted to academic researches.

In offshore applications, in which most of the problems do not involve forward speed vessels, there is a widespread use of BEM in frequency domain due to its great efficient in providing the steady-state hydrodynamic loads and motions with low computational efforts. The results provided by these codes are normally presented in the form of transfer functions, or motions Response Amplitude Operators (RAOs), which, by their turn, also carry the assumption that the floating system dynamics is linear. Nevertheless, for some practical cases, this treatment brings severe limitations, such as for evaluating the motions of an oil platform under the influence of loads induced by risers and mooring lines installed on it. With the increase of water depth, the mass and damping of mooring lines and risers become nontrivial and the platform motions can be appreciably affected by them (YANG et al., 2012).

For the modelling of these systems it is common to use dynamic time domain simulators, which consider not only the effects of waves, but also those originated by wind, current and also from the dynamics of risers and mooring lines. Specifically to the linear wave problem, most of these simulators use potential hydrodynamic coefficients previously calculated in frequency domain and properly transposed to time domain by the use of the so-called memory functions. However, one should realize that some inconsistencies may appear if the body acquires large amplitudes of motion around its mean initial position, disobeying the original linear assumption established for the calculation of the hydrodynamic loads. Another issue emerges from problems involving more than one body, in which the transient hydrodynamic interaction that results from the relative displacement of the bodies must be taken into account. The offloading operation of a Floating Production Storage and Offloading (FPSO) unit is an example of this type of problem, in which, due to the proximity of the FPSO and the shuttle tanker, the wave effects induced by the vessels have an important role in the hydrodynamic loads and, consequently, in the dynamics of such a complex operation.

The use of time domain numerical methods then arises as an alternative approach to these problems, since the hydrodynamic calculations may be coupled to the bodies equations of motion solved by the dynamic simulator. A first benefit of such a treatment would be the possibility to handle the multi-body transient problems more suitably, even when applying, in a first moment, a linear method. Moreover, in comparison to models mathematically treated in frequency domain, this approach also allows addressing future

extensions to nonlinear descriptions of both the hydrodynamic and the dynamic problems in a more straightforward manner. Such extensions may enable one, for example, to consider the instantaneous wetted surfaces of the bodies and to deal, in a more satisfactory way, with viscous damping effects that, as nonlinear phenomena, are commonly modeled by a quadratic term involving the body velocities.

Therefore, considering the facts previously pointed out, we present in this text the development of a numerical method and, subsequently, of a computational tool written in MATLAB[4] that solves the linear transient hydrodynamic problem of floating bodies under the influence of free surface waves through the use of a linear time domain boundary elements method based on Rankine sources. Independently of its own practical interest, which has given favorable results to many problems regarding floating body dynamics, the robust and accurate solution of this linear problem is a very useful first stage before attempting to handle the complete non-linear problem. As will be presented ahead, the numerical code is firstly tested through a set of verification cases involving bodies of simple (hemisphere and circular cylinders) and realistic geometries, such as FPSO units. For these tests, the code is employed for solving the diffraction, radiation and free floating problems in waves, the results being compared to analytical, numerical and experimental data.

Once verified, the code is applied for the analysis of two complex multi-body problems that are currently in the state-of-the-art concerning the computational hydrodynamic modelling. In the first case, the performance of the code when applied to the seakeeping problem of two ships in side-by-side configuration is investigated. The main challenge of this problem is related to the occurrence of wave resonant effects in the gap between the vessels, which cause all potential flow codes to have convergence problems, since they are unable to model the viscous effects that are important for the correct modelling of the flow between the hulls. In order to mitigate this problem, a damping lid method is applied in the time-domain simulations and the convergence of the time series with different damping levels is investigated. To the author's knowledge, this is the first time that certain issues concerning the numerical modelling of the resonant effects in time domain are reported in the literature specialized in side-by-side operations. Regarding the second case study, a new method to handle the multi-body problem with bodies undergoing large relative displacements is presented. Due to the transient nature of the problem, this is a case that cannot be properly analyzed by frequency domain codes, since they only consider fixed meshes. In this regard, a numerical procedure that couples the hydrodynamic solver with a re-meshing and a free surface interpolation algorithm is presented. This new implementation enables the change of relative positions between the

[4]http://www.mathworks.com/

vessels along the simulations. The numerical results are compared to data obtained in experimental tests designed and executed for verification of the code, and present a very good agreement.

1.2 Text Outline

Bearing the developments of a time domain code in mind we organized this text as follows:

Chapter 2 presents a literature review including the main publications which were consulted throughout the doctoral work.

Chapter 3 formulates the theoretical description of the problem involving floating bodies and free surface waves. The fluid is assumed incompressible and non-viscous whereas the flow is assumed irrotational. A set of nonlinear boundary conditions describing the dynamics and kinematics of the domain surroundings are then presented and linearized for providing less restrictive applications in terms of the body geometries and consumption of computational time in comparison to numerical methods that deal with nonlinear problems. Special attention is given for the determination of the velocity potential time derivative and, consequently, the pressure field. As time-domain codes require a coupled solution of the hydrodynamic and body dynamics problems in time, an imprecise prediction of this quantity may give rise to numerical instabilities and, therefore, we decided for the use of a second integral equation using the so-called acceleration potential.

In **Chapter 4** we apply Green's second identity and transform the Laplace's field equations for the velocity and acceleration potentials in two integral equations. This procedure allow us to establish a numerical model which evaluates the quantities only on the boundaries of the fluid domain and, therefore, reduces the problem dimension to two. A brief discussion about the choice of singularities distribution over the surfaces and about the kind of integral equations that result from this choice is also presented. Among a few alternatives, we have decided for a mixed source-dipole distribution, defining all the boundary surfaces but the free surface as Neumann boundaries.

Chapter 5 presents the numerical algorithms used to deal with the present time domain linear wave-body formulation. The solutions of the integral equations are calculated by means of a low order boundary elements method that transforms the continuous equations into a set of algebraic ones that may be described as two linear systems with full matrices. By the use of this method, the boundary surfaces are discretized in a finite number of plane quadrilateral/triangular panels over which the potential and its normal derivative are assumed to have constant values. The time-marching scheme is performed by a Fourth

Order Runge-Kutta method (RK4) that integrates the body equations of motion and also updates the boundary conditions.

Chapter 6 presents the hydrodynamic loads obtained by the solution of the so-called diffraction and radiation problems for an hemisphere and a vertical circular cylinder. Moreover, free floating simulations involving these geometries are also presented. The accuracy of the results obtained is investigated by comparisons performed with data computed by software WAMIT and, for the case of the hemisphere, also analytic solutions given by Hulme (1982). The convergence of the numerical method is checked by recalculating the hydrodynamic loads with different panel mesh resolutions.

Chapter 7 tests the present numerical code for a more realistic situation, presenting results of free floating FPSOs under the influence of incoming waves, being these regular or irregular, with different incidence angles. Results are presented in the form of time-series of motions, free surface wave patterns and motion RAOs, which are verified by comparisons with motion RAOs calculated by WAMIT and results obtained experimentally in the Hydrodynamic Calibrator of the TPN-USP (CH-TPN-USP).

Chapter 8 reports the performance of the method considering a multi-body problem involving two ships in side-by-side arrangement, as, for example, in a FLNG offloading operation. The chapter also describes the experimental campaign carried out in the ETSIN-UPM, in Spain, from which data is here used for validation purposes of the present method. Comparison between measurements and numerical results illustrates the limitation of potential flow solvers concerning the modelling of this hydrodynamic problem. Numerical wave resonance in the gap led to wave elevations and body motions much larger than those observed during the tests. In addition, the time domain method also presented convergence problems for frequencies associated to the gap resonance phenomenon. In order to overcome these problems, an external damping factor was introduced in the time domain simulations, bringing a significant improvement to the numerical convergence of the method. Moreover, despite the simplicity of the damping model adopted, the results showed that this technique was indeed able to improve the computational predictions, leading to a closer agreement between the experiments and the numerical results.

Chapter 9 presents a new method for dealing with multi-body hydrodynamic interactions of bodies undergoing large relative displacements, a problem that cannot be assessed directly with frequency domain codes. This is done by extending the numerical method with the possibility of including a generator of unstructured triangular panel meshes in the time loop of the code so as to account for changes of the relative positions between the bodies during the calculations. In addition, a specific higher order interpolation algorithm designed to recover properly the solutions of a previous time-step was also implemented,

enabling the calculations to progress with reasonable accuracy in time. The numerical results are compared with data of experimental tests designed specifically for validation purposes, presenting a very good agreement for most of the cases.

The final conclusions and suggestions for future works are presented in **Chapter 10**.

Chapter 2

Literature Review

Most of the developments presented herein arise from basic fluid dynamic equations that state the conservation laws of mass and linear momentum. Mathematical description of this problem may result in different governing equations which depend on the established assumptions concerning the fluid properties and also its motion. The description of water wave motions, in which a great part of the present study is related, allows one to assume the fluid as Newtonian and to describe the flow as incompressible by restricting its motions to moderate Mach number ($M_a < 0.3$). Based on these hypotheses, mass conservation is mathematically guaranteed by requiring that the divergence of the fluid velocity field is zero whereas the momentum conservation is described by the Navier-Stokes equations. Although some of these mathematical derivations are presented further ahead, we consider them merely as simple presentations of the equations that form the basis of our developments and for a full comprehension of this topic we refer to the widely used textbooks of Lamb (1945), Batchelor (1967) and Thomson (1968).

The success of a mathematical model of the physical reality depends on its quality to predict the phenomena of interest with sufficient accuracy and minimum possible effort. Although Navier-Stokes equations are supposed to be the most exact way to describe the flow of a Newtonian fluid, their mathematical solution is extremely complex and, for that reason, it is only applied in problems in which the viscous effects cannot be neglected. Fortunately, simplifications of these equations may be performed by observing that the influence of viscosity on the seakeeping prediction of floating systems, such as oil platform units, is limited to a thin boundary layer near the hull, which does not influence the dominant effects induced by the oscillatory motions and incoming waves. This is guaranteed when the Keulegan-Carpenter number KC (see equation (2.1)) is small, i.e,

the oscillatory motion amplitude A of the body is small compared to its characteristic dimension D. In the seakeeping context of floating bodies, however, this is not always true, especially, near resonant frequencies, for which even waves of small amplitude may lead to large body displacements. In this case, empirical external damping coefficients must be imposed in order to emulate the viscous effects acting on the body. Apart from this exception, in general viscous effects can still be neglected and by assuming that the vorticity throughout the fluid is zero we may treat our problem under the view of the potential flow theory.

$$KC = \frac{VT}{D} = \frac{A\omega\frac{2\pi}{\omega}}{D} = \frac{2\pi A}{D} \tag{2.1}$$

Despite of this important simplification, a set of nonlinear boundary conditions originated from the free surface and the floating body surface still render the problem difficult to be solved and, therefore, further approximations are usually applied. Following the classical work of Stokes (1847), Stoker (1957) applies a perturbation technique which proposes the expansion of the involved quantities (e.g. velocity potential, free surface elevation etc.) in a power series, turning the original nonlinear problem into a sequence of linked linear ones, which allows treating the problem in different orders of magnitude. The linear solution, in particular, forms the basis for the study of all the other wave theories. Within this scope, besides the publications aforementioned, the works developed by Sarpkaya and Isaacson (1981) and Mei, Stiassnie and Yue (2005a) are recommendable readings.

The mathematical formulation of problems involving the motion of floating bodies can be addressed following the same technique. Extensive mathematical derivations and discussions for the linear, or first order problem, are presented by John (1949), John (1950) and Wehausen (1971). The second order formulation may be found in, among several others, Pinkster (1980) and Mei, Stiassnie and Yue (2005b).

Most of the developments achieved by these studies are based on the assumption of small amplitude waves and body displacements around a mean position, which allows a major simplification of the equations and even analytical solutions for problems involving very simple geometries, as those presented in Hulme (1982) and Bhatta and Rahman (2003). These solutions have a wide range of applications, but it eventually becomes necessary to find out alternatives in order to deal with bodies with arbitrary geometries that enable one to analyze the complex designs currently observed in modern offshore structures. In this sense, the use of numerical methods becomes necessary, as for example, the boundary elements method, also known as panel method. In this method, the problem is treated by means of an integral equation which needs to be solved for obtaining the velocity potential induced by a continuous distribution of singularities over the domain surfaces.

Hess and Smith (1967) are considered pioneers in the development of panel methods, demonstrating its applicability for obtaining the fluid flow around three-dimensional body geometries in infinite fluid. In their method, the body surface is discretized in a finite number of plane quadrilateral panels with source strength considered constant over each one of them, an assumption that simplifies the integration of the singularities considerably. Under these assumptions the method is also known as a Low-Order Panel Method.

For applications in wave-body formulations the method can be segregated into two different categories based on the type of singularity employed in the integral equations. The first category makes use of the so-called free surface Green function, which automatically satisfies both the radiation and the linearized free surface conditions. Wehausen and Laitone (1960) present some of these functions derived to satisfy different types of boundary conditions, such as the ones for linear free surface waves in finite water depth. This approach is commonly used for linear and weakly-nonlinear wave-body theories in which the time dependence can be removed by assuming that the solution is harmonic in time and, therefore, the solution may be addressed by a frequency domain approach (see for instance Newman (1992), Yang, Noblesse and Löhner (2004) and Lee and Newman (2005) for an overview of marine hydrodynamics applications).

Firstly presented by Gadd (1975) and Dawson (1977), the second category of the method applies the simple Rankine sources as the basic singularity and, therefore, not only the body surface but also the free surface must be discretized. Despite this inconvenient, Rankine source methods are much easier to handle and also accept a more flexible choice of free surface conditions which allow, for example, the inclusion of nonlinear terms that have to be necessarily neglected in Green function formulations and a more suitable treatment for problems involving bodies with forward speed, as discussed in Nakos (1990) and Sclavounos and Nakos (1993).

Boundary elements methods in frequency domain are widely used for solving linear problems due to its great efficiency in providing solutions with relatively low computational efforts. This may be explained, since both the radiation and free surface conditions are automatically satisfied by the Green function and then only the wet body surface must be discretized. On the other hand, Green functions and its derivatives are very difficult to compute and may only be determined for linear free surface conditions. Besides that, the method loses efficiency when higher order effects have to be considered since the free surface needs now to be discretized and the computational efforts associated to the calculation of second-order effects are significantly increased. In addition, as only steady-state solutions are assessed, frequency domain approaches lead to some limitations concerning multi-body simulations with large relative displacements, as pointed out by Tannuri et al. (2004), Queiroz Filho and Tannuri (2009) and Bunnik (2014).

Bearing these constraints in mind, a method of solution in time domain using Rankine sources as the basic singularities appears as an interesting alternative, in which the inclusion of nonlinear terms and the solution of transient problems are handled more suitably. For these reasons, Kring (1994) extended the work of Nakos (1990) and developed a linear time domain boundary elements method for the evaluation of the transient forces and motions of floating bodies with, and without, forward speed. Giving continuity to these works, Huang (1997) applied the so-called weak-scattering-method that does not restrict the amplitudes of the incoming waves and the body motions to small values by assuming that the diffracted and radiated waves from a slender body may be neglected.

An interesting approach is observed in Kim, Kring and Sclavounos (1997), in which the linear and the second order problems are solved simultaneously in time domain by forcing the problem with a group of waves with different frequency components. This led to the straightforward calculation of the hydrodynamic forces in time domain, overcoming the time consuming procedure required for the computation of the Quadratic Transfer Function (QTF) matrices in frequency domain.

The different approaches available for nonlinear extensions is reviewed in the work of Singh and Sen (2007). Apart from the simplifications, or not, of the boundary conditions equations, the inclusion of nonlinear terms are basically related to corrections of the body and free surface positions in time. In this sense, in the linear approach the mesh grid remains fixed during the simulations whereas for the nonlinear methods a re-gridding procedure becomes necessary.

Independently of the method or approach, time domain simulations require an accurate prediction of the pressure field in order to generate a consistent and stable numerical algorithm. A main concern is the proper evaluation of the velocity potential time derivative, which in the original problem must be determined by a backward finite difference scheme in time. This procedure may give rise to numerical instabilities. One way to overcome this problem is the computation of the so-called acceleration potential, widely investigated by Tanizawa (2000). Within different schemes, four of them are considered to be the most consistent: (1) iterative method ((CAO; R.; SCHULTZ, 1994)), (2) modal decomposition method ((COINTE et al., 1991) and (KOO; KIM, 2004)), (3) indirect method ((TAYLOR; WU, 1996)) and (4) implicit boundary condition method ((VAN DAALEN, 1993) and (TANIZAWA, 1995)).

The application of a numerical method capable of satisfying the radiation condition and, therefore, of avoiding that waves reflected at the numerical boundaries have an impact on the solution is also a major concern. In practice, this condition is imposed by absorption or dissipation schemes widely discussed in the literature, as reviewed by Romate (1992).

Orlanski (1976) proposed a numerical scheme to ensure the absorption of regular waves. This condition, however, is limited to cases in which the angular frequency is known, or in the presence of very long waves, as observed by Clément (1996). In this sense, the use of numerical damping zones, introduced by Israeli and Orszag (1981), is less restrictive since it can dissipate waves within a wide frequency range. This is performed by including extra damping terms in the free surface boundary conditions applied on a limited portion of this surface. In practice, there are various differential schemes that may be applied (KIM; KOO; HONG, 2014) and the relatively easy way for implementing them together with the benefits aforementioned have led to a widespread use of this technique, which is demonstrated by the large number of works related to different approaches as, for example, Prins (1995), Bunnik (1999), Boo (2002), Shao (2010) and Zhen et al. (2010).

Fully nonlinear simulations by adopting a mixed Eulerian-Lagrangian approach is another topic with an increasing number of publications. First introduced by Longuet-Higgins and Cokelet (1976), this complex method deals with the nonlinear boundary conditions by re-gridding the moving surfaces in time. Within three and two-dimensional developments, detailed descriptions of this method may be found in Romate (1990), Cointe (1990), van Daalen (1993), Beck, Cao and Lee (1994), Ferrant (1997), Liu, Xue and Yue (2001a), Liu, Xue and Yue (2001b) and Bai and Taylor (2009). However, it is known that two main problems arise in the implementation of this method. According to Beck and Reed (2000), for a stable free surface time marching scheme, the method requires the use of smoothing techniques and the inclusion of artificial damping coefficients at the free surface points. Moreover, wave breaking phenomenon may naturally occur due to the fully nonlinear description of the free surface, and this, unfortunately, often causes the numerical solutions to break down.

Chapter 3

Theoretical Background

3.1 Problem Definition

The problem of a floating body interacting with free surface gravity waves is here considered. In this situation, incoming waves that propagate on the free surface are disturbed by the floating bodies inducing unsteady forces and moments due to the generation of pressure changes in the fluid. Floating bodies then respond by acquiring translational and rotational motions, which also force the fluid to move. Mathematical description of this problem may result in different governing equations depending on the assumptions on the motions of the body and the fluid. Moreover, it is usual to separate the equations that describe the behavior of the fluid and the floating body, which are then linked again by appropriate equations and matching conditions that define the wave-body formulations. The following items present the theoretical formulations and their correspondent assumptions and simplifications on which the solutions of our problem will be based.

3.2 The Initial Boundary Value Problem

Let us define three mutually perpendicular unit vectors $\vec{e}_1$, $\vec{e}_2$, and $\vec{e}_3$ which form the basis of two coordinate systems here denoted by:

- The first system of coordinate axes $O-(x, y, z)$ is a right-handed earth-bound axes cartesian system with origin O, with x and y axes in the mean free surface and positive z axis pointing upwards and out of the fluid. A point in space has position

or displacement vector $\vec{\delta} = (x, y, z)$.

- The second system $CoG - (X, Y, Z)$ is a body-fixed right-handed axes cartesian system with origin at the body center of gravity CoG, with positive X axis in the longitudinal direction (body bow direction) and the positive Z axis pointing upwards. The hull surface is defined exclusively in this coordinate system, being a point on the body surface described by the vector $\vec{r} = (X, Y, Z)$. The orientation of a surface element is defined by a normal vector pointing inward of the body $\vec{n} = (n_x, n_y, n_z)$.

Figure 3.1 illustrates a body floating somewhere in the sea in which incoming gravity waves propagate on a free surface S_{FS} with angular frequency ω, length λ and in a direction which makes an angle θ with the X-axis of the established body-bound reference frame.

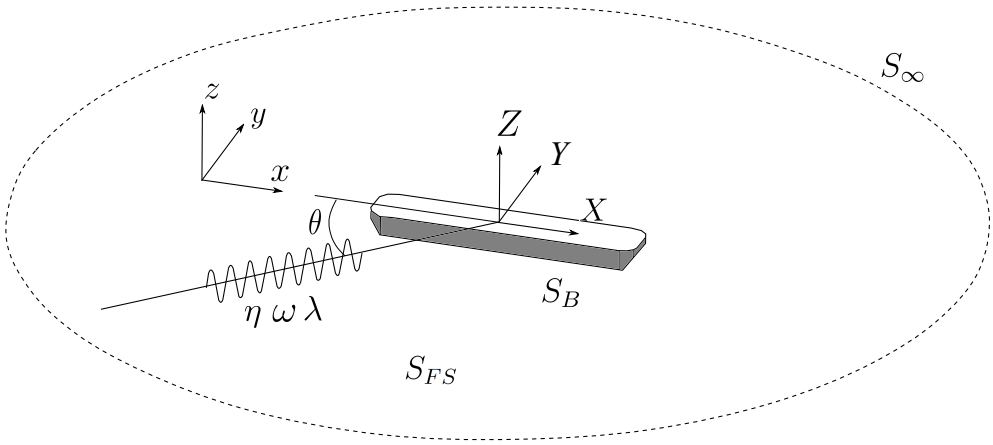

Figure 3.1: Definition of the coordinate systems

Focusing our analysis in the fluid, we consider an arbitrary control volume Ω delimited by a surface $\partial\Omega$ with normal vector $\vec{n} = (n_x, n_y, n_z)$ pointing outwards the fluid domain. The flow velocity field is then defined by $\vec{v} = (u, v, w)$ in which $u(x, y, z, t)$, $v(x, y, z, t)$ and $w(x, y, z, t)$ are the scalar components of the velocity field at time t, at a point with spatial coordinates (x, y, z).

We consider the flow to be irrotational and incompressible whereas the fluid is assumed inviscid and homogeneous, allowing the velocity field to be defined by the gradient of the potential scalar field or velocity potential Φ:

$$\vec{v} = \nabla\Phi \tag{3.1}$$

Under these assumptions, mass conservation is stated by the Laplace´s equation (3.2) whereas the conservation of linear momentum is expressed by Bernoulli's equation (3.3):

$$\nabla^2\Phi = 0 \tag{3.2}$$

$$\frac{\partial\Phi}{\partial t} + \frac{1}{2}\left(\nabla\Phi\cdot\nabla\Phi\right) + gz = -\frac{p-p_0}{\rho} + C(t) \tag{3.3}$$

where p_0 is the atmospheric pressure and $C(t)$ is a constant parameter dependent on time, normally omitted since it can be easily absorbed into the velocity potential by redefining the latter without any loss of generality of the solution.

Equations (3.2) and (3.3) compose the governing equations which describe the motion of an homogeneous and inviscid fluid under the assumptions of incompressibility and that the vorticity throughout the fluid is zero (i.e. irrotational flow). Unique solutions for Φ must then be calculated, particularizing the solutions of Laplace's equation (3.2) by the imposition of boundary conditions which, in simple words, are necessary to match the dynamics and kinematics of the fluid with the physical boundaries of the fluid domain Ω, such as, the wet surface of the floating body $S_B(t)$, the sea bottom surface S_{BO} and the free-surface $S_{FS}(t)$.

The free surface $S_{FS}(t)$, its position being not known a priori, demands the description of a kinematic and a dynamic boundary condition. The kinematic condition states that the velocities of the fluid and the free-surface boundary must be equal, whereas the dynamic one imposes that, neglecting surface tensions, the pressure on the free surface must equal the atmospheric pressure.

Thus, the dynamic boundary equation may be determined through the straightforward use of Bernoulli's equation (3.3), applying it at the exact free surface elevation, here denoted by the single-valued function $\eta(x, y, t)$:

$$\frac{\partial\Phi}{\partial t} + \frac{1}{2}\left(\nabla\Phi\cdot\nabla\Phi\right) + gz = 0 \quad \text{on } z = \eta(x, y, t) \tag{3.4}$$

As a consequence of the velocities compatibility on the free surface, fluid particles that are at the free surface will remain attached to the free surface. Furthermore, considering that these particles are vertically described by a coordinate z, a mathematical function $F(x, y, z, t) = 0$ which defines the free surface can be described as $F(x, y, z, t) = z - \eta(x, y, t) = 0$. Therefore, the kinematic condition may be expressed assuming that the

material derivative of the quantity $z - \eta(x, y, t)$ vanishes on the free surface.

$$\frac{\mathrm{D}}{\mathrm{D}t}(z - \eta) = \frac{\partial \Phi}{\partial z} - \frac{\partial \eta}{\partial t} - \frac{\partial \Phi}{\partial x}\frac{\partial \eta}{\partial x} - \frac{\partial \Phi}{\partial y}\frac{\partial \eta}{\partial y} = 0 \quad \text{on } z = \eta(x, y, t) \tag{3.5}$$

Description of the free surface by the function $\eta(x, y, t)$ excludes the possibility of studying the phenomena of overturning waves, since $\eta(x, y, t)$ may only assume one single value for the pair (x, y) at a given instant t. Despite such simplification, this approach is widely used and is sufficient for the evaluation of several hydrodynamic problems, such as the calculation of first and second order forces and motions of a floating vessel in the sea, as may be observed, for example, in Newman (1977), Pinkster (1980) and Faltinsen (1990). Other possibilities are also found in literature to deal with the case of very steep waves, in which a Lagrangian or mixed Eulerian-Lagrangian descriptions is used (see for instance Longuet-Higgins and Cokelet (1976)), but due to the difficult and time-consuming simulations associated with the numerical schemes applied, this alternative is still restricted to very simple applications. Although modern computers continue to push the limits of practicability, these drawbacks are still not acceptable for many engineering applications.

The boundary conditions associated to the floating body wet surface $S_B(t)$ and sea bottom surface S_{BO} are mathematically described by Neumann conditions which impose that the fluid particles may not penetrate these surfaces. For the sea bottom and other time-independent surfaces that may exist in the problem, this is represented by the well-known zero-flux condition (3.6).

$$\nabla \Phi \cdot \vec{n} = \frac{\partial \Phi}{\partial n} = 0 \quad \text{on } S_{BO} \tag{3.6}$$

The conditions on the wet surfaces of floating bodies and other time-dependent surfaces are treated in a very similar manner as the bottom surface. Nevertheless, the motions of these boundaries influence the movements of the fluid at their surroundings, requiring a compatibility condition between the fluid and the surfaces to guarantee an impermeability condition, as presented in equation (3.7):

$$\nabla \Phi \cdot \vec{n}(t) = \frac{\partial \Phi}{\partial n} = \frac{\partial \vec{\delta}(t)}{\partial t} \cdot \vec{n}(t) \quad \text{on } S_B(t) \tag{3.7}$$

where the time-dependent displacement $\vec{\delta}$ of a point of the floating body relative to the earth-bound system of axes is defined as:

$$\vec{\delta}(t) = \vec{\xi}_T(t) + \vec{\xi}_R(t) \times \vec{r} \tag{3.8}$$

where $\vec{\xi}_T(t) = (\xi_1, \xi_2, \xi_3)$ and $\vec{\xi}_R(t) = (\xi_4, \xi_5, \xi_6)$ are formed by the translation and rotation of the body and $\vec{r}$ is the position vector of the point on the body in the body-bound axes system, measured with relation to the center of gravity.

Notice that neither the surface point displacement $\vec{\delta}(t)$ nor the surface normal vector $\vec{n}(t)$ are known in advance for problems involving free floating bodies and, therefore, an additional set of equations which describe the motions of a rigid body need to be included. Supposing that the velocity potential Φ is determined, the pressure field is calculated through the use of equation (3.3) and, consequently, both the hydrodynamic forces and moments acting on the body are obtained by pressure integration, as presented in equations (3.9) and (3.10):

$$\vec{F} = \iint_{S_B(t)} p\,\vec{n}\,\mathrm{d}S \tag{3.9}$$

$$\vec{M} = \iint_{S_B(t)} p\,(\vec{r} \times \vec{n})\,\mathrm{d}S \tag{3.10}$$

Applying Newton's second law and supposing small angular displacements, which is consistent with the formulation that will be presented ahead, the motion equations may be written as:

$$\mathbf{M}\frac{\mathrm{d}^2\vec{\xi}}{\mathrm{d}t^2} = \begin{pmatrix} \vec{F} \\ \vec{M} \end{pmatrix} \tag{3.11}$$

where $\mathbf{M}$ is the matrix of mass/inertia and $\vec{\xi} = (\xi_1, \xi_2, \xi_3, \xi_4, \xi_5, \xi_6)$ is the vector containing the motion components in six degrees of freedom (D.O.F.) of a rigid body that correspond to surge, sway, heave, roll, pitch and yaw, respectively.

The last, but not less important, boundary condition is the radiation condition, which in the time domain approach must enforce that the waves generated by the bodies are outgoing waves only and do not reflect somewhere allowing these waves to interfere with the body motions once again. In practice, this condition is imposed by absorbing or dissipation schemes widely discussed in literature, being the numerical beach zone an

efficient, and maybe the most simple alternative, to be applied. Details on how this condition is tackled in this work can be found in section 3.3.

In order to close this Initial Boundary Value Problem (IBVP), an initial condition must be imposed at the free surface so as to determine the subsequent fluid motions. As demonstrated by Stoker (1957), for flows starting from the rest we may set the velocity potential at the initial instant $t = 0$ s as:

$$\Phi = 0 \quad \text{on } t = 0 \text{ s} \tag{3.12}$$

Summarizing, the nonlinear wave-body formulation presented is formed by an elliptic field equation represented by Laplace's equation with correspondent boundary conditions that particularize its solutions to the one we are interested in. Although Laplace's equation is a linear homogeneous partial differential equation, the boundary conditions have several sources of nonlinearities as, in some cases, they must be applied in time dependent surfaces not known in advance, conditions that make the problem very complex to be solved. Despite this complexity, numerical algorithms that deal with this fully nonlinear problem are becoming popular in recent years, thanks to the fast increase in computer processing capacity. However, most of them are still limited to two-dimensional studies or very simple three-dimensional geometries and consequently are not adequate for simulating the behavior of real ship vessels, oil platforms or the hydrodynamic interactions involved in multi-body arrangements. Therefore, as a first step we have decided to linearize the formulation and to develop a linear computational code based on the simplified formulation presented in the remainder of this chapter.

3.3 The Linear Formulation

Linearization begins by assuming that the incoming gravity waves addressed herewith have small amplitude A_I and steepness $\epsilon = kA_I$, in which k is the wave number.

In order to linearize the problem, we apply a classical perturbation technique using expansions in Stokes's series, as described, for example, by Stoker (1957). Thus, to obtain a linear formulation, we perturb all the variables using the small parameter ϵ and substitute them in the set of nonlinear equations already presented. With this approach, we may identify and collect terms of order up to ϵ for a linear problem and consequently higher orders terms for the other problems.

As already presented, free surface condition is represented by two boundary conditions

which are nonlinear equations for basically two reasons: first, there are products involving not known variables as the velocity potential, free surface elevation and their derivatives. Second, both conditions must be applied on a surface which is not known in advance and is also part of the solution. The velocity potential Φ and the wave elevation η are then perturbed using the small wave steepness parameter ϵ, as follows:

$$\Phi = \bar{\Phi} + \epsilon\Phi^{(1)} + \epsilon^2\Phi^{(2)} + \mathscr{O}(\epsilon^3) \tag{3.13}$$

$$\eta = \bar{\eta} + \epsilon\eta^{(1)} + \epsilon^2\eta^{(2)} + \mathscr{O}(\epsilon^3) \tag{3.14}$$

hereafter, the horizontal bar $(^{-})$ over the variables account for mean values, in time sense, and the superscripts $^{(i)}$ denote the different orders of magnitude.

We now substitute the perturbed quantities (3.13) and (3.14) in the free surface conditions (3.4) and (3.5), and group terms of the same order, obtaining:

$$\begin{aligned}&\frac{\partial\bar{\Phi}}{\partial t} + \frac{1}{2}\nabla\bar{\Phi}\cdot\nabla\bar{\Phi} + g\bar{\eta} + \epsilon\left(\frac{\partial\Phi^{(1)}}{\partial t} + \nabla\bar{\Phi}\cdot\nabla\Phi^{(1)} + g\eta^{(1)}\right)\\ &+ \mathscr{O}(\epsilon^2) = 0 \quad \text{on } z = \bar{\eta} + \epsilon\eta^{(1)} + \mathscr{O}(\epsilon^2)\end{aligned} \tag{3.15}$$

$$\begin{aligned}&\frac{\partial\bar{\Phi}}{\partial z} - \frac{\partial\bar{\eta}}{\partial t} - \frac{\partial\bar{\Phi}}{\partial x}\frac{\partial\bar{\eta}}{\partial x} - \frac{\partial\bar{\Phi}}{\partial y}\frac{\partial\bar{\eta}}{\partial y}\\ &+ \epsilon\left(\frac{\partial\Phi^{(1)}}{\partial z} - \frac{\partial\eta^{(1)}}{\partial t} - \frac{\partial\bar{\Phi}}{\partial x}\frac{\partial\eta^{(1)}}{\partial x} - \frac{\partial\Phi^{(1)}}{\partial x}\frac{\partial\bar{\eta}}{\partial x} - \frac{\partial\bar{\Phi}}{\partial y}\frac{\partial\eta^{(1)}}{\partial y} - \frac{\partial\Phi^{(1)}}{\partial y}\frac{\partial\bar{\eta}}{\partial y}\right)\\ &+ \mathscr{O}(\epsilon^2) = 0 \quad \text{on } z = \bar{\eta} + \epsilon\eta^{(1)} + \mathscr{O}(\epsilon^2)\end{aligned} \tag{3.16}$$

Collecting terms of order up to ϵ and dropping out the time-independent mean values, since they are only important for problems involving bodies with forward speed, we find:

$$\frac{\partial\Phi^{(1)}}{\partial t} + g\eta^{(1)} = 0 \quad \text{on } z = \eta^{(1)} \tag{3.17}$$

$$\frac{\partial\Phi^{(1)}}{\partial z} - \frac{\partial\eta^{(1)}}{\partial t} = 0 \quad \text{on } z = \eta^{(1)} \tag{3.18}$$

One should notice that equations (3.17) and (3.18) are still being applied in unknown positions. In order to overcome this problem, we may expand these equations in Taylor's

series around the undisturbed free surface position $z = 0$.

$$\left(\frac{\partial \Phi^{(1)}}{\partial t} + g\eta^{(1)}\right)|_{z=\eta} = \left(\frac{\partial \Phi^{(1)}}{\partial t} + g\eta^{(1)}\right)|_{z=0}$$
$$+ \eta^{(1)}\frac{\partial}{\partial z}\left(\frac{\partial \Phi^{(1)}}{\partial t} + g\eta^{(1)}\right)|_{z=0} = 0 \quad \text{on } z = 0 \tag{3.19}$$

$$\left(\frac{\partial \Phi^{(1)}}{\partial z} - \frac{\partial \eta^{(1)}}{\partial t}\right)|_{z=\eta} = \left(\frac{\partial \Phi^{(1)}}{\partial z} - \frac{\partial \eta^{(1)}}{\partial t}\right)|_{z=0}$$
$$+ \eta^{(1)}\frac{\partial}{\partial z}\left(\frac{\partial \Phi^{(1)}}{\partial z} - \frac{\partial \eta^{(1)}}{\partial t}\right)|_{z=0} = 0 \quad \text{on } z = 0 \tag{3.20}$$

Finally, if we keep terms of order up to ϵ, we find the linear dynamic (3.21) and kinematic (3.22) free surface conditions:

$$\frac{\partial \Phi^{(1)}}{\partial t} + g\eta^{(1)} = 0 \quad \text{on } z = 0 \tag{3.21}$$

$$\frac{\partial \Phi^{(1)}}{\partial z} - \frac{\partial \eta^{(1)}}{\partial t} = 0 \quad \text{on } z = 0 \tag{3.22}$$

An analytic solution may be found for the boundary value problem defined by the Laplace's equation with the set of boundary conditions formed by the kinematic and dynamic boundary conditions, and zero flux condition at the bottom surface. For example, for a constant water depth h, the corresponding incoming regular wave field potential is defined by the following expression:

$$\phi_I = \frac{A_I g}{\omega}\frac{\cosh k(h+z)}{\cosh kh}\cos(kx - \omega t) \quad \text{on } z \leq 0 \tag{3.23}$$

The linear wave dispersion relation is given by:

$$\omega^2 = kg \tanh kh \tag{3.24}$$

where ω is the incoming wave angular frequency.

This solution is very useful when we are dealing with a time-domain description of the problem because we may decompose the total potential Φ in a sum of a first order disturbed wave field $\phi^{(1)}$ and the incoming regular wave field ϕ_I, thus avoiding then the necessity of modelling a numerical wave maker device to simulate the later. Since ϕ_I is a known

solution we only need to include it in the zero-flux conditions accordingly.

From now on the variable of the problem Φ will be changed by $\phi^{(1)}$ redefining also the set of boundary conditions that must be imposed. As ϕ_I satisfies the free surface conditions, these will be described by simply changing the variable Φ by $\phi^{(1)}$. For the other conditions, however, we will need to include the incoming wave potential as will be described next.

From the previous section 3.2, it may be observed that the set of equations to be solved are still nonlinear since the impermeability condition for moving bodies (3.7) and the equations for forces (3.9) and moments (3.10) are also applied in a time dependent surface $S_B(t)$. In order to linearize these boundary conditions, a procedure similar to the one applied to the free surface conditions can be used by expanding the variables in Stokes's series and then applying Taylor's series around a mean position $\bar{S}_B$, assuming that the body presents only small relative displacements around it. Beginning with the impermeability condition (3.7), we define expressions for the perturbed displacement vector $\vec{\delta}(t)$ and the normal vector $\vec{n}(t)$, as follows:

$$\vec{\delta} = \bar{\vec{\delta}} + \epsilon\vec{\delta}^{(1)} + \epsilon^2\vec{\delta}^{(2)} + \mathscr{O}(\epsilon^3) \tag{3.25}$$

$$\vec{n} = \bar{\vec{n}} + \epsilon\vec{n}^{(1)} + \epsilon^2\vec{n}^{(2)} + \mathscr{O}(\epsilon^3) \tag{3.26}$$

Substituting expressions (3.25) and (3.26) in equation (3.7) and collecting terms up to order ϵ, results in:

$$\nabla\phi^{(1)} \cdot \bar{\vec{n}} = \frac{\partial\vec{\delta}^{(1)}}{\partial t} \cdot \bar{\vec{n}} - \nabla\phi_I \cdot \bar{\vec{n}} \quad \text{on } S_B(t) \tag{3.27}$$

Applying the Taylor expansion around $\bar{S}_B$, we obtain the linear boundary condition:

$$\nabla\phi^{(1)} \cdot \bar{\vec{n}} = \frac{\partial\vec{\delta}^{(1)}}{\partial t} \cdot \bar{\vec{n}} - \nabla\phi_I \cdot \bar{\vec{n}} \quad \text{on } \bar{S}_B \tag{3.28}$$

To obtain the first order forces and moments on the floating body, the integration of the pressure field p must also be performed on the mean surface $\bar{S}_B$. Moreover, since the pressure is determined by the nonlinear Bernoulli's equation (3.3), it also needs to be linearized by using the expansion technique in order to keep the formulation coherent with the established linear formulation. Following the same procedures presented before,

the next equations are then obtained:

$$p^{(1)} = -\rho \left(\frac{\partial \phi^{(1)}}{\partial t} + \frac{\partial \phi_I}{\partial t} \right) \tag{3.29}$$

$$\vec{F}^{(1)} = \iint_{\bar{S}_B} -\rho \left(\frac{\partial \phi^{(1)}}{\partial t} + \frac{\partial \phi_I}{\partial t} \right) \bar{\vec{n}} \, \mathrm{d}\bar{S}_B \tag{3.30}$$

$$\vec{M}^{(1)} = \iint_{\bar{S}_B} -\rho \left(\frac{\partial \phi^{(1)}}{\partial t} + \frac{\partial \phi_I}{\partial t} \right) (\bar{\vec{r}} \times \bar{\vec{n}}) \, \mathrm{d}\bar{S}_B \tag{3.31}$$

The first order forces and moments ($\vec{F}^{(1)}$ and $\vec{M}^{(1)}$) will cause the floating body to present a first order rotational and translational oscillatory motion. This motion is described by Newton's second law:

$$\mathbf{M} \frac{\partial^2 \vec{\xi}^{(1)}}{\partial t^2} + \mathbf{C} \frac{\partial \vec{\xi}^{(1)}}{\partial t} + \mathbf{K} \vec{\xi}^{(1)} = \begin{pmatrix} \vec{F}^{(1)} \\ \vec{M}^{(1)} \end{pmatrix} \tag{3.32}$$

where $\vec{\xi}^{(1)} = (\xi_1^{(1)}, \xi_2^{(1)}, \xi_3^{(1)}, \xi_4^{(1)}, \xi_5^{(1)}, \xi_6^{(1)})$ is a vector containing the first-order translational and rotational motions, and $\mathbf{M}$ is the mass matrix containing the mass of the floating body and the moments of inertia.

One should realize that the static term of the pressure was neglected in the previous equations, assuming that the body is initially at a state of equilibrium. However, if the body is shortly displaced from its initial position, restoring forces and moments appear, forcing the body to oscillate around the equilibrium position. This motion can be compared with the motion of a mass connected to a spring, where restoring force on the mass is proportional to the displacement of the mass. In the linear theory approach, the restoring forces and moments may be shifted to the left hand side of equation (3.32) through the construction of a matrix $\mathbf{K}$ composed by time-independent restoring coefficients, which can be expressed in the form of surface integrals over the mean wetted surface $\bar{S}_B$, by applying Gauss's divergence theorem. The matrix of hydrostatic coefficients is then determined as:

$$\mathbf{K}(3,3) = \rho g \iint_{\bar{S}_B} n_z \mathrm{d}\bar{S}_B \tag{3.33}$$

$$\mathbf{K}(3,4) = \rho g \iint_{\bar{S}_B} Y n_z \mathrm{d}\bar{S}_B \tag{3.34}$$

$$\mathbf{K}(3,5) = -\rho g \iint_{\bar{S}_B} X n_z \mathrm{d}\bar{S}_B \tag{3.35}$$

$$\mathbf{K}(4,4) = \rho g \iint_{\bar{S}_B} Y^2 n_z \mathrm{d}\bar{S}_B + \rho g \forall Z_b \tag{3.36}$$

$$\mathbf{K}(4,5) = -\rho g \iint_{\bar{S}_B} X Y n_z \mathrm{d}\bar{S}_B \tag{3.37}$$

$$\mathbf{K}(4,6) = -\rho g \forall X_b \tag{3.38}$$

$$\mathbf{K}(5,5) = \rho g \iint_{\bar{S}_B} X^2 n_z \mathrm{d}\bar{S}_B + \rho g \forall Z_b \tag{3.39}$$

$$\mathbf{K}(5,6) = \rho g \forall Y_b \tag{3.40}$$

where $\forall$ is the body displacement and (X_b, Y_b, Z_b) are the body coordinates of the center of buoyancy, which are described by:

$$\forall = -\iint_{\bar{S}_B} n_x X \mathrm{d}\bar{S}_B = -\iint_{\bar{S}_B} n_y Y \mathrm{d}\bar{S}_B = -\iint_{\bar{S}_B} n_z Z \mathrm{d}\bar{S}_B \tag{3.41}$$

$$X_b = -\frac{1}{2\forall} \iint_{\bar{S}_B} n_x X^2 \mathrm{d}\bar{S}_B \tag{3.42}$$

$$Y_b = -\frac{1}{2\forall} \iint_{\bar{S}_B} n_y Y^2 \mathrm{d}\bar{S}_B \tag{3.43}$$

$$Z_b = -\frac{1}{2\forall} \iint_{\bar{S}_B} n_z Z^2 \mathrm{d}\bar{S}_B \tag{3.44}$$

One last consideration, is related to the lack of external damping coefficients which are

sometimes necessary since the potential flow theory does not account for viscous effects. This is the case, for example, of the roll motion of a ship, which is usually overestimated when applying the potential flow theory, since this D.O.F. is associated to very low energy dissipation by wave radiation. On the other hand, for heave and pitch D.O.F. the damping is mostly dominated by wave radiation effects and, therefore, usually there is no need to add an external coefficient. In order to account for the modelling of both situations, an external matrix of linear damping coefficients $\mathbf{C}$ will be also considered, as can be observed in equation (3.32).

In order to obtain a unique solution we still need to consider the inclusion of a radiation condition to ensure that the waves diffracted and radiated by the body do not reflect at the numerical boundaries back to the body position. Indeed, since the computer memory is finite, we are obliged to truncate the free surface somewhere and impose a numerical scheme to dissipate or absorb the waves. Following Zhen et al. (2010), this condition is guaranteed in our numerical model by the inclusion at these boundaries of a damping zone, also known as numerical beach, which consists in the inclusion of an energy dissipation term in the free surface boundary conditions, as follows:

$$\frac{\partial \eta^{(1)}}{\partial t} = \frac{\partial \phi^{(1)}}{\partial z} - \nu(x,y)\eta^{(1)} \quad \text{at} \quad z = 0 \quad \text{and} \quad \sqrt{x^2+y^2} > L_{dz} \tag{3.45}$$

$$\frac{\partial \phi^{(1)}}{\partial t} = -g\eta^{(1)} - \nu(x,y)\phi^{(1)} \quad \text{at} \quad z = 0 \quad \text{and} \quad \sqrt{x^2+y^2} > L_{dz} \tag{3.46}$$

Here L_{dz} stands for the distance from the global coordinate origin to the beginning of the damping region and $\nu(x,y)$ is a function that defines the dissipation on this region, described by:

$$\nu(x,y) = a\omega \left(\frac{\sqrt{x^2+y^2} - L_{dz}}{b\lambda} \right)^2 \tag{3.47}$$

where a defines the intensity of dissipation and b the length of the damping zone. For practical purposes, these values must be tuned by preliminary tests in order to avoid the occurrence of reflected waves which may spoil the solution. An investigation is this sense is presented in Appendix A, where a study on the effects of varying the damping zone parameters is presented. In general, it is observed that the damping zone length presents a significant influence on the performance of the damping zone, whereas the intensity parameter simply cannot be set with values that are too large, since it leads the method to be unstable. In most of the cases, the combination of a damping zone length of two wave lengths $b = 2.0$ and a dissipation strength of $a = 1.0$ leads to a good performance, for all the practical wave frequencies.

The linear wave-body formulation of the problem and the necessary assumptions to guarantee the applicability of this theory were presented in this section. In a few words, the constructed Boundary Value Problem (BVP) is formed by the Laplace's equation for the velocity field, added by the linear boundary conditions applied at the mean surface positions of the domain. Once the velocity potential is known, pressure field around the body surface may be calculated and integrated to find the forces and moments which are necessary for the time progressing of the equations of motion.

This procedure is satisfactory and apparently easy to implement, except for the fact that, by now, we do not have an exact equation for the potential time-derivative $\partial\phi^{(1)}/\partial t$, which would then require the use of numerical approximations for this quantity. However, it is a well-known fact (CAO; R.; SCHULTZ, 1994) that errors on these numerical approximations for $\partial\phi^{(1)}/\partial t$ may lead to unstable schemes for the time-marching of the set of equations and, therefore, an alternative procedure must be chosen, as will be presented in the next section.

3.3.1 The Acceleration Potential

In a time domain simulation, it is essential to solve the equations of the fluid and floating body motions simultaneously. This is because we need to guarantee a dynamic equilibrium of forces between the fluid and the floating body at all times. With this in mind, an accurate calculation of the pressure field (3.29) around the floating body is of utmost importance.

Different numerical approximations to deal with this problem are found in the literature. Backward difference schemes is the simplest way to follow. This method is sufficient for studies involving fixed bodies or under prescribed motions, in which the equations of motions do not need to be solved and the hydrodynamic forces may be post-processed. On the other hand, free floating simulations also require the evaluation of the equations of motions and poor estimatives of the pressure variation by finite difference schemes normally give rise to numerical instabilities (see for instance van Daalen (1993)).

According to Koo and Kim (2004), the acceleration potential method is known to be the most accurate and consistent way to solve $\partial\phi/\partial t$. The main idea of this method is to set up a new IBVP by taking advantage of the facts that a linear expression for the acceleration potential can be found and that it also satisfies Laplace's equation. Thus, by solving the two IBVPs for ϕ and $\partial\phi/\partial t$ at each time-step, a simultaneous treatment of the hydrodynamic and body dynamic equations may be conducted.

For completeness, boundary conditions must be defined for new the IBVP which require

a complicated treatment of the free floating body conditions. Tanizawa (2000) presents a general review of the existing methods used to handle this problem, electing the following ones to be the most consistent: (1) iterative method, (CAO; R.; SCHULTZ, 1994); (2) modal decomposition method, (COINTE et al., 1991) and (KOO; KIM, 2004); (3) indirect method, (TAYLOR; WU, 1996); and (4) implicit boundary condition method, (VAN DAALEN, 1993) and (TANIZAWA, 1995).

In this work, we have decided to employ the method presented by van Daalen (1993) and Tanizawa (1995) in which the equations of motions and the IBVP for the acceleration potential are combined. As will be shown, the acceleration of the body center of gravity may be expressed in terms of the acceleration potential $\partial\phi/\partial t$ at the wet mean surface $\bar{S}_B$, avoiding iterations for the matching of both values.

The acceleration potential is defined from the material derivative of fluid velocity:

$$\vec{a} = \frac{\partial \vec{v}}{\partial t} + (\vec{v} \cdot \nabla)\vec{v} \tag{3.48}$$

where $\vec{a}$ is the fluid flow acceleration. Denoting the velocity $\vec{v}$ by $\nabla\phi$, equation (3.48) is re-written as:

$$\vec{a} = \frac{\partial \nabla\phi}{\partial t} + (\nabla\phi \cdot \nabla)\nabla\phi = \nabla\frac{\partial\phi}{\partial t} + \nabla\left(\frac{1}{2}(\nabla\phi)^2\right) = \nabla\left(\frac{\partial\phi}{\partial t} + \frac{1}{2}(\nabla\phi)^2\right) \tag{3.49}$$

Hence, an acceleration potential Ψ may be defined as:

$$\Psi = \frac{\partial\phi}{\partial t} + \frac{1}{2}(\nabla\phi)^2 \tag{3.50}$$

and the fluid acceleration expressed by:

$$\vec{a} = \nabla\Psi \tag{3.51}$$

In order to maintain the formulation consistent with the linear theory, we combine the perturbed velocity potential (3.13) and the perturbed acceleration potential (3.52) with equation (3.50). Collecting terms of order up to ϵ, we find the linear acceleration equation (3.53) .

$$\Psi = \bar{\Psi} + \epsilon\Psi^{(1)} + \epsilon^2\Psi^{(2)} + \mathscr{O}(\epsilon^3) \tag{3.52}$$

$$\Psi^{(1)} = \frac{\partial \phi^{(1)}}{\partial t} \tag{3.53}$$

Since the acceleration potential Ψ is being analyzed in terms of the linear theory, it satisfies Laplace's equation in the whole fluid domain. Therefore, a new IBVP may be written for the time-derivative of the velocity potential, or linear acceleration potential $\Psi^{(1)}$. With this intention, it is necessary to describe the appropriate boundary conditions to complete the set of equations. This may be performed by applying the time-derivative operator $\partial/\partial t$ in all the linear boundary conditions for the velocity potential. The IBVP for the linear acceleration potential, therefore, is formed by the Laplace's equation:

$$\nabla^2 \left(\frac{\partial \phi^{(1)}}{\partial t} \right) = 0 \quad \text{in fluid domain} \tag{3.54}$$

and the following boundary conditions:

1. Free-surface condition:

$$\frac{\partial \phi^{(1)}}{\partial t} = -g\eta^{(1)} \quad \text{on } z = 0 \tag{3.55}$$

   where $\eta^{(1)}$ is solved by the linear free surface dynamic condition (3.21)

2. Zero-flux condition for fixed surfaces:

$$\nabla \left(\frac{\partial \phi^{(1)}}{\partial t} \right) \cdot \bar{\vec{n}} = -\nabla \left(\frac{\partial \phi_I}{\partial t} \right) \cdot \bar{\vec{n}} \quad \text{on } S_{BO} \tag{3.56}$$

3. Zero-flux condition for moving surfaces:

$$\nabla \left(\frac{\partial \phi^{(1)}}{\partial t} \right) \cdot \bar{\vec{n}} = \frac{\partial^2 \vec{\delta}^{(1)}}{\partial t^2} \cdot \bar{\vec{n}} - \nabla \left(\frac{\partial \phi_I}{\partial t} \right) \cdot \bar{\vec{n}} \quad \text{on } \bar{S}_B \tag{3.57}$$

The acceleration on the body surface $\partial^2 \vec{\delta}^{(1)}/\partial t^2$ may be related to the acceleration of the center of gravity by applying a straightforward double time differentiation of equation (3.8). The velocities and accelerations of a point on the body surface may be written in terms of the body center of gravity position, as presented in (3.58) and in (3.59).

$$\frac{\partial \vec{\delta}^{(1)}}{\partial t} = \frac{\partial \vec{\xi}_T^{(1)}}{\partial t} + \frac{\partial \vec{\xi}_R^{(1)}}{\partial t} \times \bar{\vec{r}} \tag{3.58}$$

$$\frac{\partial^2 \vec{\delta}^{(1)}}{\partial t^2} = \frac{\partial^2 \vec{\xi}_T^{(1)}}{\partial t^2} + \frac{\partial^2 \vec{\xi}_R^{(1)}}{\partial t^2} \times \bar{\vec{r}} + \frac{\partial \vec{\xi}_R^{(1)}}{\partial t} \times \left(\frac{\partial \vec{\xi}_R^{(1)}}{\partial t} \times \bar{\vec{r}} \right) \tag{3.59}$$

Equation (3.59) is nonlinear as there is a double cross product of the angular velocity vector $\partial \vec{\xi}_R^{(1)}/\partial t$. Once more, an expansion in Stokes's series justifies the linearization of this term, resulting in the linear expression:

$$\frac{\partial^2 \vec{\delta}^{(1)}}{\partial t^2} = \frac{\partial^2 \vec{\xi}_T^{(1)}}{\partial t^2} + \frac{\partial^2 \vec{\xi}_R^{(1)}}{\partial t^2} \times \bar{\vec{r}} \tag{3.60}$$

The boundary condition (3.57) may then be re-written as:

$$\begin{aligned} \nabla \left(\frac{\partial \phi^{(1)}}{\partial t} \right) \cdot \bar{\vec{n}} &= \frac{\partial^2 \vec{\xi}_T^{(1)}}{\partial t^2} \cdot \vec{n} + \frac{\partial^2 \vec{\xi}_R^{(1)}}{\partial t^2} \times \bar{\vec{r}} \cdot \vec{n} - \nabla \left(\frac{\partial \phi_I}{\partial t} \right) \cdot \bar{\vec{n}} \\ &= \frac{\partial^2 \vec{\xi}_T^{(1)}}{\partial t^2} \cdot \vec{n} + \frac{\partial^2 \vec{\xi}_R^{(1)}}{\partial t^2} \cdot \bar{\vec{r}} \times \vec{n} - \nabla \left(\frac{\partial \phi_I}{\partial t} \right) \cdot \bar{\vec{n}} \end{aligned} \tag{3.61}$$

The body angular acceleration and the acceleration of the center of gravity may be isolated in the equation of motion (3.32), as follows:

$$\begin{bmatrix} \frac{\partial^2 \vec{\xi}_T^{(1)}}{\partial t^2} \\ \frac{\partial^2 \vec{\xi}_R^{(1)}}{\partial t^2} \end{bmatrix} = \mathbf{M}^{-1} \left[-\mathbf{C} \begin{bmatrix} \frac{\partial \vec{\xi}_T^{(1)}}{\partial t} \\ \frac{\partial \vec{\xi}_R^{(1)}}{\partial t} \end{bmatrix} - \mathbf{K} \begin{bmatrix} \vec{\xi}_T^{(1)} \\ \vec{\xi}_R^{(1)} \end{bmatrix} - \rho \begin{bmatrix} \iint_{\bar{S}_B} \frac{\partial \phi^{(1)}}{\partial t} \bar{\vec{n}} \, \mathrm{d}S \\ \iint_{\bar{S}_B} \frac{\partial \phi^{(1)}}{\partial t} \left(\bar{\vec{r}} \times \bar{\vec{n}} \right) \mathrm{d}S \end{bmatrix} \right] \tag{3.62}$$

Finalizing, the translational and rotational accelerations of equation (3.62) can be substituted in the boundary condition (3.61) in order to define a zero-flux condition for floating bodies depending on the time-derivative of the velocity potential. As will be demonstrated in the next chapters, these equations will allow us to define an integral equation in which the time-derivative of the velocity potential and its normal derivative will be the only variables to be determined and, therefore, the evaluation of the acceleration of the center of gravity and body angular acceleration can be eliminated from the IBVP defined for the acceleration potential $\partial \phi^{(1)}/\partial t$.

From now on the superscript $^{(1)}$ denoting the first order quantities of the formulation will be suppressed in order to simplify the notation.

Chapter 4

Boundary Integral Equations

Chapter 3 presented the theoretical formulation which describes the hydrodynamic forces and motions of floating bodies caused by the incidence of free surface gravity waves. This formulation is summarized in two Initial Boundary Value Problems formed by the Laplace's equation for the velocity potential ϕ and for the acceleration potential $\partial\phi/\partial t$, with the addition of appropriate boundary conditions which particularize the solutions to the ones that we are interested in.

Analytical solutions for this problem are difficult to be found and are always related to problems involving very simple geometries in which a technique of separation of variables is used. The use of this technique, however, is only applicable if the boundary is a coordinate surface of one of the special orthogonal coordinate systems for which the Laplace's equation can be separated into ordinary differential equations, which limits the type of geometries to be analyzed, as observed by Hess and Smith (1967). Among other references, examples are described in Hulme (1982) who presented an analytic solution for the first order hydrodynamic forces that arise when a hemisphere undergoes prescribed periodic oscillations in water of infinite depth and in Bhatta and Rahman (2003) in which the diffraction and radiation problem for a circular cylinder in water of finite depth is treated. Although restricted to very simple applications which are not normally encountered in real situations, these closed solutions may be very useful for the verification of new numerical tools such as the one presented in this text.

Solutions of these problems for a more extensive set of geometries are found by numerical approaches. In the context of solving Laplace's equation, three of them receive special attention: (1) Finite Difference Method (FDM), (2) Finite Elements Method (FEM) (SERVÁN-CAMAS; GARCíA-ESPINOSA, 2013) and Boundary Elements Method

(BEM). FDM and FEM, also known as field methods, discretize the differential equation straightforwardly, generating sparse matrices with the higher values confined near the main diagonal. Despite of the fact that these features facilitate reasonably the solutions of the linear system, these field methods require the discretization of the entire fluid domain, even if we are only interested in values of the velocity or acceleration potential and its derivatives at the boundaries. Moreover, three-dimensional grids may be quite difficult to generate, especially near curved boundaries of, for example, the hull of a ship-shaped vessel. Regarding the FDM, the method only allows for structured-grids, demanding a greater control of the mesh that might not be adequate for some applications.

When dealing with the solution of BVPs for which Green functions may be obtained, an alternative to these field methods is the use of the boundary elements method. By applying Green's second identity, Laplace's equation may be re-written as an integral equation, reducing the number of dimensions to two. Grid generation becomes easier comparing to the field methods since only the boundary surfaces must be discretized, enabling also a re-meshing procedure during the simulations if necessary, see for instance van Daalen (1993) for 2D and Huang (1997) for 3D applications. A drawback of this method, however, is related to the generation of full matrices, which in turn increase the processing time to solve the linear systems and may also require more computer memory than FDM and FEM.

As one may observe, advantages and disadvantages of the methods can be listed and none of them is proved to be more efficient in relation to the others for a generic case. However, BEM has been receiving special attention when the seakeeping problem is concerned or, more generally, when the potential flow theory may be assumed. For this reason and considering the other advantages described above, we chose a boundary elements method to handle the Initial Boundary Value Problems previously presented. The next item of this chapter, therefore, presents the mathematical procedures to transform the Laplace's equations for the velocity and acceleration potentials into integral ones. The mathematical procedure for this transformation has already been presented by a vast number of authors, as for example the textbook of Bertram (2000).

4.1 Integral Equations

Let us consider the three-dimensional fluid domain Ω' delimited by a surface $\partial\Omega'$ illustrated in figure 4.1.

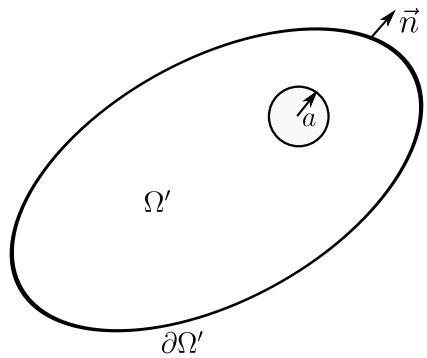

Figure 4.1: Surface of integration for the Second Green's Identity derivation

We define two scalar fields of class $\mathscr{C}^2$ in Ω' denoted by φ and ψ, which satisfy Laplace's equation $\nabla^2\varphi = \nabla^2\psi = 0$. Through the use of the divergence theorem, we derive the Green's second identity (4.1).

$$\begin{aligned}\iint_{\partial\Omega'} \left[\psi\frac{\partial\varphi}{\partial n} - \varphi\frac{\partial\psi}{\partial n}\right] \mathrm{d}\partial\Omega' &= \iiint_{\Omega'} \nabla\cdot(\psi\nabla\varphi - \varphi\nabla\psi)\,\mathrm{d}\Omega' = \\ &= \iiint_{\Omega'} (\psi\nabla^2\varphi - \varphi\nabla^2\psi)\,\mathrm{d}\Omega' = 0 \end{aligned} \tag{4.1}$$

Hereafter we denote the scalar field φ by the Rankine's source potential $G(\vec{\gamma};\vec{x})$ (4.2), in which $\vec{x} = (x, y, z)$ is the position of the Rankine's source, $\vec{\gamma} = (\xi', \eta', \zeta')$ is a field point and r is the distance between $\vec{x}$ and $\vec{\gamma}$.

$$G(\vec{\gamma};\vec{x}) = \frac{1}{r} = \frac{1}{\sqrt{(x-\xi')^2 + (y-\eta')^2 + (z-\zeta')^2}} \tag{4.2}$$

Thus, changing the scalar field ψ by the velocity potential ϕ, we obtain the following identity:

$$\iint_{\partial\Omega'} \left[\phi(\vec{\gamma})\frac{\partial}{\partial n}\left(\frac{1}{r}\right) - \frac{1}{r}\frac{\partial\phi(\vec{\gamma})}{\partial n}\right] \mathrm{d}\partial\Omega' = 0 \tag{4.3}$$

One should realize that the Rankine's source (4.2) presents a singularity when $r = 0$ and consequently the identity (4.3) is not valid when source and field points are coincident. This problem can be overcome, by surrounding the source point by a small sphere of radius a and surface $\partial\Omega'_a$. If the source point is positioned at the surface $\partial\Omega'$, we consider a hemisphere with the same radius. Therefore, the sum $\partial\Omega' + \partial\Omega'_a$ forms a closed surface surrounding the fluid domain interior to $\partial\Omega'$ but exterior to $\partial\Omega'_a$ where the Rankine's

source is now regular. Under these considerations, we can rewrite identity (4.3) in terms of surface integrals on $\partial\Omega'$ and $\partial\Omega'_a$, as follows:

$$\iint\limits_{\partial\Omega'+\partial\Omega'_a} \left[\phi(\vec{\gamma})\frac{\partial}{\partial n}\left(\frac{1}{r}\right) - \frac{1}{r}\frac{\partial\phi(\vec{\gamma})}{\partial n}\right] \mathrm{d}\partial\Omega' = 0 \quad \text{or} \tag{4.4}$$

$$\iint\limits_{\partial\Omega'} \left[\phi(\vec{\gamma})\frac{\partial}{\partial n}\left(\frac{1}{r}\right) - \frac{1}{r}\frac{\partial\phi(\vec{\gamma})}{\partial n}\right] d\partial\Omega' = -\iint\limits_{\partial\Omega'_a} \left[\phi(\vec{\gamma})\frac{\partial}{\partial n}\left(\frac{1}{r}\right) - \frac{1}{r}\frac{\partial\phi}{\partial n}(\vec{\gamma})\right] \mathrm{d}\partial\Omega' \tag{4.5}$$

Now, we should evaluate the contribution of the right-hand term of expression (4.5) in the limit of $a \to 0$. For convenience, we choose a spherical coordinate system (a, α, β) in which $(0 \leq a \leq \infty)$, $(0 \leq \alpha \leq 2\pi)$ and $(0 \leq \beta \leq \pi)$. The relations with the rectangular coordinates are defined by:

$$\begin{aligned} x &= a\sin\beta\cos\alpha \\ y &= a\sin\beta\sin\alpha \\ z &= a\cos\alpha \end{aligned} \tag{4.6}$$

Hence, the right-hand term of identity (4.5) may be replaced by:

$$-\int_0^{\pi}\int_0^{2\pi} \left[\phi\frac{\partial}{\partial n}\left(\frac{1}{r}\right) - \frac{1}{r}\frac{\partial\phi}{\partial n}\right]_{r=a} a^2\sin\beta\,\mathrm{d}\alpha\,\mathrm{d}\beta \tag{4.7}$$

If the source point is located inside $\partial\Omega'$, in the limit of $a \to 0$ and assuming that for a sufficiently small, $\phi(\vec{\gamma})$ and $\partial\phi(\vec{\gamma})/\partial n$ are constant and regular on $\partial\Omega'_a$, it follows that:

$$\begin{aligned} &\lim_{a\to 0} -\phi\int_0^{\pi}\int_0^{2\pi}\left[\frac{1}{a^2}a^2\sin\beta\right]\mathrm{d}\alpha\,\mathrm{d}\beta + \frac{\partial\phi}{\partial n}\int_0^{\pi}\int_0^{2\pi}\left[\frac{1}{a}a^2\sin\beta\right]\mathrm{d}\alpha\,\mathrm{d}\beta = \\ &\lim_{a\to 0} -\phi\int_0^{\pi}\int_0^{2\pi}[\sin\beta]\,\mathrm{d}\alpha\,\mathrm{d}\beta + \frac{\partial\phi}{\partial n}\int_0^{\pi}\int_0^{2\pi}[a\sin\beta]\,\mathrm{d}\alpha\,\mathrm{d}\beta = \\ &\lim_{a\to 0} -\phi\int_0^{\pi}[2\pi\sin\beta]\,\mathrm{d}\beta + \frac{\partial\phi}{\partial n}\int_0^{\pi}[2\pi a\sin\beta]\,\mathrm{d}\beta = \\ &\lim_{a\to 0} -\phi\,4\pi + \frac{\partial\phi}{\partial n}(\vec{\gamma})\,4\pi a = -4\pi\phi \end{aligned} \tag{4.8}$$

On the other hand, if the source point is located on the surface $\partial\Omega'$, we obtain:

$$\lim_{a\to 0} -\phi \int_0^{\frac{\pi}{2}} \int_0^{2\pi} \left[\frac{1}{a^2} a^2 \sin\beta\right] \mathrm{d}\alpha\, \mathrm{d}\beta + \frac{\partial\phi}{\partial n} \int_0^{\frac{\pi}{2}} \int_0^{2\pi} \left[\frac{1}{a} a^2 \sin\beta\right] \mathrm{d}\alpha\, \mathrm{d}\beta =$$

$$\lim_{a\to 0} -\phi \int_0^{\frac{\pi}{2}} \int_0^{2\pi} [\sin\beta]\, \mathrm{d}\alpha\, \mathrm{d}\beta + \frac{\partial\phi}{\partial n} \int_0^{\frac{\pi}{2}} \int_0^{2\pi} [a \sin\beta]\, \mathrm{d}\alpha\, \mathrm{d}\beta =$$

$$\lim_{a\to 0} -\phi \int_0^{\frac{\pi}{2}} [2\pi \sin\beta]\, \mathrm{d}\beta + \frac{\partial\phi}{\partial n} \int_0^{\frac{\pi}{2}} [2\pi a \sin\beta]\, \mathrm{d}\beta =$$

$$\lim_{a\to 0} -\phi\, 2\pi + \frac{\partial\phi}{\partial n}(\vec{\gamma})\, 2\pi a = -2\pi\phi \tag{4.9}$$

Finally, if the point source is positioned outside $\partial\Omega'$, identity (4.3) is valid without modifications and the integral equation for the velocity potential ϕ can be stated as:

$$\iint_{\partial\Omega'} \left[\phi(\vec{\gamma}) \frac{\partial}{\partial n}\left(\frac{1}{r}\right) - \frac{1}{r}\frac{\partial\phi(\vec{\gamma})}{\partial n}\right] \mathrm{d}\partial\Omega' = \begin{cases} -4\pi\phi(\vec{x}) & \text{for } \vec{x} \text{ inside } \Omega' \\ -2\pi\phi(\vec{x}) & \text{for } \vec{x} \text{ on } \partial\Omega' \\ 0 \quad \text{for } \vec{x} \text{ outside } \Omega' \end{cases} \tag{4.10}$$

Likewise, the integral equation for the linear acceleration potential $\partial\phi/\partial t$ can be constructed following the same mathematical developments presented for the integral equation for velocity potential (4.10), which results in equation (4.11).

$$\iint_{\partial\Omega'} \left[\frac{\partial\phi(\vec{\gamma})}{\partial t} \frac{\partial}{\partial n}\left(\frac{1}{r}\right) - \frac{1}{r}\frac{\partial}{\partial t}\left(\frac{\partial\phi(\vec{\gamma})}{\partial n}\right)\right] \mathrm{d}\partial\Omega' = \begin{cases} -4\pi\frac{\partial\phi(\vec{x})}{\partial t} & \text{for } \vec{x} \text{ inside } \Omega' \\ -2\pi\frac{\partial\phi(\vec{x})}{\partial t} & \text{for } \vec{x} \text{ on } \partial\Omega' \\ 0 \quad \text{for } \vec{x} \text{ outside } \Omega' \end{cases} \tag{4.11}$$

The classification of the kind of integral equation that should be solved depends on the type of boundary conditions which need to be imposed. For example, on the mean wet body surface a Neumman condition must be imposed in order to guarantee the impermeability of body surface and, therefore, since the equations present fixed limits of integration, equations (4.10) and (4.11) are classified as Fredholm integral equations of the second kind. van Daalen (1993) presents a brief discussion on the combinations of the choices of singularity distributions over the surface and the type of integral equations that lead to stable numerical algorithms. According to his work, the choice for a Fredholm integral equation of the second kind is by far the most used option. This equation results in matrices with large coefficients concentrated close to the main diagonal, which may be

solved by direct inversion or more efficiently by iterative methods when it is necessary to solve the linear system at all time-steps.

The choice of the type of boundary condition to be imposed on the free surface is more flexible since we can choose either a Neumann or a Dirichlet description. By choosing a Neumann boundary condition, we maintain the system of equations with only Fredholm equations of the second kind, keeping all the benefits aforementioned. However, if we observe the free surface kinematic condition (3.22), it is possible to realize that after the integral equation is solved and the velocity potential ϕ is known at all the boundary surfaces, an additional numerical spatial differentiation would be necessary to define the free surface elevation and then advance in time.

Alternatively, it is possible to apply a mixed source-dipole distribution, defining all the boundary surfaces, but the free surface, as Neumann boundaries. An advantage is that the normal derivative of the potential on the free surface and the velocity potential on the body surface are now calculated straightforwardly at all the time-steps. Moreover, as mentioned in van Daalen (1993), a choice for a mixed scheme reduces the leakage of flux considerably and leads to better results in comparison to the source-only distribution. For these reasons, we chose to implement a mixed source-dipole distribution, and the mathematical implications of this choice will be described in more details in the next chapter.

Chapter 5

The Numerical Model

The mathematical problem described in the previous chapters may be decomposed in two parts denoted by elliptical (or spatial) and time-marching problems. In a general description, most of the numerical algorithms which deal with wave-body formulations in time domain solves the elliptical problem at a certain time-step, whereas the time-marching one is used to update the boundary conditions to a new time level. In this work, the solution of the integral equations which compose the elliptical problem will be calculated by means of a boundary elements method and the time-marching one will be performed by a Fourth-Order Runge-Kutta method (RK4).

Describing it in more details, let us consider a free floating body under the influence of waves in a scenario of infinite water depth in which the velocity and the acceleration potential vanishes at the sea bottom, and so, it does not need to be discretized. The simulation begins at $t = 0$ with the free surface and the body at rest, leading to the consistent initial conditions of $\phi = \partial\phi/\partial t = 0$ on the free surface and $\partial\phi/\partial n = \partial^2\phi/\partial t\partial n = 0$ on the body's surface.

The process is initialized by forcing the system with the analytical incoming wave field. The elliptical problems are then solved providing $\partial\phi/\partial n$ and $\partial^2\phi/\partial t\partial n$ on the free surface, and ϕ and $\partial\phi/\partial t$ on the body surface. Progressing, the first order forces and moments acting on the body may be then obtained by pressure integration, followed by the determination of the new acceleration, velocity and position of the body center of gravity at each stage of the RK4 scheme, which are then used for the calculation of the new body boundary conditions for the velocity and acceleration potentials integral equations. Free surface boundary conditions are also updated inside the RK4 scheme. At each of the RK4 stages, the kinematic and the dynamic conditions are evaluated, providing the new

free surface elevation and velocity potential, which are used to define the new free surface boundary conditions for the acceleration and velocity potential integral equations. These steps are then followed until the desired simulation time T_s is reached. A schematic view of this procedure is presented in figure 5.1.

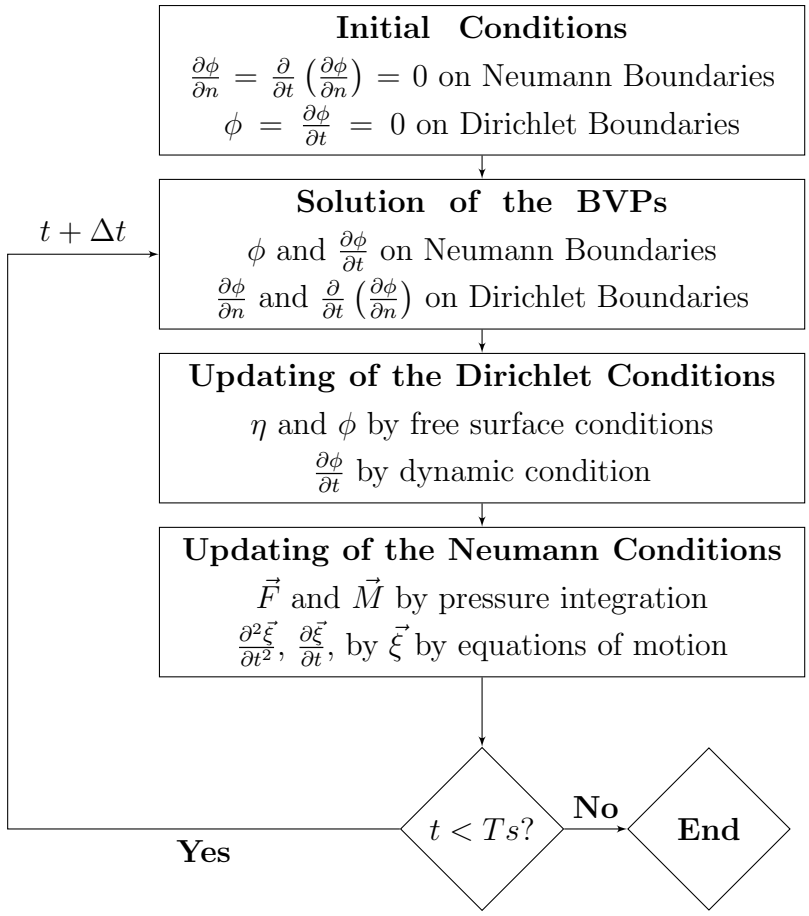

Figure 5.1: Loop structure of the numerical method

The algorithm briefly described may be simplified if we are dealing with simulations considering only bodies with prescribed motions or fixed, as the accelerations, velocities and positions of the body are known in advance. Moreover, as mentioned before, these simulations do not require the calculation of the pressure field at each time step since the equations of motions are not integrated in time. In this case, the pressure field may be post-processed, calculating the time derivative of the velocity potential ϕ with a centered difference scheme in time. Therefore, only the integral equation for the velocity potential must be solved and faster algorithms are then built up.

The next items of this chapter present the numerical methods used for the solution of the elliptical problem and for the time-marching procedures.

5.1 Boundary Elements Method

The boundary elements method (also known as panel method) is here applied to solve the integral equations (4.10) and (4.11).

In this work we apply a Low-Order Panel Method which uses plane quadrilateral/triangular panels (surface elements) to discretize the surfaces and assume that the variable quantities are constant over each panel, simplifying reasonably the integration of the singularities. Hess and Smith (1967) is considered a pioneering work in this topic, applying it to a wide variety of flow problems with bodies in infinite fluid. This method is by far the simplest option among other possibilities, such as the Higher Order Panel Methods which use curved panels and linear or quadratic representations of the variable quantities over surface patches (see for instance Maniar (1995) and Qiu (2001)). The use of higher order methods certainly would increase the accuracy of the solution if the number of unknowns are maintained the same, but on the other hand, the integral equations would become much more difficult to solve. The developments of higher-order methods emerged mainly to overcome the difficulties of the low-order method to evaluate spatial derivatives that arise from problems involving forward speed bodies and nonlinear terms. These problems, however, will not be faced in this linear version and the low-order method was then considered sufficient to achieve the established objectives.

The boundary surfaces $\partial\Omega'$ are discretized in N_p plane quadrilateral/triangular panels in which a unique point is selected to be a collocation point where the boundary conditions are imposed and the variable quantities are determined. It is quite obvious that the larger the number of panels the better is the surface domain representation and the assumption that the variable quantities are constant over each panel.

The next step is to derive discrete representations of the integral equations (4.10) and (4.11). Bearing this in mind, we consider a sum of N_p integrals over the separated element surfaces $\partial\Omega'_j$ for all collocation points $\vec{x}$, obtaining equations (5.1) and (5.2) for the velocity and acceleration potential, respectively, as follows:

$$\sum_{j=1}^{N_p} \iint_{\partial\Omega'_j} \left[\phi_j(\vec{\gamma}) \frac{\partial}{\partial n}\left(\frac{1}{r_{ij}}\right) - \frac{1}{r_{ij}} \frac{\partial \phi_j(\vec{\gamma})}{\partial n} \right] \mathrm{d}\partial\Omega'_j = -2\pi\phi_i(\vec{x}) \quad i = 1 : N_p \tag{5.1}$$

$$\sum_{j=1}^{N_p} \iint_{\partial\Omega'_j} \left[\frac{\partial \phi_j(\vec{\gamma})}{\partial t} \frac{\partial}{\partial n}\left(\frac{1}{r_{ij}}\right) - \frac{1}{r_{ij}} \frac{\partial}{\partial t}\left(\frac{\partial \phi_j(\vec{\gamma})}{\partial n}\right) \right] \mathrm{d}\partial\Omega'_j = -2\pi \frac{\partial \phi_i(\vec{x})}{\partial t} \quad i = 1 : N_p \tag{5.2}$$

where r_{ij} is a matrix with the distances between collocations points i and field points j defined by:

$$r_{ij} = \sqrt{(x_i - \xi'_j)^2 + (y_i - \eta'_j)^2 + (z_i - \zeta'_j)^2} \quad j = 1 : N_p \quad i = 1 : N_p \tag{5.3}$$

Assuming that the velocity and acceleration potentials and their normal derivatives are constant over each planar panel $\partial\Omega'_j$, we may take these quantities out of the integrals, resulting in the discretized equations (5.4) and (5.5) for the velocity and acceleration potential, respectively.

$$\sum_{j=1}^{N_p} \left[\phi_j(\vec{\gamma}) \iint_{\partial\Omega'_j} \frac{\partial}{\partial n}\left(\frac{1}{r_{ij}}\right) \mathrm{d}\partial\Omega'_j - \frac{\partial\phi_j(\vec{\gamma})}{\partial n} \iint_{\partial\Omega'_j} \frac{1}{r_{ij}} \mathrm{d}\partial\Omega'_j \right] = -2\pi\phi_i(\vec{x}) \quad i = 1 : N_p \tag{5.4}$$

$$\sum_{j=1}^{N_p} \left[\frac{\partial\phi_j(\vec{\gamma})}{\partial t} \iint_{\partial\Omega'_j} \frac{\partial}{\partial n}\left(\frac{1}{r_{ij}}\right) \mathrm{d}\partial\Omega'_j - \frac{\partial}{\partial t}\left(\frac{\partial\phi_j(\vec{\gamma})}{\partial n}\right) \iint_{\partial\Omega'_j} \frac{1}{r_{ij}} \mathrm{d}\partial\Omega'_j \right] = -2\pi \frac{\partial\phi_i(\vec{x})}{\partial t} \quad i = 1 : N_p \tag{5.5}$$

In a more compact notation, equations (5.4) and (5.5) may be replaced by equations (5.6) and (5.7)

$$\sum_{j=1}^{N_p} \left[\phi_j D_{ij} - \frac{\partial\phi_j}{\partial n} S_{ij} \right] = -2\pi\phi_i \quad i = 1 : N_p \tag{5.6}$$

$$\sum_{j=1}^{N_p} \left[\frac{\partial\phi_j}{\partial t} D_{ij} - \frac{\partial}{\partial t}\left(\frac{\partial\phi_j}{\partial n}\right) S_{ij} \right] = -2\pi \frac{\partial\phi_i}{\partial t} \quad i = 1 : N_p \tag{5.7}$$

where S_{ij} and D_{ij} are known in literature as the source and dipole influence coefficients, respectively.

Concluding, substitution of ϕ_j and $\partial\phi_j/\partial t$ for Dirichlet boundaries (i.e free surface), and $\partial\phi_j/\partial n$ and $\partial^2\phi_j/\partial t\partial n$ for Neumann boundaries (i.e body surface, bottom etc.) results in two linear systems of $N = N_p$ equations with the following structures:

$$\begin{bmatrix} (D_{ij} + 2\pi\delta_{ij}) & -S_{ij} \end{bmatrix}_{N_p \times N_p} \begin{bmatrix} \phi_j \\ \frac{\partial\phi_j}{\partial n} \end{bmatrix}_{N_p \times 1} = \begin{bmatrix} S_{ij}\frac{\partial\phi_j}{\partial n} \\ -(D_{ij} + 2\pi\delta_{ij})\phi_j \end{bmatrix}_{N_p \times 1} \tag{5.8}$$

$$\left[\begin{array}{cc} (D_{ij}+2\pi\delta_{ij}) & -S_{ij} \end{array}\right]_{N_p\times N_p} \left[\begin{array}{c} \frac{\partial\phi_j}{\partial t} \\ \frac{\partial}{\partial t}\left(\frac{\partial\phi_j}{\partial n}\right) \end{array}\right]_{N_p\times 1} = \left[\begin{array}{c} S_{ij}\frac{\partial}{\partial t}\left(\frac{\partial\phi_j}{\partial n}\right) \\ -(D_{ij}+2\pi\delta_{ij})\frac{\partial\phi_j}{\partial t} \end{array}\right]_{N_p\times 1} \tag{5.9}$$

where the δ_{ij} is the Kronecker's delta function.

The imposition of the boundary conditions for forced and fixed body simulations is relatively straightforward. For fixed bodies, $\partial\phi_j/\partial n$ and $\partial^2\phi_j/\partial t\partial n$ are set to zero and the free surface boundary conditions are updated step-by-step by the integration of the kinematic and dynamic free-surface conditions in time. For forced body simulations, these values are not zero, but on the other hand they are known at each time-step and must be updated accordingly.

The simulation of free floating bodies, however, demands more attention since we need to couple the body dynamics with the hydrodynamic problem. As the algorithm requires the calculation of the body velocity and acceleration at each time-step, it is necessary to relate these quantities or the equations which determine them with the systems of equations (5.8) and (5.9).

For a better comprehension, some equations already defined in section 3.3.1 of chapter 3 will be here restated without renumbering. Thus, consider equations (3.61) and (3.62):

$$\begin{aligned} \nabla\left(\frac{\partial\phi^{(1)}}{\partial t}\right)\cdot\bar{\vec{n}} &= \frac{\partial^2\vec{\xi}_T^{(1)}}{\partial t^2}\cdot\vec{n} + \frac{\partial^2\vec{\xi}_R^{(1)}}{\partial t^2}\times\bar{\vec{r}}\cdot\vec{n} - \nabla\left(\frac{\partial\phi_I}{\partial t}\right)\cdot\bar{\vec{n}} \\ &= \frac{\partial^2\vec{\xi}_T^{(1)}}{\partial t^2}\cdot\vec{n} + \frac{\partial^2\vec{\xi}_R^{(1)}}{\partial t^2}\cdot\bar{\vec{r}}\times\vec{n} - \nabla\left(\frac{\partial\phi_I}{\partial t}\right)\cdot\bar{\vec{n}} \end{aligned} \tag{3.61}$$

$$\left[\begin{array}{c} \frac{\partial^2\vec{\xi}_T}{\partial t^2} \\ \frac{\partial^2\vec{\xi}_R}{\partial t^2} \end{array}\right] = \mathbf{M}^{-1}\left[-\mathbf{C}\left[\begin{array}{c} \frac{\partial\vec{\xi}_T}{\partial t} \\ \frac{\partial\vec{\xi}_R}{\partial t} \end{array}\right] - \mathbf{K}\left[\begin{array}{c} \vec{\xi}_T^{(1)} \\ \vec{\xi}_R^{(1)} \end{array}\right] - \rho\left[\begin{array}{c} \iint_{\bar{S}_B}\frac{\partial\phi}{\partial t}\,\bar{\vec{n}}\,\mathrm{d}S \\ \iint_{\bar{S}_B}\frac{\partial\phi}{\partial t}\,(\bar{\vec{r}}\times\bar{\vec{n}})\,\mathrm{d}S \end{array}\right]\right] \tag{3.62}$$

which express the body boundary condition for the acceleration potential and the acceleration of the body center of gravity isolated in the equations of motion, respectively.

A first alternative to couple the body acceleration with the linear system (5.9) is the direct substitution of (3.61) into the first line of the right-hand term. Nevertheless, an iterative procedure is necessary to solve these equations since neither the body accelerations ($\partial^2\vec{\xi}_T/\partial t^2$, $\partial^2\vec{\xi}_R/\partial t^2$) nor the acceleration potential $\partial\phi/\partial t$ are known. Although the simplicity of this method for programming and the excellent convergence showed by

Cao, R. and Schultz (1994), this procedure may lead to very time-consuming algorithms and, therefore, was avoided in our developments.

Following the works of van Daalen (1993) and Tanizawa (1995), the approach applied here combines equation (3.62) and the boundary condition (3.61) to eliminate the body acceleration of the equations, the acceleration potential $\partial\phi/\partial t$ remaining as the only unknown.

5.1.1 Integration of the Influence Coefficients

Once the numerical method is established, we need to assess the behaviour of the spatial integrals represented by the source and dipole coefficients in order to choose an appropriate numerical integration method. In fact, their behaviours may vary significantly in a range from smooth, quasi-singular to singular, depending on the variation of the element surface, collocation and field points positions. Maniar (1995) presents an empirical classification of each of these integrand shapes by comparing a characteristic length scale (L) of the element surface to the distance (d) between the field point and the panel centroid. According to his work, when $L/d \ll 1$, the variation of the integrands is small and their behaviours are smooth, defining the often called far-field influence coefficients. When $L/d \sim \mathscr{O}(1)$, the variations are rapid and the integrands are nearly-singular, categorizing the integrals as near-field influence coefficients. Finally, when the field point lies on the surface element, more specifically at the panel centroid position, both integrands become singular and the integrals are called self-influence coefficients.

Maniar (1995) also states that the integrals categorized as near-field and self-influence coefficients contribute dominantly to the global matrices and shall be carefully evaluated. Bearing this in mind, we dedicate the following discussions for their evaluations, presenting the different approaches applied for the calculation of each integral. All the coefficients are calculated with an absolute error of 10^{-5}.

As will be demonstrated, the integration of the far-field influence coefficients by gaussian quadratures present an easy and fast convergence option, using a small number of gaussian points. Regarding the evaluation of the near-field influence coefficients, although several authors apply the partitioning technique of Maniar (1995) (such as Danmeier (1999) and Kim, Lee and Kerwin (2007)), in this work the coefficients are calculated by simply increasing the number of gaussian points until the desired convergence is reached.

The evaluation of the self-influence coefficients, however, demands a more sophisticated approach in which a subdivision of the element surfaces in triangles become essential for an accurate calculation. In fact, convergence of the results are not achieved even using a

very large number of gaussian points. It is worth mentioning that only the source self-influence coefficients evaluation must be assessed. Since we are dealing exclusively with planar panels, the dipole coefficients vanish if the collocation point is located at the same plane of the panel.

5.1.1.1 Near and Far-Field Influence Coefficients

The integrals representing the near and far-field influence coefficients are calculated in a straightforward manner. This is performed in an iso-parametric domain and numerically calculated by a Gauss-Legendre quadrature method. The surface elements (or panels) in the physical domain (x, y, z) are parameterized by a vectorial function $\vec{r}(u, v)$ of two parameters u and v, defined over a quadrilateral unitary domain $\{(u, v)|-1 \leq u \leq 1, -1 \leq v \leq 1\}$ at the plane uv, as follows:

$$\vec{r}(u, v) = x(u, v)\vec{e}_1 + y(u, v)\vec{e}_2 + z(u, v)\vec{e}_3 \tag{5.10}$$

in which $x(u, v)$, $y(u, v)$ and $z(u, v)$ are denoted as parametric equations.

In order to exemplify how the parametric equations are derived, consider a quadrilateral surface element with vertices (x_1, y_1, z_1), (x_2, y_2, z_2), (x_3, y_3, z_3) and (x_4, y_4, z_4), and the iso-parametric computational domain, as illustrated in Figure 5.2(a) and 5.2(b), respectively.

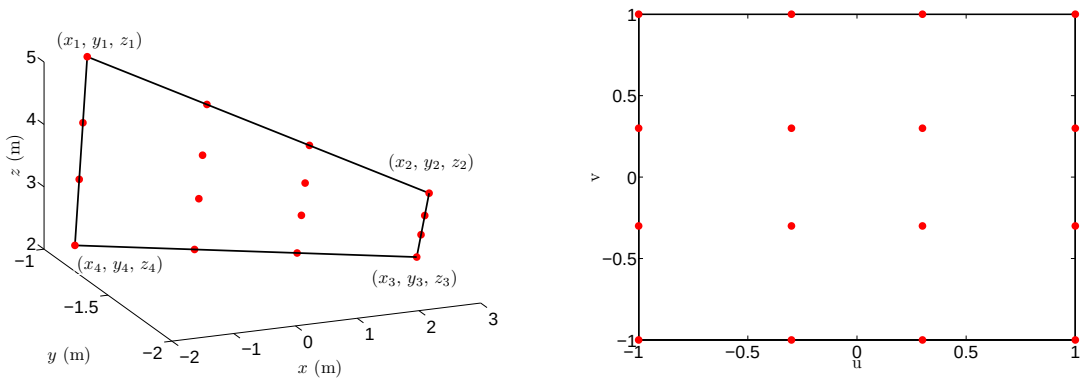

(a) (b)

Figure 5.2: Physical domain (a) and computational iso-parametric domain (b)

Taking the coordinate x, for example, we first define two spatial curves $\alpha_x(u)$ and $\beta_x(u)$ which parameterize the paths $x_1 \rightarrow x_2$ and $x_4 \rightarrow x_3$ in terms of u, respectively.

$$\beta_x(u) = \frac{(u+1)(x_2 - x_1)}{2} + x_1 \tag{5.11}$$

$$\alpha_x(u) = \frac{(u+1)(x_3 - x_4)}{2} + x_4 \tag{5.12}$$

Once the coordinates in the direction of u are defined, now, we need to parameterize the region in between these spatial curves $\alpha_x(u)$ and $\beta_x(u)$ in terms of v, obtaining the parametric equation $x(u, v)$:

$$x(u,v) = \frac{(v+1)}{2}\left[\frac{(u+1)(x_3 - x_4)}{2} + x_4\right] + \left[-\frac{(v+1)}{2} + 1\right]\left[\frac{(u+1)(x_2 - x_1)}{2} + x_1\right] \tag{5.13}$$

The parametric equations $y(u, v)$ and $z(u, v)$ are then defined, analogously, and described by:

$$y(u,v) = \frac{(v+1)}{2}\left[\frac{(u+1)(y_3 - y_4)}{2} + y_4\right] + \left[-\frac{(v+1)}{2} + 1\right]\left[\frac{(u+1)(y_2 - y_1)}{2} + y_1\right] \tag{5.14}$$

$$z(u,v) = \frac{(v+1)}{2}\left[\frac{(u+1)(z_3 - z_4)}{2} + z_4\right] + \left[-\frac{(v+1)}{2} + 1\right]\left[\frac{(u+1)(z_2 - z_1)}{2} + z_1\right] \tag{5.15}$$

Thus, the integrations of an arbitrary function $f(x, y, z)$ over each panel surface may be performed by:

$$\iint\limits_{\partial\Omega'_j} f(x,y,z)\mathrm{d}\Omega'_j = \int\limits_{-1}^{1}\int\limits_{-1}^{1} f(x(u,v), y(u,v), z(u,v))||J(u,v)||\mathrm{d}u\mathrm{d}v \tag{5.16}$$

where $J(u, v)$ is the Jacobian of the transformation, which is calculated by the following cross product

$$J(u,v) = \frac{\partial\vec{r}}{\partial u} \times \frac{\partial\vec{r}}{\partial v} \tag{5.17}$$

Further on, by applying the Gauss-Legendre quadrature, we may approximate the integral by a weighted sum of the integrand values, obtaining

$$\int\limits_{-1}^{1}\int\limits_{-1}^{1} f(x(u,v), y(u,v), z(u,v))||J(u,v)||\mathrm{d}u\mathrm{d}v \approx \sum_{i=1}^{n}\sum_{k=1}^{n} w_i w_k f(u_i, v_k)||J(u_i, v_k)|| \tag{5.18}$$

where w_i and w_k are the weights and u_i and v_i are the ith roots of the Legendre's polynomial $P_n(x)$.

Figure 5.3 and 5.6 present typical relations between the characteristic surface element scale (L) and distance between the panel centroid and the field point (d) for far and near fields classification of the integrals, respectively. Moreover, the correspondent function values multiplied by the Jacobian of the transformation are also presented. In the figures, the source and dipole terms are denoted as I^S_{Far} and I^D_{Far} for the far field influence coefficients, and I^S_{Near} and I^D_{Near} for the near field ones. Notice that in a far field condition the integrand are very smooth whereas in the near field a rapid increase of the integrand (in this case at $v = 1$ edge) is clearly perceivable.

As stated before, this behavior influences directly the evaluation of the integrals, demanding a specific analysis concerning the number of gaussian points necessary for the convergence achievement. Concerning the far field influence coefficients, the convergence analysis of the source and dipole terms are presented in Figures 5.4 and 5.5, respectively. In accordance to the smooth function behavior observed in Figure 5.3, a very fast convergence of the integrals is observed for both terms, requiring only $n = 3$ gaussian points to achieve an absolute error of 10^{-5}, between two successive evaluations (n and $n + 1$ gaussian points). Therefore, any far field influence coefficients are evaluated in the code using $n = 4$ gaussian points aiming at guaranteeing the convergence.

The same analysis for the near field influence coefficients is presented in Figures 5.7 and 5.8 for the source and dipole terms, respectively. Firstly, we observe that the convergence is reached with a number of gaussian points much larger than the ones used in the far field analysis, which is strictly related to the rapid variation of the function at the edge $v = 0$. Moreover, the source and dipole coefficients present different behaviors and consequently required distinct number of gaussian points, which turns more difficult to set a unique value using as reference only the ratio L/d. In order to overcome this problem, each of the near field influence coefficients are evaluated in the code until the error of two successive calculations present an absolute error lower than 10^{-5}, which in general occurs in a range of $10 \leq n \leq 30$ gaussian points.

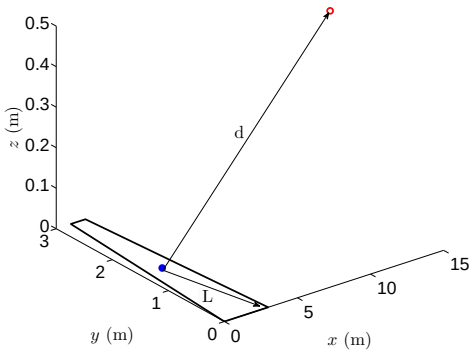

(a)

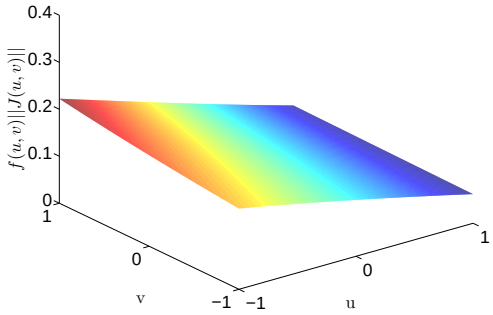

(b)

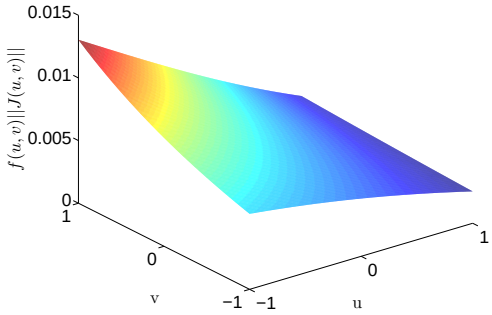

(c)

Figure 5.3: Typical relative positions between the field point (red marker) and panel centroid (blue marker) for a far field influence coefficient classification ($L \ll 1/d$) (a) and the correspondent function values in the parametric domain for the source (b) and dipole (c) terms

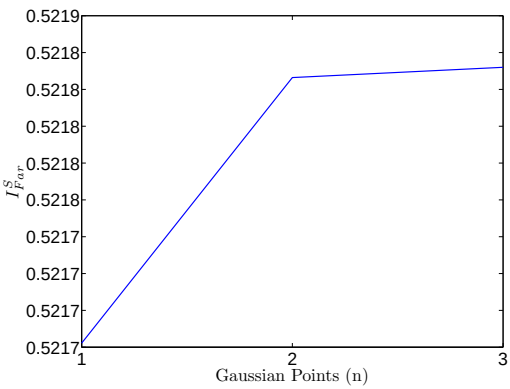

(a)

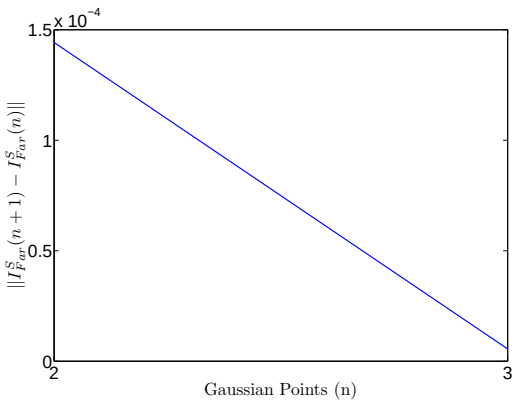

(b)

Figure 5.4: Convergence of the source far field influence coefficient I^S_{Far}

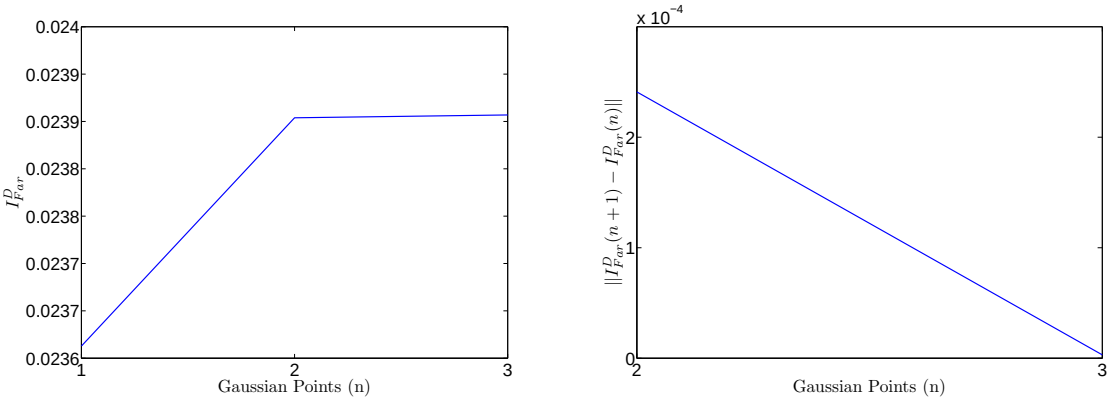

(a) (b)

Figure 5.5: Convergence of the dipole far field influence coefficient I^D_{Far}

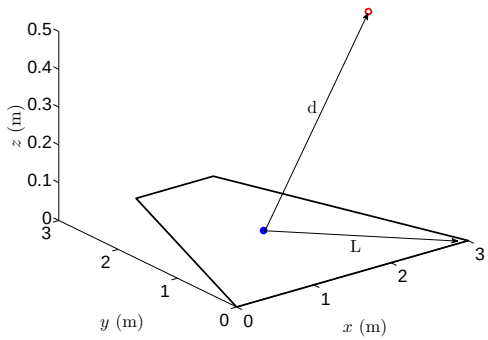

(a)

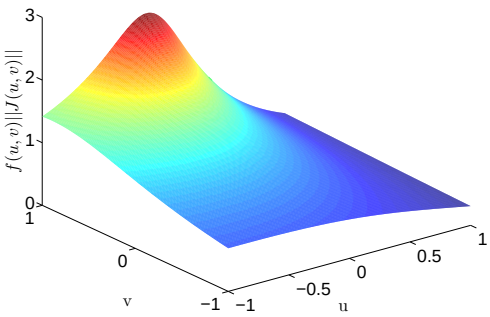

(b)

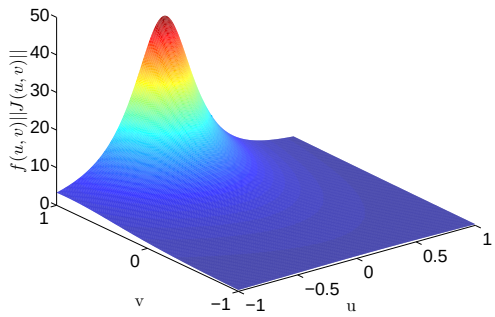

(c)

Figure 5.6: Typical relative positions between the field point (red marker) and panel centroid (blue marker) for a near field influence coefficient classification ($L/d \sim \mathscr{O}(1)$) (a) and the correspondent function values in the parametric domain for the source (b) and dipole (c) terms

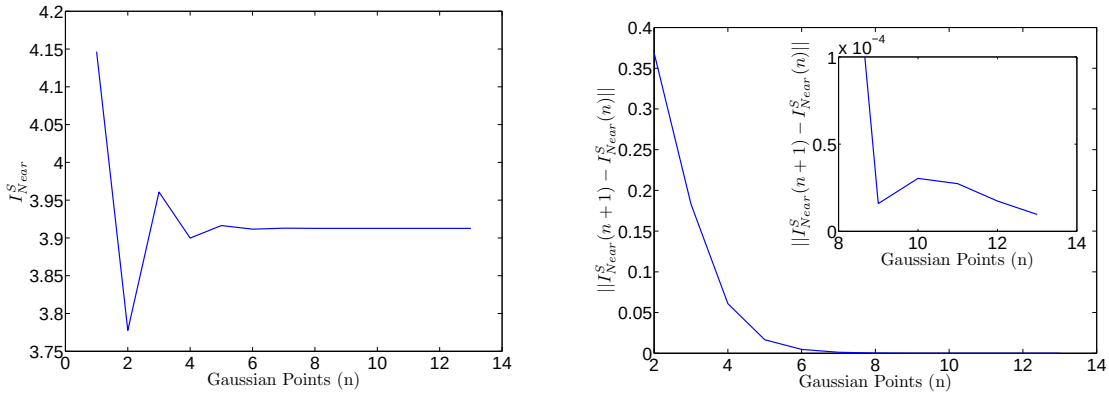

(a) (b)

Figure 5.7: Convergence of the source near field influence coefficient I^S_{Near}

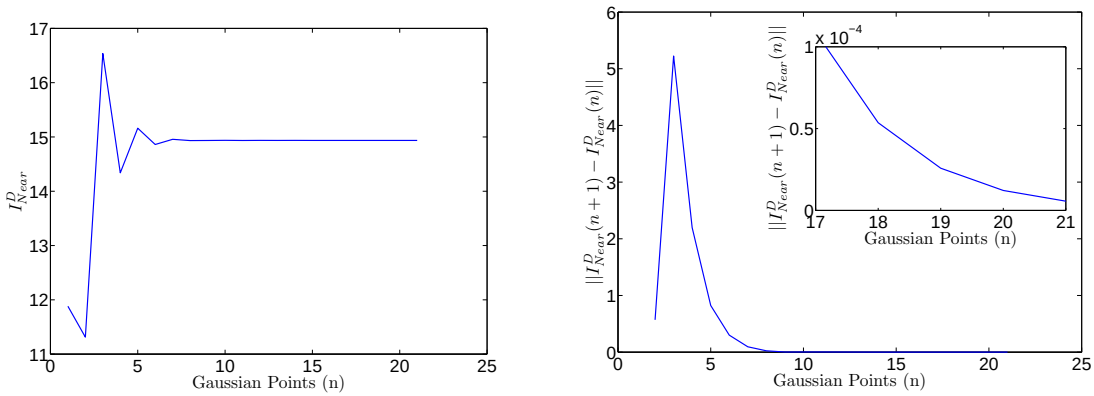

(a) (b)

Figure 5.8: Convergence of the dipole near field influence coefficient I^D_{Near}

5.1.1.2 Self-Influence Coefficients

Now we turn our attention for the evaluation of the self-influence coefficients that is related to the situation in which the field point coincides with the panel centroid. In order to elucidate the complexity of such a problem, Figure 5.9 presents the singular function behavior of the source term I^S_{Self}, which presents a notable and undetermined peak value at the center of the parametric domain. In addition, Figure 5.10 presents the convergence analysis of this coefficient using the same integration approach followed for the evaluation of the far and near field coefficients. Notice that even using $n = 150$ gaussian points the error remained higher than the established criteria of 10^{-5}. Therefore, a more sophisticated approach must be used aiming at evaluating these terms. The analysis of the dipole coefficient I^D_{Self} is neglected, since by definition, the scalar product $\vec{r} \cdot \vec{n}$ equals

zero if the field point is located at the same plane of the panel, and then, the integral vanishes in this situation.

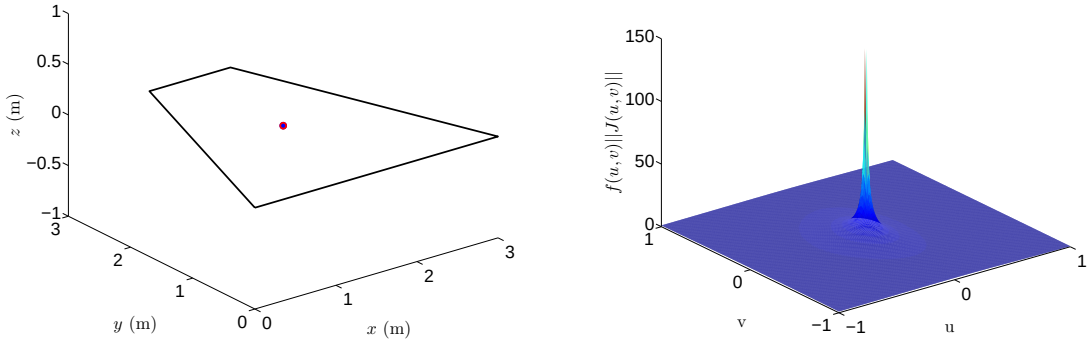

(a) (b)

Figure 5.9: Typical relative positions between the field point (red marker) and panel centroid (blue marker) for a self-influence coefficient classification ($d = 0$) (a) and the correspondent function values in the parametric domain for the source term (b)

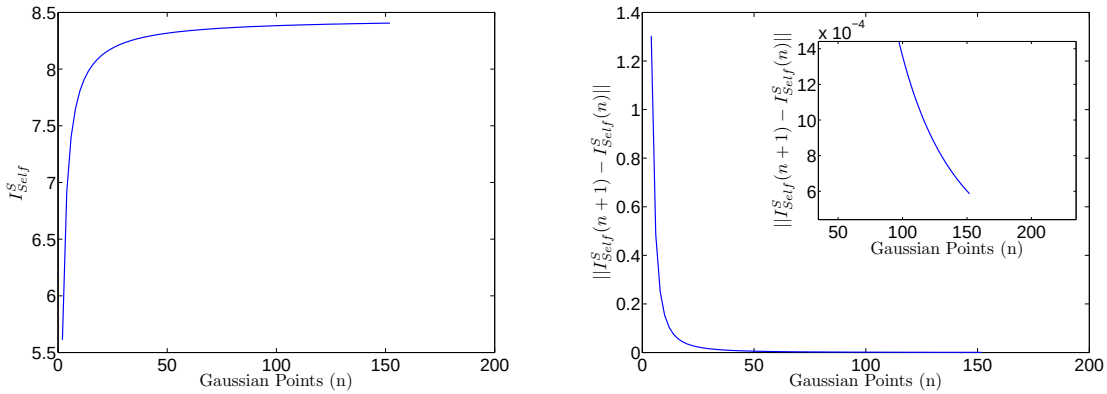

(a) (b)

Figure 5.10: Convergence of the source self-influence coefficient I^S_{Self}

The procedure here applied to evaluate the self-influence coefficients is based on the works of Maniar (1995) and Kim, Lee and Kerwin (2007), which remove the singularity of the integrand by partitioning the quadrilateral parametric space into four triangles. Following their works, we introduce the quadratic transformations (5.19) to (5.22) for the triangles $\Delta^{(1)}$, $\Delta^{(2)}$, $\Delta^{(3)}$ and $\Delta^{(4)}$, respectively. In this method, the apex of each triangle is located at the panel centroid and their bases at the sides of the square, as illustrated in Figure 5.11, in which u_t and v_t are two parameters defined in a new parametric quadrilateral domain $\{(u_t, v_t)|0 \leq u_t \leq 1, -1 \leq v_t \leq 1\}$.

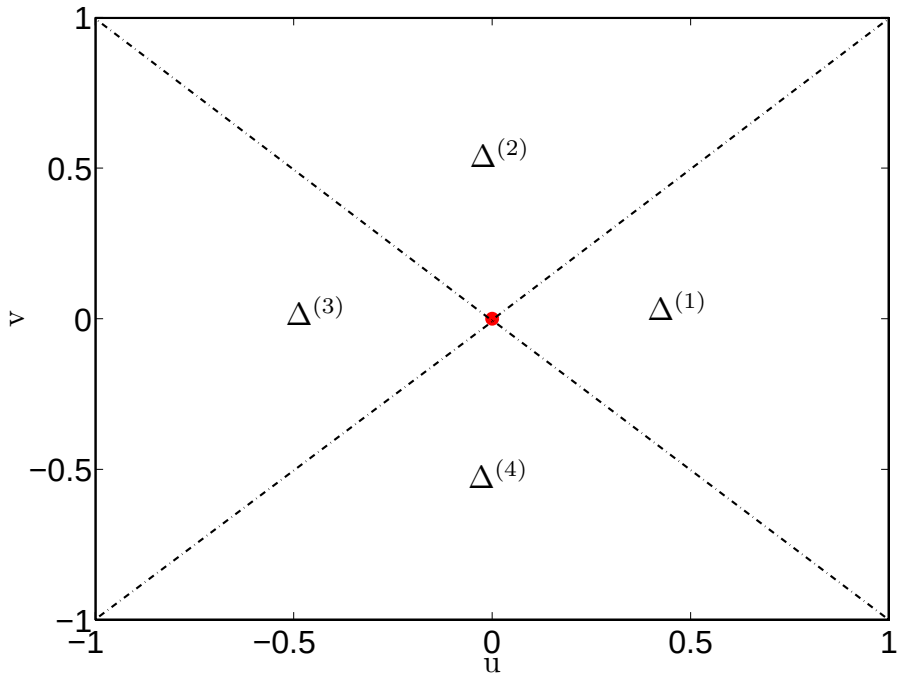

Figure 5.11: Triangulation of the parametric space. Figure adapted from Maniar (1995)

$$\Delta^{(1)}: \begin{array}{ll} u & = u_t \\ v & = u_t v_t \end{array} \tag{5.19}$$

$$\Delta^{(2)}: \begin{array}{ll} u & = u_t v_t \\ v & = u_t \end{array} \tag{5.20}$$

$$\Delta^{(3)}: \begin{array}{ll} u & = -u_t \\ v & = -u_t v_t \end{array} \tag{5.21}$$

$$\Delta^{(4)}: \begin{array}{ll} u & = -u_t v_t \\ v & = -u_t \end{array} \tag{5.22}$$

The integral I^S_{Self} may then be evaluated by summing the contribution of each of the four triangles, as presented in expression (5.23). Notice that the four integrals must be evaluated with the associated quadratic transformations (5.19) to (5.22).

$$I^S_{Self} = \sum_{m=1}^{4} \iint_{\Delta^{(m)}} f(u_t, v_t)||J(u,v)||||J_t(u_t, v_t)||\mathrm{d}u_t \mathrm{d}v_t \tag{5.23}$$

in which $J_t(u_t, v_t)$ is the Jacobian of the new transformation.

Figure 5.12 illustrates the four integrands obtained from the new transformations, where it is possible to observe a considerable enhancement in terms of the functions smoothness. As a consequence, these new surfaces can easily be integrated by using the standard gaussian integration method presented before.

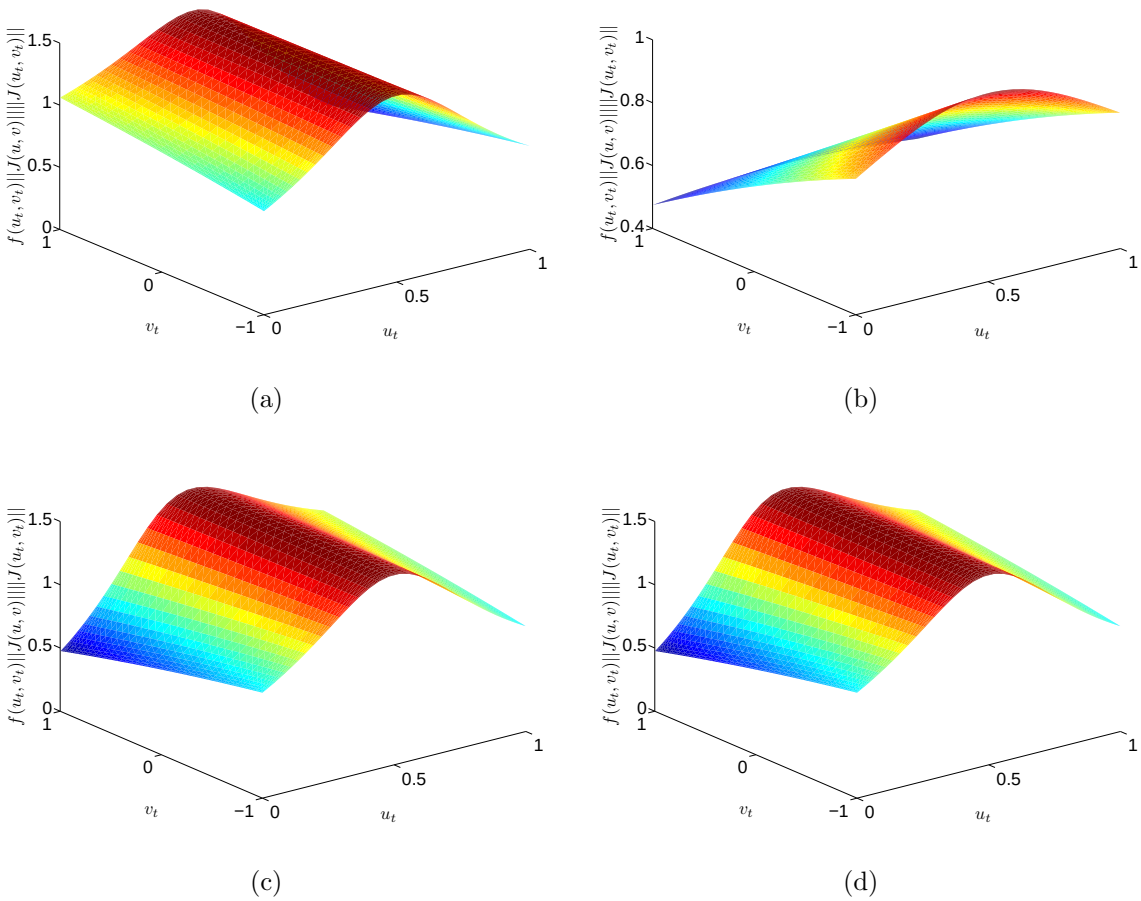

Figure 5.12: Function values obtained from the new transformations: $\Delta^{(1)}$ (a), $\Delta^{(2)}$ (b), $\Delta^{(3)}$ (c) and $\Delta^{(4)}$ (d)

The improvements brought through the use of this partitioning approach are demonstrated in Figure 5.13, in which the convergence analysis presented in Figure 5.10 is restated with the inclusion of the new reached results. It is evident that using the partitioning method a tremendous improvement in the convergence of the integral is achieved, in which an absolute error of 10^{-5} is rapidly obtained with much less gaussian points than the direct method. Typically, by using 10 gaussian points the convergence of the integral is reached.

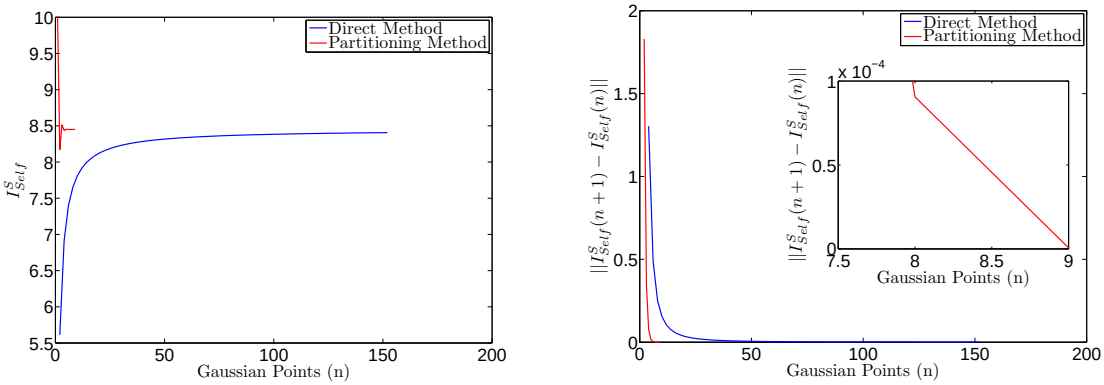

(a) (b)

Figure 5.13: Comparison of the direct and partitioning methods for the convergence of the source self-influence coefficient I^S_{Self}

5.2 Time-Marching Scheme

As mentioned before, the time-marching of both fluid and body motion equations are performed by a Fourth Order Runge-Kutta method which provides high accuracy and stability to numerical methods, such as the one we are dealing with, as already pointed out by Tanizawa (2000). Particularly, the method demands four intermediate calculations to advance the simulation single time step Δt. The method was implemented as follows:

$$k_1 = h(t_n, y) \tag{5.24}$$

$$k_2 = h(t_n + h/2, y + hk_1/2) \tag{5.25}$$

$$k_3 = h(t_n + h/2, y + hk_2/2) \tag{5.26}$$

$$k_4 = h(t_n + h, y + hk_3) \tag{5.27}$$

$$y_{n+1} = y_n + \frac{h}{6}(k_1 + 2k_2 + 2k_3 + k_4) \tag{5.28}$$

In the equations above, y denotes generically all the variables that must be calculated within a time-step Δt, such as the body position $\vec{\xi}$, free surface elevation η and the velocity potential at the undisturbed water surface. For the calculation of the body motions, the set of six second order differential equations (one for each degree of freedom) are transformed into a set of twelve first order equations prior to their evaluations in RK4 scheme.

One last discussion, but also very important for the consistency of the method, is related to two numerical conditions which must be satisfied at the beginning of the simulations.

First, we need to enforce a rest condition over all the boundary surfaces to respect the initial conditions of the IBVPs and then guarantee a correct determination of the subsequently fluid and body motions. Second, the numerical model should avoid impulsive responses in the domain since it may induce long transient periods with no physical interest to our analysis. In our numerical model, these conditions are satisfied by the use of a ramp function $f_r(t)$ that multiplies the boundary velocities and accelerations, guaranteeing a smooth and slow increase of the variables until the achievement of a steady-state solution. The ramp function is defined by:

$$f_r(t) = \begin{cases} \frac{1}{2}\left[1 - \cos(\frac{\pi t}{T_r})\right] & \text{if} \quad t \leq T_r \\ 1 \quad \text{if} \quad t > T_r \end{cases} \tag{5.29}$$

where T_r is the ramp time which is normally set as a multiple of a characteristic wave period involved in the simulations. If one needs to obtain the transient solution, such in a numerical decay test, very small values of T_r must be used.

Chapter 6

Verification Tests with Simple Geometries

Since one of the main goals of the numerical method described in this text is the evaluation of the body motions caused by the action of free surface gravity waves, we need to check its capability to predict the hydrodynamic loads involved in such a problem. Upon the already established linear theory assumption, the superposition of solutions is valid and the hydrodynamic loads, induced by the free floating body motions under waves, may be assumed as a sum of two different components, which may be calculated by the well known diffraction and radiation problems. The diffraction problem consist on the calculation of the hydrodynamic forces and moments, or exciting forces and moments, induced by the interaction of the wave field with a fixed body. The radiation problem refers to the calculation of the forces induced by harmonic oscillations of the body in still water and in the absence of incoming waves. When presenting numerical results for the forces exerted on oscillating bodies it is usual to quote values for the added mass and damping coefficients, which measure the components in phase with acceleration and velocity of the body, respectively, and this convention will be applied here.

This chapter presents the computations of the hydrodynamic loads resulting from the diffraction and radiation problems in infinite water depth, considering simple geometries such as an hemisphere and a circular cylinder. Ultimately, the response of these bodies in regular waves is also presented. Benchmark results were obtained from calculations performed with the software WAMIT which solves the same Boundary Value Problem here defined, but in the frequency domain. Lee and Newman (2005) presented a review about case studies already analyzed with WAMIT, which includes both a Low-Order and a

Higher-Order numerical approach. It is important to emphasize that the objective of this analysis is to validate the present numerical results and not to compare the performance of both Low-Order models. In fact, they would not be comparable to each other, since one treats the problem in time domain and the other in frequency domain. Therefore, for comparison purposes, all the numerical results obtained by WAMIT were run using the Higher-Order method, since for the type of geometries here assessed, the convergence of the results are reached faster, with very low computational efforts and errors that are insignificant when comparing the results to analytical solutions, ensuring the accuracy of this benchmark data. For the hemisphere radiation problem, the added mass and potential damping coefficients are compared to analytical solutions presented by Hulme (1982).

Convergence analyses were performed testing three panel grid resolutions for the free surface and the body wet surface. Aiming at maintaining the results dependent only on the number of panels, the mesh number of panels was increased using a constant factor that multiplies both sides of the quadrilateral panels, thus, keeping constant the panels aspect ratio.

6.1 Geometries Discretization

An hemisphere surface of unitary radius $r_h = 1$ m was discretized in three different grids with 200, 800 and 3200 panels and a circular cylinder, of radius $r_c = 1$ m and draught $T_c = 1$ m, in 120, 500 and 2000 panels. Notice that we tried to set the scale factor value to four by duplicating the discretization parameters in each direction by two. In the circular cylinder case the panels are more concentrated near the intersection region formed by the encounter of the free surface and the body surface. This was done to guarantee a minimum resolution of panels for cases involving high frequency waves in which their lengths are small and the velocity profile confined to this region. Moreover, as observed by Hess and Smith (1967), if several small elements are in the vicinity of a larger one, the accuracy of the solution is associated with the larger elements. For the hemisphere this was guaranteed by increasing the total number of panels. The six body meshes considered in the calculations are displayed in Figure 6.1.

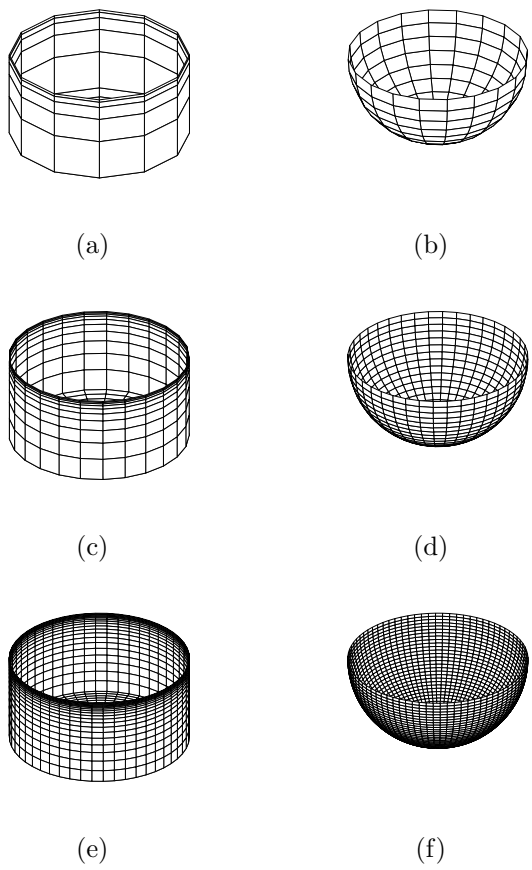

Figure 6.1: Circular cylinder and hemisphere panel meshes used in the computations. Figures (a), (c) and (e) refers to the 120, 500 and 2000 circular cylinder panel meshes, respectively. Figures (b), (d) and (f) refers to the 200, 800 and 3200 hemisphere panel meshes, respectively.

The free surface length depends directly on the wave lengths that will be simulated and due to the limitations of computer memory, we need to truncate the free surface within reasonable numbers, bearing also in mind that a percentage of this area must be designated for energy dissipation since the radiation condition must be satisfied. For these computations, we considered circular free surfaces meshes with radius $r_{fs} = 30$ m, providing sufficient space for the propagation of the waves considered herein. Similar to the body surfaces, three different panel meshes are considered containing 289, 1225 and 4900 panels and, again, an increasing factor value of approximate four was used. Figure 6.2 displays the meshes used in the computations where it is possible to observe that a high number of panels is situated near the body surface. Once again, a minimum number of panels is needed to ensure that the waves are being properly considered.

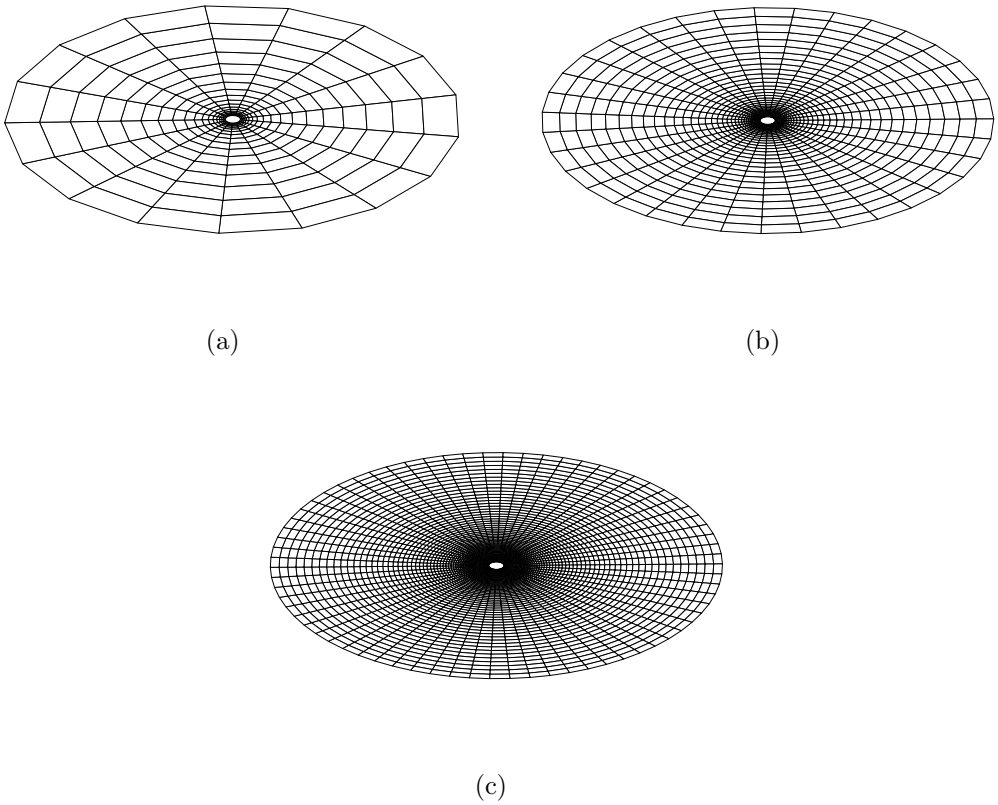

Figure 6.2: Free surface panel meshes used in the computations. Figures (a), (b) and (c) refers to the 289, 1225 and 4900 free surface panel meshes, respectively.

A set of six panel meshes are then constructed by grouping the body and free surface meshes in pairs. Denoting the meshes with the lowest number of panels as coarse meshes, the intermediates as medium meshes and the ones with greatest resolution as fine meshes, Table 6.1 presents the main numbers of the panel meshes that will be simulated.

Table 6.1: Main numbers of the panel meshes used in the computations

	Hemisphere			**Circular Cylinder**		
	Coarse	**Medium**	**Fine**	**Coarse**	**Medium**	**Fine**
Body Mesh	200	800	3200	120	500	2000
Free Surface Mesh	289	1225	4900	289	1225	4900
Final Mesh	489	2025	8100	409	1725	6900

6.2 Fixed Body Simulations

We begin our numerical results presentation simulating cases of fixed bodies interacting with incoming regular waves. Table 6.2 presents the main features of the set of 24 regular waves in a frequency range between 1.716 rad/s and 9.905 rad/s, which were tested in our numerical model. All the waves present unitary amplitudes $A_I = 1$ m. For all the simulations the time step was set to $\Delta t = T/60$ s and the numerical beach coefficients were set to $a = 1.0$ and $b = 2.0$, with the exception of waves 1 to 3, which were simulated considering $b = 1.0$, since their lengths were such that the damping zone would not fit into the domain.

It is important to emphasize that despite the fact that the wave amplitudes present the same magnitude order of the body geometry dimensions, the numerical method here developed treats the problem upon the linear theory assumption and, therefore, its solutions have a linear dependence on the wave amplitude. Thus, if not specified, all the simulations that will be presented in this thesis consider waves of unitary amplitudes so as to make possible a direct comparison of the solution quantities in terms of RAOs calculated by other numerical tools or experimental activities.

Table 6.2: Regular incoming waves used in the simulations

ID	ω **(rad/s)**	**T(s)**	λ**(m)**	**ID**	ω **(rad/s)**	**T(s)**	λ**(m)**
1	1.716	3.662	20.932	13	4.429	1.419	3.142
2	1.981	3.172	15.707	14	4.952	1.269	2.514
3	2.215	2.837	12.563	15	5.425	1.158	2.094
4	2.426	2.590	10.473	16	5.860	1.072	1.795
5	2.620	2.398	8.979	17	6.264	1.003	1.571
6	2.801	2.243	7.856	18	6.644	0.946	1.396
7	2.971	2.115	6.983	19	7.004	0.897	1.256
8	3.132	2.006	6.284	20	7.672	0.819	1.047
9	3.431	1.831	5.236	21	8.287	0.758	0.898
10	3.706	1.695	4.488	22	8.859	0.709	0.785
11	3.962	1.586	3.927	23	9.396	0.669	0.698
12	4.202	1.495	3.491	24	9.905	0.634	0.628

As mentioned before, simulations start from a rest condition and during a pre-specified time is controlled by a ramp function in order to provide a smooth transition to the steady-state solution. The regular incoming wave is imposed in the problem as a boundary condition. As previously discussed, we could decompose the total potential in a sum of an analytic potential of regular waves and a disturbed wave part which enabled us to change the problem variable. This approach brings several benefits to our model if we do not need to make comparisons which involve the wave generation itself. For example, once the

waves are generated at the body surroundings, we do not need to have great concentrations of panels at the whole free surface allowing us to sparse the free surface panels from the body towards the free surface edge. Moreover, due to energy conservation, as the waves propagate away from the body their amplitudes decrease and, therefore, less effort to dissipate the waves are necessary in comparison to a situation in which is necessary to damp the total potential (incoming wave + disturbed waves). Both of these examples reduce the number of necessary panels to discretize the free surface and, consequently, improve the code performance to reproduce the results in relation to wave generation approaches.

Despite of the benefits pointed out above, it is important to emphasize that even concentrating small panels near the body surface and using numerical damping zones, a minimum number of panels per wave length is required to correctly satisfy the dispersion relation of waves in infinite water depth and, also, avoid signal modulations induced by the lack of panels. In order to illustrate it, we perform simulations with the cylinder body considering three wave frequencies of $\omega = 4.202$ rad/s, $\omega = 6.264$ rad/s and $\omega = 9.905$ rad/s with respective wave lengths of $\lambda = 3.491$ m, $\lambda = 1.571$ m and $\lambda = 0.628$ m. The time series of the horizontal F_x and vertical F_z hydrodynamic forces are presented in Figures 6.3, 6.4, 6.5 and 6.6, 6.7, 6.8, respectively.

It is possible to realize that as the angular frequency increases larger differences in terms of amplitude and phase between the hydrodynamic forces calculated with each mesh are observed. Wave reflections due to the lack of panels are clearly observed for the coarse mesh when simulating waves with frequency higher than $\omega = 6.264$ rad/s. For the highest frequency, for example, the vertical forces calculated by the coarse mesh present non physical results with order of magnitude much larger than those obtained with the other meshes. Moreover, a slightly variation of phase may also be observed. Results for the medium and fine meshes present better agreement for all the frequencies, but the highest one, what indicates that only the fine mesh is capable to correctly propagate waves of such small length.

The results for the hemisphere body are not presented since the same behavior was observed. This was expected since the propagation of waves is related to the free surface meshes which are the same for both geometries.

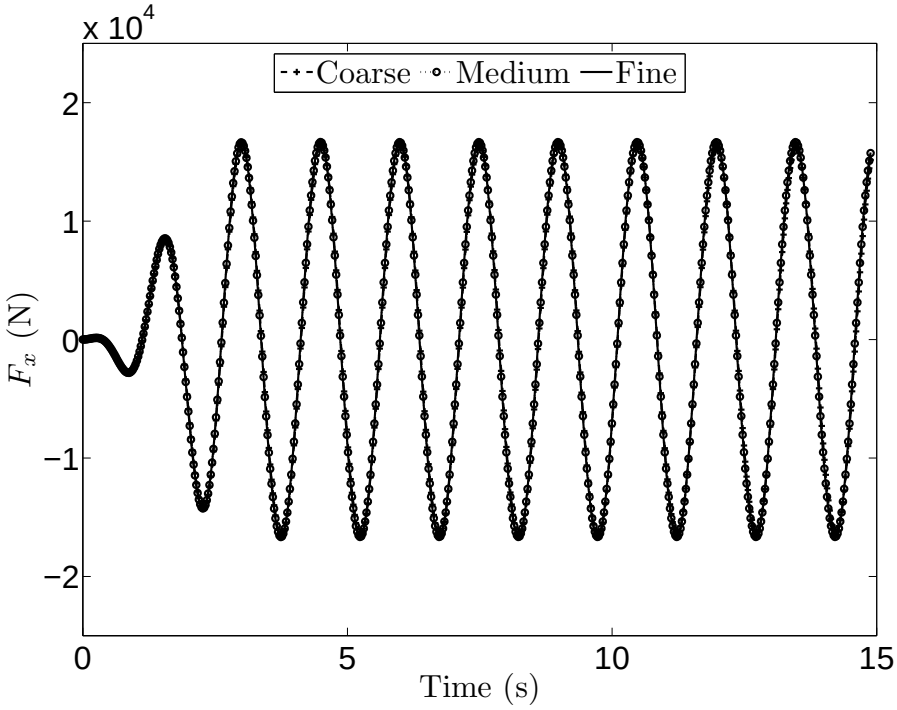

Figure 6.3: Hydrodynamic horizontal force F_x induced by a wave with frequency of $\omega =$ 4.202 rad/s. Cylinder body

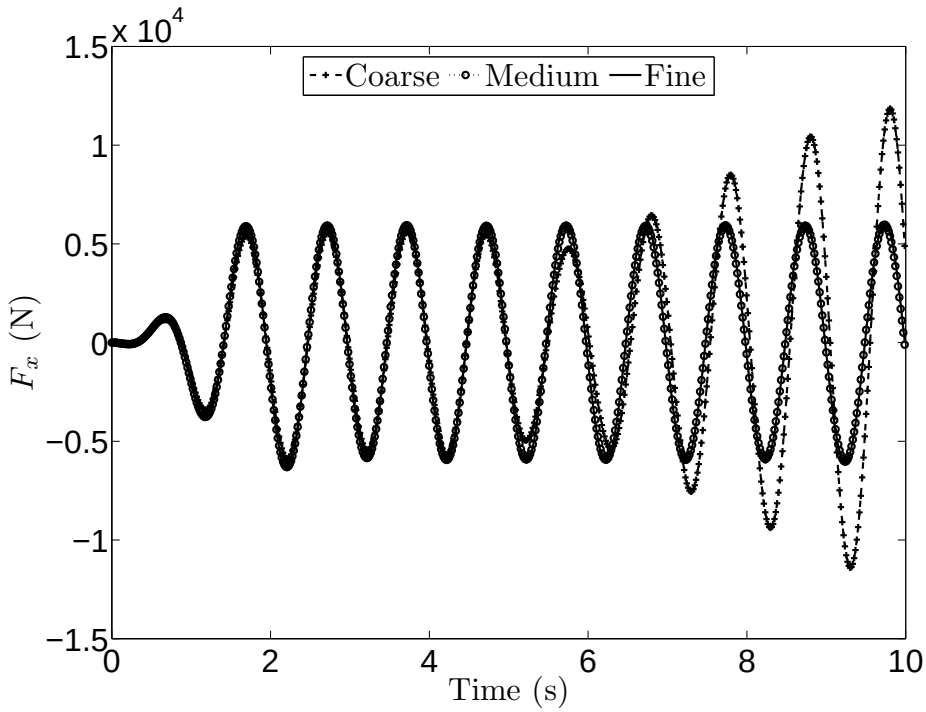

Figure 6.4: Hydrodynamic horizontal force F_x induced by a wave with frequency of $\omega =$ 6.264 rad/s. Cylinder body

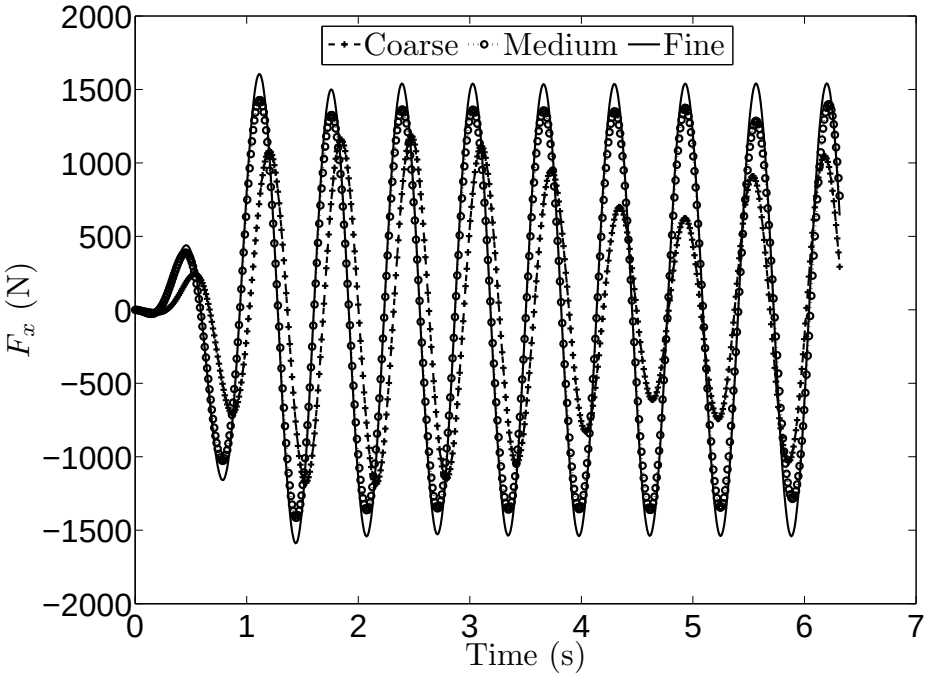

Figure 6.5: Hydrodynamic horizontal force F_x induced by a wave with frequency of $\omega =$ 9.905 rad/s. Cylinder body

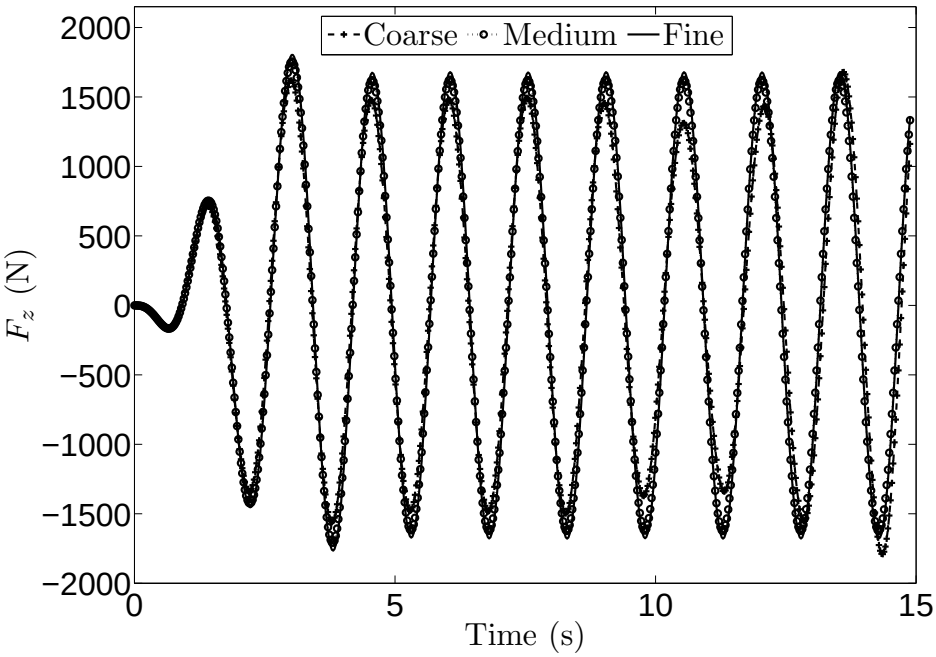

Figure 6.6: Hydrodynamic vertical force F_z induced by a wave with frequency of $\omega = 4.202$ rad/s. Cylinder body

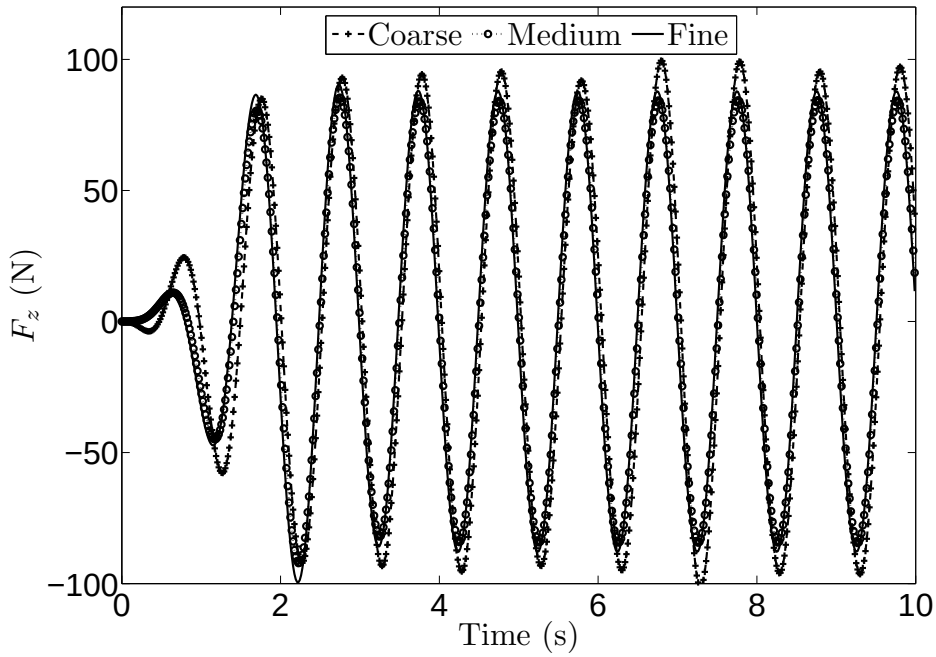

Figure 6.7: Hydrodynamic vertical force F_z induced by a wave with frequency of $\omega = 6.264$ rad/s. Cylinder body

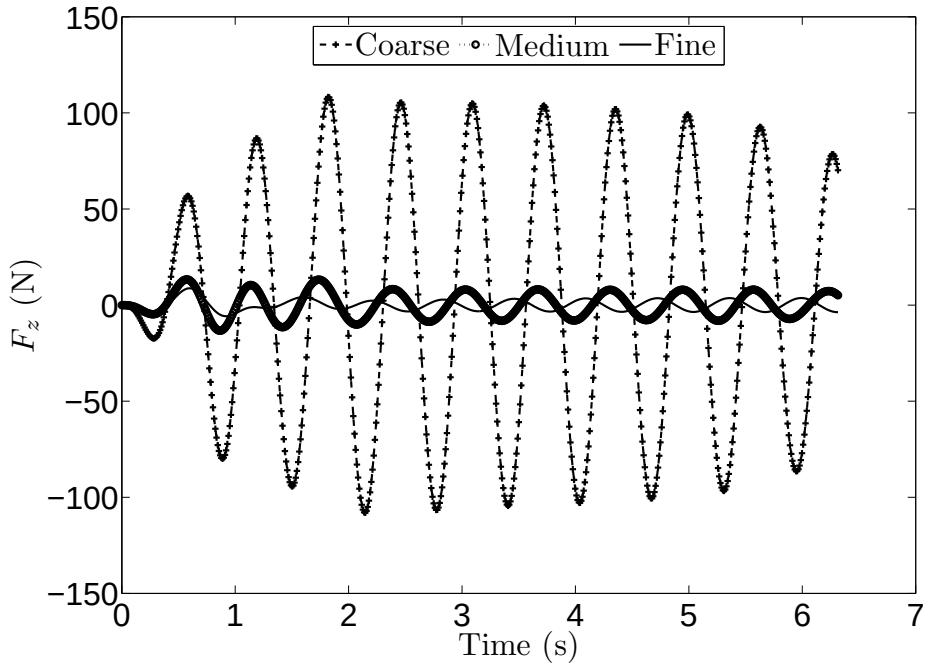

Figure 6.8: Hydrodynamic vertical force F_z induced by a wave with frequency of $\omega = 9.905$ rad/s. Cylinder body

In order to check the convergence of the results we compare the horizontal and vertical non-

dimensional forces for all panel meshes and wave frequencies presented in Table 6.2. For the circular cylinder, the non-dimensional moment M_y around the y-axis is also presented. The non-dimensional forces and moments are calculated using the following definitions:

$$\begin{array}{cc} \text{Hemisphere} & \text{Circular Cylinder} \\ \bar{F}_x = \dfrac{f_x}{\frac{2}{3}\pi r_h^3 \rho g} & \bar{F}_x = \dfrac{f_x}{\rho g \pi r_c^2 T_c} \\ \bar{F}_z = \dfrac{f_z}{\frac{2}{3}\pi r_h^3 \rho g} & \bar{F}_z = \dfrac{f_z}{\rho g \pi r_c^2 T_c} \\ & \bar{M}_y = \dfrac{m_y}{\rho g \pi r_c^3 T_c} \end{array} \tag{6.1}$$

where f_x, f_z and m_y are the, respective, amplitudes of the forces F_x and F_z and moment M_y. Note that for the medium and fine mesh, the amplitude values are easily determined by the forces and moments time series, since a steady-state solution is available. For the coarse mesh, however, only a short sample of the time series may be used because the solution is spoiled with numerical reflections.

The convergence analysis for the non-dimensional horizontal and vertical hydrodynamic forces for the hemisphere body is presented in Tables 6.3 and 6.4, respectively. In order to better visualize the results, the data are also illustrated in Figures 6.9 and 6.10. The WAMIT results used as benchmark data was obtained using the Higher Order approach with a *panel size* parameter of 0.05, which was defined by a prior grid convergence analysis. From the results, it may be observed that the relative errors between both calculations tend to reduce with the increase of the number of panels, achieving very low values for the mesh with finest resolution. One should notice that, even considering the fine mesh, some relative errors are still higher, especially for the vertical hydrodynamic forces. Nevertheless, we may also realize that these errors are being obtained with very low values which any insignificant difference may result in very large relative errors.

The simulations with the circular cylinder presented very similar trends in comparison to the hemisphere ones. Again, convergence of the results is confirmed increasing the number of panels and very low relative errors are observed for most of the wave frequencies. Tables 6.5, 6.6 and 6.7 present the convergence analyses performed with the horizontal force, vertical force and the moment in relation to the y-axis, respectively. Once more, the data are illustrated in Figures 6.11, 6.12 and 6.13. In general, a good agreement between WAMIT results and the present values is observed.

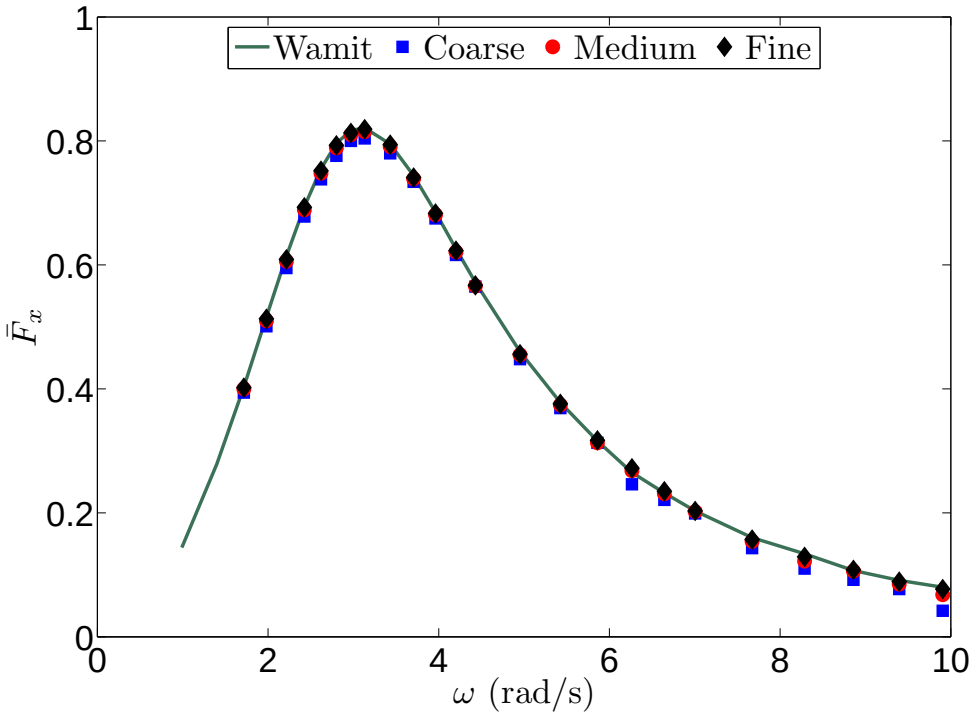

Figure 6.9: Convergence analysis of the non-dimensional horizontal hydrodynamic force $\bar{F}_x$ for the hemisphere body

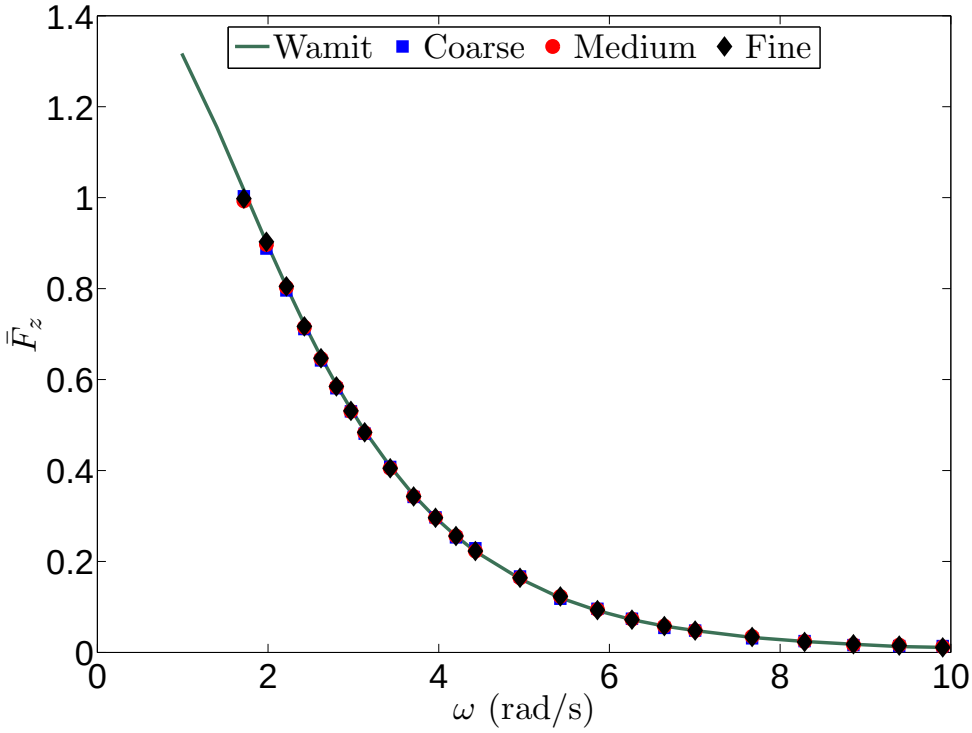

Figure 6.10: Convergence analysis of the non-dimensional vertical hydrodynamic force $\bar{F}_z$ for the hemisphere body

Table 6.3: Convergence analysis of the non-dimensional horizontal hydrodynamic force $\bar{F}_x$ for the hemisphere body. WAMIT values are used as reference for the relative errors

			Coarse		**Medium**		**Fine**	
ID	ω	**WAMIT**	$\bar{F}_x$	$\frac{\lvert\bar{F}_x-\text{WAMIT}\rvert}{\text{WAMIT}}$	$\bar{F}_x$	$\frac{\lvert\bar{F}_x-\text{WAMIT}\rvert}{\text{WAMIT}}$	$\bar{F}_x$	$\frac{\lvert\bar{F}_x-\text{WAMIT}\rvert}{\text{WAMIT}}$
1	1.716	0.403	0.394	0.023	0.400	0.009	0.402	0.003
2	1.981	0.516	0.501	0.029	0.510	0.012	0.513	0.005
3	2.215	0.614	0.595	0.031	0.606	0.014	0.609	0.008
4	2.426	0.694	0.678	0.023	0.689	0.007	0.693	0.002
5	2.620	0.755	0.738	0.023	0.748	0.010	0.752	0.005
6	2.801	0.796	0.776	0.025	0.789	0.009	0.793	0.004
7	2.971	0.817	0.800	0.020	0.810	0.009	0.813	0.004
8	3.132	0.821	0.804	0.021	0.815	0.008	0.819	0.003
9	3.431	0.795	0.780	0.019	0.791	0.006	0.794	0.002
10	3.706	0.744	0.734	0.014	0.739	0.007	0.741	0.004
11	3.962	0.685	0.675	0.014	0.681	0.005	0.683	0.002
12	4.202	0.626	0.616	0.016	0.621	0.007	0.623	0.005
13	4.429	0.572	0.565	0.013	0.566	0.010	0.567	0.009
14	4.952	0.460	0.448	0.026	0.455	0.011	0.456	0.010
15	5.425	0.378	0.369	0.023	0.374	0.009	0.376	0.004
16	5.860	0.316	0.313	0.012	0.313	0.011	0.317	0.003
17	6.264	0.265	0.246	0.072	0.268	0.010	0.272	0.028
18	6.644	0.232	0.221	0.048	0.231	0.001	0.235	0.014
19	7.004	0.203	0.199	0.016	0.202	0.002	0.203	0.003
20	7.672	0.160	0.143	0.101	0.154	0.035	0.157	0.014
21	8.287	0.134	0.110	0.180	0.122	0.086	0.129	0.033
22	8.859	0.107	0.092	0.141	0.106	0.011	0.108	0.004
23	9.396	0.091	0.077	0.156	0.085	0.067	0.089	0.029
24	9.905	0.080	0.042	0.470	0.068	0.142	0.077	0.030

Table 6.4: Convergence analysis of the non-dimensional vertical hydrodynamic force $\bar{F}_z$ for the hemisphere body. WAMIT values are used as reference for the relative errors

			Coarse		**Medium**		**Fine**	
ID	ω	**WAMIT**	$\bar{F}_z$	$\frac{\lvert\bar{F}_z-\text{WAMIT}\rvert}{\text{WAMIT}}$	$\bar{F}_z$	$\frac{\lvert\bar{F}_z-\text{WAMIT}\rvert}{\text{WAMIT}}$	$\bar{F}_z$	$\frac{\lvert\bar{F}_z-\text{WAMIT}\rvert}{\text{WAMIT}}$
1	1.716	1.017	1.003	0.015	0.993	0.024	0.998	0.019
2	1.981	0.902	0.888	0.016	0.897	0.006	0.903	0.000
3	2.215	0.805	0.796	0.011	0.803	0.002	0.805	0.001
4	2.426	0.722	0.711	0.015	0.715	0.009	0.717	0.007
5	2.620	0.650	0.642	0.013	0.646	0.007	0.647	0.005
6	2.801	0.589	0.581	0.013	0.584	0.008	0.585	0.006
7	2.971	0.535	0.530	0.009	0.530	0.008	0.531	0.007
8	3.132	0.487	0.481	0.012	0.483	0.008	0.484	0.007
9	3.431	0.409	0.408	0.000	0.405	0.008	0.405	0.008
10	3.706	0.346	0.342	0.013	0.343	0.010	0.343	0.010
11	3.962	0.296	0.297	0.004	0.296	0.002	0.296	0.003
12	4.202	0.256	0.253	0.010	0.256	0.002	0.256	0.001
13	4.429	0.222	0.229	0.031	0.223	0.005	0.223	0.004
14	4.952	0.162	0.167	0.031	0.164	0.010	0.164	0.009
15	5.425	0.120	0.118	0.018	0.123	0.029	0.123	0.024
16	5.860	0.092	0.096	0.039	0.094	0.017	0.093	0.009
17	6.264	0.072	0.074	0.021	0.073	0.002	0.072	0.003
18	6.644	0.058	0.054	0.072	0.058	0.007	0.058	0.002
19	7.004	0.048	0.048	0.011	0.048	0.004	0.048	0.016
20	7.672	0.033	0.031	0.041	0.035	0.077	0.034	0.057
21	8.287	0.024	0.025	0.048	0.024	0.000	0.023	0.016
22	8.859	0.018	0.016	0.119	0.017	0.056	0.018	0.002
23	9.396	0.013	0.014	0.026	0.016	0.150	0.015	0.114
24	9.905	0.011	0.014	0.246	0.012	0.073	0.011	0.007

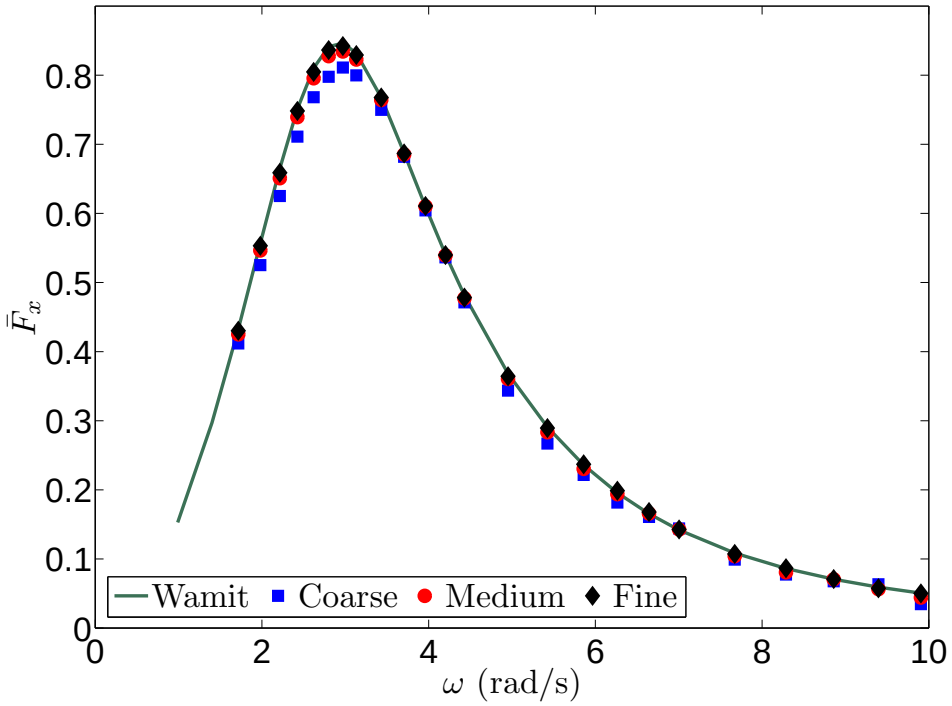

Figure 6.11: Convergence analysis of the non-dimensional horizontal hydrodynamic force $\bar{F}_x$ for the circular cylinder body

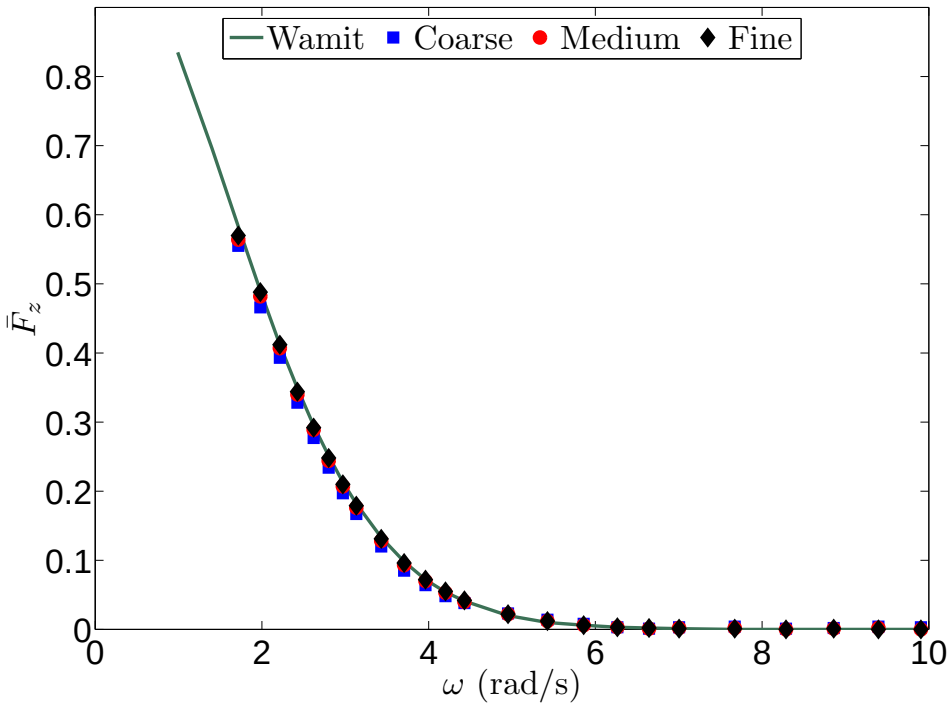

Figure 6.12: Convergence analysis of the non-dimensional vertical hydrodynamic force $\bar{F}_z$ for the circular cylinder body

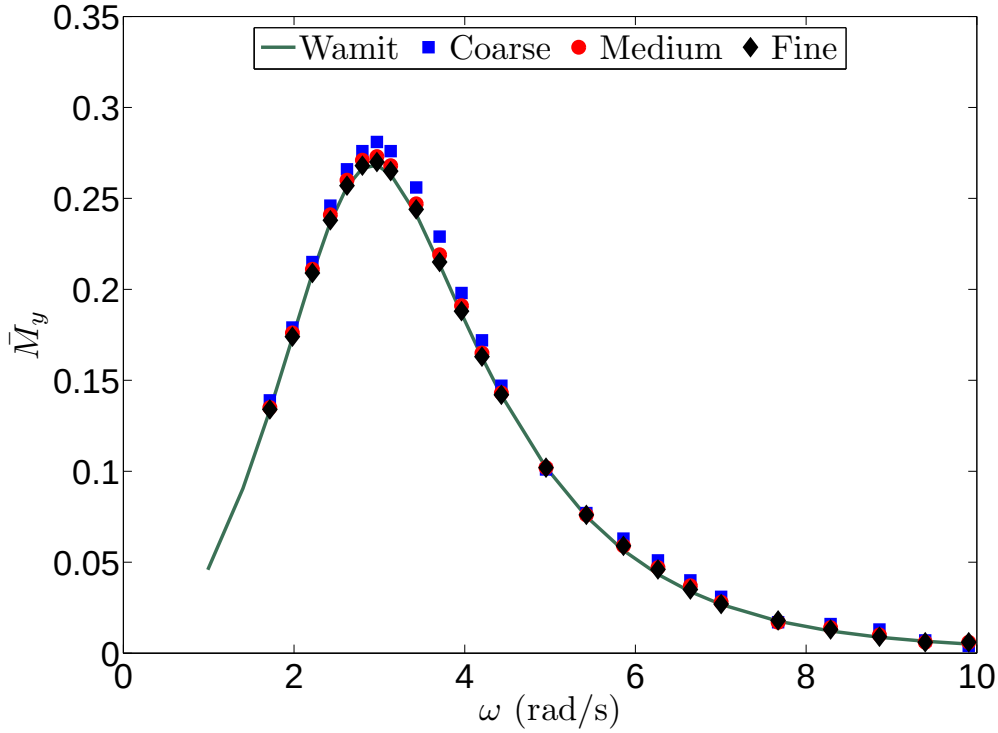

Figure 6.13: Convergence analysis of the non-dimensional hydrodynamic moment $\bar{M}_y$ for the circular cylinder body

Table 6.5: Convergence analysis of the non-dimensional horizontal hydrodynamic force $\bar{F}_x$ for the circular cylinder body. WAMIT values are used as reference for the relative errors

			Coarse		**Medium**		**Fine**	
ID	ω	**WAMIT**	$\bar{F}_x$	$\frac{\lvert\bar{F}_x-\text{WAMIT}\rvert}{\text{WAMIT}}$	$\bar{F}_x$	$\frac{\lvert\bar{F}_x-\text{WAMIT}\rvert}{\text{WAMIT}}$	$\bar{F}_x$	$\frac{\lvert\bar{F}_x-\text{WAMIT}\rvert}{\text{WAMIT}}$
1	1.716	0.432	0.412	0.048	0.425	0.017	0.430	0.005
2	1.981	0.557	0.525	0.056	0.546	0.018	0.553	0.006
3	2.215	0.665	0.625	0.060	0.651	0.021	0.659	0.009
4	2.426	0.751	0.711	0.053	0.739	0.016	0.748	0.004
5	2.620	0.810	0.768	0.052	0.796	0.018	0.805	0.007
6	2.801	0.841	0.798	0.052	0.828	0.016	0.836	0.006
7	2.971	0.847	0.811	0.042	0.834	0.014	0.842	0.005
8	3.132	0.832	0.800	0.039	0.823	0.011	0.829	0.003
9	3.431	0.768	0.750	0.023	0.764	0.005	0.768	0.000
10	3.706	0.687	0.682	0.008	0.685	0.003	0.687	0.001
11	3.962	0.610	0.604	0.009	0.610	0.001	0.611	0.002
12	4.202	0.541	0.536	0.008	0.539	0.003	0.540	0.002
13	4.429	0.481	0.471	0.021	0.477	0.009	0.478	0.007
14	4.952	0.368	0.344	0.067	0.360	0.021	0.364	0.010
15	5.425	0.291	0.267	0.082	0.283	0.025	0.289	0.005
16	5.860	0.236	0.222	0.060	0.230	0.023	0.237	0.005
17	6.264	0.196	0.182	0.072	0.194	0.010	0.199	0.016
18	6.644	0.165	0.161	0.028	0.166	0.003	0.168	0.016
19	7.004	0.142	0.144	0.017	0.143	0.006	0.143	0.006
20	7.672	0.108	0.099	0.087	0.104	0.039	0.107	0.010
21	8.287	0.086	0.077	0.102	0.081	0.065	0.087	0.005
22	8.859	0.071	0.068	0.041	0.071	0.000	0.071	0.004
23	9.396	0.059	0.063	0.072	0.056	0.048	0.057	0.028
24	9.905	0.050	0.035	0.315	0.044	0.126	0.050	0.007

Table 6.6: Convergence analysis of the non-dimensional vertical hydrodynamic force $\bar{F}_z$ for the circular cylinder body. WAMIT values are used as reference for the relative errors

			Coarse		**Medium**		**Fine**	
ID	ω	**WAMIT**	$\bar{F}_z$	$\frac{\lvert\bar{F}_z-\text{WAMIT}\rvert}{\text{WAMIT}}$	$\bar{F}_z$	$\frac{\lvert\bar{F}_z-\text{WAMIT}\rvert}{\text{WAMIT}}$	$\bar{F}_z$	$\frac{\lvert\bar{F}_z-\text{WAMIT}\rvert}{\text{WAMIT}}$
1	1.716	0.583	0.555	0.047	0.564	0.032	0.570	0.021
2	1.981	0.490	0.466	0.049	0.482	0.015	0.488	0.003
3	2.215	0.412	0.393	0.047	0.407	0.012	0.412	0.002
4	2.426	0.349	0.328	0.058	0.340	0.023	0.344	0.012
5	2.620	0.295	0.277	0.061	0.289	0.022	0.292	0.009
6	2.801	0.251	0.234	0.066	0.244	0.025	0.248	0.011
7	2.971	0.213	0.197	0.074	0.207	0.028	0.210	0.012
8	3.132	0.182	0.167	0.082	0.176	0.031	0.179	0.013
9	3.431	0.133	0.120	0.097	0.128	0.038	0.131	0.014
10	3.706	0.098	0.085	0.126	0.093	0.046	0.096	0.017
11	3.962	0.072	0.064	0.114	0.070	0.035	0.072	0.002
12	4.202	0.054	0.048	0.115	0.053	0.024	0.055	0.009
13	4.429	0.041	0.038	0.057	0.040	0.005	0.042	0.022
14	4.952	0.020	0.023	0.141	0.022	0.090	0.022	0.074
15	5.425	0.010	0.014	0.362	0.012	0.186	0.012	0.105
16	5.860	0.006	0.008	0.462	0.006	0.156	0.006	0.057
17	6.264	0.003	0.003	0.044	0.003	0.063	0.003	0.018
18	6.644	0.002	0.001	0.293	0.001	0.164	0.002	0.063
19[1]	7.004	0.001	0.003	–	0.002	–	0.001	–
20[1]	7.672	0.000	0.004	–	0.002	–	0.001	–
21[1]	8.287	0.000	0.001	–	0.000	–	0.000	–
22[1]	8.859	0.000	0.002	–	0.001	–	0.001	–
23[1]	9.396	0.000	0.004	–	0.002	–	0.000	–
24[1]	9.905	0.000	0.003	–	0.000	–	0.000	–

[1]The relative errors are omitted because the comparison involves very low values for which any insignificant differences result in very large relative errors

Table 6.7: Convergence analysis of the non-dimensional hydrodynamic moment $\bar{M}_y$ for the circular cylinder body. WAMIT values are used as reference for the relative errors

			Coarse		**Medium**		**Fine**	
ID	ω	**WAMIT**	$\bar{M}_y$	$\frac{\lvert\bar{M}_y-\text{WAMIT}\rvert}{\text{WAMIT}}$	$\bar{M}_y$	$\frac{\lvert\bar{M}_y-\text{WAMIT}\rvert}{\text{WAMIT}}$	$\bar{M}_y$	$\frac{\lvert\bar{M}_y-\text{WAMIT}\rvert}{\text{WAMIT}}$
1	1.716	0.133	0.139	0.044	0.135	0.015	0.134	0.005
2	1.981	0.173	0.179	0.034	0.176	0.013	0.174	0.004
3	2.215	0.209	0.215	0.029	0.211	0.010	0.209	0.001
4	2.426	0.237	0.246	0.036	0.241	0.016	0.238	0.007
5	2.620	0.256	0.266	0.037	0.260	0.013	0.257	0.004
6	2.801	0.267	0.276	0.036	0.271	0.015	0.268	0.005
7	2.971	0.268	0.281	0.046	0.273	0.017	0.270	0.005
8	3.132	0.263	0.276	0.048	0.268	0.019	0.265	0.007
9	3.431	0.241	0.256	0.061	0.247	0.024	0.244	0.010
10	3.706	0.214	0.229	0.070	0.219	0.023	0.215	0.008
11	3.962	0.187	0.198	0.063	0.191	0.024	0.188	0.010
12	4.202	0.163	0.172	0.055	0.165	0.017	0.163	0.005
13	4.429	0.142	0.147	0.034	0.143	0.008	0.142	0.001
14	4.952	0.102	0.101	0.010	0.102	0.001	0.102	0.003
15	5.425	0.075	0.077	0.027	0.076	0.016	0.076	0.013
16	5.860	0.056	0.063	0.124	0.059	0.050	0.059	0.037
17	6.264	0.043	0.051	0.176	0.047	0.084	0.046	0.057
18	6.644	0.034	0.040	0.185	0.037	0.088	0.035	0.049
19	7.004	0.027	0.031	0.172	0.028	0.050	0.027	0.020
20	7.672	0.018	0.017	0.050	0.017	0.034	0.018	0.004
21	8.287	0.012	0.016	0.348	0.014	0.117	0.013	0.082
22[1]	8.859	0.009	0.013	–	0.010	–	0.009	–
23[1]	9.396	0.007	0.007	–	0.006	–	0.006	–
24[1]	9.905	0.005	0.004	–	0.006	–	0.006	–

6.3 Forced Motion Simulations

This item presents the simulations of forced harmonic oscillations imposed on both the hemisphere and the circular cylinder body. Unlike the fixed body simulations, this study does not contain incident waves and the hydrodynamic loads are generated only by body oscillatory motions with unitary amplitude. Again, all the simulations were run with a time step of $\Delta t = T/60$ s and with the numerical beach coefficients set to $a = 1.0$ and $b = 1.0$ or $b = 2.0$, depending on the wave length.

In linear theory it is quite usual to decompose the total hydrodynamic force induced by

[1]The relative errors are omitted because the comparison involves very low values for which any insignificant differences result in very large relative errors

harmonic oscillations in two different components associated to added mass and radiation damping, which are in phase with the body acceleration and velocity, respectively. To derive these quantities let us consider, for example, a pure heave forced harmonic oscillation with amplitude A_3 and angular frequency ω, as follows:

$$\xi_3(t) = A_3 \sin(\omega t) \tag{6.2}$$

The body velocity and acceleration are then easily found by:

$$\frac{\partial \xi_3(t)}{\partial t} = \omega A_3 \cos(\omega t) \tag{6.3}$$

$$\frac{\partial^2 \xi_3(t)}{\partial t^2} = -\omega^2 A_3 \sin(\omega t) \tag{6.4}$$

We now assume that the hydrodynamic forces induced by this motion may be separated into a component in phase with the body acceleration and another with the body velocity, as described next:

$$F_3(t) = A_{33} \frac{\partial^2 \xi_3(t)}{\partial t^2} + B_{33} \frac{\partial \xi_3(t)}{\partial t} \tag{6.5}$$

where the coefficients, A_{ij} and B_{ij}, refer to the added mass and radiation damping, respectively, on the ith degree of freedom induced by a motion in the jth degree of freedom.

Combining equations (6.3), (6.4) and (6.5), it follows that:

$$F_3(t) = -\omega^2 A_3 A_{33} \sin(\omega t) + \omega A_3 B_{33} \cos(\omega t) \tag{6.6}$$

By using Fourier's formula we can determine the coefficients that multiply the sine and cosine functions and consequently define the added mass and radiation damping coefficients. Therefore, multiplying equation (6.6) by $\sin(\omega t)$ and integrating over one period $T = 2\pi/\omega$, the coefficient A_{33} is calculated by:

$$A_{33} = -\frac{1}{A_3 \pi \omega} \int_{t-\frac{T}{2}}^{t+\frac{T}{2}} F_3(t) \sin(\omega t) \mathrm{d}t \tag{6.7}$$

Analogously, we multiply equation (6.6) by $\cos(\omega t)$ and integrating over one period $T =$

$2\pi/\omega$, the coefficient B_{33} is calculated by:

$$B_{33} = \frac{1}{A_3\pi} \int_{t-\frac{T}{2}}^{t+\frac{T}{2}} F_3(t)\cos(\omega t)\mathrm{d}t \tag{6.8}$$

Numerically, the integral terms in equations (6.7) and (6.8) are calculated by the trapezoidal rule. This must be performed marching in time and consequently we define a time series for the coefficients A_{33} and B_{33} which tends to assume a constant value if the hydrodynamic force is in steady state. In other words, we are applying a moving window Fourier analysis of the temporal series with a window width equal to one oscillation period.

In order to illustrate it, Figure 6.14 presents the time series for the hydrodynamic force F_3, for the added mass A_{33} and for the radiation damping B_{33}. Notice that the coefficient curves present some oscillations at the beginning of the simulation, warning us that the hydrodynamic forces are still in a transient period. Going further, we observe that after a certain instant of time, the signals become practically constant, indicating that the force is in steady state. After a constant behavior of the curve is observed, the added mass and radiation damping coefficients are then determined by an average of its values. The calculation of the added mass and radiation damping coefficients for other degrees of freedom follows the same approach.

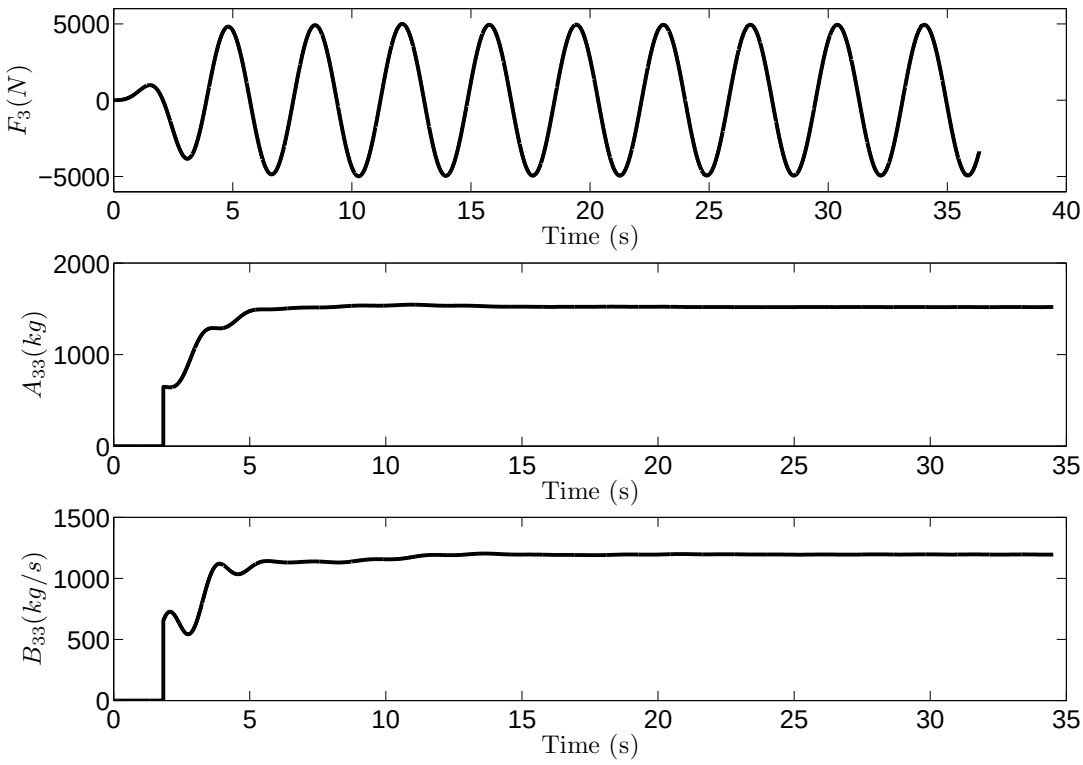

Figure 6.14: Determination of A_{33} and B_{33} coefficients

The calculations of the added mass and radiation damping coefficients are then repeated using the same angular frequencies described in Table 6.2. Convergence analysis of the results are performed simulating each case for the coarse, medium and fine meshes presented in Table 6.1. Aiming at verifying the results, the coefficients obtained with the hemisphere body are compared to the analytical solution presented by Hulme (1982), whereas the ones for the circular cylinder body are compared to data calculated by the software WAMIT. Again, these values are used as a reference for determination of relative errors. The added mass and radiation damping coefficients $\bar{A}_{ij}$ and $\bar{B}_{ij}$ are normalized as follows:

$$
\begin{array}{lll}
\text{Hemisphere} & \text{Circular Cylinder} & \\
\bar{A}_{ij} = \dfrac{A_{ij}}{\frac{2}{3}\pi r_h^3 \rho} & \bar{A}_{ij} = \dfrac{A_{ij}}{\rho \pi r_c^2 T_c} & \text{for} \quad i,j \leq 3 \\
\bar{B}_{ij} = \dfrac{B_{ij}}{\frac{2}{3}\pi r_h^3 \rho \omega} & \bar{B}_{ij} = \dfrac{B_{ij}}{\rho \pi r_c^2 T_c \omega} & \text{for} \quad i,j \leq 3 \\
 & \bar{A}_{ij} = \dfrac{A_{ij}}{\rho \pi r_c^3 T_c} & \text{for} \quad i,j \geq 4 \\
 & \bar{B}_{ij} = \dfrac{B_{ij}}{\rho \pi r_c^3 T_c \omega} & \text{for} \quad i,j \geq 4
\end{array}
\tag{6.9}
$$

The non-dimensional added mass and radiation damping coefficients for heave and surge modes of the hemisphere body are presented in Tables 6.8, 6.9, 6.10 and 6.11 with the respective plots illustrated in Figures 6.15, 6.16, 6.17 and 6.18. Notice that the present calculations agree very well with the analytical solutions derived by Hulme (1982) for all the angular frequencies analyzed. In addition, differences between the results obtained with each panel mesh are very small, pointing out that for this body geometry very low computational costs are necessary for a reasonable numerical prediction of these coefficients.

The same behaviour is not observed in the circular cylinder results, presented in Tables 6.12, 6.13, 6.14 and 6.15 and displayed in the plots 6.19, 6.20, 6.21 and 6.22. Although a fine agreement is observed for the medium and fine meshes, calculations performed with the coarse mesh does not provide accurate results as, for example, the added mass coefficients for the heave mode presented in Figure 6.21. Looking for the pitch mode coefficients $\bar{A}_{55}$ and $\bar{B}_{55}$ we conclude that even the fine mesh is insufficient to predict accurately the same values calculated by the WAMIT higher order scheme. This may be justified by the presence of an edge near the cylinder bottom which renders the convergence of the Low-Order method much more difficult, specially because the meshes were constructed concentrating the panels near the free surface and scattering them towards the bottom edge of the cylinder.

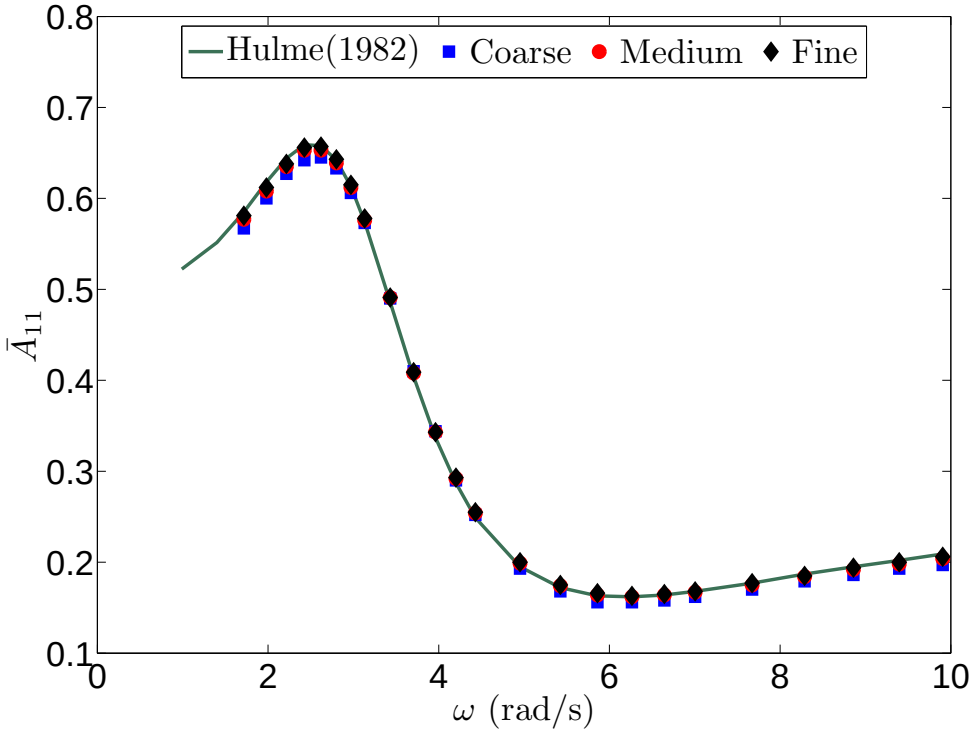

Figure 6.15: Convergence analysis of the added mass coefficient $\bar{A}_{11}$ for the hemisphere body

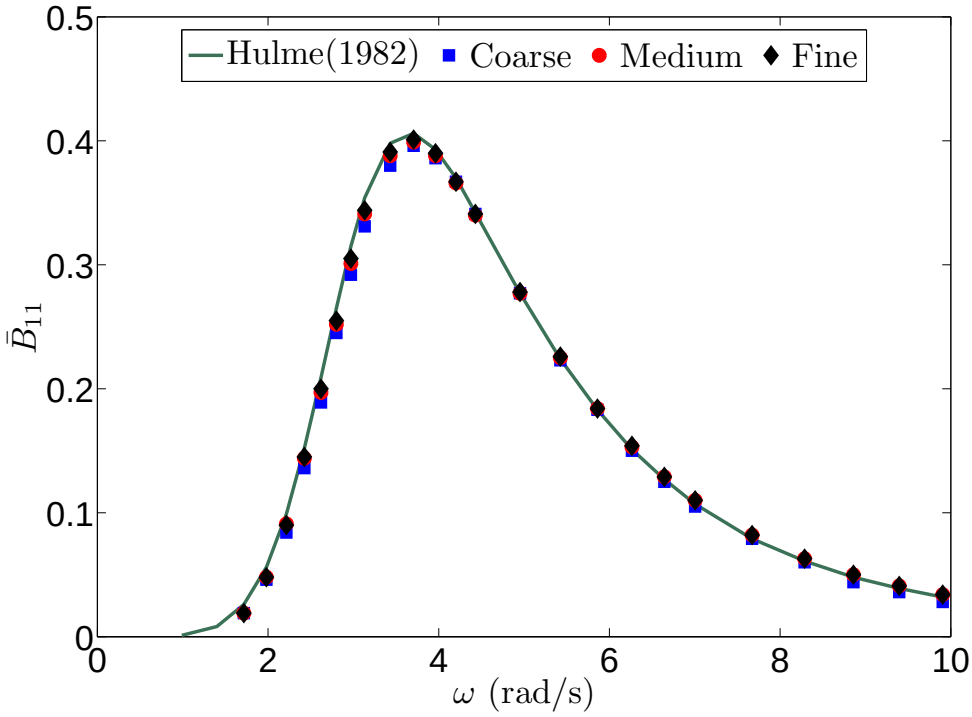

Figure 6.16: Convergence analysis of the radiation damping coefficient $\bar{B}_{11}$ for the hemisphere body

Table 6.8: Convergence analysis of the non-dimensional added mass $\bar{A}_{11}$ for the hemisphere body. Hulme (1982) values are used as reference for the relative errors

			Coarse		**Medium**		**Fine**	
ID	ω	**(HULME, 1982)**	$\bar{A}_{11}$	$\frac{\lvert\bar{A}_{11}-\text{HULME}\rvert}{\text{HULME}}$	$\bar{A}_{11}$	$\frac{\lvert\bar{A}_{11}-\text{HULME}\rvert}{\text{HULME}}$	$\bar{A}_{11}$	$\frac{\lvert\bar{A}_{11}-\text{HULME}\rvert}{\text{HULME}}$
1	1.716	0.585	0.567	0.030	0.577	0.014	0.581	0.006
2	1.981	0.618	0.600	0.028	0.608	0.016	0.612	0.009
3	2.215	0.644	0.627	0.027	0.635	0.014	0.638	0.009
4	2.426	0.659	0.642	0.025	0.653	0.008	0.656	0.005
5	2.620	0.658	0.645	0.021	0.653	0.008	0.657	0.002
6	2.801	0.642	0.633	0.014	0.639	0.004	0.643	0.001
7	2.971	0.613	0.606	0.011	0.612	0.001	0.615	0.004
8	3.132	0.574	0.573	0.002	0.576	0.003	0.578	0.007
9	3.431	0.486	0.490	0.009	0.491	0.009	0.491	0.011
10	3.706	0.404	0.410	0.016	0.408	0.011	0.409	0.012
11	3.962	0.337	0.344	0.020	0.343	0.018	0.343	0.019
12	4.202	0.287	0.290	0.013	0.292	0.020	0.293	0.021
13	4.429	0.249	0.252	0.009	0.254	0.019	0.255	0.021
14	4.952	0.195	0.193	0.011	0.199	0.018	0.200	0.023
15	5.425	0.172	0.168	0.022	0.174	0.013	0.175	0.019
16	5.860	0.163	0.156	0.045	0.164	0.007	0.166	0.013
17	6.264	0.162	0.156	0.036	0.162	0.002	0.163	0.009
18	6.644	0.164	0.158	0.037	0.164	0.003	0.165	0.004
19	7.004	0.168	0.162	0.036	0.167	0.006	0.168	0.002
20	7.672	0.177	0.170	0.038	0.175	0.010	0.177	0.002
21	8.287	0.187	0.179	0.039	0.184	0.015	0.185	0.006
22	8.859	0.195	0.186	0.047	0.192	0.017	0.194	0.007
23	9.396	0.202	0.193	0.043	0.198	0.020	0.200	0.010
24	9.905	0.209	0.197	0.056	0.204	0.023	0.206	0.012

Table 6.9: Convergence analysis of the non-dimensional radiation damping $\bar{B}_{11}$ for the hemisphere body. Hulme (1982) values are used as reference for the relative errors

			Coarse		**Medium**		**Fine**	
ID	ω	**(HULME, 1982)**	$\bar{B}_{11}$	$\frac{\lvert\bar{B}_{11}-\text{HULME}\rvert}{\text{HULME}}$	$\bar{B}_{11}$	$\frac{\lvert\bar{B}_{11}-\text{HULME}\rvert}{\text{HULME}}$	$\bar{B}_{11}$	$\frac{\lvert\bar{B}_{11}-\text{HULME}\rvert}{\text{HULME}}$
1	1.716	0.026	0.019	0.258	0.019	0.257	0.019	0.252
2	1.981	0.056	0.046	0.172	0.048	0.129	0.048	0.135
3	2.215	0.099	0.084	0.145	0.091	0.082	0.090	0.083
4	2.426	0.152	0.136	0.101	0.144	0.052	0.145	0.042
5	2.620	0.209	0.189	0.097	0.197	0.060	0.200	0.046
6	2.801	0.265	0.245	0.078	0.252	0.051	0.255	0.038
7	2.971	0.315	0.292	0.073	0.301	0.042	0.305	0.032
8	3.132	0.354	0.331	0.065	0.341	0.037	0.344	0.027
9	3.431	0.398	0.380	0.044	0.388	0.026	0.391	0.018
10	3.706	0.406	0.396	0.025	0.399	0.018	0.401	0.013
11	3.962	0.393	0.386	0.017	0.388	0.013	0.390	0.009
12	4.202	0.370	0.367	0.006	0.366	0.009	0.367	0.005
13	4.429	0.342	0.341	0.003	0.340	0.007	0.341	0.004
14	4.952	0.277	0.277	0.001	0.277	0.001	0.278	0.004
15	5.425	0.224	0.223	0.002	0.225	0.008	0.226	0.009
16	5.860	0.183	0.183	0.005	0.184	0.008	0.184	0.010
17	6.264	0.151	0.150	0.007	0.153	0.016	0.154	0.017
18	6.644	0.127	0.125	0.012	0.129	0.020	0.129	0.020
19	7.004	0.107	0.105	0.019	0.110	0.024	0.110	0.024
20	7.672	0.079	0.079	0.001	0.082	0.034	0.082	0.033
21	8.287	0.061	0.060	0.019	0.063	0.042	0.063	0.039
22	8.859	0.048	0.044	0.080	0.050	0.053	0.050	0.049
23	9.396	0.039	0.036	0.070	0.041	0.059	0.041	0.055
24	9.905	0.032	0.028	0.107	0.034	0.070	0.034	0.067

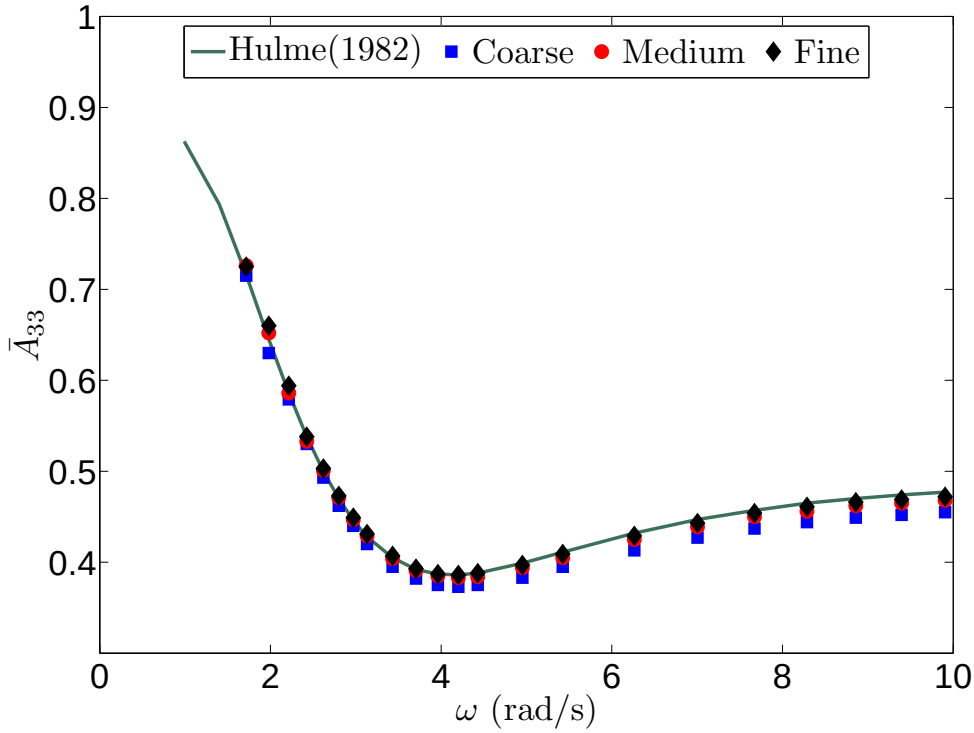

Figure 6.17: Convergence analysis of the added mass coefficient $\bar{A}_{33}$ for the hemisphere body

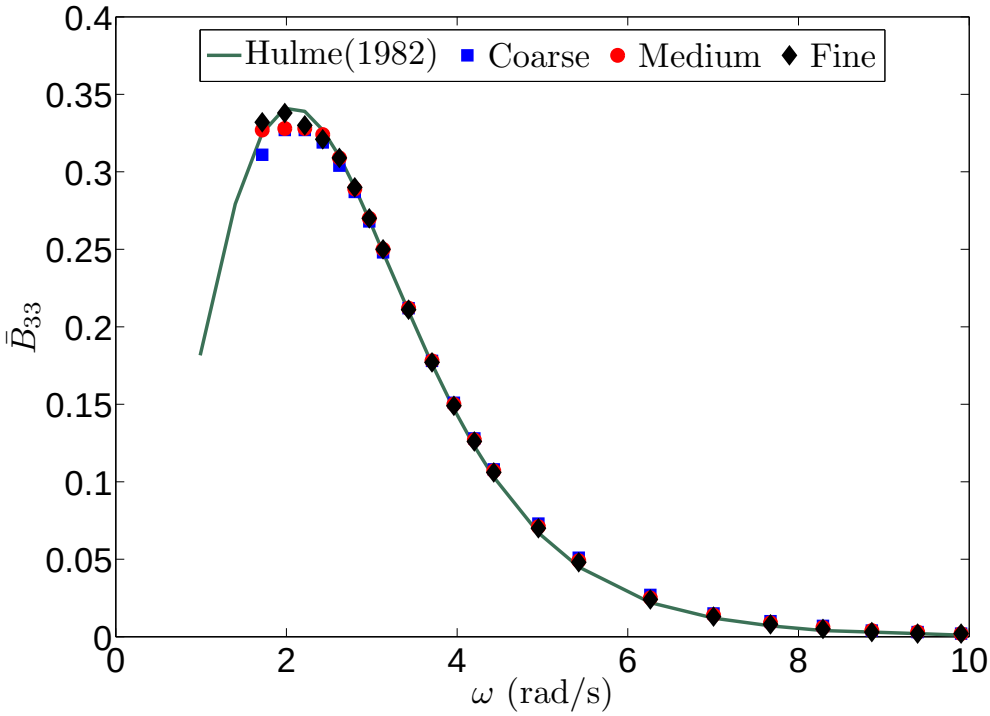

Figure 6.18: Convergence analysis of the radiation damping coefficient $\bar{B}_{33}$ for the hemisphere body

Table 6.10: Convergence analysis of the non-dimensional added mass $\bar{A}_{33}$ for the hemisphere body. Hulme (1982) values are used as reference for the relative errors

			Coarse		**Medium**		**Fine**	
ID	ω	**(HULME, 1982)**	$\bar{A}_{33}$	$\frac{\lvert\bar{A}_{33}-\text{HULME}\rvert}{\text{HULME}}$	$\bar{A}_{33}$	$\frac{\lvert\bar{A}_{33}-\text{HULME}\rvert}{\text{HULME}}$	$\bar{A}_{33}$	$\frac{\lvert\bar{A}_{33}-\text{HULME}\rvert}{\text{HULME}}$
1	1.716	0.716	0.715	0.001	0.726	0.014	0.725	0.014
2	1.981	0.645	0.630	0.023	0.652	0.010	0.660	0.024
3	2.215	0.586	0.579	0.012	0.586	0.000	0.594	0.014
4	2.426	0.538	0.530	0.015	0.533	0.010	0.538	0.001
5	2.620	0.500	0.493	0.014	0.501	0.002	0.503	0.007
6	2.801	0.470	0.462	0.017	0.471	0.003	0.473	0.008
7	2.971	0.446	0.440	0.015	0.447	0.002	0.449	0.007
8	3.132	0.428	0.420	0.018	0.429	0.001	0.431	0.007
9	3.431	0.405	0.395	0.023	0.404	0.002	0.407	0.005
10	3.706	0.392	0.382	0.026	0.391	0.004	0.393	0.002
11	3.962	0.387	0.375	0.031	0.385	0.006	0.387	0.001
12	4.202	0.386	0.373	0.034	0.383	0.008	0.386	0.001
13	4.429	0.388	0.375	0.035	0.384	0.010	0.388	0.002
14	4.952	0.399	0.383	0.039	0.394	0.013	0.397	0.004
15	5.425	0.411	0.395	0.040	0.405	0.015	0.409	0.006
16 [1]	5.860	–	–	–	–	–	–	–
17	6.264	0.432	0.413	0.044	0.425	0.017	0.429	0.007
18 [1]	6.644	–	–	–	–	–	–	–
19	7.004	0.447	0.427	0.046	0.439	0.017	0.443	0.008
20	7.672	0.457	0.437	0.044	0.450	0.017	0.454	0.008
21	8.287	0.465	0.444	0.045	0.456	0.018	0.461	0.009
22	8.859	0.470	0.449	0.045	0.462	0.017	0.466	0.008
23	9.396	0.474	0.452	0.047	0.465	0.019	0.469	0.010
24	9.905	0.477	0.455	0.046	0.468	0.020	0.472	0.011

[1] These values were not calculated since the analytical results were not presented in (HULME, 1982)

Table 6.11: Convergence analysis of the non-dimensional radiation damping $\bar{B}_{33}$ for the hemisphere body. Hulme (1982) values are used as reference for the relative errors

			Coarse		**Medium**		**Fine**	
ID	ω	**(HULME, 1982)**	$\bar{B}_{33}$	$\frac{\lvert\bar{B}_{33}-\text{HULME}\rvert}{\text{HULME}}$	$\bar{B}_{33}$	$\frac{\lvert\bar{B}_{33}-\text{HULME}\rvert}{\text{HULME}}$	$\bar{B}_{33}$	$\frac{\lvert\bar{B}_{33}-\text{HULME}\rvert}{\text{HULME}}$
1	1.716	0.325	0.311	0.046	0.327	0.004	0.332	0.020
2	1.981	0.341	0.327	0.040	0.328	0.039	0.338	0.009
3	2.215	0.339	0.327	0.036	0.328	0.032	0.330	0.026
4	2.426	0.327	0.319	0.024	0.324	0.009	0.321	0.018
5	2.620	0.310	0.304	0.017	0.309	0.004	0.309	0.003
6	2.801	0.290	0.287	0.012	0.289	0.001	0.290	0.000
7	2.971	0.269	0.268	0.005	0.270	0.002	0.270	0.002
8	3.132	0.248	0.248	0.001	0.250	0.005	0.250	0.005
9	3.431	0.210	0.212	0.011	0.212	0.010	0.211	0.009
10	3.706	0.176	0.178	0.015	0.178	0.013	0.177	0.010
11	3.962	0.147	0.151	0.028	0.150	0.022	0.149	0.017
12	4.202	0.123	0.128	0.038	0.127	0.030	0.126	0.022
13	4.429	0.103	0.108	0.048	0.107	0.034	0.106	0.025
14	4.952	0.067	0.073	0.077	0.071	0.056	0.070	0.040
15	5.425	0.045	0.051	0.122	0.049	0.080	0.048	0.057
16[1]	5.860	–	–	–	–	–	–	–
17	6.264	0.022	0.027	0.215	0.025	0.135	0.024	0.092
18[1]	6.644	–	–	–	–	–	–	–
19	7.004	0.012	0.015	–	0.014	–	0.013	–
20[2]	7.672	0.007	0.010	–	0.009	–	0.008	–
21[2]	8.287	0.004	0.007	–	0.006	–	0.005	–
22[2]	8.859	0.003	0.004	–	0.004	–	0.003	–
23[2]	9.396	0.002	0.003	–	0.003	–	0.002	–
24[2]	9.905	0.001	0.002	–	0.002	–	0.002	–

[1]These values were not calculated since the analytical results were not presented in Hulme (1982)

[2]The relative errors are omitted because the comparison involves very low values which any insignificant differences result in very large relative errors

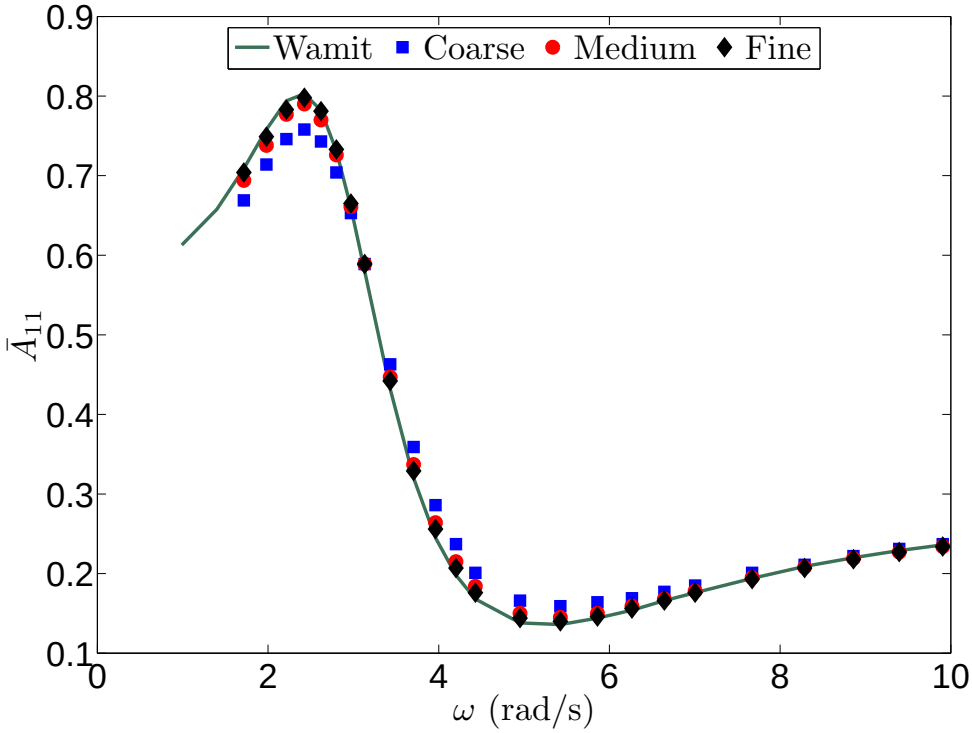

Figure 6.19: Convergence analysis of the added mass coefficient $\bar{A}_{11}$ for the circular cylinder body

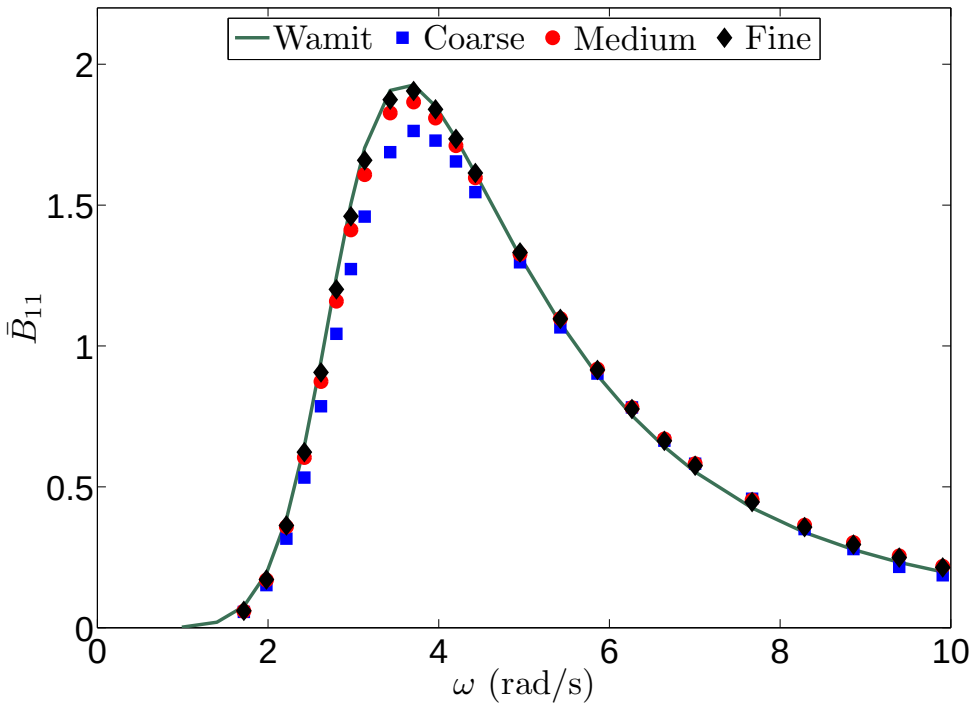

Figure 6.20: Convergence analysis of the radiation damping coefficient $\bar{B}_{11}$ for the circular cylinder body

Table 6.12: Convergence analysis of the non-dimensional added mass $\bar{A}_{11}$ for the circular cylinder body. WAMIT values are used as reference for the relative errors

			Coarse		**Medium**		**Fine**	
ID	ω	**WAMIT**	$\bar{A}_{11}$	$\frac{\lvert\bar{A}_{11}-\text{WAMIT}\rvert}{\text{WAMIT}}$	$\bar{A}_{11}$	$\frac{\lvert\bar{A}_{11}-\text{WAMIT}\rvert}{\text{WAMIT}}$	$\bar{A}_{11}$	$\frac{\lvert\bar{A}_{11}-\text{WAMIT}\rvert}{\text{WAMIT}}$
1	1.716	0.709	0.669	0.056	0.694	0.021	0.704	0.008
2	1.981	0.758	0.714	0.058	0.738	0.027	0.749	0.012
3	2.215	0.794	0.746	0.060	0.777	0.021	0.783	0.014
4	2.426	0.803	0.758	0.057	0.790	0.016	0.798	0.007
5	2.620	0.782	0.743	0.049	0.770	0.015	0.781	0.001
6	2.801	0.731	0.704	0.036	0.726	0.006	0.733	0.004
7	2.971	0.660	0.653	0.010	0.661	0.003	0.665	0.009
8	3.132	0.580	0.589	0.015	0.589	0.014	0.589	0.015
9	3.431	0.432	0.463	0.074	0.447	0.036	0.442	0.025
10	3.706	0.320	0.359	0.121	0.337	0.052	0.329	0.030
11	3.962	0.245	0.286	0.166	0.264	0.076	0.256	0.044
12	4.202	0.198	0.237	0.200	0.215	0.089	0.207	0.049
13	4.429	0.168	0.201	0.198	0.184	0.094	0.176	0.048
14	4.952	0.138	0.166	0.201	0.150	0.088	0.144	0.042
15	5.425	0.136	0.159	0.171	0.145	0.064	0.140	0.028
16	5.860	0.144	0.164	0.142	0.150	0.044	0.146	0.016
17	6.264	0.154	0.169	0.094	0.159	0.029	0.156	0.008
18	6.644	0.166	0.177	0.069	0.168	0.017	0.166	0.002
19	7.004	0.176	0.185	0.049	0.178	0.012	0.176	0.001
20	7.672	0.194	0.201	0.036	0.195	0.004	0.193	0.004
21	8.287	0.209	0.211	0.009	0.208	0.002	0.207	0.007
22	8.859	0.220	0.222	0.008	0.219	0.004	0.218	0.008
23	9.396	0.229	0.231	0.009	0.227	0.008	0.227	0.010
24	9.905	0.236	0.237	0.004	0.234	0.009	0.234	0.010

Table 6.13: Convergence analysis of the non-dimensional radiation damping $\bar{B}_{11}$ for the circular cylinder body. WAMIT values are used as reference for the relative errors

			Coarse		**Medium**		**Fine**	
ID	ω	**WAMIT**	$\bar{B}_{11}$	$\frac{\lvert\bar{B}_{11}-\text{WAMIT}\rvert}{\text{WAMIT}}$	$\bar{B}_{11}$	$\frac{\lvert\bar{B}_{11}-\text{WAMIT}\rvert}{\text{WAMIT}}$	$\bar{B}_{11}$	$\frac{\lvert\bar{B}_{11}-\text{WAMIT}\rvert}{\text{WAMIT}}$
1	1.716	0.076	0.056	0.265	0.059	0.223	0.060	0.205
2	1.981	0.193	0.151	0.218	0.169	0.126	0.171	0.113
3	2.215	0.385	0.316	0.179	0.358	0.069	0.363	0.056
4	2.426	0.645	0.533	0.173	0.604	0.064	0.623	0.035
5	2.620	0.946	0.786	0.168	0.874	0.076	0.906	0.042
6	2.801	1.245	1.043	0.162	1.159	0.069	1.201	0.036
7	2.971	1.505	1.273	0.154	1.412	0.062	1.460	0.030
8	3.132	1.703	1.459	0.143	1.608	0.056	1.659	0.026
9	3.431	1.907	1.688	0.114	1.827	0.042	1.874	0.017
10	3.706	1.926	1.763	0.085	1.866	0.032	1.905	0.011
11	3.962	1.851	1.729	0.066	1.809	0.023	1.840	0.006
12	4.202	1.737	1.655	0.047	1.711	0.015	1.735	0.001
13	4.429	1.612	1.546	0.041	1.597	0.009	1.614	0.001
14	4.952	1.318	1.297	0.016	1.326	0.006	1.332	0.010
15	5.425	1.081	1.066	0.013	1.097	0.015	1.096	0.014
16	5.860	0.896	0.902	0.007	0.918	0.025	0.915	0.021
17	6.264	0.753	0.782	0.037	0.781	0.037	0.776	0.030
18	6.644	0.642	0.664	0.034	0.670	0.044	0.663	0.034
19	7.004	0.553	0.582	0.052	0.582	0.053	0.575	0.040
20	7.672	0.425	0.458	0.079	0.453	0.066	0.446	0.050
21	8.287	0.338	0.350	0.035	0.364	0.075	0.357	0.055
22	8.859	0.277	0.279	0.008	0.302	0.092	0.295	0.066
23	9.396	0.232	0.216	0.071	0.255	0.096	0.249	0.070
24	9.905	0.198	0.186	0.060	0.218	0.098	0.214	0.079

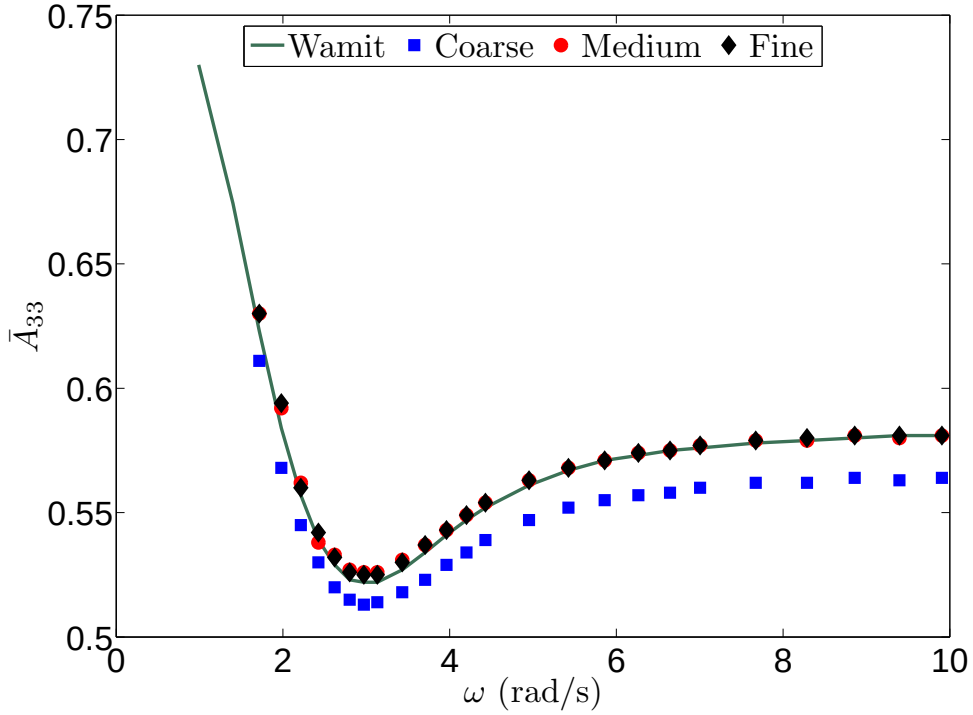

Figure 6.21: Convergence analysis of the added mass coefficient $\bar{A}_{33}$ for the circular cylinder body

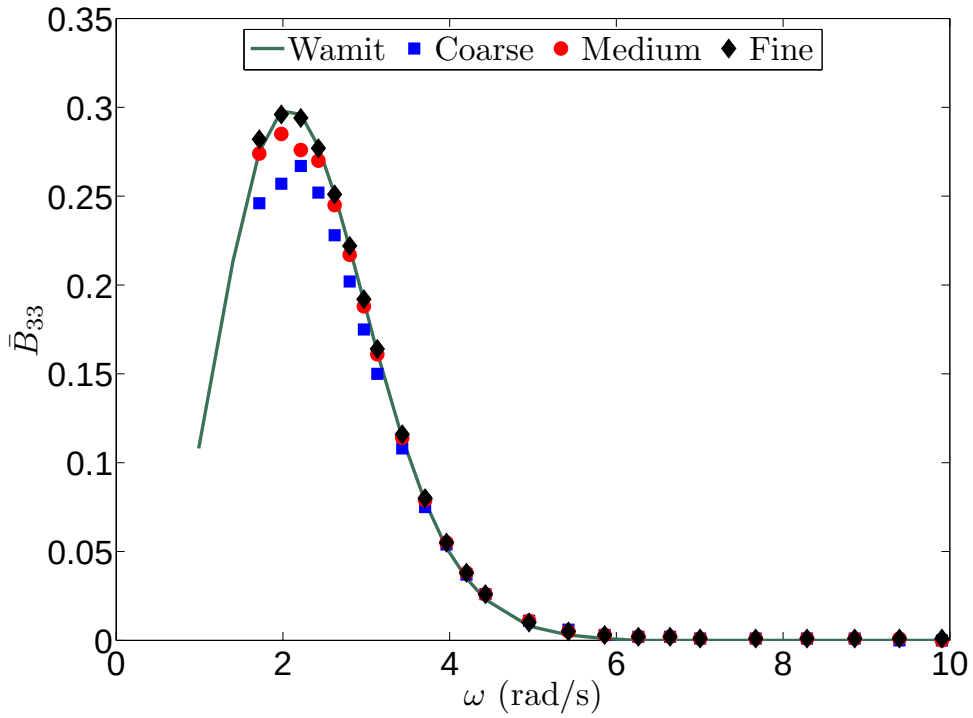

Figure 6.22: Convergence analysis of the radiation damping coefficient $\bar{B}_{33}$ for the circular cylinder body

Table 6.14: Convergence analysis of the non-dimensional added mass $\bar{A}_{33}$ for the circular cylinder body. WAMIT values are used as reference for the relative errors

			Coarse		**Medium**		**Fine**	
ID	ω	**WAMIT**	$\bar{A}_{33}$	$\frac{\lvert\bar{A}_{33}-\text{WAMIT}\rvert}{\text{WAMIT}}$	$\bar{A}_{33}$	$\frac{\lvert\bar{A}_{33}-\text{WAMIT}\rvert}{\text{WAMIT}}$	$\bar{A}_{33}$	$\frac{\lvert\bar{A}_{33}-\text{WAMIT}\rvert}{\text{WAMIT}}$
1	1.716	0.623	0.611	0.020	0.630	0.012	0.630	0.011
2	1.981	0.584	0.568	0.028	0.592	0.013	0.594	0.017
3	2.215	0.557	0.545	0.020	0.562	0.009	0.560	0.005
4	2.426	0.539	0.530	0.017	0.538	0.002	0.542	0.006
5	2.620	0.529	0.520	0.016	0.533	0.008	0.532	0.007
6	2.801	0.523	0.515	0.016	0.527	0.007	0.526	0.006
7	2.971	0.522	0.513	0.016	0.526	0.008	0.525	0.006
8	3.132	0.522	0.514	0.017	0.526	0.007	0.525	0.006
9	3.431	0.527	0.518	0.019	0.531	0.006	0.530	0.005
10	3.706	0.534	0.523	0.020	0.537	0.005	0.537	0.004
11	3.962	0.541	0.529	0.023	0.543	0.003	0.543	0.003
12	4.202	0.547	0.534	0.024	0.549	0.003	0.549	0.003
13	4.429	0.552	0.539	0.025	0.554	0.003	0.554	0.002
14	4.952	0.561	0.547	0.026	0.563	0.002	0.563	0.002
15	5.425	0.567	0.552	0.026	0.568	0.002	0.568	0.003
16	5.860	0.571	0.555	0.028	0.571	0.001	0.571	0.001
17	6.264	0.573	0.557	0.028	0.574	0.001	0.574	0.002
18	6.644	0.575	0.558	0.029	0.575	0.000	0.575	0.001
19	7.004	0.576	0.560	0.028	0.577	0.001	0.577	0.002
20	7.672	0.578	0.562	0.028	0.579	0.001	0.579	0.002
21	8.287	0.579	0.562	0.029	0.579	0.000	0.580	0.001
22	8.859	0.580	0.564	0.028	0.581	0.001	0.581	0.001
23	9.396	0.581	0.563	0.030	0.580	0.001	0.581	0.000
24	9.905	0.581	0.564	0.030	0.581	0.001	0.581	0.000

Table 6.15: Convergence analysis of the non-dimensional radiation damping $\bar{B}_{33}$ for the circular cylinder body. WAMIT values are used as reference for the relative errors

			Coarse		**Medium**		**Fine**	
ID	ω	**WAMIT**	$\bar{B}_{33}$	$\frac{\lvert\bar{B}_{33}-\text{WAMIT}\rvert}{\text{WAMIT}}$	$\bar{B}_{33}$	$\frac{\lvert\bar{B}_{33}-\text{WAMIT}\rvert}{\text{WAMIT}}$	$\bar{B}_{33}$	$\frac{\lvert\bar{B}_{33}-\text{WAMIT}\rvert}{\text{WAMIT}}$
1	1.716	0.275	0.246	0.105	0.274	0.004	0.282	0.026
2	1.981	0.298	0.257	0.138	0.285	0.046	0.296	0.007
3	2.215	0.296	0.267	0.097	0.276	0.068	0.294	0.006
4	2.426	0.278	0.252	0.093	0.270	0.027	0.277	0.002
5	2.620	0.251	0.228	0.091	0.245	0.022	0.251	0.000
6	2.801	0.221	0.202	0.084	0.217	0.015	0.222	0.005
7	2.971	0.191	0.175	0.079	0.188	0.013	0.192	0.009
8	3.132	0.162	0.150	0.071	0.161	0.007	0.164	0.014
9	3.431	0.114	0.108	0.047	0.114	0.007	0.116	0.024
10	3.706	0.078	0.075	0.038	0.079	0.019	0.080	0.034
11	3.962	0.052	0.054	0.033	0.055	0.050	0.055	0.060
12[1]	4.202	0.035	0.037	–	0.038	–	0.038	–
13[1]	4.429	0.023	0.026	–	0.026	–	0.026	–
14[1]	4.952	0.008	0.011	–	0.011	–	0.010	–
15[1]	5.425	0.003	0.006	–	0.005	–	0.005	–
16[1]	5.860	0.001	0.003	–	0.003	–	0.003	–
17[1]	6.264	0.000	0.002	–	0.002	–	0.002	–
18[1]	6.644	0.000	0.002	–	0.002	–	0.002	–
19[1]	7.004	0.000	0.001	–	0.001	–	0.001	–
20[1]	7.672	0.000	0.001	–	0.001	–	0.001	–
21[1]	8.287	0.000	0.001	–	0.001	–	0.001	–
22[1]	8.859	0.000	0.001	–	0.001	–	0.001	–
23[1]	9.396	0.000	0.000	–	0.001	–	0.001	–
24[1]	9.905	0.000	0.000	–	0.000	–	0.001	–

[1]The relative errors are omitted because the comparison involves very low values for which any insignificant differences result in very large relative errors

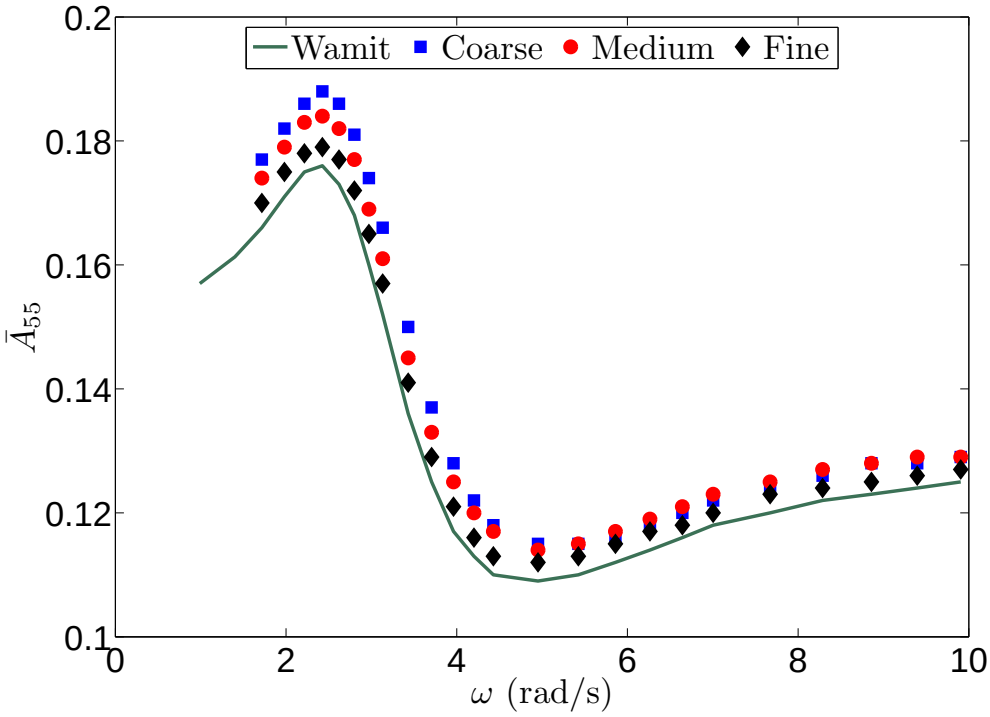

Figure 6.23: Convergence analysis of the added mass coefficient $\bar{A}_{55}$ for the circular cylinder body

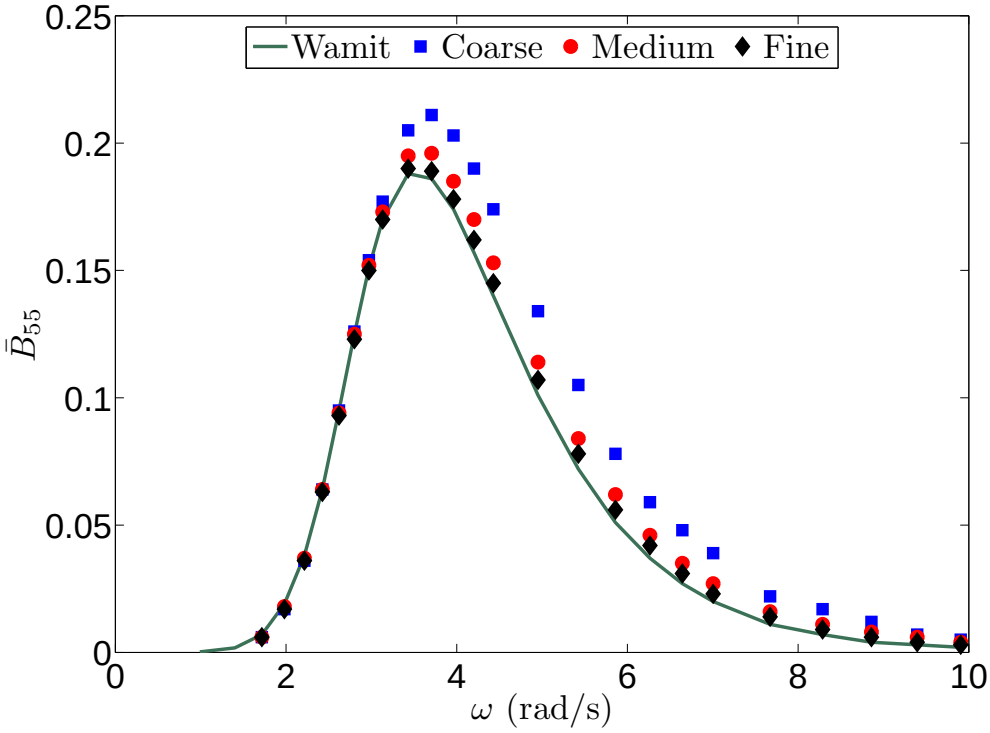

Figure 6.24: Convergence analysis of the radiation damping coefficient $\bar{B}_{55}$ for the circular cylinder body

Table 6.16: Convergence analysis of the non-dimensional added mass $\bar{A}_{55}$ for the circular cylinder body. WAMIT values are used as reference for the relative errors

			Coarse		**Medium**		**Fine**	
ID	ω	**WAMIT**	$\bar{A}_{55}$	$\frac{\lvert\bar{A}_{55}-\text{WAMIT}\rvert}{\text{WAMIT}}$	$\bar{A}_{55}$	$\frac{\lvert\bar{A}_{55}-\text{WAMIT}\rvert}{\text{WAMIT}}$	$\bar{A}_{55}$	$\frac{\lvert\bar{A}_{55}-\text{WAMIT}\rvert}{\text{WAMIT}}$
1	1.716	0.166	0.177	0.064	0.174	0.045	0.170	0.020
2	1.981	0.171	0.182	0.064	0.179	0.044	0.175	0.019
3	2.215	0.175	0.186	0.066	0.183	0.044	0.178	0.019
4	2.426	0.176	0.188	0.069	0.184	0.048	0.179	0.021
5	2.620	0.173	0.186	0.073	0.182	0.049	0.177	0.023
6	2.801	0.168	0.181	0.078	0.177	0.053	0.172	0.025
7	2.971	0.160	0.174	0.088	0.169	0.057	0.165	0.028
8	3.132	0.152	0.166	0.094	0.161	0.061	0.157	0.031
9	3.431	0.136	0.150	0.104	0.145	0.066	0.141	0.033
10	3.706	0.125	0.137	0.102	0.133	0.065	0.129	0.032
11	3.962	0.117	0.128	0.093	0.125	0.065	0.121	0.033
12	4.202	0.113	0.122	0.084	0.120	0.062	0.116	0.032
13	4.429	0.110	0.118	0.074	0.117	0.059	0.113	0.029
14	4.952	0.109	0.115	0.057	0.114	0.052	0.112	0.027
15	5.425	0.110	0.115	0.044	0.115	0.047	0.113	0.023
16	5.860	0.112	0.116	0.036	0.117	0.043	0.115	0.021
17	6.264	0.114	0.118	0.035	0.119	0.041	0.117	0.020
18	6.644	0.116	0.120	0.033	0.121	0.040	0.118	0.019
19	7.004	0.118	0.122	0.033	0.123	0.040	0.120	0.019
20	7.672	0.120	0.124	0.034	0.125	0.040	0.123	0.019
21	8.287	0.122	0.126	0.034	0.127	0.040	0.124	0.018
22	8.859	0.123	0.128	0.036	0.128	0.041	0.125	0.019
23	9.396	0.124	0.128	0.033	0.129	0.039	0.126	0.017
24	9.905	0.125	0.129	0.038	0.129	0.038	0.127	0.016

Table 6.17: Convergence analysis of the non-dimensional radiation damping $\bar{B}_{55}$ for the circular cylinder body. WAMIT values are used as reference for the relative errors

			Coarse		**Medium**		**Fine**	
ID	ω	**WAMIT**	$\bar{B}_{55}$	$\frac{\lvert\bar{B}_{55}-\text{WAMIT}\rvert}{\text{WAMIT}}$	$\bar{B}_{55}$	$\frac{\lvert\bar{B}_{55}-\text{WAMIT}\rvert}{\text{WAMIT}}$	$\bar{B}_{55}$	$\frac{\lvert\bar{B}_{55}-\text{WAMIT}\rvert}{\text{WAMIT}}$
1	1.716	0.007	0.006	0.108	0.006	0.163	0.006	0.179
2	1.981	0.019	0.017	0.067	0.018	0.064	0.017	0.094
3	2.215	0.038	0.036	0.039	0.037	0.028	0.036	0.054
4	2.426	0.064	0.064	0.001	0.064	0.005	0.063	0.013
5	2.620	0.095	0.095	0.002	0.094	0.007	0.093	0.018
6	2.801	0.125	0.126	0.011	0.125	0.000	0.123	0.013
7	2.971	0.151	0.154	0.022	0.152	0.009	0.150	0.007
8	3.132	0.170	0.177	0.039	0.173	0.018	0.170	0.002
9	3.431	0.188	0.205	0.091	0.195	0.036	0.190	0.010
10	3.706	0.186	0.211	0.136	0.196	0.052	0.189	0.018
11	3.962	0.174	0.203	0.171	0.185	0.066	0.178	0.026
12	4.202	0.157	0.190	0.207	0.170	0.081	0.162	0.033
13	4.429	0.140	0.174	0.247	0.153	0.092	0.145	0.038
14	4.952	0.101	0.134	0.323	0.114	0.129	0.107	0.059
15	5.425	0.072	0.105	0.455	0.084	0.168	0.078	0.080
16	5.860	0.051	0.078	0.527	0.062	0.203	0.056	0.097
17	6.264	0.037	0.059	0.607	0.046	0.254	0.042	0.126
18	6.644	0.027	0.048	0.797	0.035	0.300	0.031	0.150
19	7.004	0.020	0.039	0.987	0.027	0.352	0.023	0.179
20	7.672	0.011	0.022	1.009	0.016	0.468	0.014	0.247
21[1]	8.287	–	0.017	–	0.011	–	0.009	–
22[1]	8.859	–	0.012	–	0.008	–	0.006	–
23[1]	9.396	–	0.007	–	0.006	–	0.004	–
24[1]	9.905	–	0.005	–	0.004	–	0.003	–

6.4 Free Floating Simulations

The results presented so far still did not involve calculations considering the body equations of motions coupled with the integral equations derived from the hydrodynamic problem and, therefore, they cannot be used to evaluate whether the coupling scheme, previously proposed by van Daalen (1993) and Tanizawa (1995), is implemented correctly or not. With this objective, next we apply our numerical code for the evaluation of free motions of the hemisphere and cylinder bodies. The calculations are performed with the panel meshes presented in Table 6.1. In the simulations, the incident regular waves with

[1]The relative errors are omitted because the comparison involves very low values which any insignificant differences result in very large relative errors

unitary amplitude $A_I = 1$ m propagate in the x positive direction with the angular frequencies presented in Table 6.2. The time-step and the numerical beach zone coefficients were set with the same values used for the fixed and forced motion simulations.

For the calculation of the body motions in waves, we had also to define matrices of mass/inertias for each one of the geometries evaluated. Moreover, for the calculations involving the cylinder, in which the pitch D.O.F was also evaluated, an arbitrary linear external damping coefficient C_{55} was also considered. This external coefficient was included, since the pitch motion of the cylinder presents very low damping by wave radiation, which renders the time convergence of the method in the resonance frequency very difficult. For comparison purposes, the same external damping value was applied in the WAMIT model. The main parameters considered in the simulations are presented in Table 6.18.

Typical time histories of the heave motions of the cylinder and hemisphere are exemplified in Figures 6.25 and 6.26, respectively. These simulations were carried out with incoming waves with frequencies equal to the heave natural frequencies of each body. For a better visualization of the curves only a part of the steady-state portion of the signals are presented. It is worth mentioning that the time histories presented a regular behaviour even simulating the body responses for more than a hundred wave cycles, attesting the stability of the code. In fact, the simulation could be continued for much longer, without compromising the quality of the results.

Table 6.18: Main characteristics of the cylinder and hemisphere and simulation settings

Parameters	**Cylinder**	**Hemisphere**
Radius (m)	1.00	1.00
Draught (m)	1.00	1.00
Mass (kg)	3.14E+3	2.09E+3
Pitch Inertia[1] (kg.m^2)	1.57E+3	–
COG X coordinate[2] (m)	0.00	0.00
COG Y coordinate[2] (m)	0.00	0.00
COG Z coordinate[2] (m)	-0.50	-0.50
C55 (kg.m^2/s)	4.35E+2	–

[1]Values were calculated in relation to the body center of gravity
[2]Values are described in relation to the global coordinate system (x,y,z)=(0,0,0)

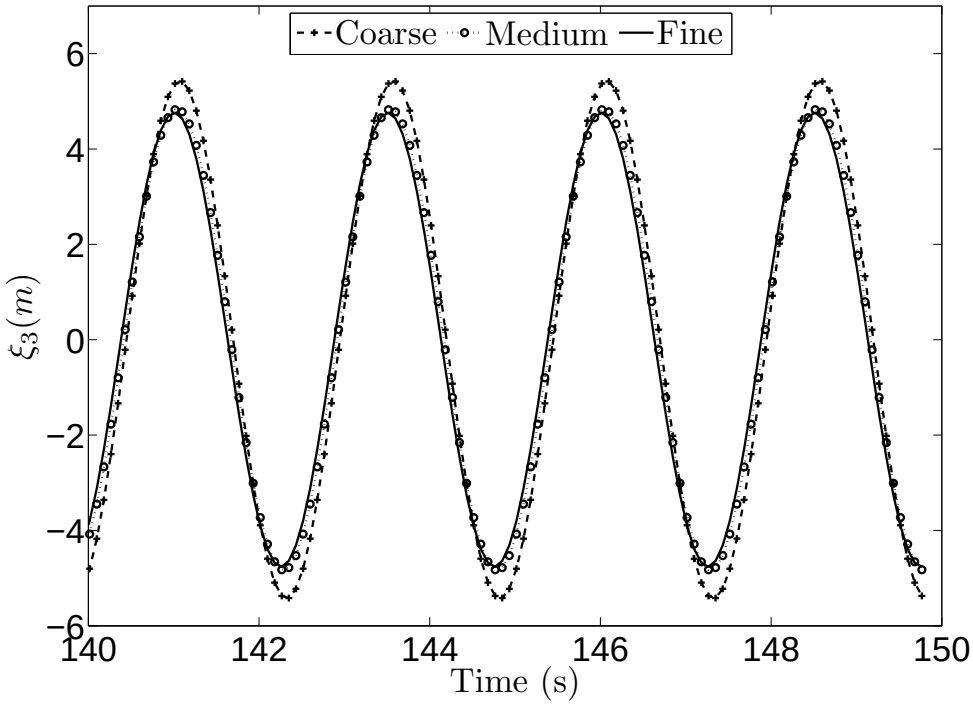

Figure 6.25: Time history of the cylinder heave motion for the coarse, medium and fine meshes. Incoming wave with angular frequency $\omega = 2.51$ rad/s

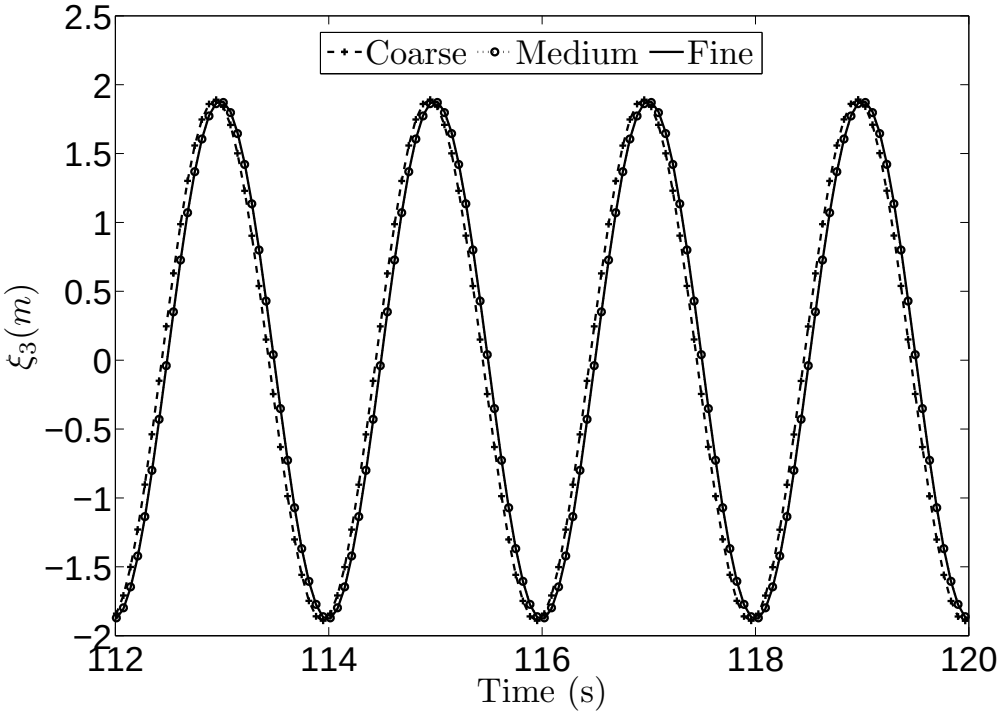

Figure 6.26: Time history of the hemisphere heave motion for the coarse, medium and fine meshes. Incoming wave with angular frequency $\omega = 3.13$ rad/s

The convergence of the bodies motions results for each wave frequency described in Table 6.2 is evaluated next. Furthermore, the results are compared with data provided by the software WAMIT. This evaluation is done in frequency domain by calculating the motions RAOs taking the rms (root mean squared) of a steady-state portion of each motion time series.

The cylinder RAOS of surge, heave and pitch motions obtained with the present method and WAMIT are plotted in Figures 6.27, 6.28 and 6.29, respectively. Overall, a good agreement is observed with the WAMIT results. As can be seen, the results converge with the increasing number of panels, which is attested by the very similar results obtained with the medium and fine meshes. Notice, however, that by applying the coarse mesh, the curves tend to present an oscillatory behaviour, which is intensified with the increasing wave frequency. As discussed before, this occurs due to the low resolution of panels per wave length that causes the appearance of an amplitude modulation in the signal.

The analogous results for the hemisphere body are presented in Figures 6.30 and 6.31 for surge and heave motions, respectively. In general, the same conclusions pointed out for the cylinder are maintained, in which the medium and fine mesh results agreed very well with the WAMIT data. Furthermore, these results demonstrate the capability of our code to predict the motions of floating bodies under no forward speed in waves, confirming that the second integral equation defined for the acceleration potential is correctly implemented and the equilibrium between the dynamic and hydrodynamic forces was conserved during the whole simulation.

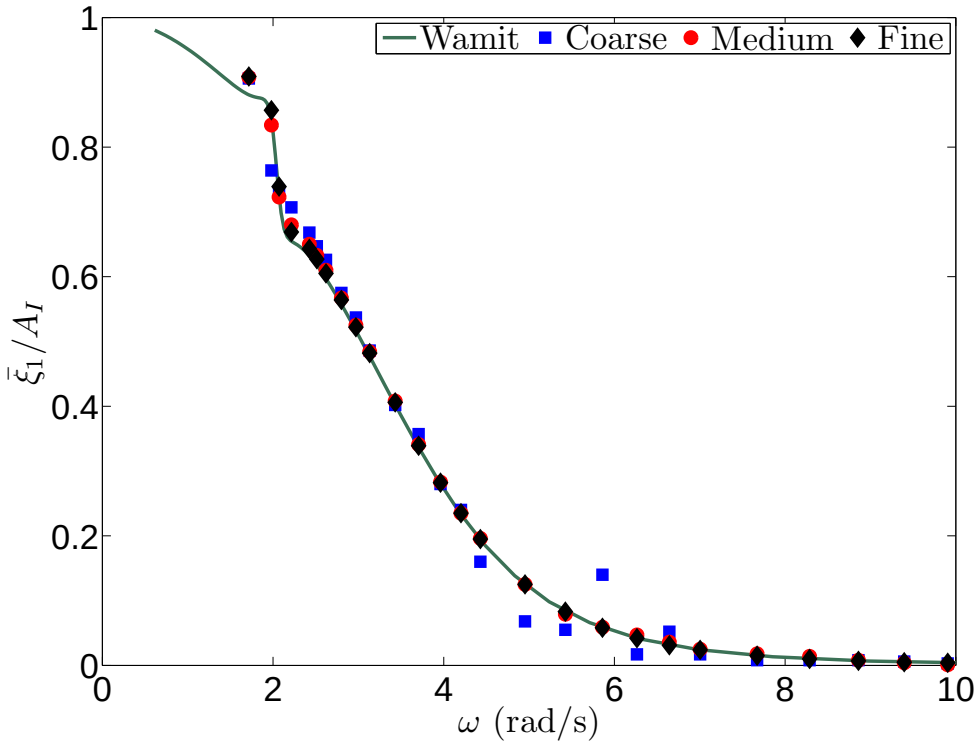

Figure 6.27: Convergence analysis of the cylinder surge RAO and comparison with WAMIT data

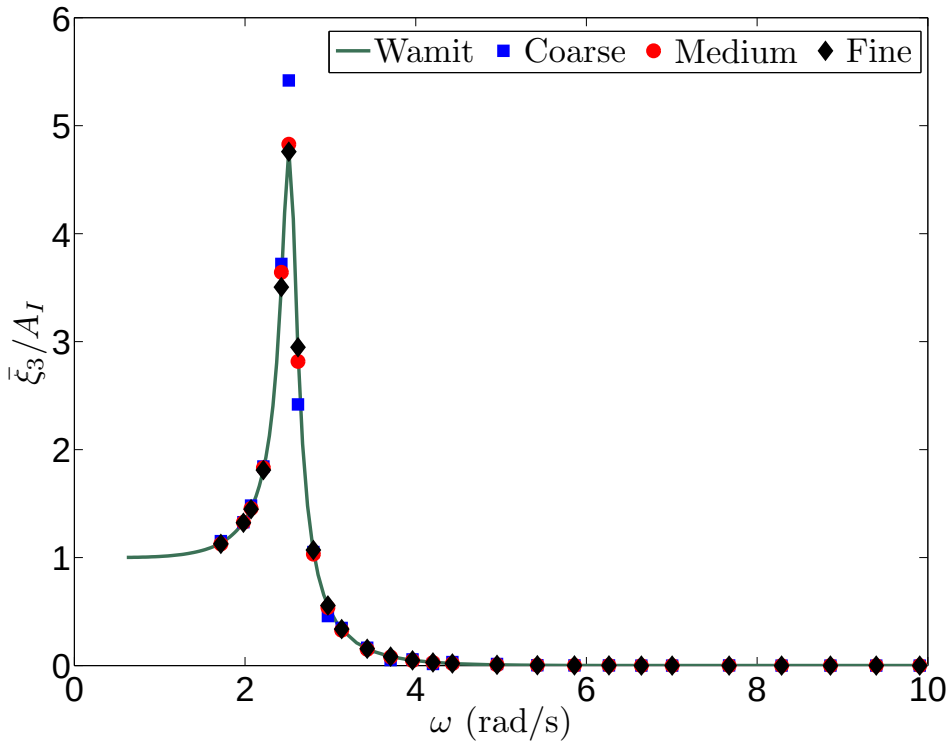

Figure 6.28: Convergence analysis of the cylinder heave RAO and comparison with WAMIT data

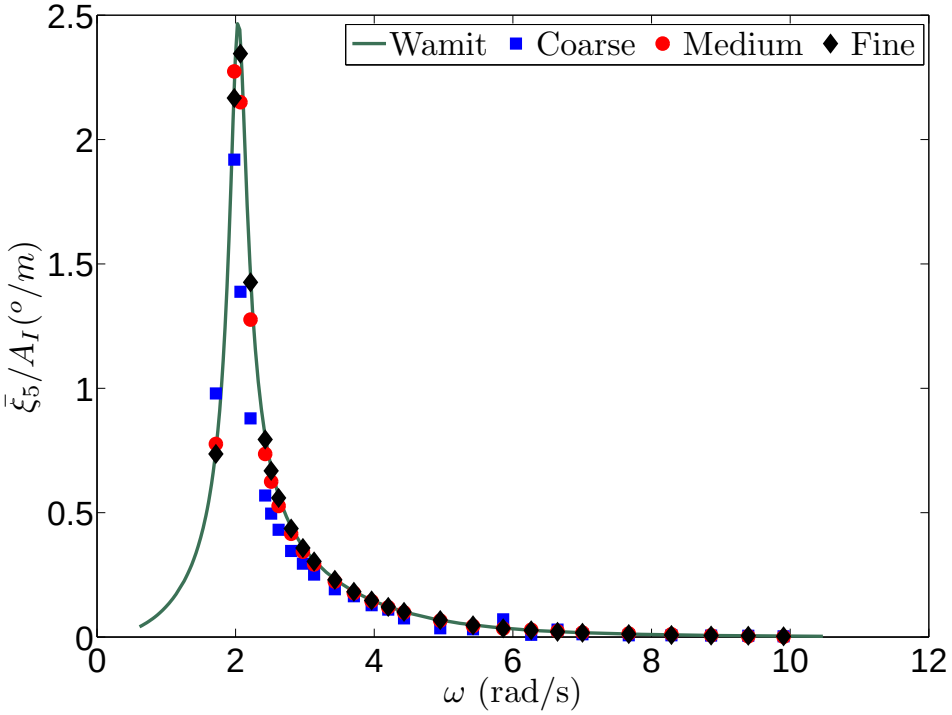

Figure 6.29: Convergence analysis of the cylinder pitch RAO and comparison with WAMIT data

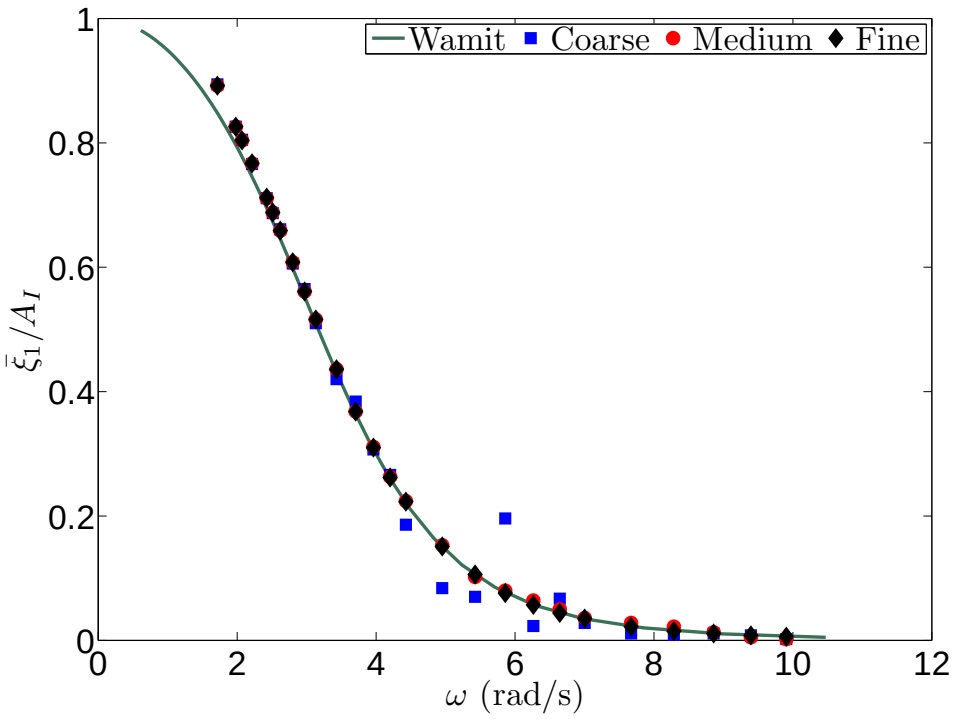

Figure 6.30: Convergence analysis of the sphere surge RAO and comparison with WAMIT data

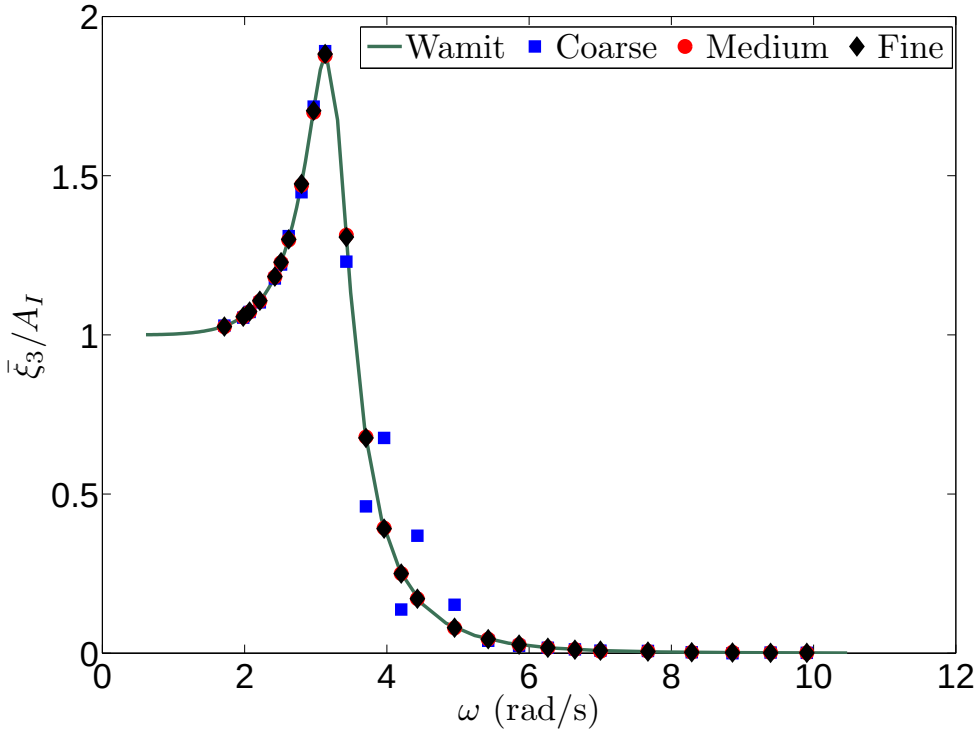

Figure 6.31: Convergence analysis of the sphere heave RAO and comparison with WAMIT data

Chapter 7

Verification Tests with Free Floating FPSOs

Floating Production Storage and Offloading (FPSO) units are floating vessels widely used by the offshore oil and gas industry, being also considered as the principal exploration solution for the recent oil discoveries in the pre-salt layer, in Brazil. One of the reasons for that is related to positive features of this kind of platform, such as the possibility of bypassing the construction stages using the hull of a converted oil tanker vessel, the large space to allocate the process plant and also its capability to store considerable amounts of oil which avoids the laying of extensive long distance pipelines from the oil well to an onshore terminal.

Designed to operate with forward speed, an anchored ship hull may suffer with the incidence of waves, presenting large motions and accelerations. For beam seas, for example, even a moderate sea state condition may imply in severe resonant roll motion, which are further aggravated by the very low energy dissipation by wave generation. In a tentative to avoid this inconvenience, the FPSO may be anchored in a single point mooring arrangement (SPM) allowing the vessel to rotate freely to best respond to weather conditions or in a spread mooring system (SMS) which is designed to maintain an appropriate vessel heading for the most severe waves, facilitating the offloading operations.

Independently on the mooring arrangement, several aspects must be assessed during the design stages. Specifically on the hydrodynamic task, extensive studies of topics such as seakeeping, definition of heading (only for SMS) and offloading operations must be performed, requiring both the conduction of experimental tests and numerical predictions using reliable and validated tools.

In this sense, we test our numerical model for two FPSO hull types aiming at verifying its capability to evaluate the free floating motions of real hull shapes in waves. The first is a 349,000 m^3 FPSO "box shaped" hull, in loaded draught, which is constructed intentionally for oil and gas exploration. The second is a 311,110 m^3 Very Large Crude Carrier (VLCC) vessel converted to perform the tasks of an FPSO. In the former case, the results of our code is confronted with the ones provided by WAMIT for three wave incidence angles and a wide range of frequencies. For the latter, the results are compared to experimental results previously conducted at the Hydrodynamic Calibrator of the Numerical Offshore Tank of the University of Sao Paulo (CH-TPN-USP). This experiment were conceptualized in the context of another research project that aimed at studying the FPSO roll motion and, therefore, our comparisons are restricted to beam waves only.

7.1 FPSO "Box Shaped" Hull

The main characteristics of the FPSO "Box Shaped" hull and the settings of the simulations are listed in Table 7.1. It can be observed that we have included external linear restoring coefficients for the surge, sway and yaw D.O.F. aiming at maintaining the solutions with zero mean. Although our numerical code does not calculate drift forces, this was necessary since a slight non-symmetrical topology of the panel mesh induces non-physical numerical drifts, as was observed during preliminary simulation tests. In addition, external damping coefficients associated to these D.O.F. were simply tuned to avoid long transient periods. Another remark is the inclusion of an empirical linear external roll damping coefficient of 5% of its critical value, so as to avoid very large roll motions and provide a faster numerical convergence, since our numerical code does not consider viscous effects.

Table 7.1: Principal characteristics of the FPSO "Box Shaped" hull and the settings of the simulations

Length over all	306.00	m
Beam moulded	54.00	m
Depth moulded	31.50	m
Draught	23.20	m
Mass	3.49E+08	kg
Roll Inertia[1]	1.16E+11	kg.m^2
Pitch Inertia[1]	2.09E+12	kg.m^2
Yaw Inertia [1]	2.12E+12	kg.m^2
COG X coordinate[2]	0.93	m
COG Y coordinate[2]	0.00	m
COG Z coordinate[2]	-5.14	m
K11	1.00E+05	kg/s^2
K22	1.00E+05	kg/s^2
K66	1.00E+09	kg/s^2
C11	1.00E+07	kg/s
C22	1.00E+07	kg/s
C44	6.03E+09	kg.m/s
C66	6.00E+09	kg.m/s

Calculations were done for wave incidences of 0°, 45° and 90°, which represents stern, stern-quartering and beam waves, respectively. The simulations were conducted considering two distinct approaches. In the first one, the motions of the FPSO are calculated for a set of 13 regular waves, whose main characteristics are presented in Table 7.2. In the second approach, we apply a white noise spectrum, in which not only one wave, but a simultaneous package of different wave components with the same amplitude is taken into account. In this work, we considered a discrete number of wave frequencies in the range 0.18-0.9 rad/s with an interval of 0.005 rad/s. As will be presented ahead, through the use of this procedure we may obtain the RAOs of the dynamic system performing only a single code run for each incidence angle, which is much more efficient than using the standard procedure of choosing several regular waves.

[1]Values were calculated in relation to the body center of gravity

[2]Values are described in relation to the global coordinate system (x,y,z)=(0,0,0)

Table 7.2: Regular incoming waves used in the FPSO "Box Shaped" hull simulations

ID	ω **(rad/s)**	**T(s)**	λ**(m)**
1	0.898	7.000	76.504
2	0.698	9.000	126.466
3	0.571	11.000	188.919
4	0.483	13.000	263.861
5	0.419	15.000	351.295
6	0.370	17.000	451.219
7	0.331	19.000	563.633
8	0.299	21.000	688.538
9	0.273	23.000	825.933
10	0.251	25.000	975.819
11	0.233	27.000	1138.195
12	0.217	29.000	1313.062
13	0.203	31.000	1500.419

Figures 7.1 and 7.2 display the FPSO body and the free surface meshes used in the simulations. Convergence was reached using 1764 panels on the body surface and 5000 panels on the free surface. For the analysis considering regular waves, the time-step was set to $\Delta t = T/60$ s and for the transient wave package $\Delta t = min(T)/60$, in which $min(T)$ is the lowest period within the set of wave components.

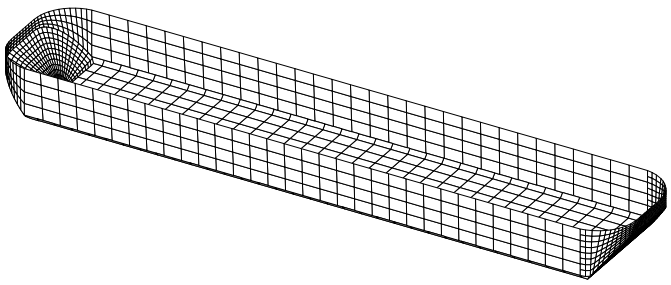

Figure 7.1: FPSO "Box Shaped" panel mesh

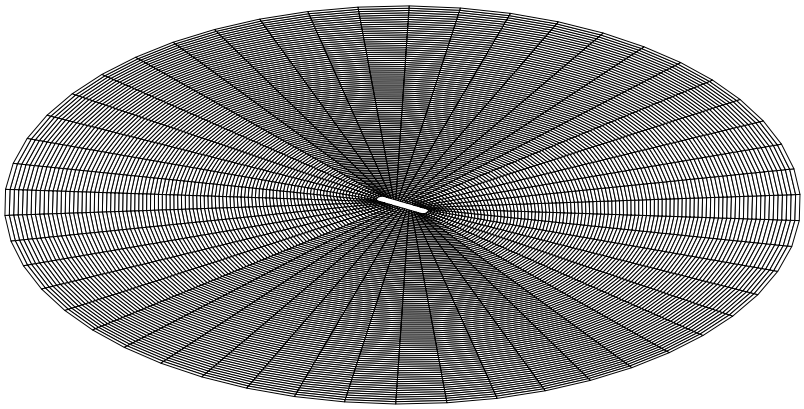

Figure 7.2: Free surface panel mesh for the FPSO "Box Shaped" simulations

We first present, in Figure 7.3, nine snapshots of the free surface elevation around the FPSO at different instants of the simulation, considering an incoming stern regular wave of angular frequency $\omega = 0.370$ rad/s. The amplitude of the incoming regular wave is scaled so as to better visualize the disturbed wave patterns. One should realize that during the first 100 seconds, approximately, the free surface presents a transient behavior in which we cannot recognize a clear wave pattern around the hull, which is then followed by a steady state wave pattern in which the incoming waves are less disturbed by the FPSO.

The sequence of events described above may also be observed by the FPSO motion time series, presented in Figures 7.4, 7.5 and 7.6 where we clearly realize a transient period during the first wave cycles. Moreover, we also realize that the motion in surge presents a longer transient due to the additional external restoring.

The group of disturbed waves generated during the transient period must be dissipated by the damping zone in order to ensure that the solution reaches a steady state. Therefore, a precise tuning of the damping zone parameters considering the characteristics of the regular waves in analysis must be assessed. This was performed by preliminary test runs that led to a numerical beach of two wave lengths long ($b = 2.0$) and intensity $a = 1.0$.

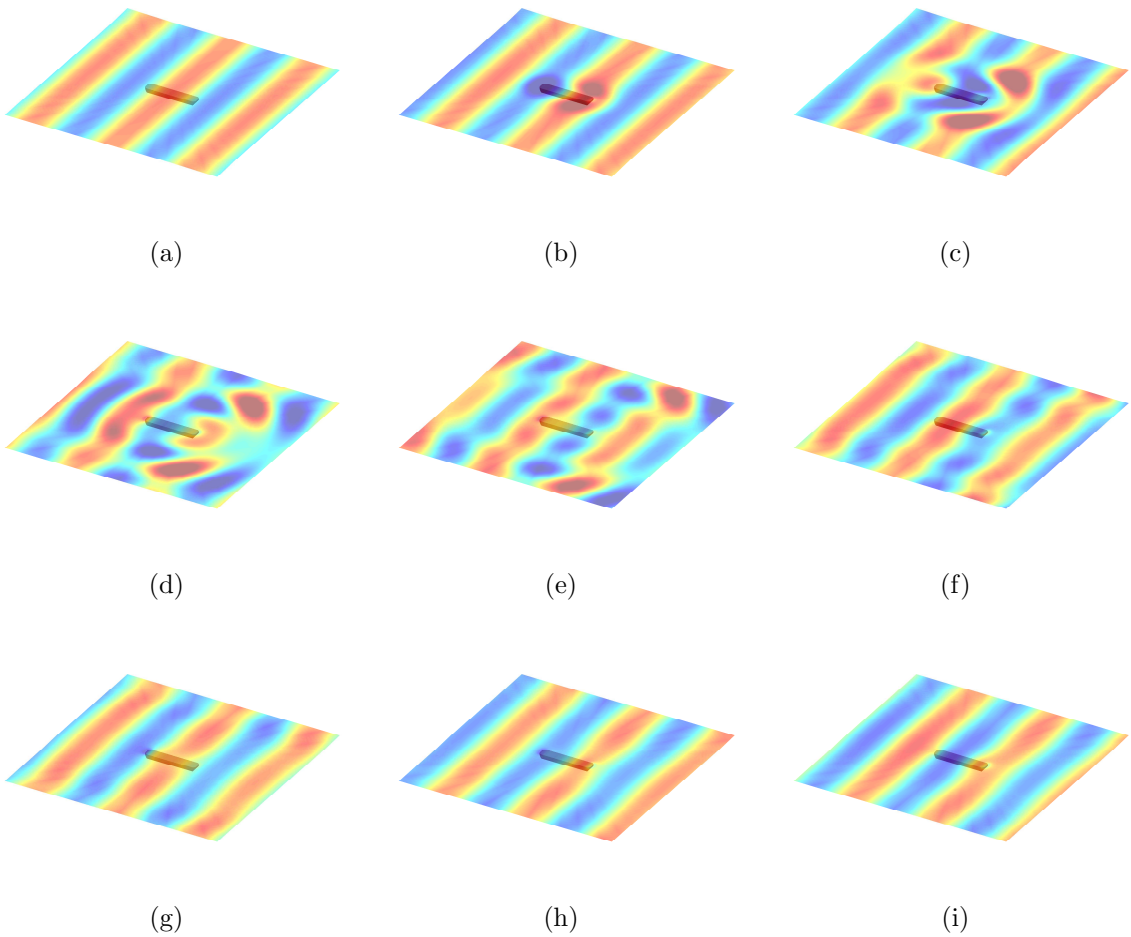

Figure 7.3: Snapshots of the simulation at 9 different instants of time. Wave Amplitude $A_I = 1$ m and frequency $\omega = 0.370$ rad/s. (a) $t = 0$ s, (b) $t = 20$ s,(c) $t = 40$ s, (d) $t = 60$ s, (e) $t = 80$ s, (f) $t = 100$ s, (g) $t = 120$ s, (h) $t = 140$ s and (i) $t = 160$ s

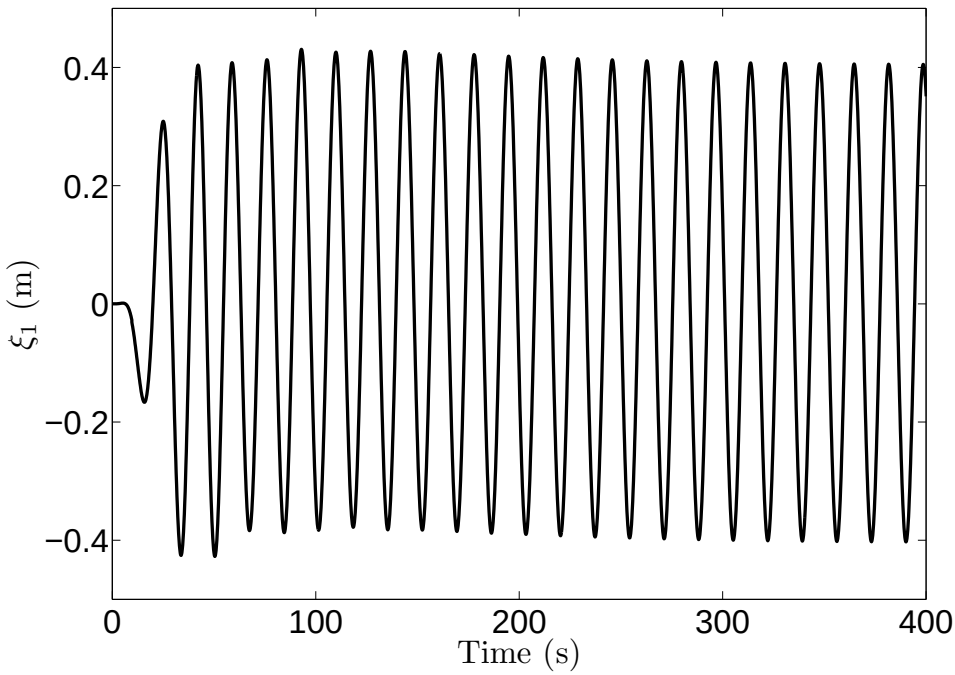

Figure 7.4: Typical surge motion time series obtained by the present numerical code. Motions were induced by a wave of angular frequency $\omega = 0.370$ rad/s and incidence angle 0°

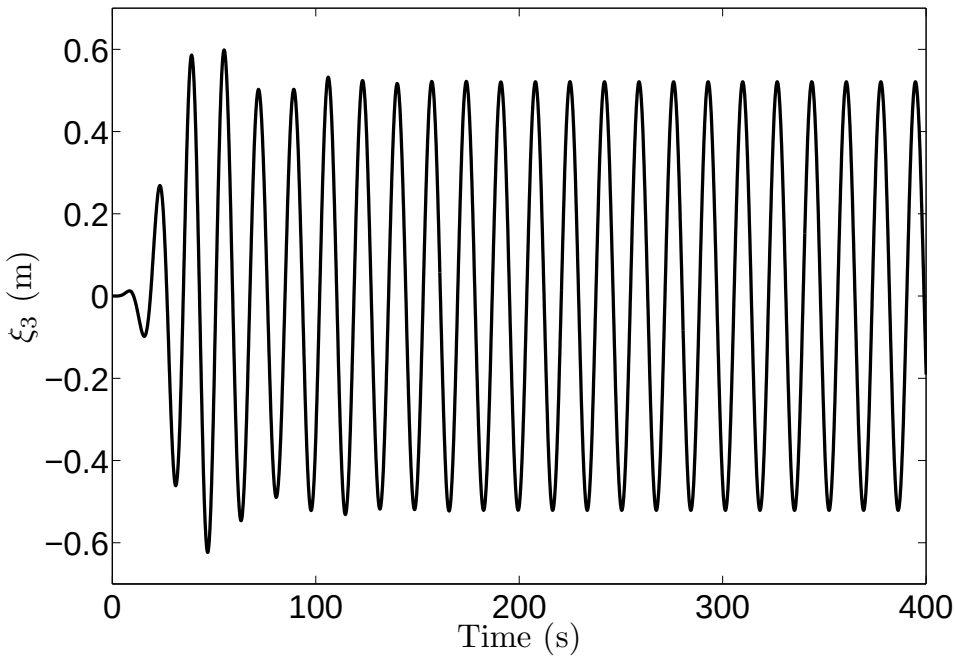

Figure 7.5: Typical heave motion time series obtained by the present numerical code. Motions were induced by a wave of angular frequency $\omega = 0.370$ rad/s and incidence angle 0°

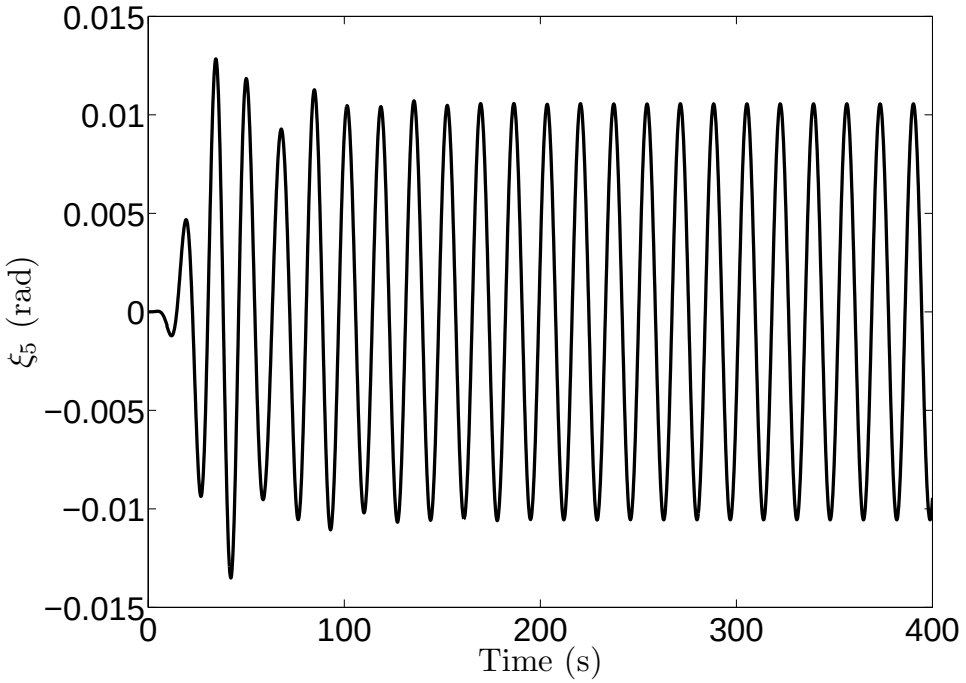

Figure 7.6: Typical pitch motion time series obtained by the present numerical code. Motions were induced by a wave of angular frequency $\omega = 0.370$ rad/s and incidence angle 0°

Next, we present examples of output time series obtained through the simulations using the white noise spectrum (S_{wn}), presented in Figure 7.7, for a wave incidence angle of 0°. Figure 7.8 presents the undisturbed incoming wave time history at the position of the FPSO "Box Shaped" CoG, which is obtained from the realization of the white noise energy spectrum into a time series representation. One should realize that at a specific time a constructive wave is formed exactly at the body position, resulting in a very large free surface elevation that occurs by the fact that the time series was generated considering all the wave components with zero phase values. The correspondent motion time histories of surge, heave and pitch are presented in Figure 7.9.

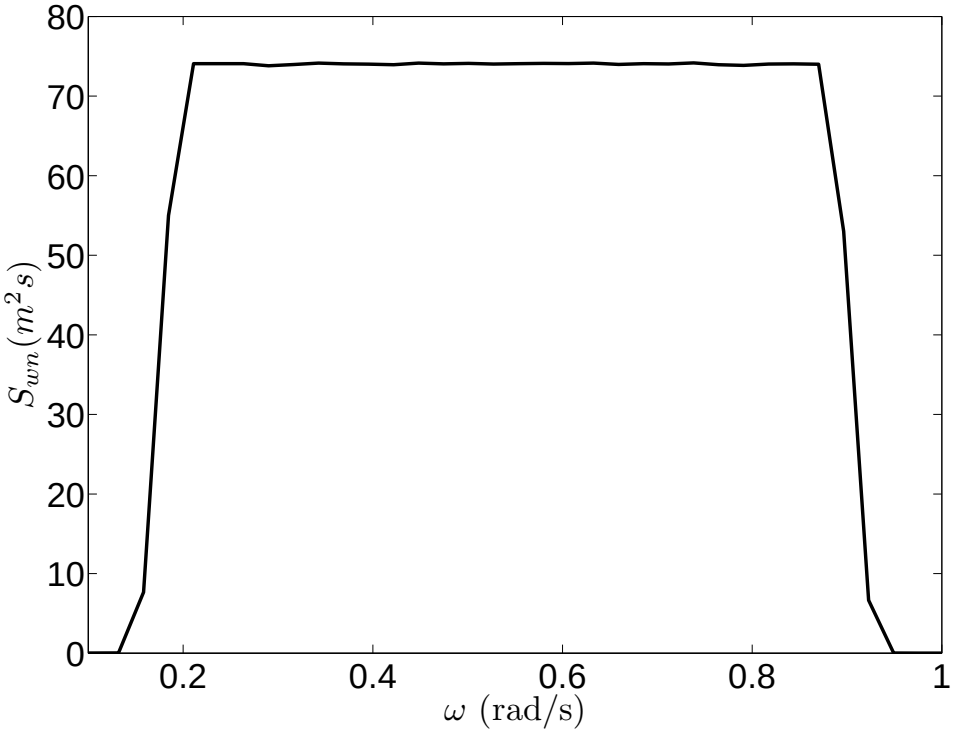

Figure 7.7: Numerical white noise spectrum

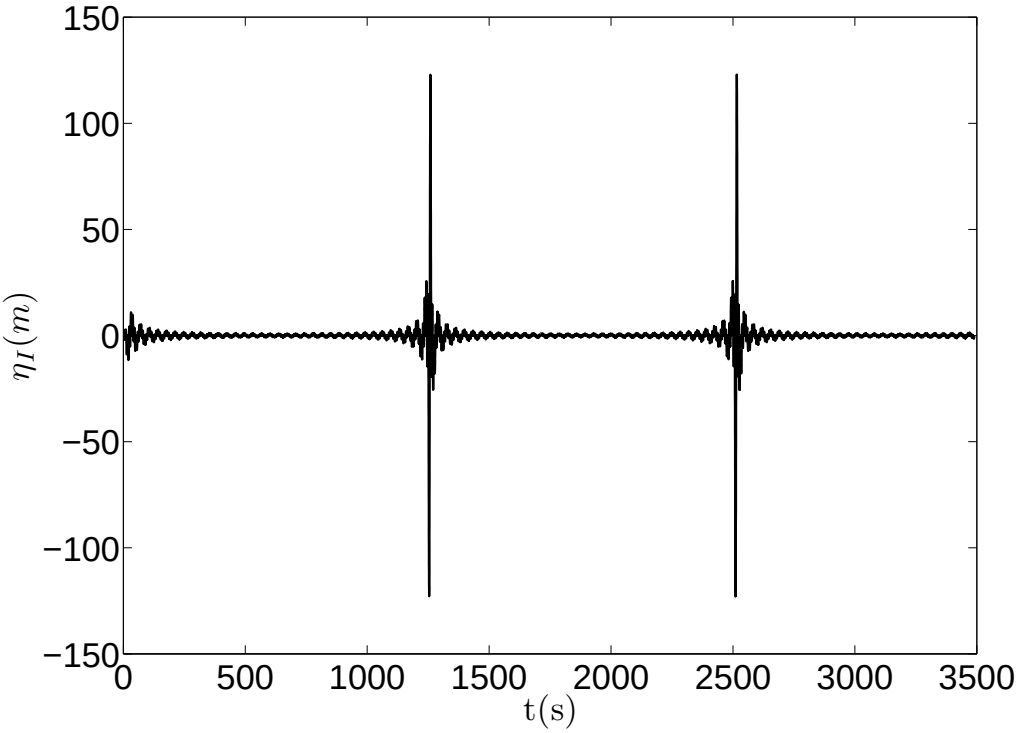

Figure 7.8: Incoming wave elevation time series generated by a white noise spectrum

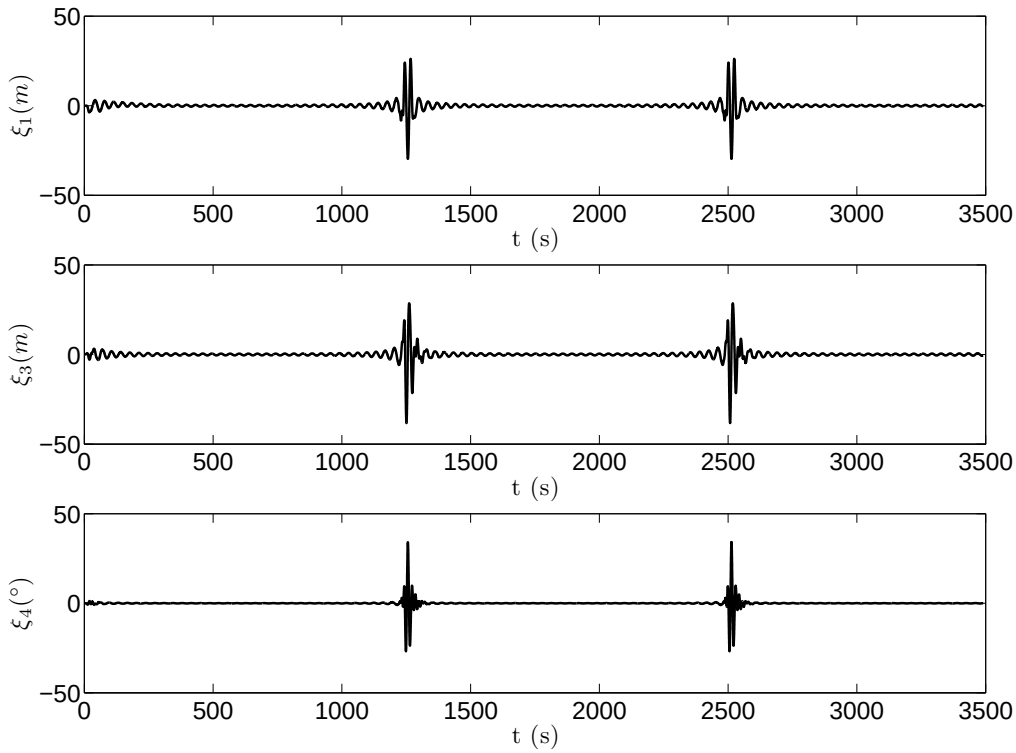

Figure 7.9: Motion time series for sway (ξ_2), heave (ξ_3) and roll (ξ_4) induced by a wave generated by a white noise spectrum

In order to verify the results, we compare the present values with RAOs obtained with the frequency domain software WAMIT. For regular waves, this is done by taking the root mean square (rms) of a steady-state portion of each motion time series. For the analysis of the white-noise waves a more sophisticated approach is applied using the cross power spectral density (cpsd)[1] between the motions and the incoming wave time series. The results are compared by the RAOs for each D.O.F and incoming wave incidence angles, and are presented in Figures 7.10, 7.11, 7.12, 7.13, 7.14 and 7.15 for surge, sway, heave, roll, pitch and yaw D.O.F., respectively.

As can be seen, except for some small deviations, specially for values near the peaks, a very good agreement between both codes is observed for all D.O.F. and wave angles analyzed, demonstrating, therefore, the capability of our code to predict the motions of a floating body under no forward speed with more realistic geometries than the hemisphere and cylinder ones. Moreover, the use of the white noise spectrum for the determination of the RAOs also presents a very good agreement with WAMIT with the advantage of rendering the calculations much more efficient, since only one code run per wave incidence angle must be executed. These results also point out that standard sea spectra, such as

[1]Analysis was performed with the cpsd function available in MATLAB version 7.10.0

JONSWAP and Pierson-Moskowitz, may also be applied for the evaluation of motions in sea conditions, which may be performed simply by changing the white noise spectrum for a sea one. In this case, however, the realization in time of the sea spectra is often performed considering random phases between the frequencies.

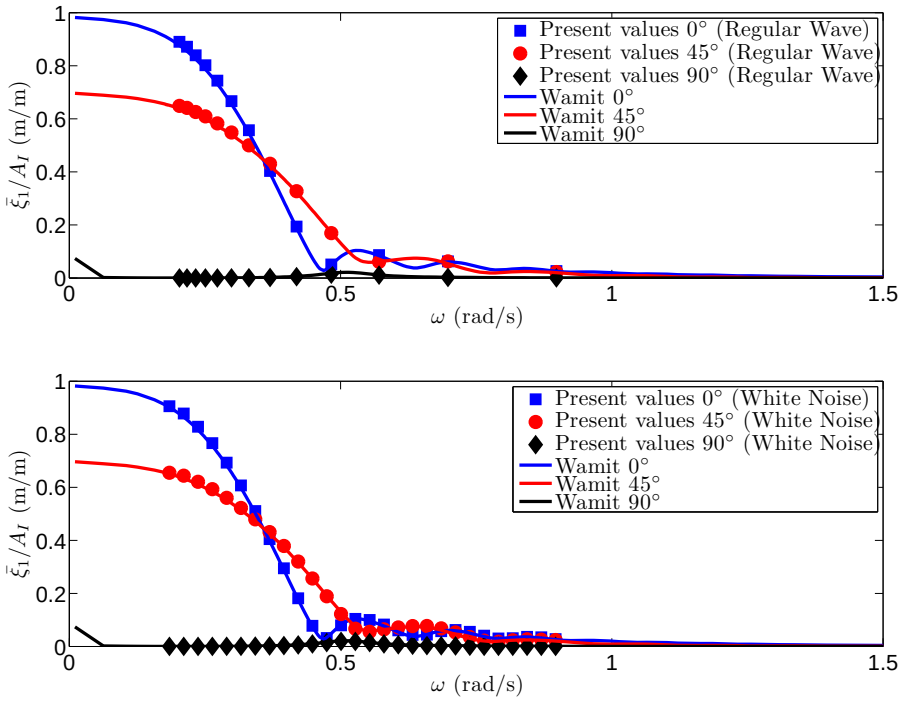

Figure 7.10: Surge response amplitude operators considering three different wave incidence angle 0°, 45°, 90°. Regular Wave Analysis (Above) and White Noise Analysis (Below)

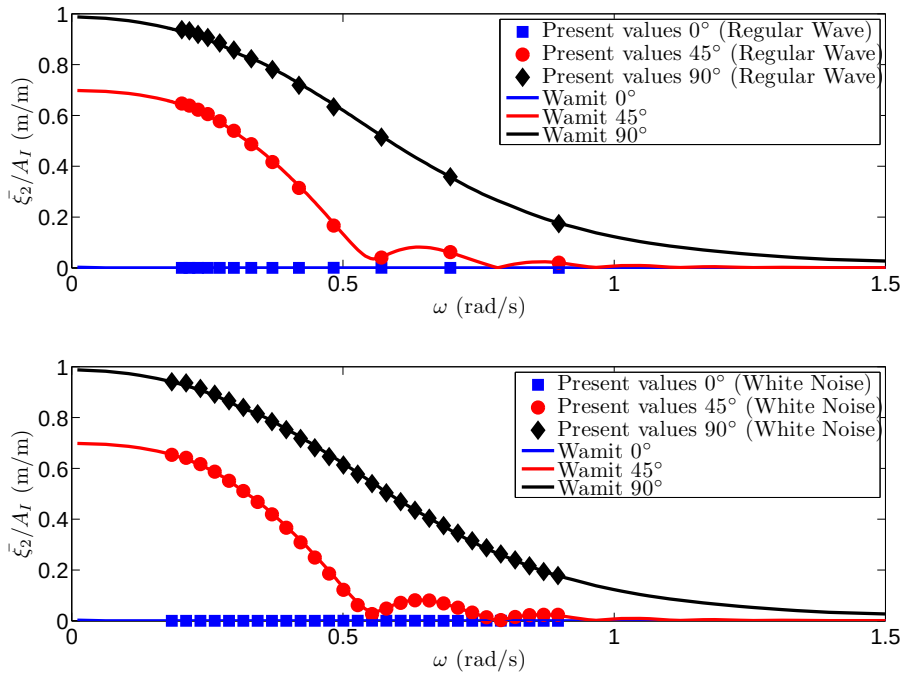

Figure 7.11: Sway response amplitude operators considering three different wave incidence angle 0°, 45°, 90°. Regular Wave Analysis (Above) and White Noise Analysis (Below)

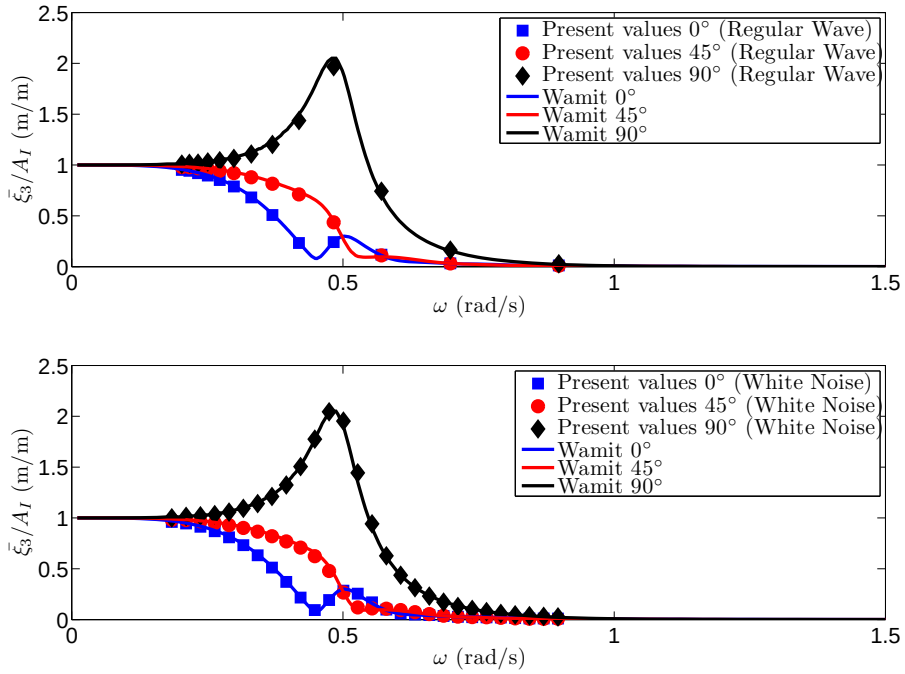

Figure 7.12: Heave response amplitude operators considering three different wave incidence angle 0°, 45°, 90°. Regular Wave Analysis (Above) and White Noise Analysis (Below)

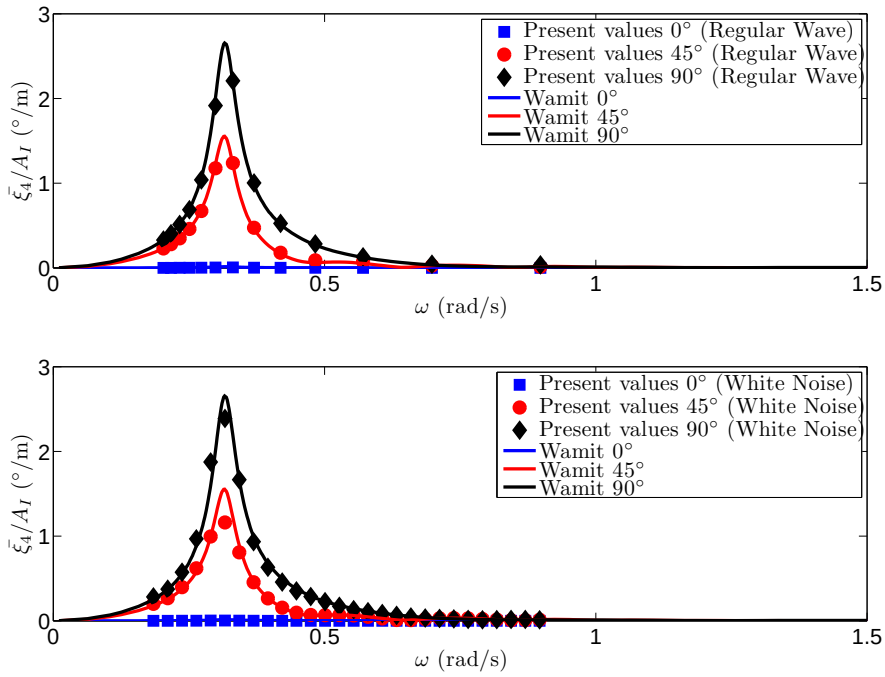

Figure 7.13: Roll response amplitude operators considering three different wave incidence angle 0°, 45°, 90°. Regular Wave Analysis (Above) and White Noise Analysis (Below)

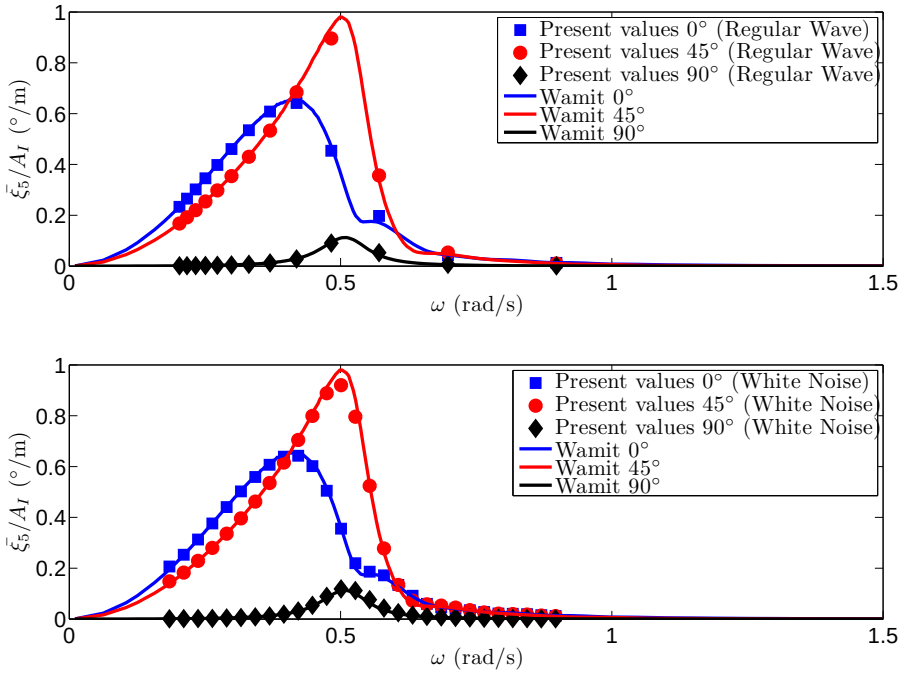

Figure 7.14: Pitch response amplitude operators considering three different wave incidence angle 0°, 45°, 90°. Regular Wave Analysis (Above) and White Noise Analysis (Below)

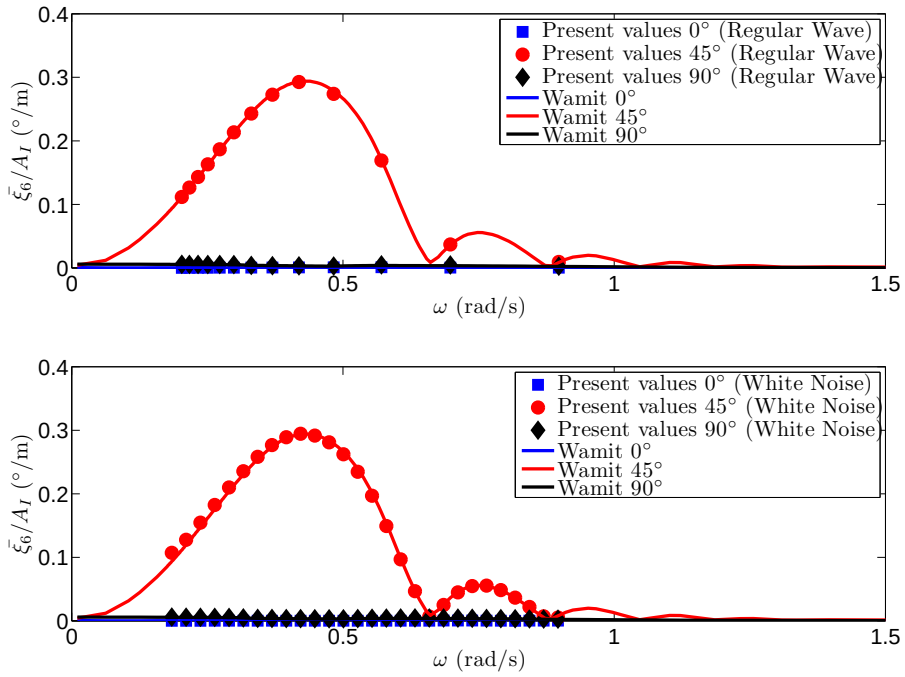

Figure 7.15: Yaw response amplitude operators considering three different wave incidence angle 0°, 45°, 90°. Regular Wave Analysis (Above) and White Noise Analysis (Below)

7.2 FPSO VLCC Hull

Numerical simulations were also conducted for a converted FPSO VLCC hull type. The results are compared to experimental data previously obtained in wave tests carried out at the CH-TPN-USP, in Sao Paulo, Brazil, which is a wave basin with dimensions of 14 m×14 m and water depth of 4 m (MELLO et al., 2010). This tank is equipped with a set of 148 independent flaps for the generation and active absorption of waves, which provides good precision and stability for the wave field during the tests. A perspective view of the wave basin is presented in Figure 7.16.

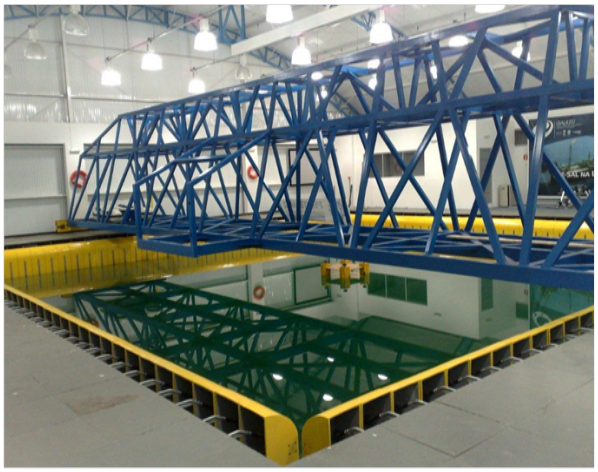

Figure 7.16: Hydrodynamic Calibrator of the Numerical Offshore Tank at the University of Sao Paulo (CH-TPN-USP)

7.2.1 Experimental Setup

For the execution of the tests, a 1 : 90 small-scale model of the VLCC hull was positioned at the center of tank and equipped with reflective targets used by an optical tracking system which was mounted on the carriage for the measurement of 6 D.O.F motions of the model. In addition, a set of four soft springs were attached to the model and fixed to four vertical bars positioned at the corners of the wave basin in order to restrain its drift. The equivalent restoring coefficients in the horizontal plane were determined by pull-out tests. As the main goal of the tests was the study of roll motions, only beam waves were considered in the test matrix, which included regular, transient and sea wave conditions. Figure 7.17 presents a view of the model during the tests.

Concerning the regular waves, a study increasing the incoming wave amplitude for a fixed wave frequency $\omega_I = 0.443$ rad/s (near to the roll resonance frequency) was conducted aiming at investigating the nonlinear roll motions response and its associated damping coefficients. For this study, however, only the regular wave of smallest steepness will be considered, being in accordance with the linear wave theory here adopted. The transient wave, by its turn, was used for a fast RAO determination, in which a wave package with a constant amplitude of 3 meters and frequencies in between 0.349 rad/s and 0.785 rad/s, in full scale, was applied. In this wave package, the maximum wave steepness is around 3%, being also within the scope of the linear wave theory.

It is important to mention that, in this study, irregular waves were not used for comparison purposes. Although this is not being evaluated, the simulations with irregular seas would be carried out in a similar manner as those conducted for the white-noise spectrum

presented in section 7.1, which is a good indication that the code is capable to properly conduct this kind of computation with reasonable accuracy. Indeed, since the problem is being treated based on the linear theory, the numerical analysis of irregular waves is merely treated as a superposition of different regular wave components of distinct amplitudes, frequencies and phases. In practice, this is performed by simply changing the white-noise spectrum, applied in section 7.1, for a representative sea-wave energy spectrum, such as JONSWAP, Pierson-Moskowitz etc.

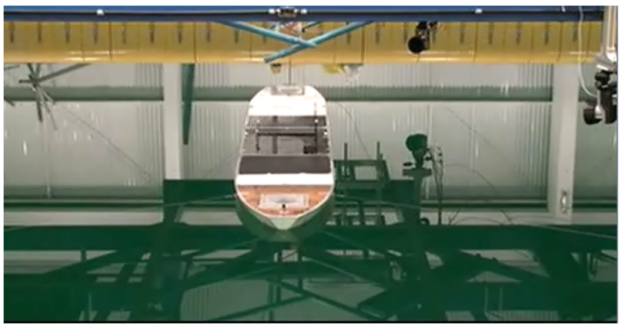

Figure 7.17: General view of the FPSO VLCC model positioned in CH-TPN-USP

The main characteristics of the FPSO model (in full scale) are listed in Table 7.3. Model center of gravity and inertia of roll, pitch and yaw were calibrated using ballast weights.

Table 7.3: Main characteristics of the FPSO VLCC hull and the settings of the simulations

Length over all	334.44	m
Beam moulded	54.72	m
Depth moulded	21.51	m
Draught	21.51	m
Mass	3.09E+08	kg
Roll Inertia[1]	1.05+11	kg.m^2
Pitch Inertia[1]	1.79E+12	kg.m^2
Yaw Inertia [1]	1.83E+12	kg.m^2
COG X coordinate[2]	10.10	m
COG Y coordinate[2]	0.00	m
COG Z coordinate[2]	-6.76	m
K22	8.67E+05	kg/s^2
C44(5%C_{crit})	5.48E+09	kg.m/s
C44(6%C_{crit})	6.03E+09	kg.m/s

[1]Values were calculated in relation to the body center of gravity
[2]Values are described in relation to the global coordinate system (x,y,z)=(0,0,0)

7.2.2 Numerical Simulations

The numerical simulations for the RAO determination were conducted considering a set of 45 regular waves, which covered a frequency range between 0.307 to 0.873 rad/s, as may be observed in Table 7.4. As viscous damping effects may not be neglected when evaluating roll motions, the numerical results were tested with two different external roll damping coefficients $C44$, also presented in Table 7.3, which were calculated as 5% and 6% of the critical damping C_{crit}.

Table 7.4: Regular incoming waves used in the FPSO VLCC hull simulations

ID	ω **(rad/s)**	**T(s)**	λ**(m)**	**ID**	ω **(rad/s)**	**T(s)**	λ**(m)**
1	0.307	20.466	653.992	23	0.517	12.153	230.605
2	0.323	19.453	590.805	24	0.534	11.766	216.156
3	0.340	18.480	533.201	25	0.550	11.424	203.762
4	0.356	17.649	486.350	26	0.566	11.101	192.405
5	0.372	16.890	445.413	27	0.582	10.796	181.971
6	0.388	16.194	409.435	28	0.598	10.507	172.364
7	0.390	16.111	405.247	29	0.614	10.233	163.498
8	0.395	15.907	395.052	30	0.631	9.958	154.807
9	0.400	15.708	385.238	31	0.647	9.711	147.245
10	0.404	15.552	377.647	32	0.663	9.477	140.224
11	0.405	15.514	375.784	33	0.679	9.254	133.693
12	0.415	15.140	357.893	34	0.695	9.041	127.608
13	0.420	14.960	349.422	35	0.711	8.837	121.930
14	0.425	14.784	341.249	36	0.728	8.631	116.302
15	0.430	14.612	333.359	37	0.744	8.445	111.353
16	0.435	14.444	325.739	38	0.760	8.267	106.714
17	0.437	14.378	322.765	39	0.776	8.097	102.359
18	0.443	14.183	314.081	40	0.792	7.933	98.265
19	0.453	13.870	300.367	41	0.808	7.776	94.412
20	0.469	13.397	280.223	42	0.825	7.616	90.561
21	0.485	12.955	262.039	43	0.841	7.471	87.148
22	0.501	12.541	245.569	44	0.857	7.332	83.924
				45	0.873	7.197	80.876

The body and free surface meshes used in the simulations are illustrated in Figures 7.18 and 7.19, respectively. The meshes designed for the FPSO and the free surface were defined after a convergence test and were composed of 1088 and 3600 panels, respectively. The free surface mesh was constructed with radius $r_{fs} = 2000$ m and with a high panel concentration near the FPSO position. Once more, the time-step was set to $\Delta t = T/60$ s and the damping zone coefficients considered $b = 2.0$ and $a = 1.0$.

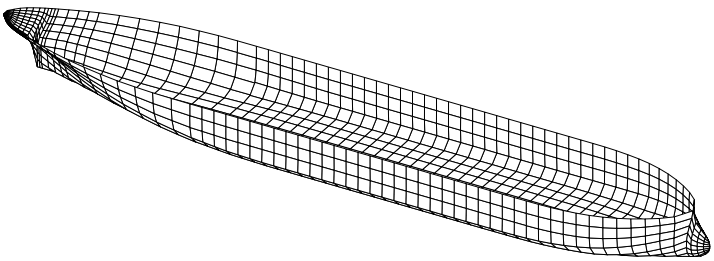

Figure 7.18: FPSO VLCC hull panel mesh

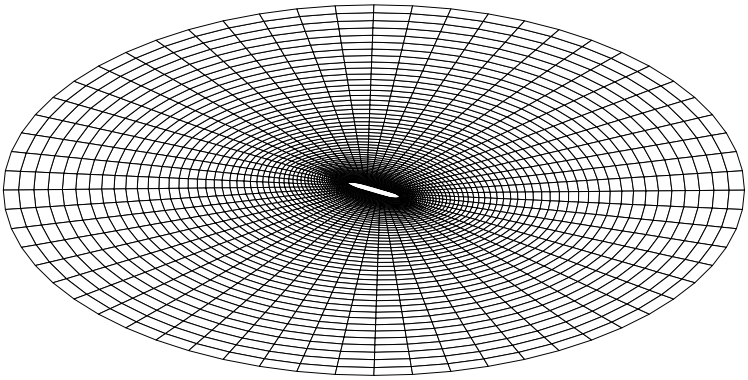

Figure 7.19: Free surface panel mesh for the FPSO simulations

Figures 7.20, 7.21 and 7.22 present the comparisons between numerical results and experimental data for sway, heave and roll D.O.F., respectively. As expected, the change of the external roll damping coefficients brought higher deviations at frequencies near to the natural frequency. In addition, this variation did not influence the heave motions and had only a slight impact in the sway ones, which is justified by the existence of a nonzero hydrodynamic crossing term coefficient, originated from the radiation problem, coupling these two degrees of freedom. In general, the numerical method recovered well the experimental curves, being capable of predicting the motion amplitudes with reasonable accuracy.

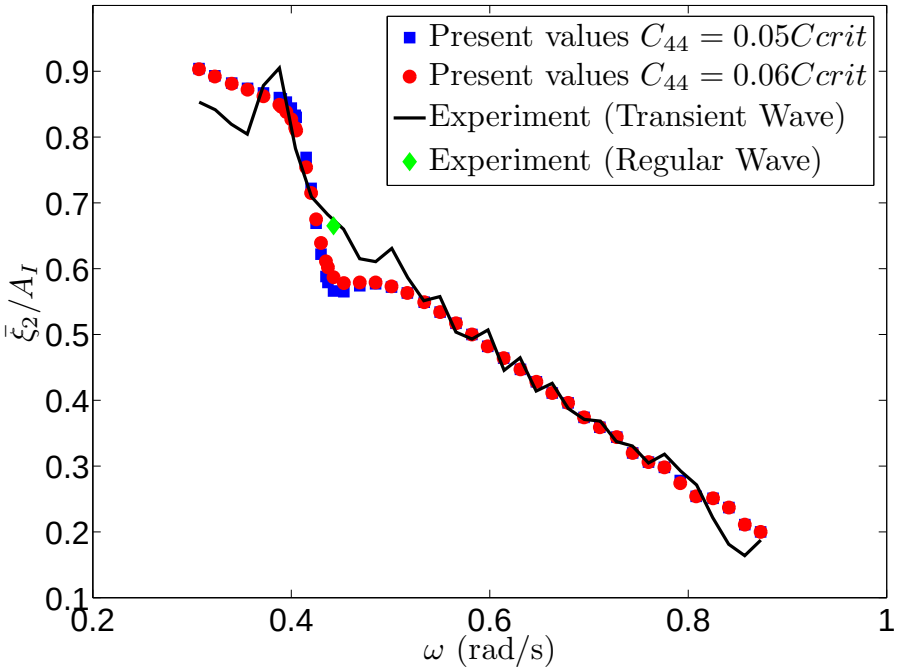

Figure 7.20: Comparison between numerical results and experimental data of sway response amplitude operator for the FPSO VLCC hull

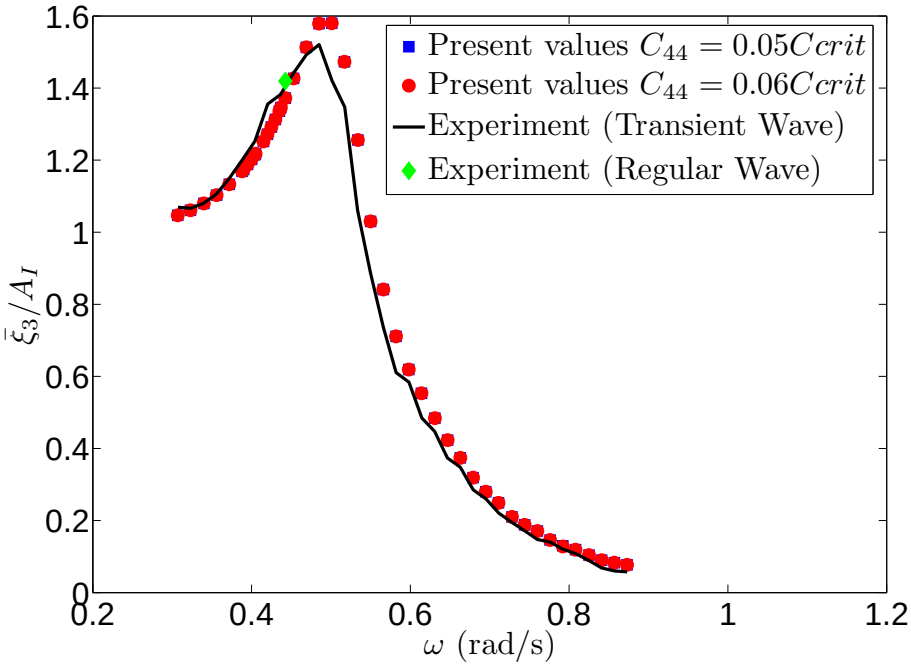

Figure 7.21: Comparison between numerical results and experimental data of heave response amplitude operator for the FPSO VLCC hull

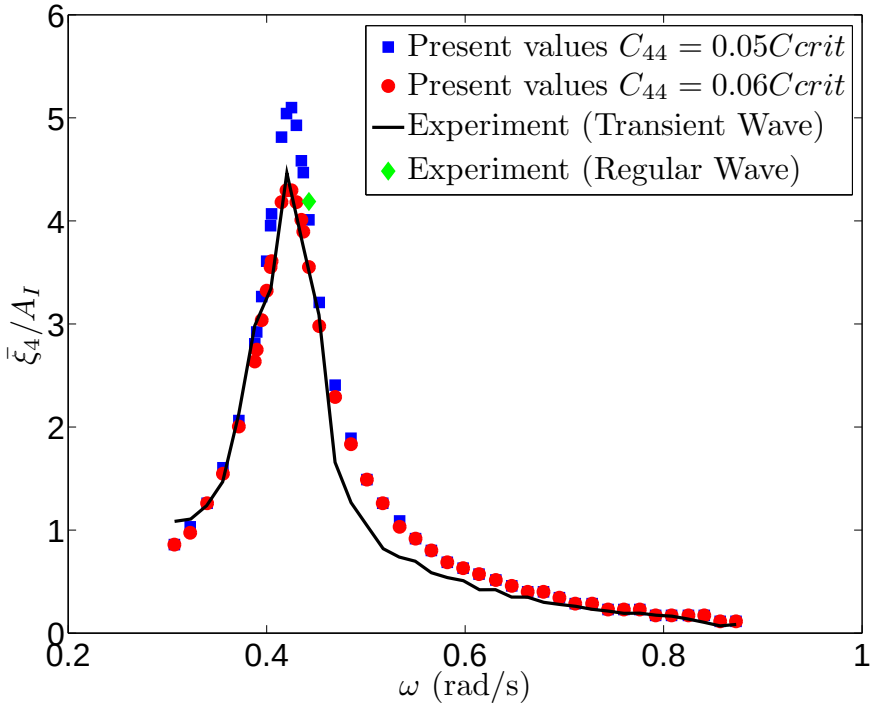

Figure 7.22: Comparison between numerical results and experimental data of roll response amplitude operator for the FPSO VLCC hull

Direct comparisons between numerical and experimental time series of motion for sway (ξ_2), heave (ξ_3) and roll (ξ_4), considering $C_{44} = 0.05C_{crit}$ and $C_{44} = 0.06C_{crit}$ are presented in Figures 7.23 and 7.24, respectively. These motions arise from the FPSO interaction with a regular wave of frequency $\omega = 0.443$ rad/s and amplitude $A_I = 0.92$ m, both in full scale. The time series are synchronized considering only the motion data of one D.O.F., in this case heave, so as to preserve the phase information with the other D.O.F.. A good agreement is observed for the heave motion time series, in which the experimental and numerical curves are practically coincident. On the other hand, although the roll and sway motion phases were predicted accurately, slightly discrepancies in amplitude may be noticed, specially in Figure 7.24, where an external coefficient of $C_{44} = 0.06C_{crit}$ is being applied. This result is contradictory with the comparisons made for the roll RAO, see Figure 7.22, obtained with the transient wave, in which the consideration of the higher damping coefficient clearly improved the agreement. However, as could also be observed in the figure, the roll RAO measured in the experiment considering transient and regular waves presented different amplitudes, which do not allow a tuning of the linear damping coefficient that is equally accurate for both cases. In spite of this fact, good predictions were obtained with the numerical method, attesting once again that the equilibrium between the dynamic and hydrodynamic forces was preserved during the whole simulation.

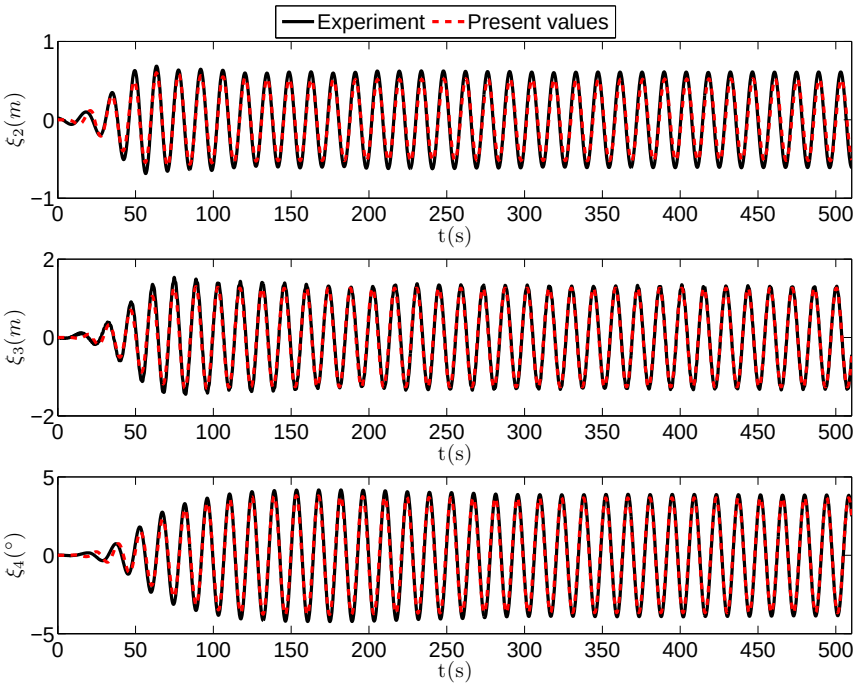

Figure 7.23: Comparison between numerical and experimental motion time series for sway (ξ_2), heave (ξ_3) and roll (ξ_4), considering $C_{44} = 0.05C_{crit}$

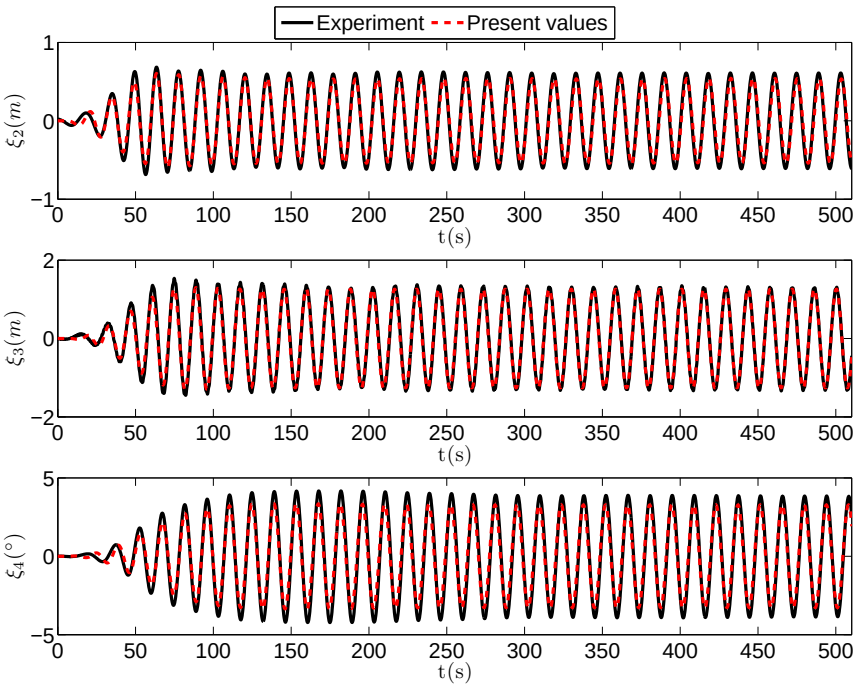

Figure 7.24: Comparison between numerical and experimental motion time series for sway (ξ_2), heave (ξ_3) and roll (ξ_4), considering $C_{44} = 0.06C_{crit}$

Chapter 8

Multi-Body Simulations in Side-by-Side Arrangement

The hydrodynamic interaction of two vessels in a side-by-side arrangement is currently receiving substantial attention due to its practical application in the offloading process involving the so-called Floating Liquefied Natural Gas (FLNG) units and Liquefied Natural Gas (LNG) carriers. As a result, much attention has been given to the analysis of multi-body interaction effects with regard to the prediction of risk of collision between the vessels (ZHAO et al., 2011). In this regard, the correct modelling of the fully coupled dynamics of this multi-body problem and also the prediction of the vessels relative motions are important aspects when planning such a complex operation (KOO; KIM, 2005). Indeed, this analysis must also be taken in to account in the design of a mooring system for this kind of operation (KASHIWAGI; ENDO; YAMAGUCHI, 2005).

Wave resonant effects in the gap is one of the challenging problems in the hydrodynamic modelling of two bodies arranged in a side-by-side configuration. These resonances create different mode shapes of wave elevation in the gap at each associated resonant frequency, which is a behaviour quite similar to the one that takes place in moonpools (MOLIN, 2001). The three basic modes are normally referred to as the piston mode, longitudinal and transversal sloshing. An approximation formula for the estimation of these frequencies in open boundaries may be found in Molin et al. (2002). A comprehensive numerical investigation with the purpose of studying the different resonant frequencies and modes is given by Sun, Taylor and Taylor (2010).

Although, in reality, resonant effects in the wave height may occur in the gap, they are largely dampened by viscous effects and, therefore, the conventional potential flow

methods are known to overestimate the hydrodynamic forces, the wave elevation in the gap and consequently the body motions. This occurs because these methods are unable to model the viscous effects, namely skin friction and flow separation on the hull side, that are deemed important, especially the latter, for the flow in the small gap between the hulls ((MOLIN et al., 2009) and (KRISTIANSEN; FALTINSEN, 2010)).

CFD applications for dealing with the viscous effects in this resonant problem are certainly envisaged, but, to this moment, the high computational effort they demand still renders these applications infeasible for practical engineering purposes. For this reason, mixed approaches combining the benefits provided by viscous and potential flow solvers may be considered as a promising alternative to handle the problem. Kristiansen and Faltinsen (2012) applied this methodology in a two-dimensional numerical wave tank with a floating body. Elie et al. (2013) presented numerical results computed with their three-dimensional SWENSE (Spectral Wave Explicit Navier-Stokes Equations) numerical method for two side-by-side fixed barges in different regular waves incident angles.

However, for the time being, computational methods most often applied to model the side-by-side problem are based on the potential flow theory, in which suppression methods to deal with the resonant problems are used as an attempt to better reproduce the physics of the phenomenon. In the context of linear frequency domain diffraction/radiation codes, Huijsmans, Pinkster and de Wilde (2001) imposed a no flux vertical condition by applying a rigid lid along the gap length. Newman (2003) improved the lid method using the generalized mode technique with a set of basis functions composed of Chebyshev polynomials. This method allows wave motion in the gap, in which the wave elevation is controlled by imposing damping factors for each generalized mode.

In a different approach, Chen (2005) formulated a suppression method, namely the damping lid method, introducing a damping force directly into the conventional free surface boundary conditions. A major advantage of this method is that only one value of damping factor is needed. A first attempt for applying this method is presented in Fournier, Naciri and Chen (2006), where comparisons between numerical and experimental results for a Floating Storage and Regasification Unit (FSRU) and a LNG carrier positioned in side-by-side attested that the method was effective in attenuating the wave elevation in the confined zone, which consequently led to a better reproduction of the first order motions and drift forces. Following the same approach, Pauw, Huijsmans and Voogt (2007) applied the damping lid method for the investigation of resonant effects for LNG carriers. Experimental tests were conducted considering only one ship model, which was positioned at half-gap witdh from the lateral tank wall. Results were discussed in terms of wave elevation in the gap, motion RAOs (Response Amplitude Operators) and wave drift Quadratic Transfer Functions (QTFs). The authors concluded that the damping factor

has a much greater effect on the drift forces than on the first order quantities and that an unique value of damping parameter was not enough to provide a full agreement with the test data. Furthermore, a slight frequency shift in wave elevations and vessels motions between measurements and diffraction results was observed. Bunnik, Pauw and Voogt (2009) overcame the frequency shift problem by applying the damping lid technique not only in the gap but also inside the hulls, in order to remove the so-called irregular frequencies (those generated by the spurious numerical solution of internal problems inside the hulls). In fact, the authors have shown that such inconsistence of the numerical scheme was related to the rigid lid imposed inside the bodies to remove irregular frequencies of the solution, which was introducing a strong grid dependence into the computations.

Clauss, Dudek and Testa (2013) compared numerical and experimental results considering a barge-LNG carrier system and found numerical resonance peaks in the heave RAO, but not in the wave elevation inside the gap. In contrast with the majority of the previous works, they concluded that no external damping was necessary for modelling the wave elevations observed in the gap. This sort of discrepancy found among recent works on the theme emphasizes that additional systematic studies are still needed for a more comprehensive understanding of the flow phenomena and the performance of the computational techniques available for modelling them.

The analysis of multi-body hydrodynamic interactions have also being studied in time domain ((BUCHNER; DIJK; DE WILDE, 2011), (KOO; KIM, 2005), (NACIRI; WAALS; DE WILDE, 2007) and (ZHAO et al., 2013)). This approach is often used when the fully-coupled analysis involving not only the bodies, but also the mooring lines and fenders must be assessed, a situation in which a time domain approach must be necessarily applied. All these works, however, were based on the use of Cummins's equations (CUMMINS, 1962), in which frequency domain hydrodynamic coefficients are used as input data for the time domain calculations.

An alternative approach is to treat the hydrodynamic problem directly in time domain. Kim and Kim (2008) applied a time domain boundary elements method for studying the motion responses of adjacent vessels. They reproduced the resonant modes but did not make any attempt to suppress the resonant effects. Although the authors presented only linear results, the method can be extended to nonlinear problems by considering the nonlinear restoring and Froude-Krylov forces. Applications of time domain codes to side-by-side problems, including nonlinear results, were also presented by Yan, Ma and Cheng (2009) and Hong and Nam (2011). In the latter, a poor convergence on the time series of the second order sway forces was observed for resonant frequencies. These studies were based on the finite element method technique and also disregarded any sort of artificial damping in the gap.

Although the number of studies related to the application of time domain hydrodynamic solvers is still small in comparison to the conventional frequency domain method, it does represent a promising approach for the seakeeping analysis of fully coupled multi-body systems comprised by floating bodies, mooring lines, fenders etc. Nevertheless, the performance of suppression methods modeled in time domain potential flow solvers is a topic that still requires further investigation.

With this in mind, this chapter discusses the performance of the present time domain code applied to a multi-body system in side-by-side configuration. In order to provide benchmark data for the TDRPM numerical simulations, fundamental tests with simplified geometries were carried out at the model basin of CEHINAV-Technical University of Madrid (UPM). Moreover, the results were also compared to the ones calculated by the software WAMIT, which was also used for the conceptual planning of the experiments.

8.1 Experimental Setup

The experimental tests considered a multi-body system comprising two bodies of canonical geometries, namely a barge and a geosim, arranged in two different side-by-side configurations. The main characteristics of the models are presented in Table 8.1 and illustrated in Figures 8.1 and 8.2, the latter presenting the geosim geometry in detail. The tests were conducted at the towing tank of the CEHINAV-Technical University of Madrid (UPM). The tank is 100 m long, 3.8 m wide and the water depth is 2.5 m.

Table 8.1: Main characteristics of the barge and geosim models

Parameters	**Barge**	**Geosim**
Length over all	1.67 m	2.00 m
Beam	0.665 m	0.40 m
Depth	0.205 m	0.32 m
Draught	0.12 m	0.18 m
Displacement	133.26 kg	83.30 kg
Pitch Inertia[1]	–	31.84 kg.m^2
COG X coordinate[2]	–	0.00 m
COG Y coordinate[2,3]	–	-0.25/-0.5 m
COG Z coordinate[2]	–	0.00 m

[1]Values were calculated in relation to the body center of gravity
[2]Values are described in relation to the global coordinate system (x,y,z)=(0,0,0)
[3]The Y coordinate of the COG is half of the gap width

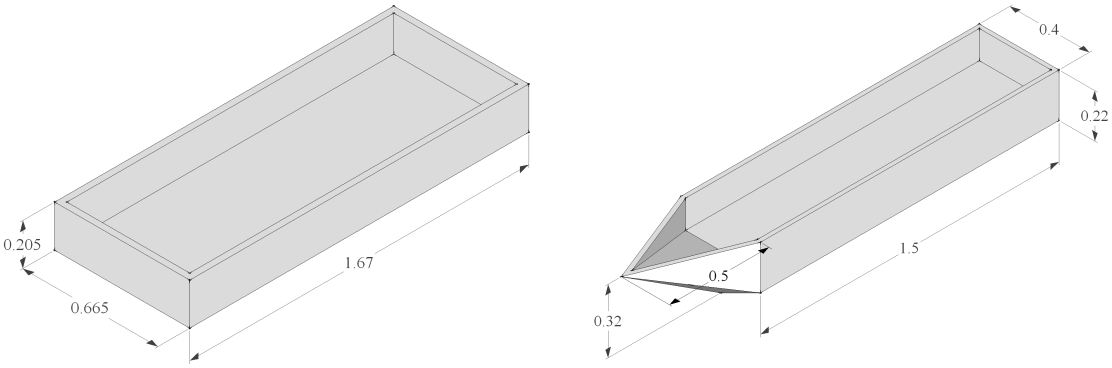

Figure 8.1: (b) Barge geometry and main dimensions in meters. (b) Geosim geometry and main dimensions in meters

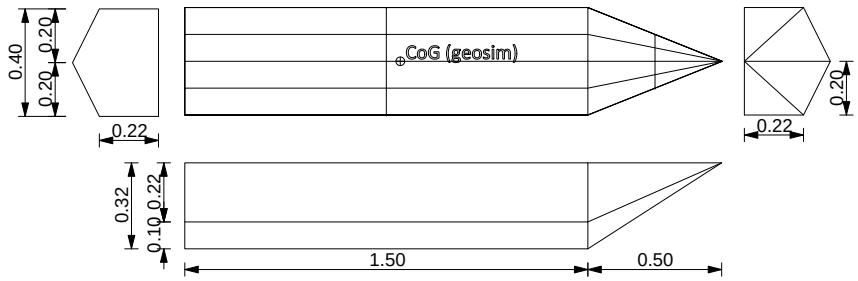

Figure 8.2: Details of the geosim geometry and main dimensions in meters

The test conditions were restricted to very simple configurations, aiming at providing benchmark data for the numerical results. Bearing this in mind, during the tests the barge was kept fixed and the geosim was attached to mechanical guiding arms, which restrained its sway, roll and yaw motions. Moreover, the geosim drift in surge was controlled by two springs linking the mechanical device to the model. This procedure enabled one to keep the gap width and length practically constant during the measurements, providing a convenient configuration for numerical modelling. Also for the purpose of calibration of the numerical method, the mass of the guiding arms and the total mass and inertia of the complete system were determined and are presented in Table 8.2.

Table 8.2: Main characteristics of the geosim including the mechanical guiding arms data

Feature	Geosim
Guiding arms mass	5.5 kg
Total Mass	88.80 kg
Pitch radius of gyration	0.598 m
Heave Period	0.95 s
Pitch Period	1.26 s

The geosim model was positioned in the tank with its longitudinal axis coincident with the longitudinal axis of the tank and the barge was located aside of the geosim, as represented in the sketch shown in Figure 8.3.

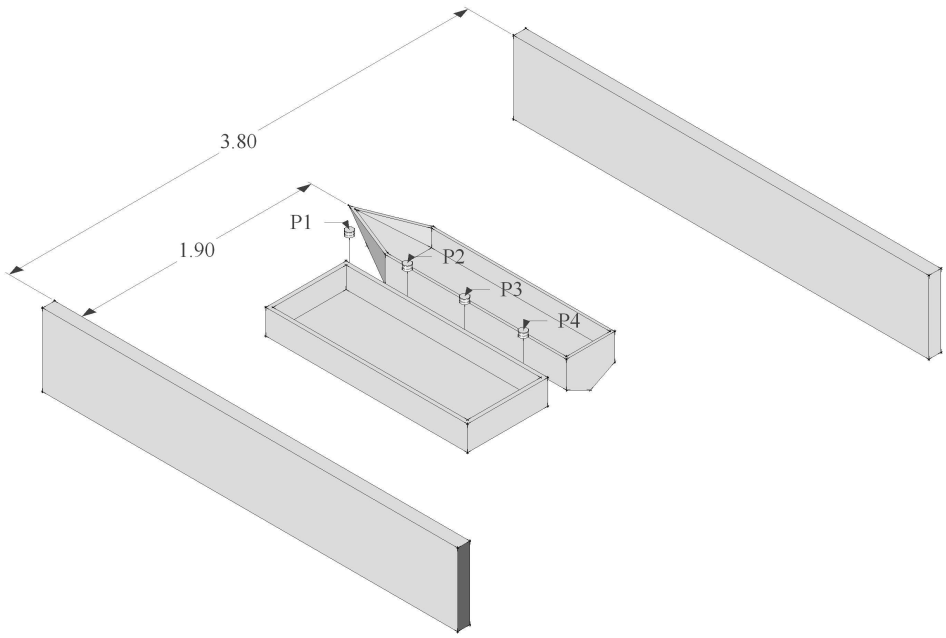

Figure 8.3: Models positions in relation to the towing tank walls. Dimensions in meters

Geosim heave and pitch motions were tracked by means of a laser system installed in the towing tank carriage. Additionally, four wave probes (P1, P2, P3 and P4, see Figure 8.3) were used for monitoring the wave elevation in different locations, three of them being positioned inside the gap. The relative distances between the wave probes are presented in Table 8.3. Figures 8.4 and 8.5 present two photographs of the experimental setup, including the probes arrangement.

Table 8.3: Relative distances between the wave probes

L(P1-P2)	0.48 m
L(P2-P3)	0.475 m
L(P3-P4)	0.485 m
L(P4-Stern Geosim)	0.28 m

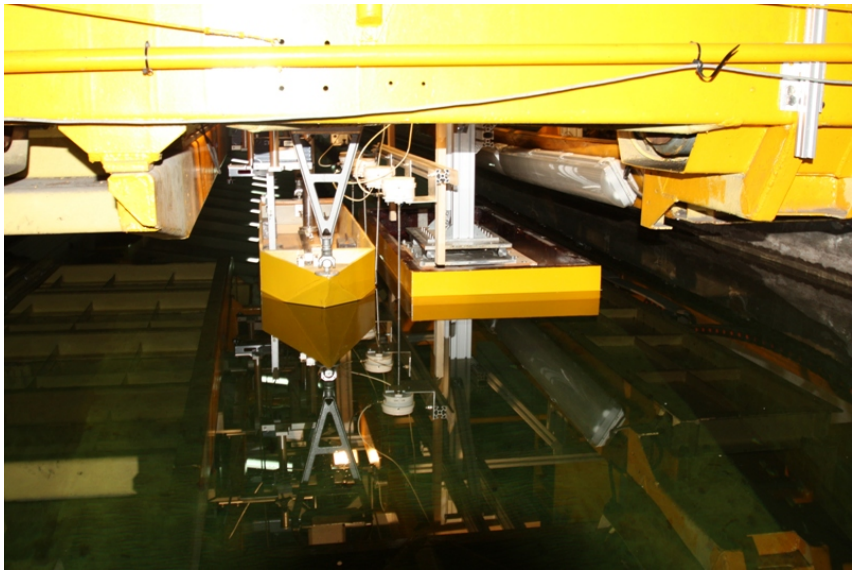

Figure 8.4: General view of the models positioned in the tank

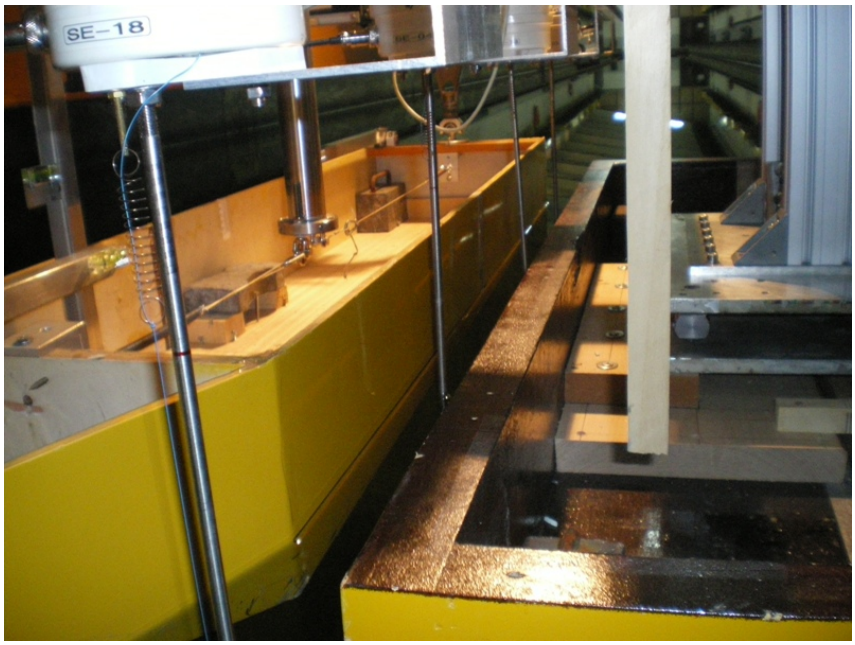

Figure 8.5: Wave probes arranged along the gap centerline

Since the experiments were conducted in a towing tank, special care had to be taken in order to minimize the influence of reflected waves from the tank walls within the frequency range of interest (namely, the range where the gap resonant modes are expected to occur). In fact, the distance between the models was defined considering previous numerical results calculated by the software WAMIT, which aimed at evaluating the expected gap resonant frequencies and whether the presence of the tank walls would interfere with the

experimental measurements at these frequencies. As will be demonstrated in the next section, by adopting proper gap widths, it was possible to restrict the influence of the tank walls to a range of frequencies different to the one in which we were interested in.

Once these preliminar investigations were performed, two experimental setups of gap widths 0.05 m and 0.10 m were selected and denoted as Cases 1 and 2, respectively. These tests were conducted focusing on the study of linear effects and included a set of 49 and 32 regular waves of small amplitude for Cases 1 and 2, respectively. The main characteristics of the waves may be observed in Tables 8.4 and 8.5. The wave height for every frequency was determined considering a wave steepness smaller or equal to $H/\lambda \leq 3\%$ (limit established for the highest wave frequencies) and the maximum allowed wave height was 0.04 m in order to guarantee a stable propagation of the waves along the tank. For Case 1, which was tested first, the number of waves was larger because some of them were used with the intent of evaluating the influence of the tank walls and also checking whether the preliminary numerical models were providing reasonable results. For Case 2 the test matrix was reduced to 32 waves, concentrating most of the waves within the frequency range where gap resonance had been predicted by the numerical models. Due to the limitations concerning the width of the towing tank, only head waves were considered.

Table 8.4: Regular waves tested for the gap width 0.05 m

ID	ω **(rad/s)**	**T(s)**	**H(m)**	**ID**	ω **(rad/s)**	**T(s)**	**H(m)**
1	4.000	1.571	0.040	18	7.400	0.849	0.034
2	4.250	1.478	0.040	19	7.600	0.827	0.032
3	4.500	1.396	0.040	20	7.700	0.816	0.031
4	4.750	1.323	0.040	21	7.800	0.806	0.030
5	5.000	1.257	0.040	22	7.900	0.795	0.030
6	5.250	1.197	0.040	23	8.000	0.785	0.029
7	5.400	1.164	0.040	24	8.125	0.773	0.028
8	5.500	1.142	0.040	25	8.250	0.762	0.027
9	5.600	1.122	0.040	26	8.375	0.750	0.026
10	5.750	1.093	0.040	27	8.500	0.739	0.026
11	6.000	1.047	0.040	28	8.625	0.728	0.025
12	6.200	1.013	0.040	29	8.750	0.718	0.024
13	6.400	0.982	0.040	30	8.875	0.708	0.023
14	6.600	0.952	0.040	31	9.000	0.698	0.023
15	6.800	0.924	0.040	32	9.250	0.679	0.022
16	7.000	0.898	0.038	33	9.500	0.661	0.020
17	7.200	0.873	0.036	34	9.750	0.644	0.019
				35	10.000	0.628	0.018

Table 8.5: Regular waves tested for the gap width 0.1 m

ID	ω (rad/s)	T(s)	H(m)	ID	ω (rad/s)	T(s)	H(m)
1	4.000	1.571	0.040	14	7.750	0.811	0.031
2	4.500	1.396	0.040	15	7.875	0.798	0.030
3	5.000	1.257	0.040	16	8.000	0.785	0.029
4	5.500	1.142	0.040	17	8.125	0.773	0.028
5	6.000	1.047	0.040	18	8.250	0.762	0.027
6	6.500	0.967	0.040	19	8.375	0.750	0.026
7	6.750	0.931	0.040	20	8.500	0.739	0.026
8	7.000	0.898	0.038	21	8.750	0.718	0.024
9	7.125	0.882	0.036	22	9.000	0.698	0.023
10	7.250	0.867	0.035	23	9.250	0.679	0.022
11	7.375	0.852	0.034	24	9.500	0.661	0.020
12	7.500	0.838	0.033	25	9.750	0.644	0.019
13	7.625	0.824	0.032	26	10.000	0.628	0.018

8.1.1 Investigation of the Tank Walls Effects

The higher order WAMIT module was applied with the intent of investigating the influence of the tank walls on the experimental results. Since WAMIT is formulated in frequency domain and applies the well known free surface Green function, which eliminates the necessity of discretizing the free surface, the code is more suitable to be used for exhaustive variations of important parameters that must be assessed in the problem, if compared to the present time domain solver.

For this analysis, numerical models with and without tank walls were computed in WAMIT. The numerical models with the tank walls were emulated for both cases (1 and 2) by introducing sets of bodies images (barge + geosim) with respect to the tank walls. Moreover, since two tank walls should be considered and the exact solution of the problem would only be reached by using an infinite series of images, a convergence analysis was performed in order to determine the minimum number of images above which the results would not be significantly affected. In total, 5 sets of body images had to be considered for achieving a reasonable convergence, resulting in a model composed of 12 bodies, as illustrated in Figure 8.6. In order to reduce the computational effort of the WAMIT computations, a symmetry plane, illustrated in Figure 8.7, was also considered, resulting in a model of 6 bodies plus a symmetry plane.

Concerning the bodies meshes, the *panel size* parameter was set to 0.1 and 0.2 for Cases 1 and 2, respectively, values that were also defined after a convergence analysis of the mesh. One should notice that a smaller value of panel size was required for Case 1, since

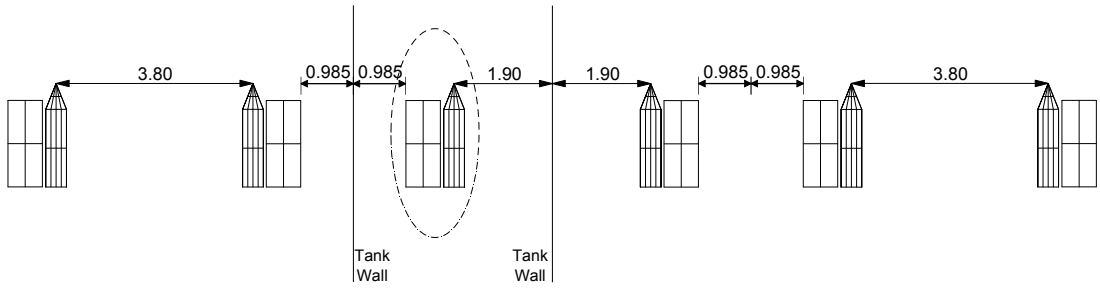

Figure 8.6: Body images considered in the multi-body model. Dimensions in meters

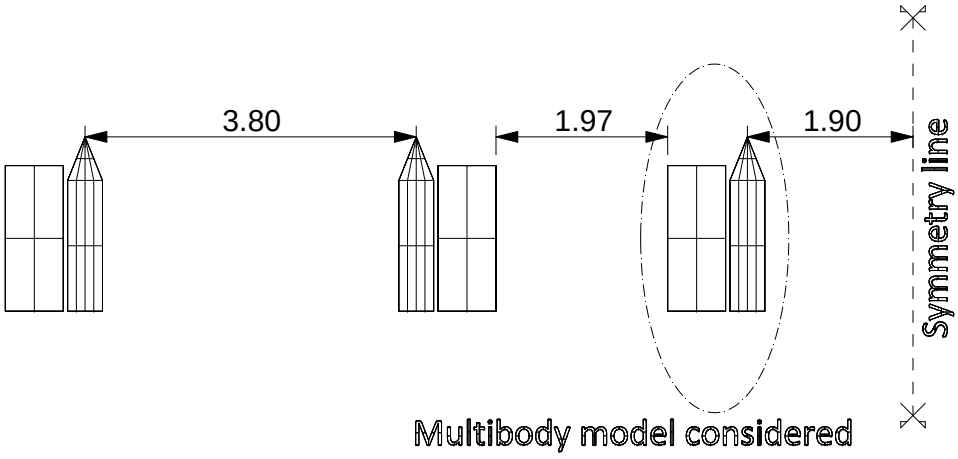

Figure 8.7: Symmetry line applied for the frequency domain computations. Dimensions in meters

the gap width was smaller.

Figure 8.8 presents a comparison between RAO calculations with the WAMIT model and the measured data for Case 1. The comparison refers to the geosim heave and pitch RAOs and shows that the heave motion amplifications observed in the experiment for frequencies between 3.5 rad/s and 7.0 rad/s are caused by waves reflected by the tank walls. The evidence for this comes from the fact that the WAMIT numerical model with walls was indeed able to capture the same trends of the experimental curve. Moreover, one should also notice that the influence of the walls tends to be minimized for higher frequencies ($>$ 7rad/s), for which both WAMIT numerical models present similar results. It is also worth mentioning that the pitch motion is not significantly affected by the presence of the walls.

The influence of the tank walls on the wave elevations at the gap centerline is investigated in Figure 8.9, from which it can be inferred that the wall effects are of minor degree. Both WAMIT numerical models (with and without walls) present good agreement with the experimental data for wave frequencies lower than 8 rad/s, in the same range where

the heave motions are significantly influenced by the tank walls. Nonetheless, one should realize that the numerical results provided by both models (with and without walls) present significant wave amplifications for a range of frequencies between 8.0 and 9.0 rad/s, which are in general much larger than the observed experimental values.

As aforementioned, potential flow solvers present some difficulties when dealing with physical problems that contain narrow gaps, tending to provide unrealistic wave elevations and body motions for the associated gap resonant frequencies, where the potential flow physics is not enough to represent the hydrodynamic phenomenon. A more complete discussion about this issue will be presented in the next sections, along with the description of the numerical modelling based on the time domain solver.

Analogous results for Case 2 are presented in Figures 8.10 and 8.11. By analyzing both figures, it is possible to observe that the results present a behavior similar to the ones obtained for Case 1, once again emphasizing that the influence of the tank walls is more pronounced for wave frequencies lower than 7.0 rad/s.

Based on these analyses, it was possible to conclude that although the experimental data was conducted in a towing tank with walls relatively close to the model bodies, the influence of reflected waves was restricted to frequencies below the range of main interest to this study, namely the range where gap resonant effects are caused by the hydrodynamic interaction of the models in side-by-side configuration.

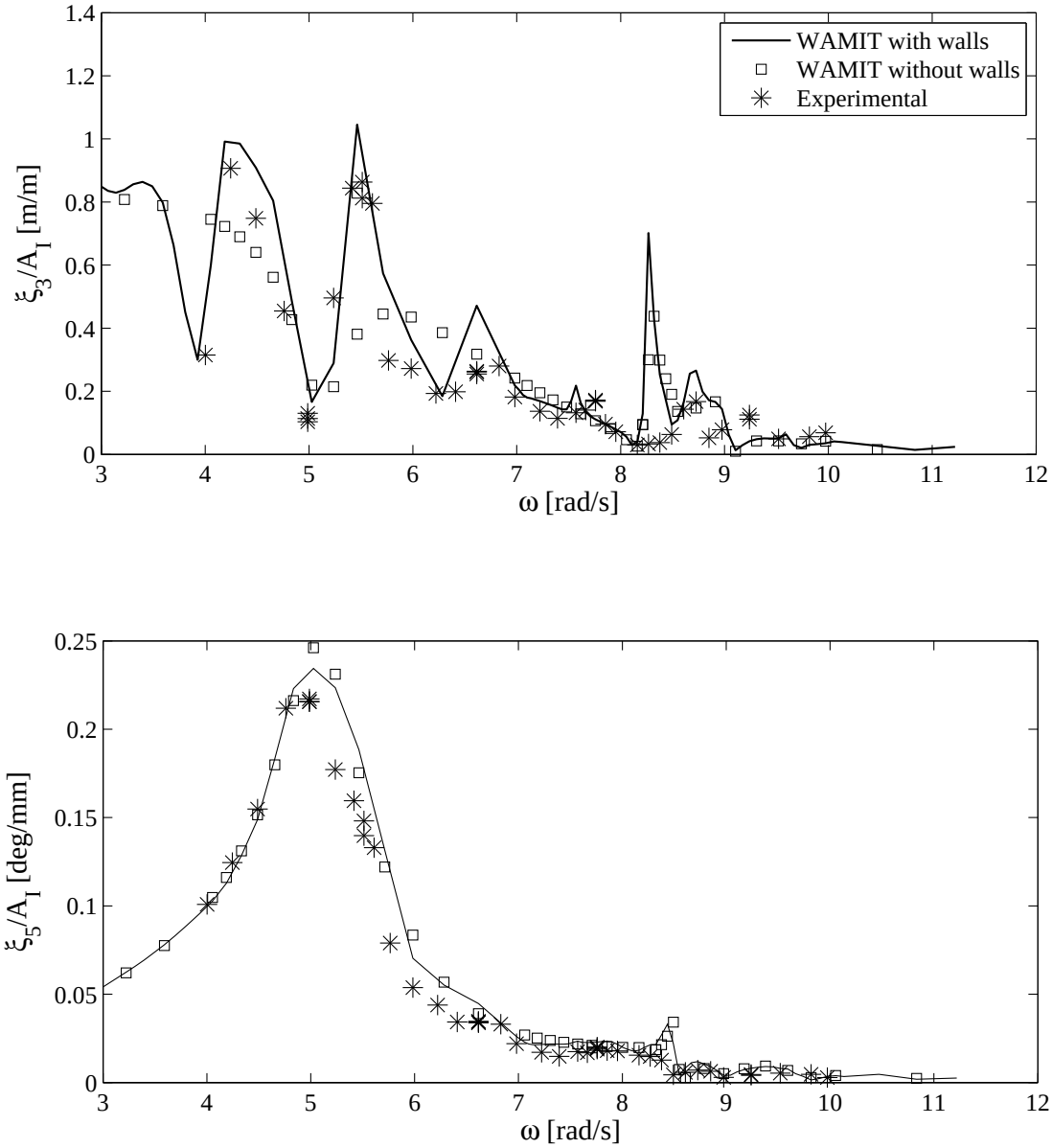

Figure 8.8: Case 1: Comparison between WAMIT numerical data and experimental values in terms of heave (top) and pitch (bottom) RAOs. Gap width = 0.05 m

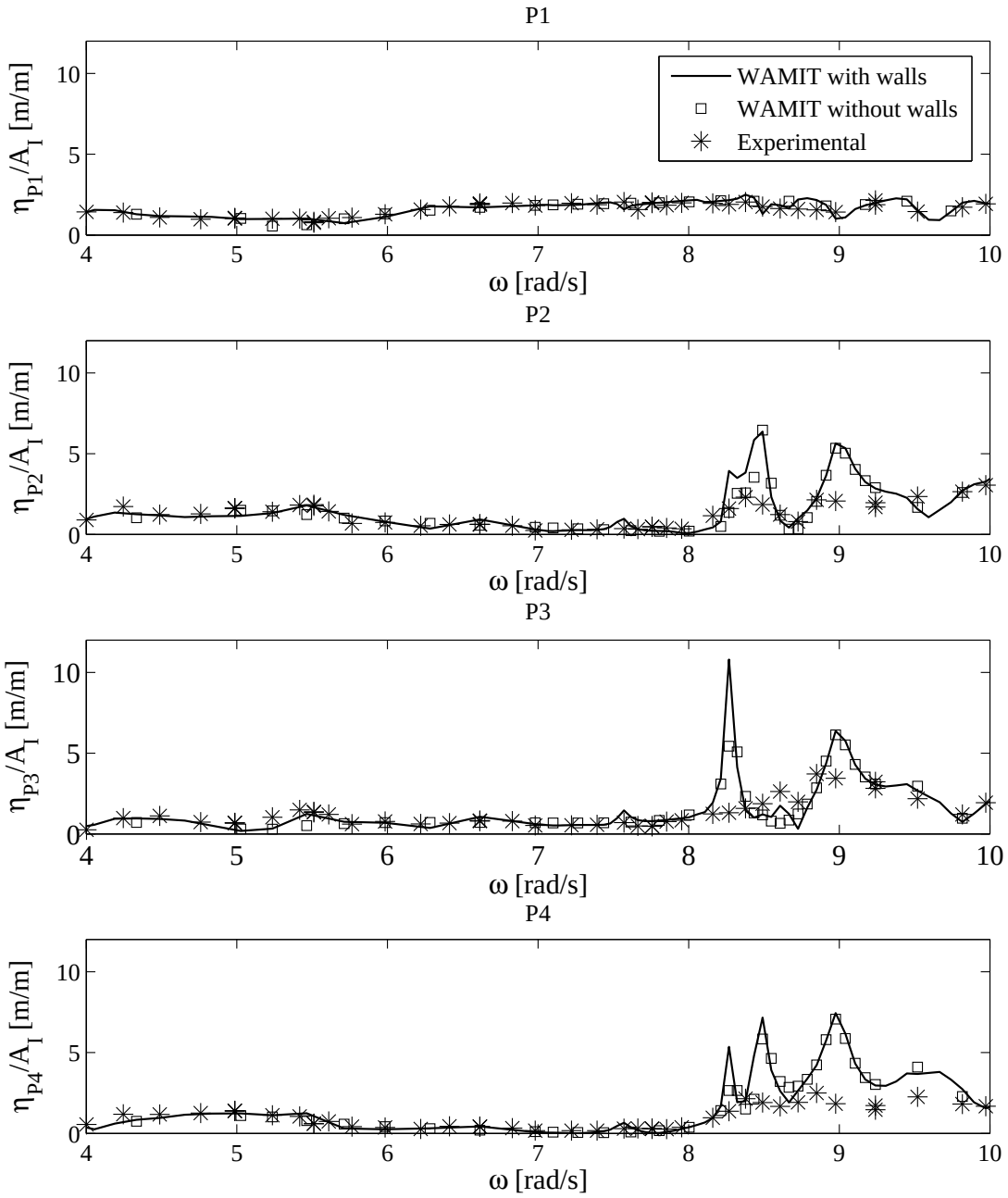

Figure 8.9: Case 1: Comparison between WAMIT numerical data and experimental values in terms of wave elevations RAOs in different points positioned along the gap centerline. Gap width = 0.05m

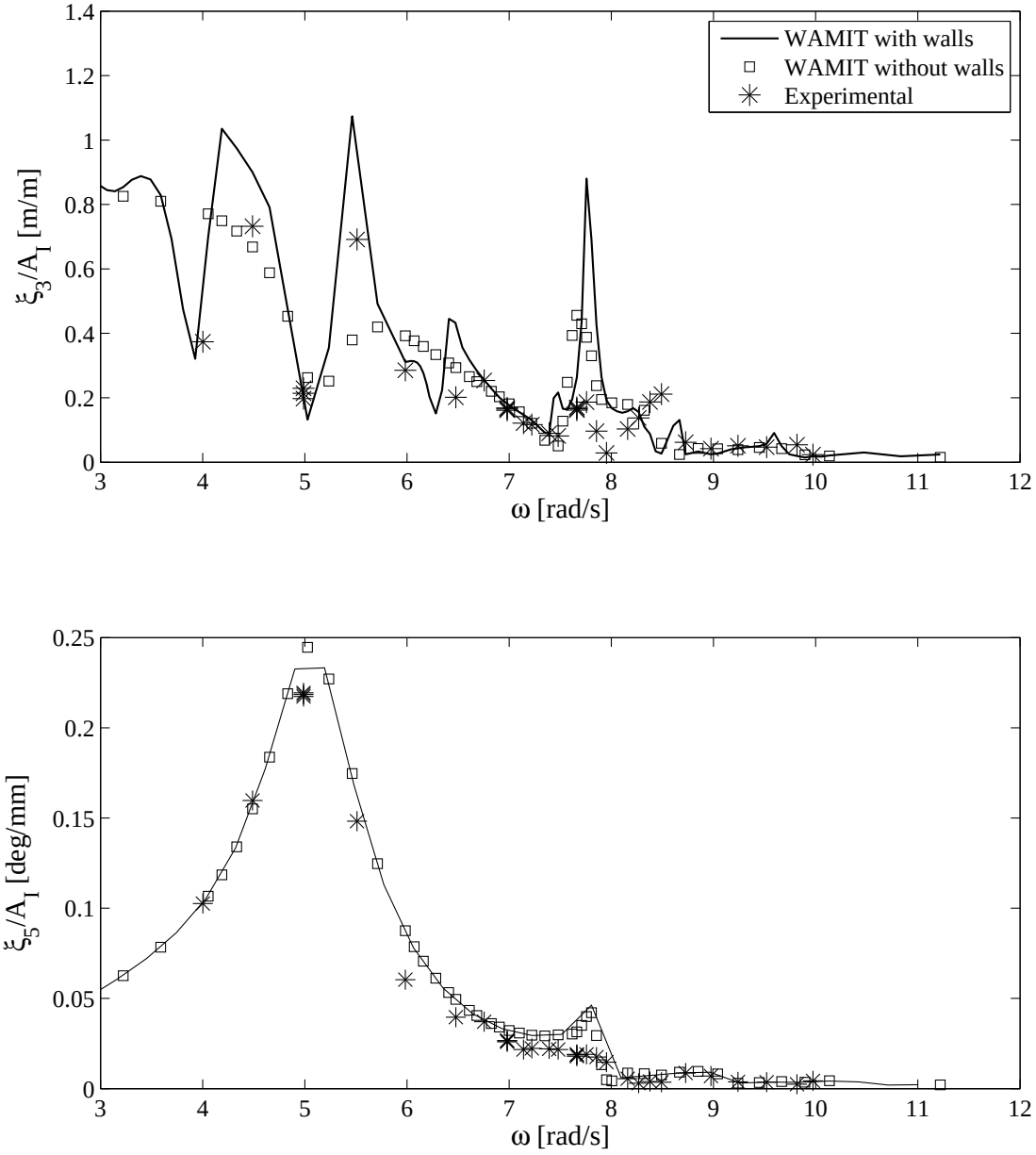

Figure 8.10: Case 2: Comparison between WAMIT numerical data and experimental values in terms of heave (top) and pitch (below) RAOs. Gap width = 0.1 m

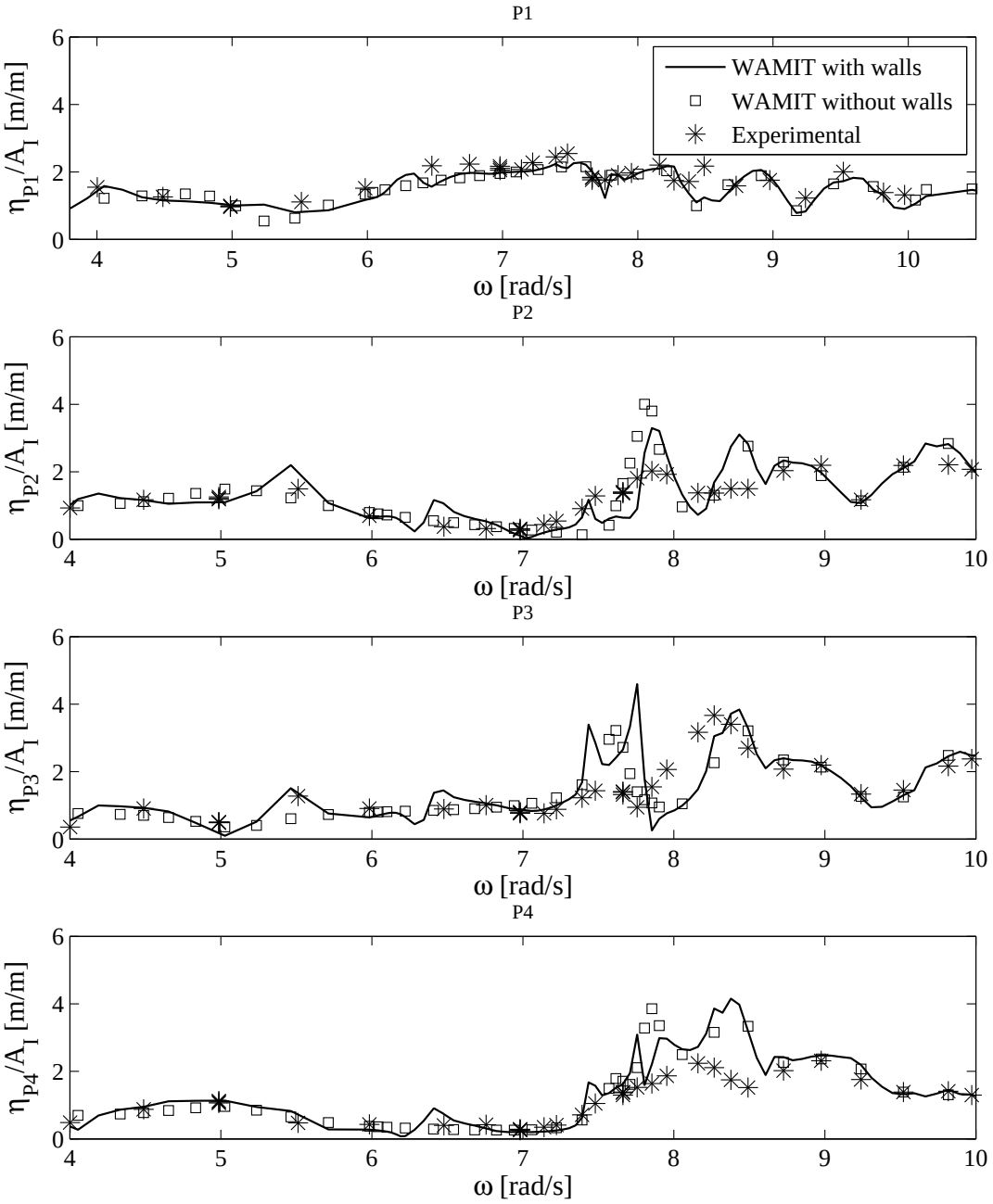

Figure 8.11: Case 2: Comparison between WAMIT numerical data and experimental values in terms of wave elevations RAOs in different points positioned along the gap centerline. Gap width = 0.1 m

8.2 Time Domain Numerical Model

The barge and geosim hulls used in the time domain simulations were modeled with 1584 and 1504 quadrangular panels, respectively. For the free surface meshes, 4797 panels were applied in Case 1 and 5751 panels in Case 2, the difference being associated exclusively

to the number of panels required to model the gap surface (750 panels for Cases 1 and 1500 for Case 2). These values were obtained after a convergence analysis in terms of the geosim motions and wave elevations.

Since the analysis conducted with WAMIT did not indicate significant wall effects in the gap resonant frequencies, the walls have been neglected in the time-domain simulations, thus reducing significantly the number of panels and, consequently, the total processing time.

By taking Case 1 (gap equal to 0.05 m) as an example, Figures 8.12 and 8.13 present the bodies (with the gap) and free surface meshes used in the computations, respectively. Notice that the meshes have been refined towards the bodies edges, with a larger concentration of panels near the gap region in order to improve the numerical convergence. In addition, the free surface mesh has been designed to allow a smooth transition from the gap region to the outer free surface. The same mesh topology has been applied in Case 2.

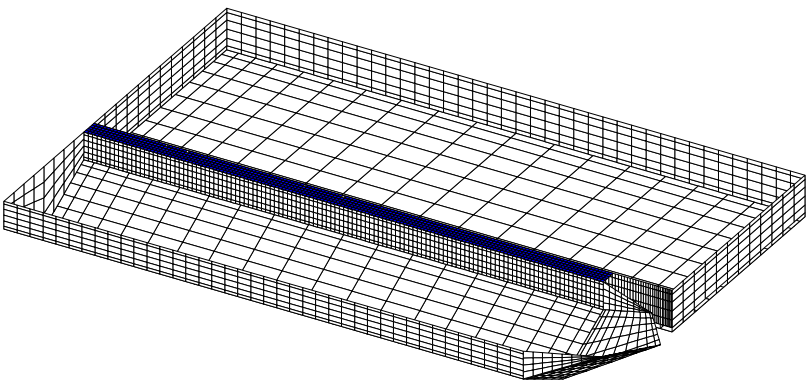

Figure 8.12: Barge, geosim and gap panel meshes for Case 1

The present method was run for several regular wave frequencies within the range of frequencies tested experimentally. Each simulation has provided a set of time series describing the geosim motions in the 3 D.O.F. (surge, heave and pitch) and the wave elevation at the wave probes locations (Table 8.3), from which the signal amplitudes have been characterized with the root mean square (rms) from a steady state interval. The time-step of each simulation has been set to $\Delta t = T/30$ s, whereas the numerical damping zone has been set with two wave lengths ($b = 2.0$) and intensity $a = 1.0$ for all cases.

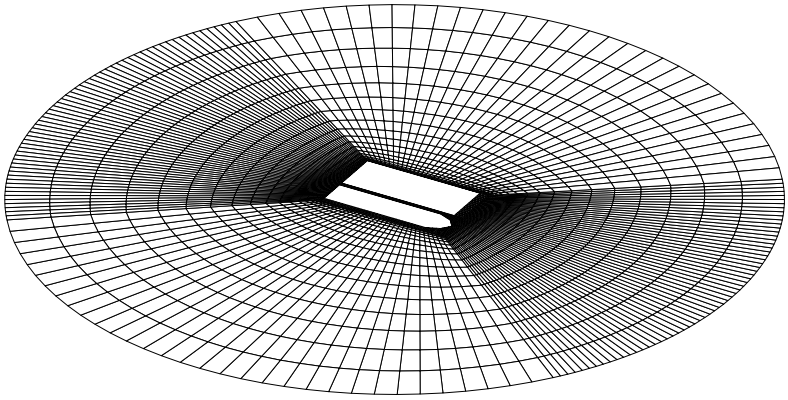

Figure 8.13: Free surface panel mesh for Case 1

8.2.1 Comparisons with WAMIT and Experimental Data

The comparison between the present method, WAMIT and experimental results in terms of geosim motions and wave elevations for Case 1 are presented in Figures 8.14 and 8.15, whereas for Case 2 they are presented in Figures 8.16 and 8.17. One should notice that only the WAMIT model without walls is being considered, since the results are focused exclusively on the range of frequencies in which the influence of tank walls can be disregarded (see section 8.1.1).

The overall agreement between the time-domain and WAMIT results is good for all the RAO curves. Even considering the fact that the present method is formulated in time domain, such an agreement was indeed expected since the boundary value problem solved by both computational codes is exactly the same. Also, it is clear that the numerical results tend to overestimate, in both cases, the experimental data for some frequency intervals.

For Case 1 (Figure 8.14), one should notice that in the frequency range $8 - 9$ rad/s there is a numerical resonance, which may be identified by the spurious peaks in the heave and pitch RAOs at approximately 8.3 and 8.5 rad/s, respectively. The same trends are observed for the wave elevations RAOs (Figure 8.15), especially for the measurement points that are in fact inside the gap between the bodies (P2, P3 and P4). Since the wave probe P1 was positioned outside the gap, it does not present significant influence from the resonant effects, resulting in a smoother RAO curve when compared to the other probes. At this location, a perfect agreement between numerical and experimental results was observed.

The wave modes associated to the resonant frequencies of 8.3 and 8.5 rad/s are presented

in Figure 8.18, which illustrates the envelopes of wave elevation inside the gap in spatial domain calculated by the time domain solver for Case 1. For the resonant wave frequency 8.3 rad/s, it is possible to observe that the wave elevation in the gap presents a piston type resonant mode, in which the wave behaves like a column of water moving up and down in the region between the vessels (MOLIN, 2001). Regarding the resonant frequency 8.5 rad/s, one may realize that instead of a piston mode, a second longitudinal mode is visualized. It is interesting to observe that this mode is related to the spurious amplification of the pitch motion at this same frequency (Figure 8.14).

The same qualitative behavior observed for Case 1 may be stated for Case 2 (Figures 8.16 and 8.17). In this case, however, since the gap width was increased to 0.10 m, the numerical resonant frequencies are slightly shifted towards lower frequencies $7.5 - 8.5$ rad/s. In this configuration, the numerical resonant peaks for heave and pitch RAOs are approximately 7.7 and 7.8 rad/s. Once again, these resonant frequencies coincide with the piston and second longitudinal modes of the gap, respectively, as may be observed in Figure 8.19. It is also interesting to observe that, for waves that are outside of the gap resonant frequency range, the numerical results agree with the experimental data very well.

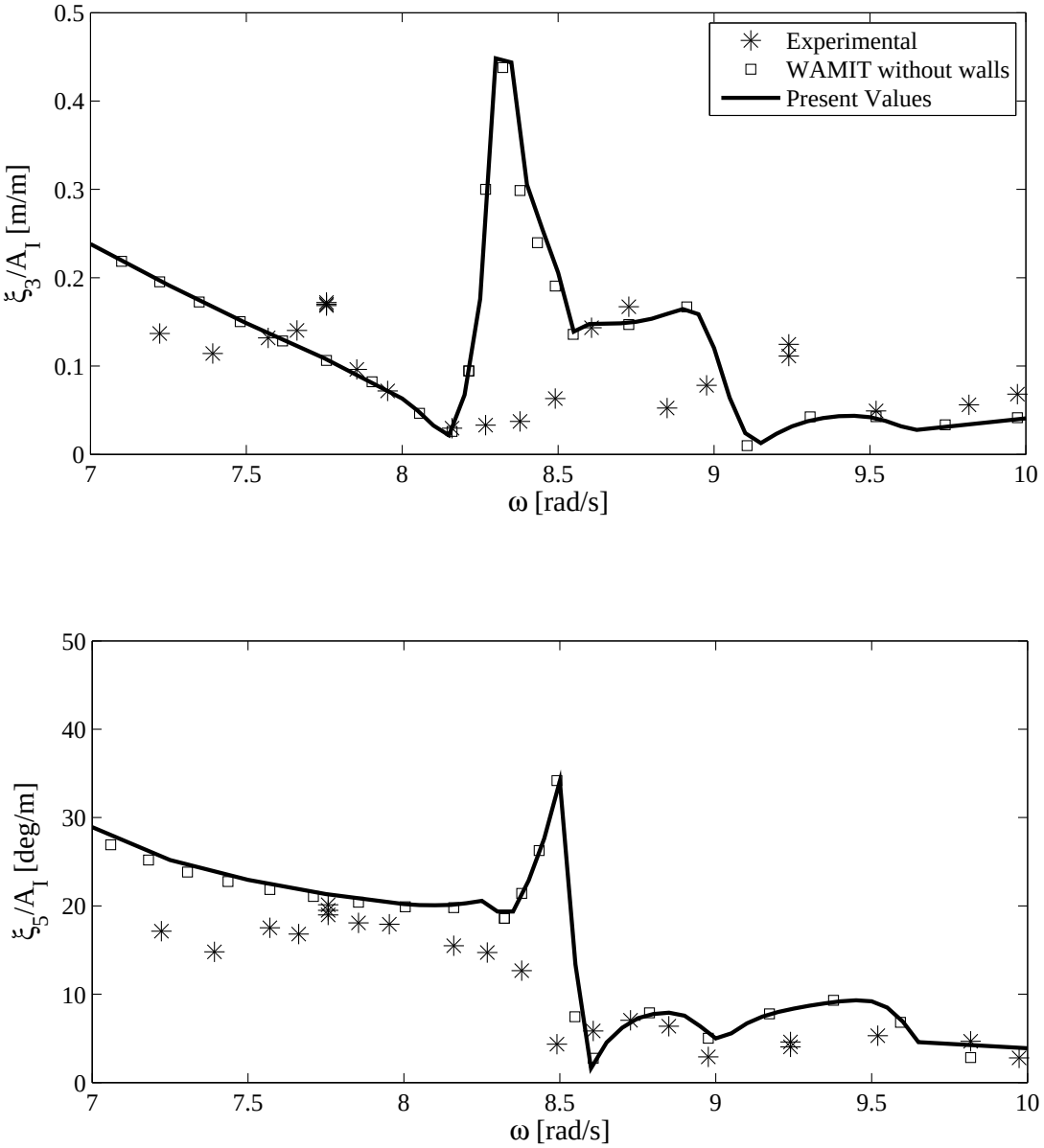

Figure 8.14: Case 1: Comparison between WAMIT, present values and experimental data in terms of heave (top) and pitch (bottom) RAOs. Gap width = 0.05 m

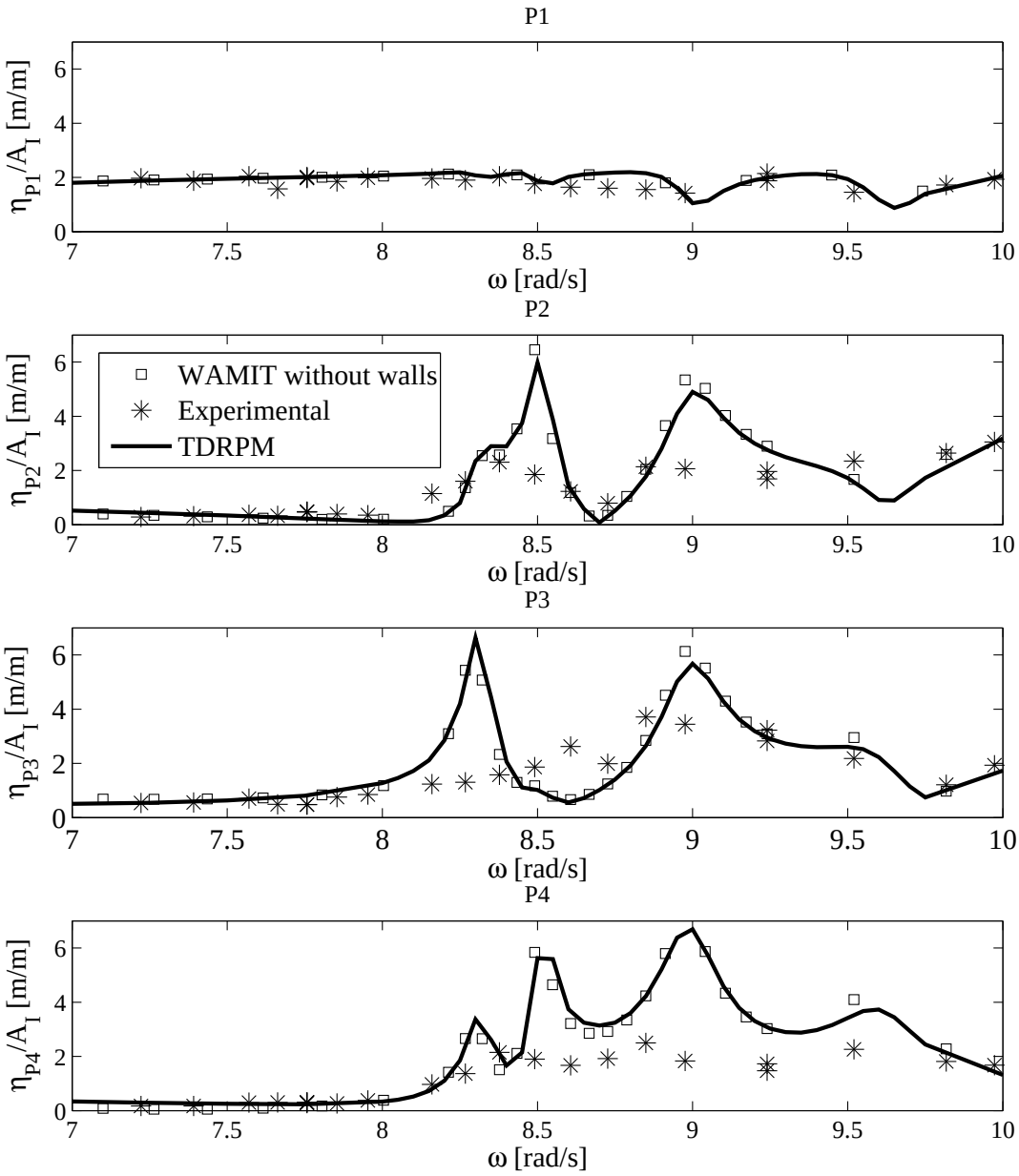

Figure 8.15: Case 1: Comparison between WAMIT, present values and experimental data in terms of wave elevations RAOs in different points positioned along the gap centerline. Gap width = 0.05 m

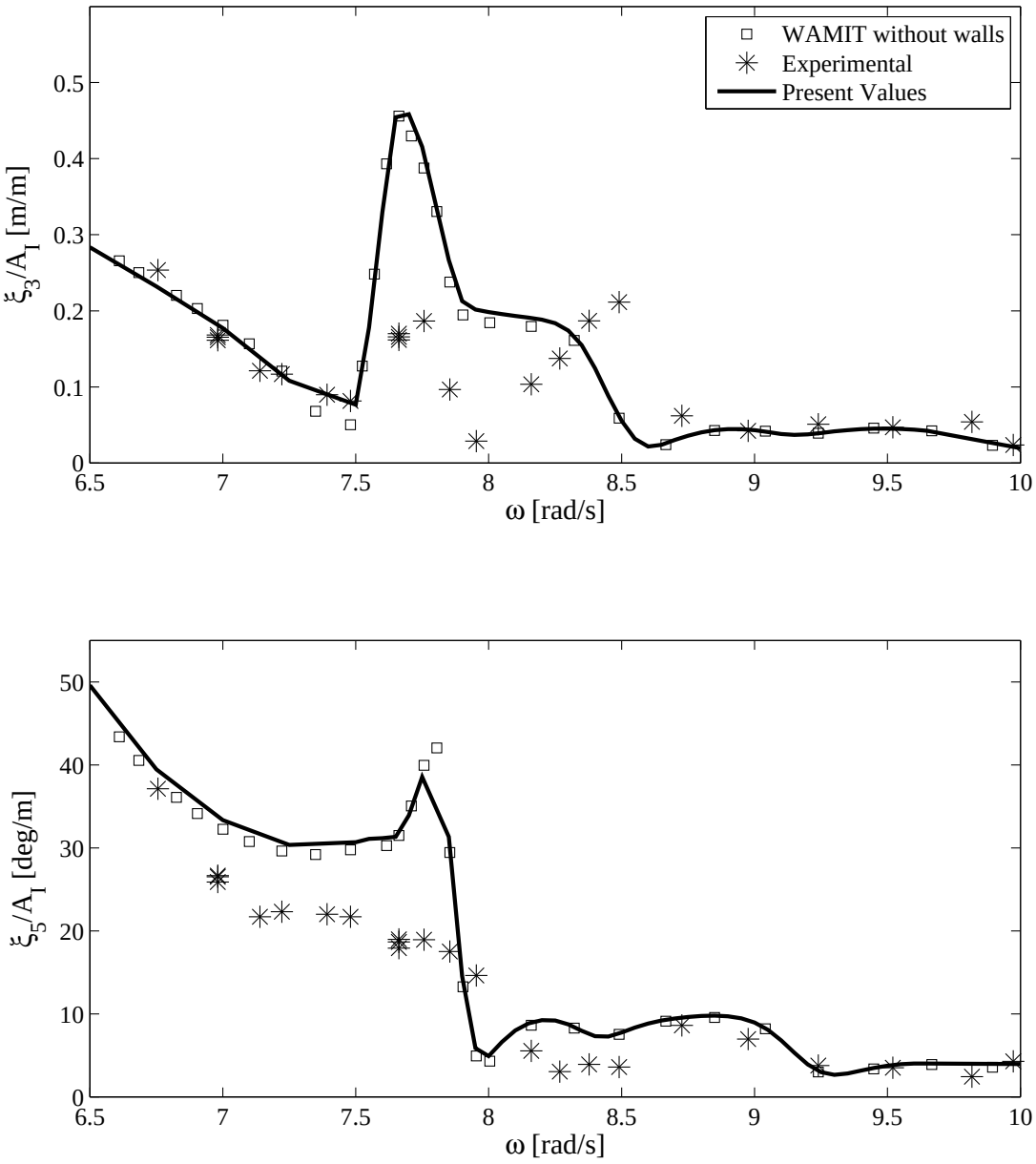

Figure 8.16: Case 2: Comparison between WAMIT, present values and experimental values in terms of heave (top) and pitch (bottom) RAOs. Gap width = 0.1 m

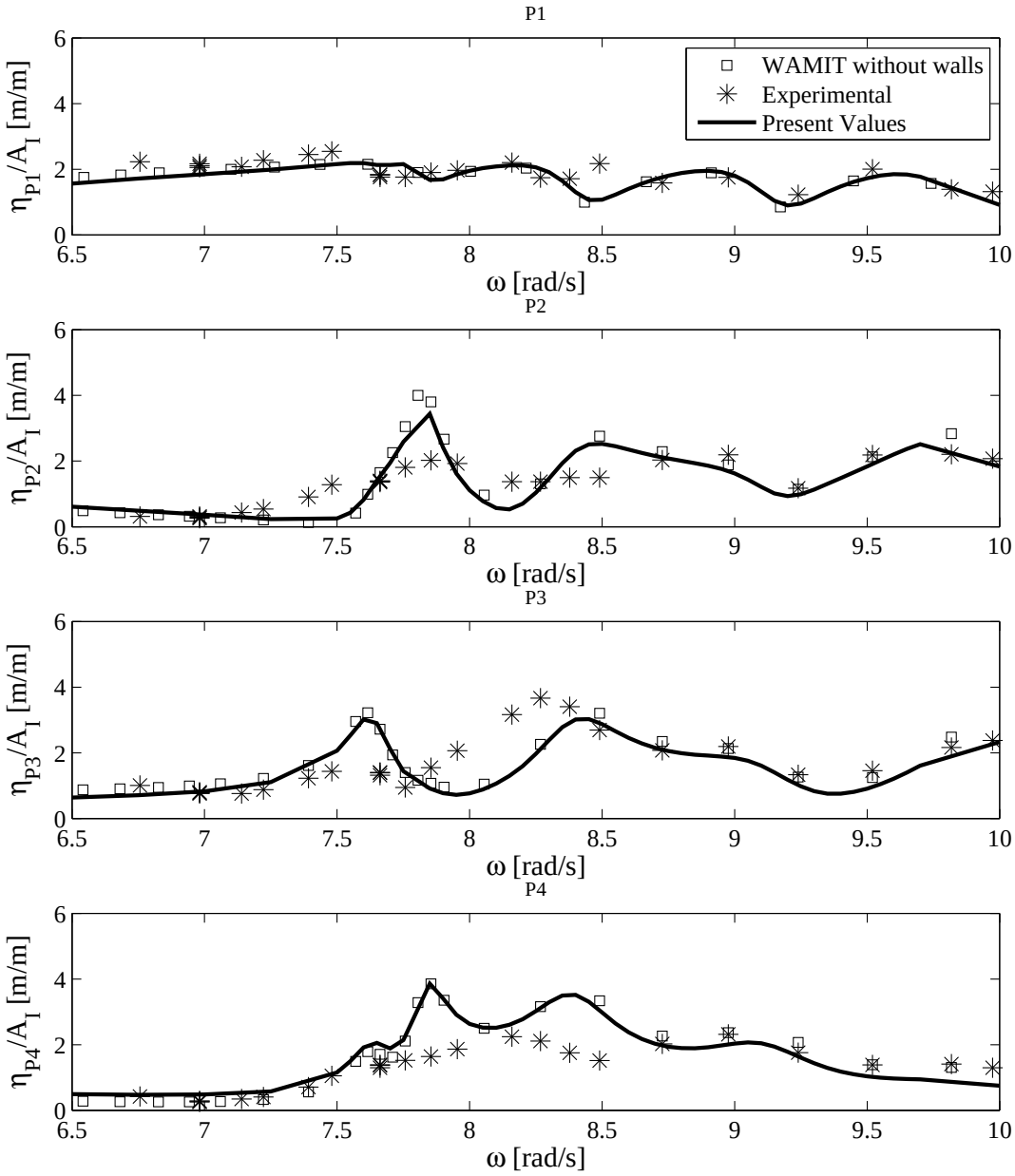

Figure 8.17: Case 2: Comparison between WAMIT, present values and experimental values in terms of wave elevations RAOs in different points positioned along the gap centerline. Gap width = 0.1 m

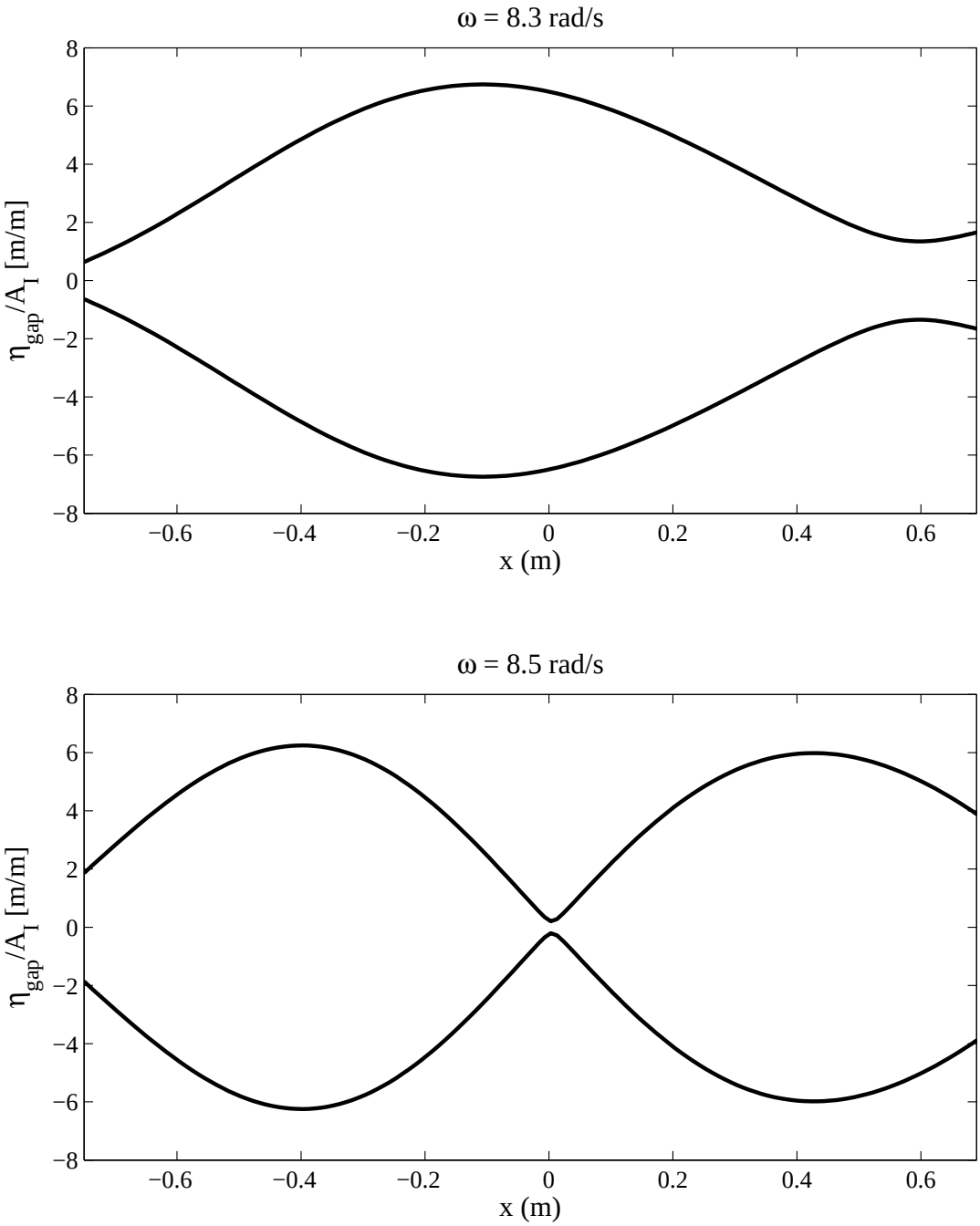

Figure 8.18: Case 1: Gap wave elevation envelopes in spatial domain computed with the present method. Incoming wave frequencies $\omega = 8.3$ rad/s (top) and $\omega = 8.5$ rad/s (bottom). Wave propagates from positive to negative x coordinates. Gap width = 0.05 m

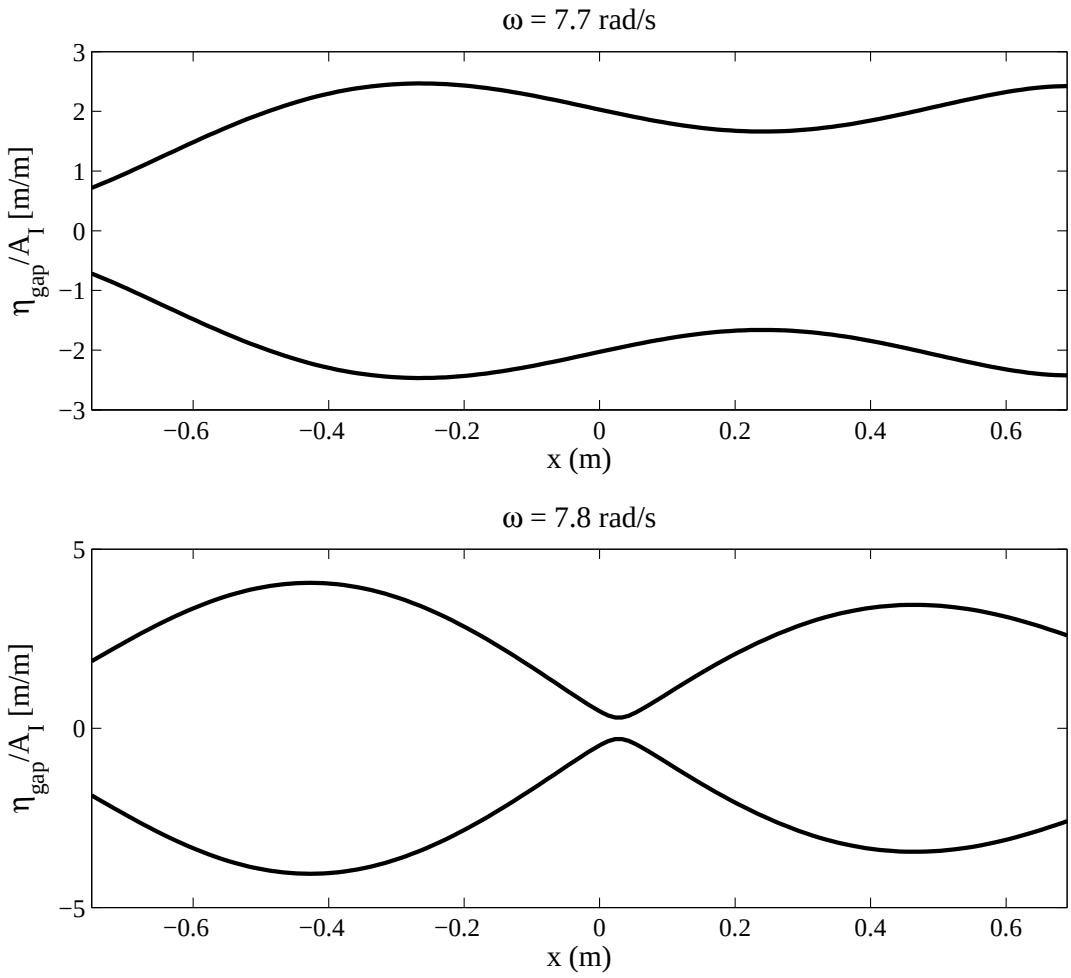

Figure 8.19: Case 2: Gap wave elevation envelopes in spatial domain computed with the present method. Incoming wave frequencies $\omega = 7.7$ rad/s (top) and $\omega = 7.8$ rad/s (bottom). Wave propagates from positive to negative x coordinates. Gap width = 0.10 m

8.2.2 Damping Lid Approach

Numerical methods based on the potential flow theory are known to have a poor performance when dealing with multiple bodies arranged in a side-by-side configuration, tending to provide unrealistically high wave elevations in the gap between the vessels, which lead to poor estimations of forces and motions. In practice, the wave elevations would be limited by viscous effects that are not accounted for by potential flow solvers. In this regard, the application of suppression methods to handle these gap resonant problem becomes an interesting alternative for a better representation of the physical problem.

In addition to the unrealistic values observed when the mathematical problem is solved in

time domain, a very slow numerical convergence for frequencies near the resonant ones is also observed. In these cases, a considerable number of wave cycles is necessary to reach a steady state.

In order to deal with these gap resonant effects, a new development was implemented in the numerical method, in which the free surface boundary conditions (kinematic and dynamic) are reformulated by means of the damping lid technique used in frequency domain by Chen (2005), Fournier, Naciri and Chen (2006), Pauw, Huijsmans and Voogt (2007) and Bunnik, Pauw and Voogt (2009). In this method, a constant damping factor ϵ is included in the free surface boundary conditions ((3.21) and (3.22)), as presented in equations (8.1) and (8.2):

$$\frac{\partial \eta}{\partial t} = \frac{\partial \phi}{\partial z} - \epsilon \eta \quad \text{on } z = 0 \text{ in the gap,} \tag{8.1}$$

$$\frac{\partial \phi}{\partial t} = -\eta g - \epsilon \phi \quad \text{on } z = 0 \text{ in the gap.} \tag{8.2}$$

One should notice that the undamped free surface elevation is recovered by setting the damping factor ϵ equal to zero. As will be heuristically demonstrated later, the imposition of the damping parameter attenuates the numerical convergence problems, stabilizing the solutions much faster. Another characteristic of the method is that the damping parameter influences the results only in the resonant frequency range. Moreover, one of the main advantages of this method is that it does not require the use of additional degrees of freedom in the model, as the technique applied by Newman (2003). Instead, only one value of damping factor is included in the free surface boundary conditions.

On the other hand, it is important to mention that the ϵ value is, for the moment, not defined rationally, but it is merely "tuned" with the experimental data considering that the coefficient depends neither on the wave amplitude or frequency. Thus, for comparison purposes only three different damping factors have been used $\epsilon = (0.0, 0.0625, 0.125)$ 1/s. Despite the simplicity of this technique, it will be shown that reasonable results can be obtained in terms of wave elevations and body motions in most of the cases.

First, a sensitivity analysis concerning the behavior of the time series of motions and wave elevations with respect to the varying damping factor ϵ is presented. Considering as an example the results of Case 1, Figures 8.20 and 8.21 display the time histories for heave and pitch motions considering waves with frequencies 8.3 and 8.5 rad/s, which correspond to the gap resonant frequencies for heave and pitch motions, respectively. The results show that the imposition of a damping factor on the gap is effective in reducing

the amplitudes of heave and pitch motions at their respective resonant frequencies. Notice that, for the wave frequency of 8.3 rad/s (heave resonance frequency), the amplitudes of the pitch motions are not affected by the variation of ϵ values, while the opposite occurs for the heave motion when the wave frequency of 8.5 rad/s (pitch resonance frequency) is considered.

The time series of wave elevations at points P2, P3 and P4 are presented in Figures 8.22 and 8.23 for the wave frequencies 8.3 and 8.5 rad/s, respectively. As for the geosim motions, the use of the damping lid technique reduces the wave amplitudes in the gap, which is a good indication that the method may be used in order to emulate the wave behavior observed in the experiments more closely.

One should also realize that the inclusion of the damping factor in the formulation clearly favors the convergence of the time series (Figures 8.22 and 8.23). It is possible to observe that the time series obtained with non-zero ϵ values reached a steady state much faster than the cases with zero ϵ. In fact, with zero ϵ more than 150 wave cycles in the simulation were necessary to stabilize the motions and wave elevations. This behavior is analogous for the motions and wave elevations obtained in Case 2.

The associated envelopes of wave elevation in the gap for Case 1 are presented in Figures 8.24(a) and 8.24(b). In these figures, the experimental amplitudes of the three monitored points in the gap are also included for comparison purposes. It can be noticed that the damping lid technique implemented in this work greatly improved the results, presenting a much better agreement between the computed wave elevations and the experimental data, especially for the damping factor value of $\epsilon = 0.125$ 1/s, which provided the best fit with the measured data.

Figures 8.25(a) and 8.25(b) present the wave elevation envelopes for Case 2, considering the resonant frequencies $\omega = 7.7$ and $\omega = 7.8$ rad/s. Once more, the damping technique provides a considerable improvement to the wave profile patterns in the gap, reproducing the test data reasonably well. In this case, the damping factor $\epsilon = 0.0625$ 1/s presented a slightly better performance in relation to $\epsilon = 0.125$ 1/s.

The influence of the damping factors on the motions RAOs is presented in Figures 8.26 and 8.27 for Cases 1 and 2, respectively. In general, the damping factor decreases the resonant values in the frequency range of interest, eliminating the spurious characteristic of the curves. Nevertheless, in both cases, the numerical results of heave motion present different trends when compared to the experimental data. Regarding the pitch motions, the inclusion of the damping coefficient improves the matching with the test data, recovering the trends of the RAOs.

For the wave elevations RAOs in the gap, the use of the damping factor also improved the predicted wave amplitudes in comparison to the measured data, eliminating most of the irregular oscillations observed for $\epsilon = 0.0$ 1/s. For probes P2 and P4, the application of the method enabled to recover the wave amplitudes inside the gap reasonably well. Concerning P3, a larger discrepancy between the results is observed, since the experimental data presented higher elevations in comparison to the numerical predictions even without the inclusion of a damping factor. It is also noticeable that all the numerical results tend to the same asymptotic value when the waves are outside of the resonant frequency range.

One should notice, however, that although the damping lid method applied does not intend to capture the physics of the flow in the gap, the use of this simplified technique, which incorporates damping factors independent on the wave amplitudes and frequencies, has provided reasonable numerical results with a fair agreement with the experimental data for most of the cases. Overall, in terms of the motions and wave elevations, the value of damping of $\epsilon = 0.125$ 1/s has provided the best agreement with the test results in general.

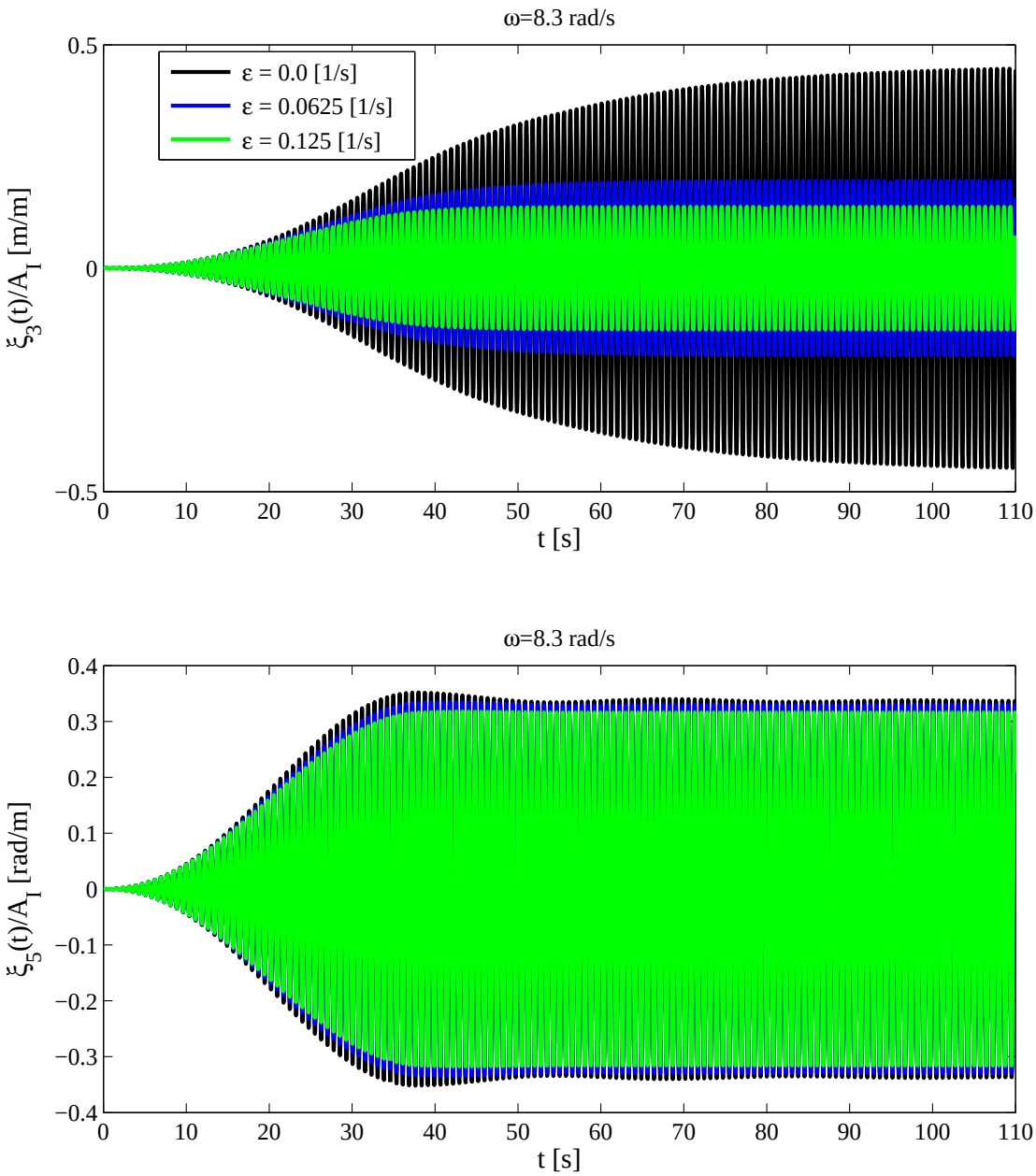

Figure 8.20: Case 1: Numerical heave (top) and pitch (bottom) motions time series for different values of damping factor ϵ. Incoming wave frequency $\omega = 8.3$ rad/s. Gap width=0.05 m

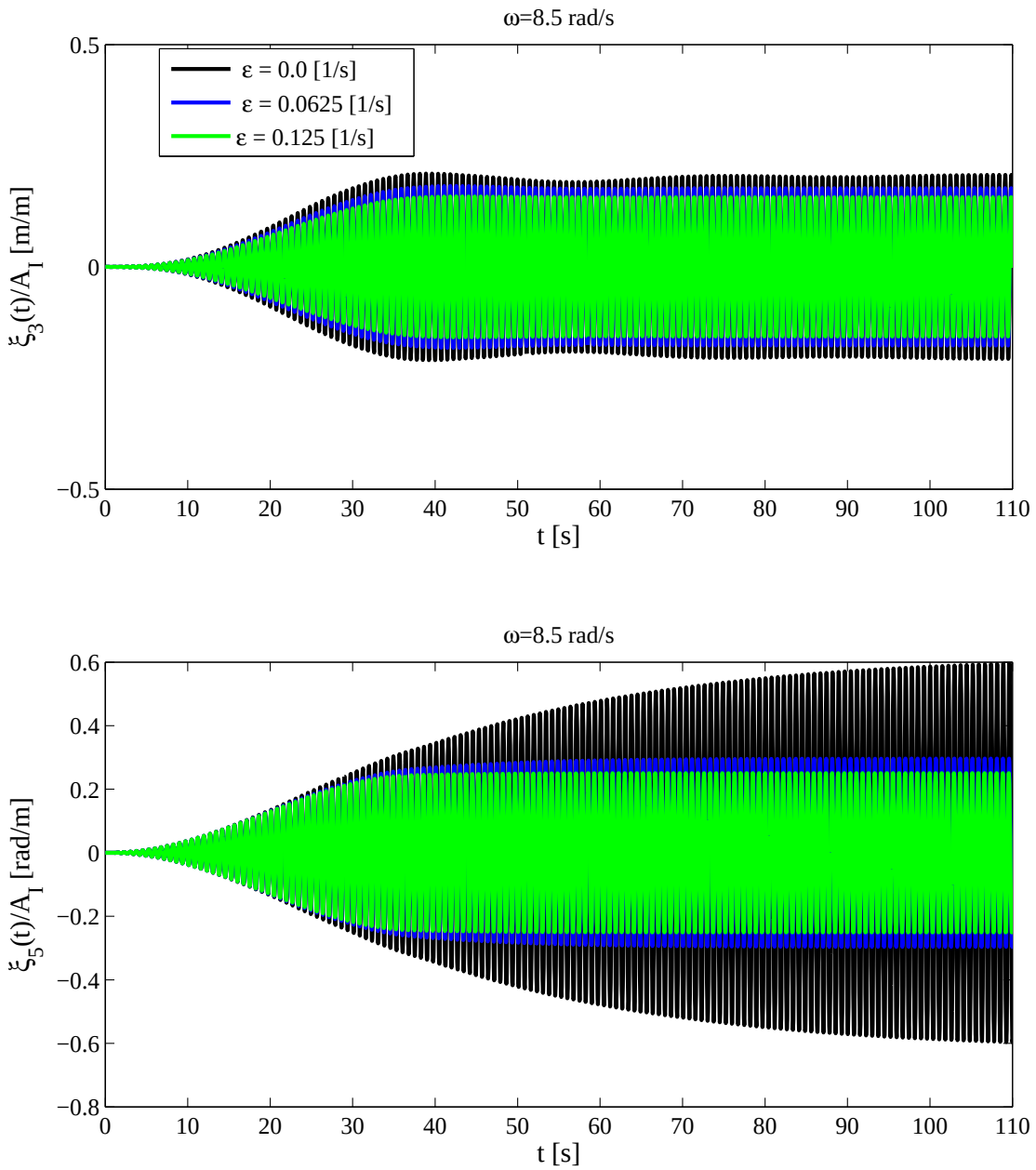

Figure 8.21: Case 1: Numerical heave (top) and pitch (bottom) motions time series for different values of damping factor ϵ. Incoming wave frequency $\omega = 8.5$ rad/s. Gap width=0.05 m

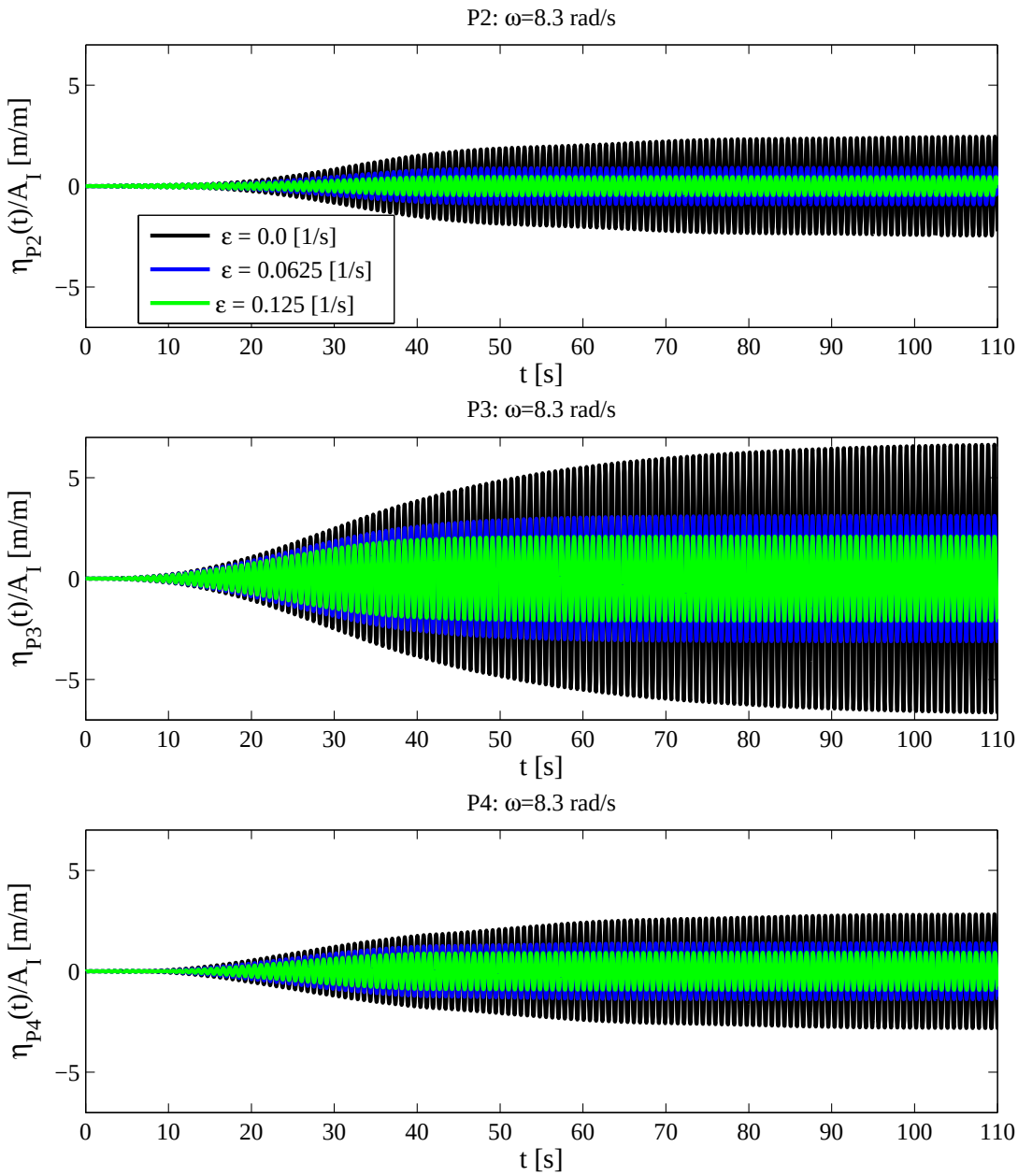

Figure 8.22: Case 1: Numerical wave elevation time series at P2 (top), P3 (middle) and P4 (bottom) for different values of damping factors ϵ. Incoming wave frequency $\omega = 8.3$ rad/s. Gap width = 0.05 m

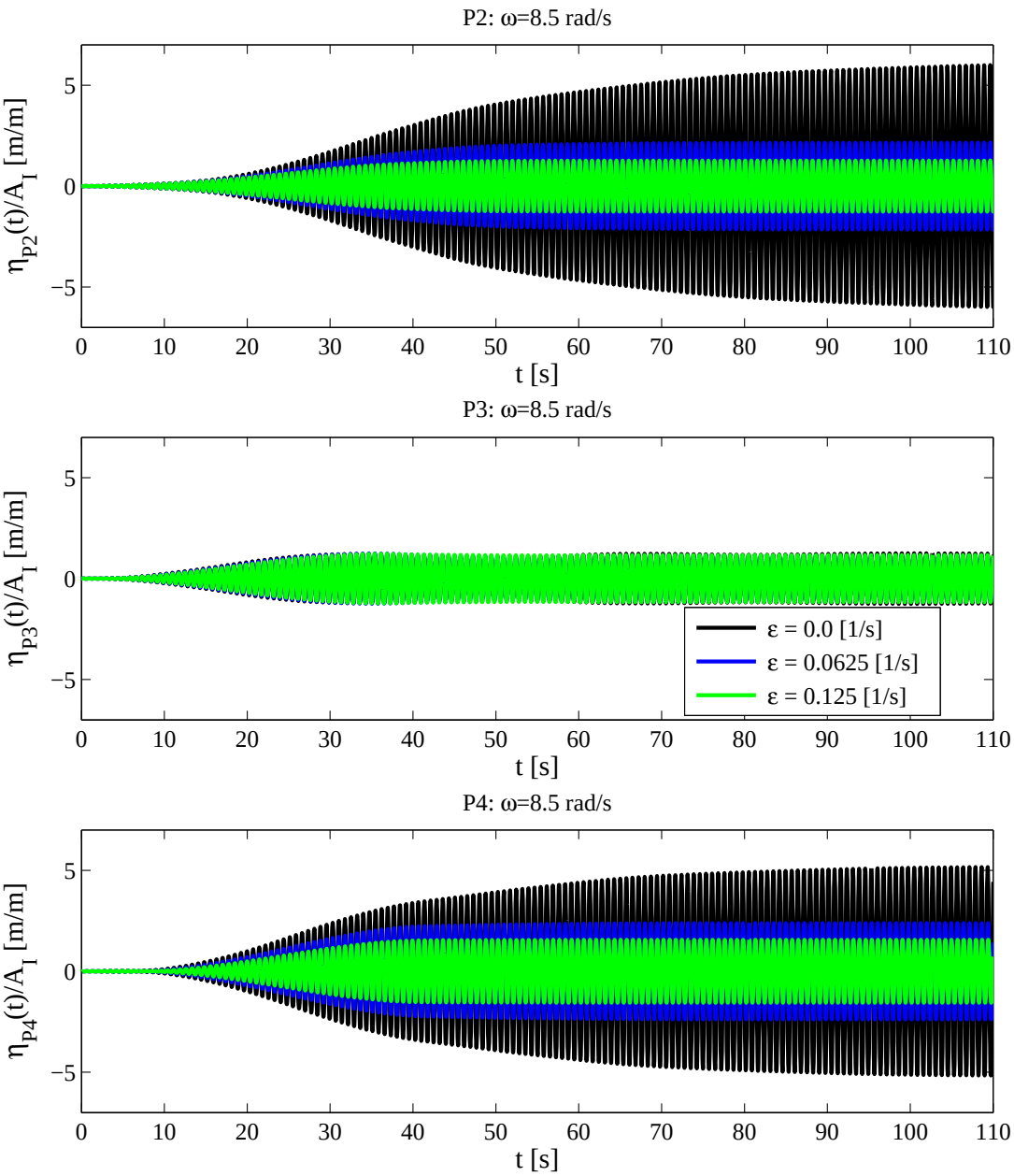

Figure 8.23: Case 1: Numerical wave elevation time series at P2 (top), P3 (middle) and P4 (bottom) for different values of damping factors ϵ. Incoming wave frequency $\omega = 8.5$ rad/s. Gap width = 0.05 m

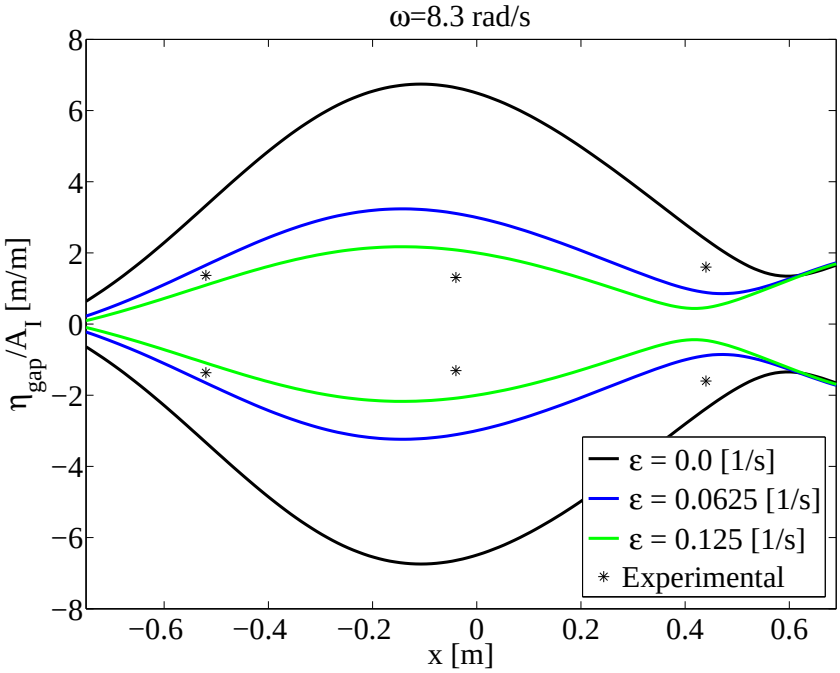

(a)

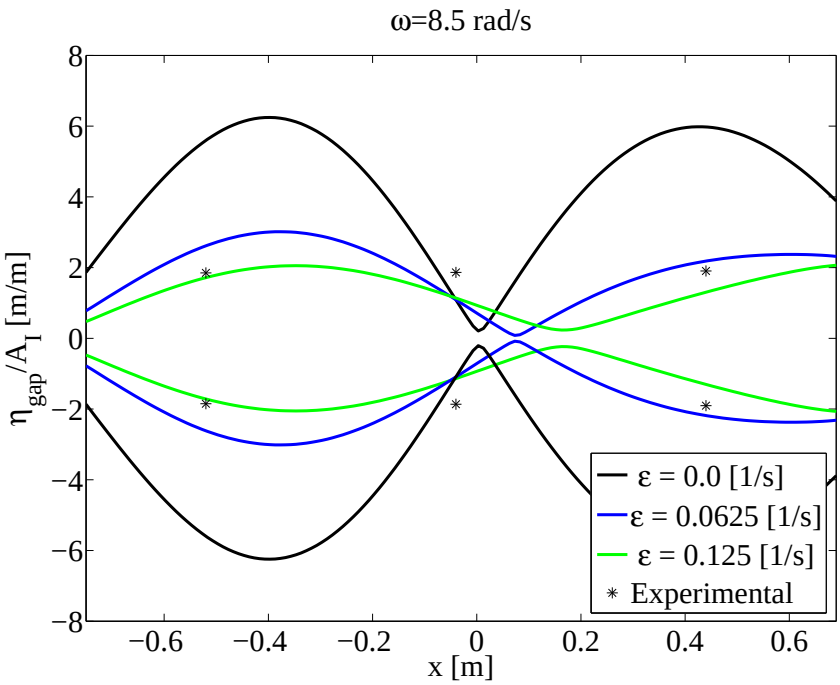

(b)

Figure 8.24: Case 1: Comparison between numerical and experimental data of the gap wave elevation envelopes in spatial domain for different values of damping factors ϵ. (a) Incoming wave frequency $\omega = 8.3$ rad/s. (b) Incoming wave frequency $\omega = 8.5$ rad/s. Wave propagates from positive to negative x coordinates. Gap width = 0.05 m

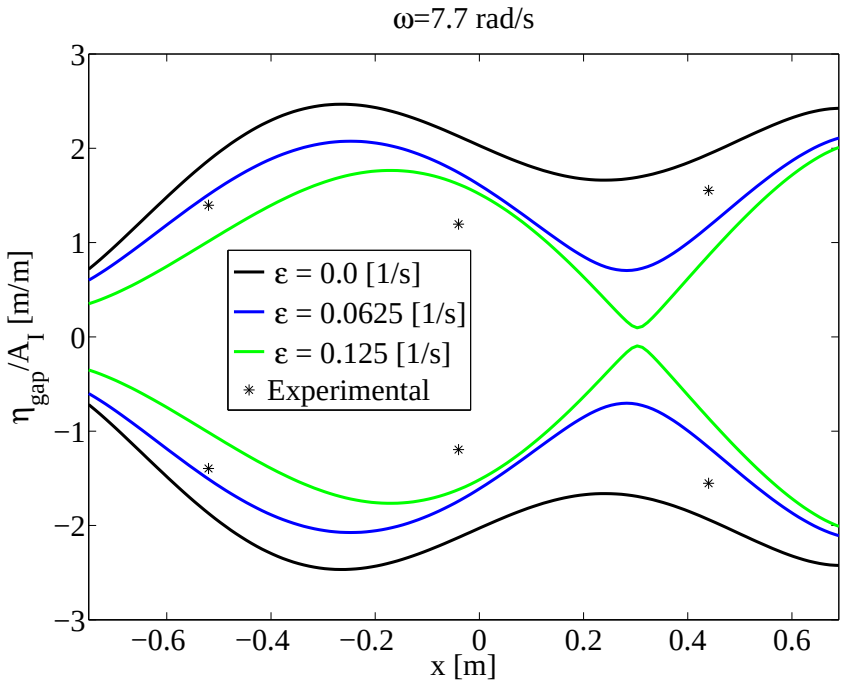

(a)

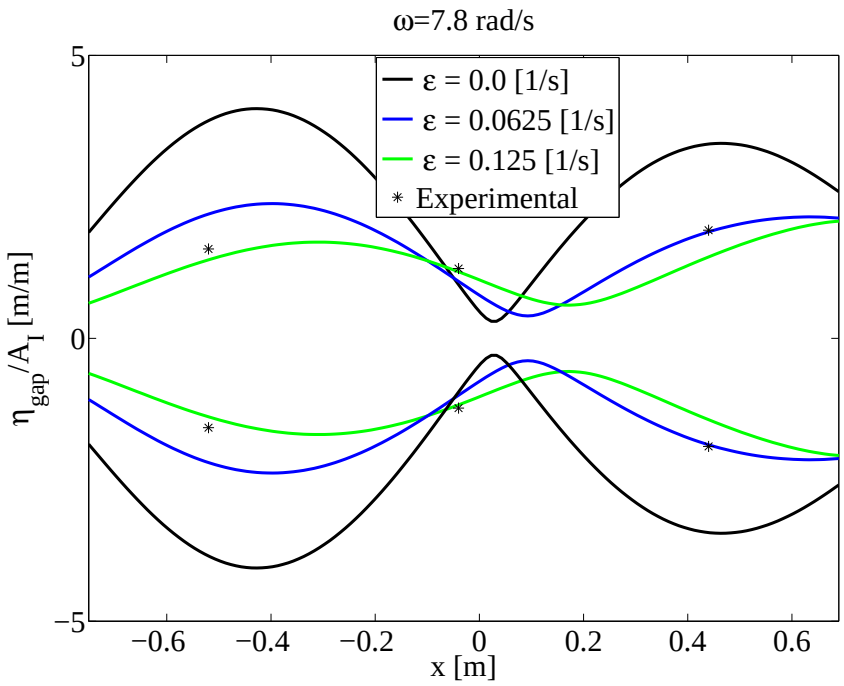

(b)

Figure 8.25: Case 1: Comparison between numerical and experimental data of the gap wave elevation envelopes in spatial domain for different values of damping factors ϵ. (a) Incoming wave frequency $\omega = 7.7$ rad/s. (b) Incoming wave frequency $\omega = 7.8$ rad/s. Wave propagates from positive to negative x coordinates. Gap width = 0.10 m

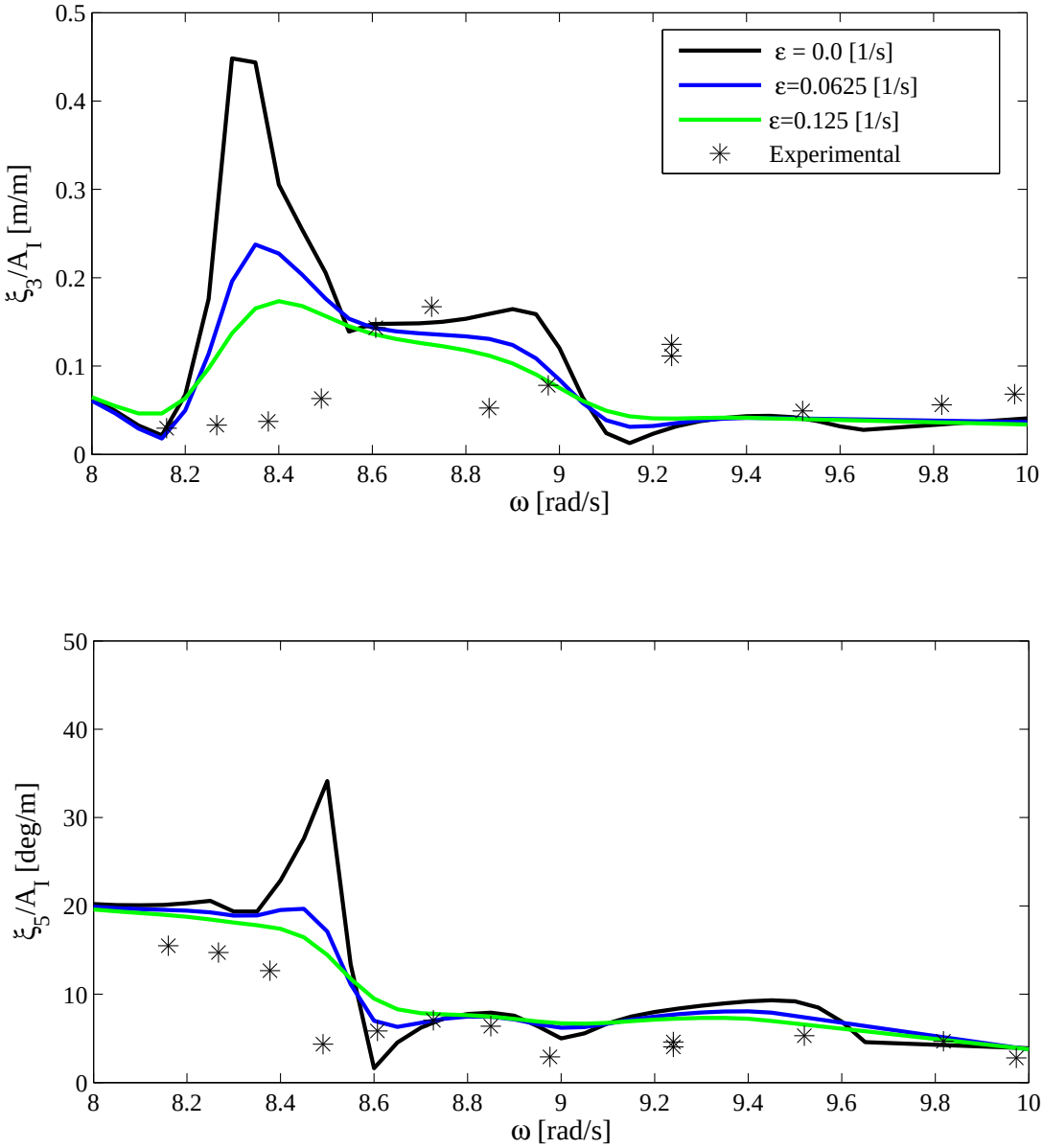

Figure 8.26: Case 1: Numerical and experimental comparisons in terms of heave (top) and pitch (bottom) motions RAOs for different values of damping factors ϵ. Gap width = 0.05 m

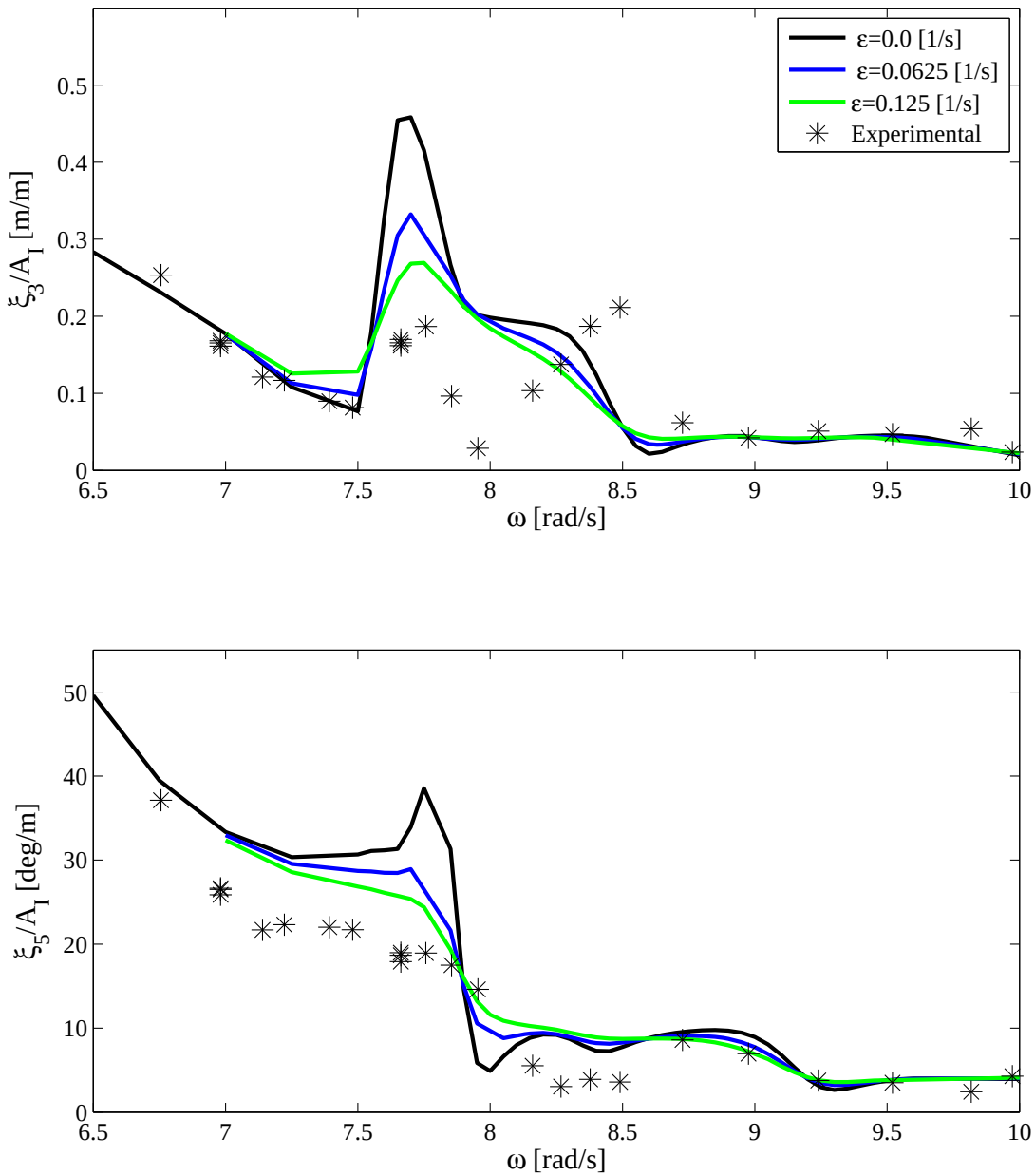

Figure 8.27: Case 2: Numerical and experimental comparisons in terms of heave (top) and pitch (bottom) motions RAOs for different values of damping factors ϵ. Gap width = 0.10 m

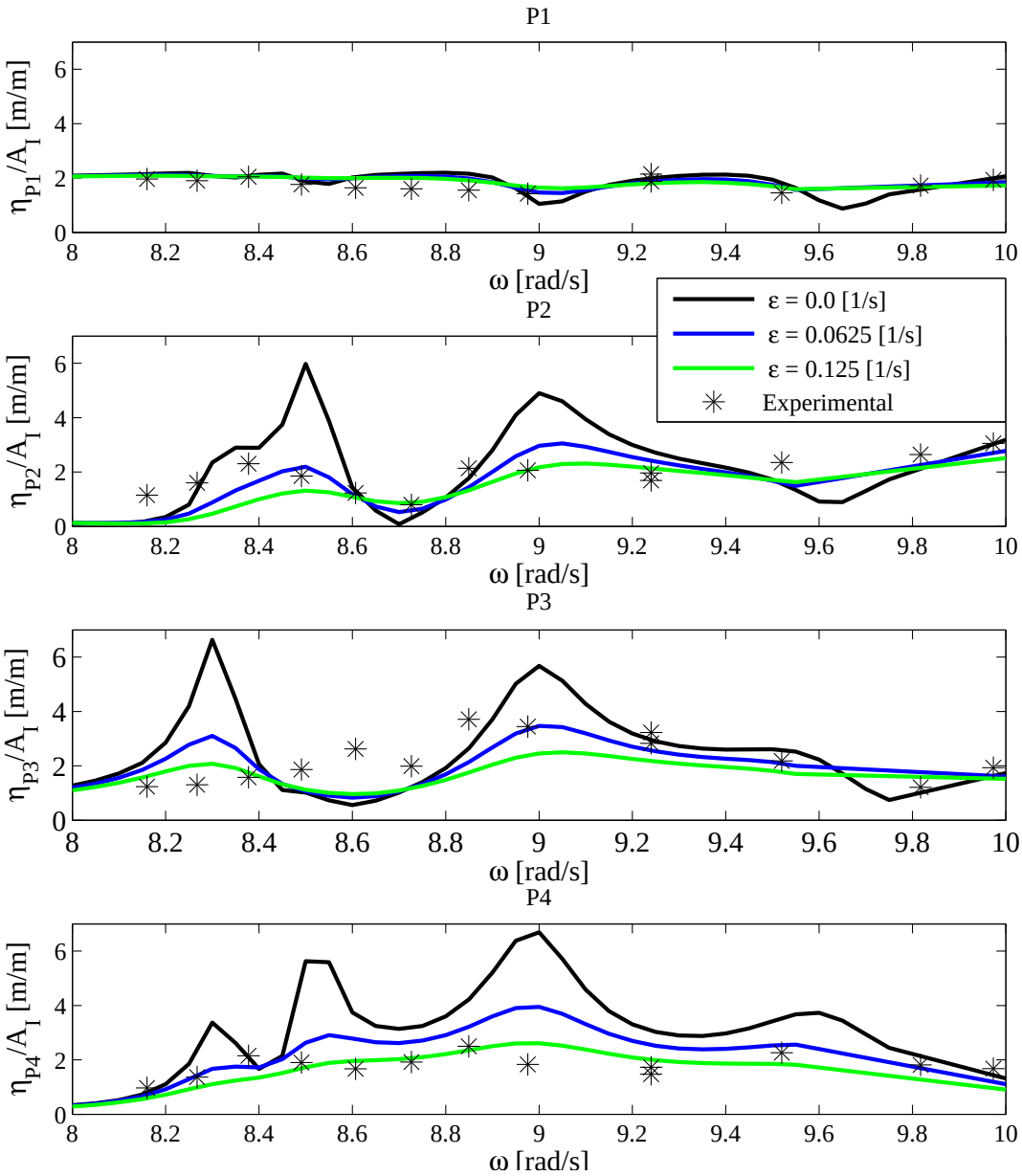

Figure 8.28: Case 1: Numerical and experimental comparisons of wave elevations in the gap for different values of damping factors ϵ. Gap width = 0.05 m

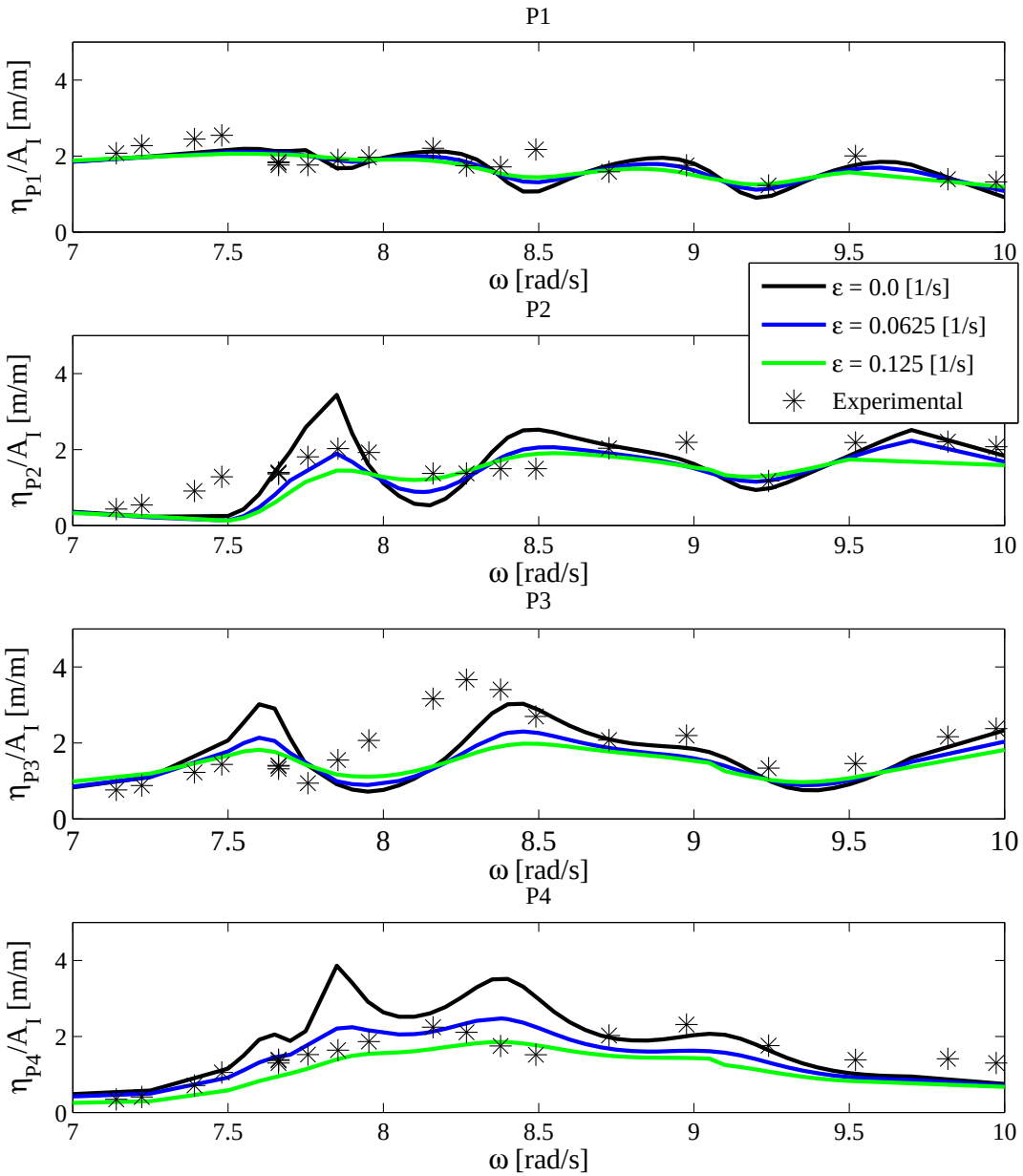

Figure 8.29: Case 2: Numerical and experimental comparisons of wave elevations in the gap for different values of damping factors ϵ. Gap width = 0.10 m

Chapter 9

Multi-Body Simulations with Large Relative Displacements

The seakeeping analysis of offshore systems is commonly assessed by the use of dynamic time domain simulators, which consider not only the loads induced by the waves, but also those originated by wind, current and from the dynamics of risers and mooring lines. Almost all of these simulators evaluate the wave forces by using potential hydrodynamic coefficients previously calculated in frequency domain, which are then post-processed and transformed to time domain by writing the equation of the floating body in terms of convolutions of its motions with the so-called impulsive response functions. This equation is often referred to as the Cummins's equations (CUMMINS, 1962):

$$(\mathbf{M} + \mathbf{A}(\omega_\infty)) \frac{\partial^2 \vec{\xi}(t)}{\partial t^2} + \int_0^\infty \mathbf{R}(\tau) \frac{\partial \vec{\xi}(t)}{\partial t}(t-\tau)\mathrm{d}\tau + \mathbf{K}\vec{\xi}(t) = \begin{pmatrix} \vec{F}(t) \\ \vec{M}(t) \end{pmatrix} \tag{9.1}$$

where $\mathbf{M}$ is the matrix of mass/inertia, $\mathbf{A}(\omega_\infty)$ is the matrix of added mass/inertia coefficients in infinite frequency, $\vec{\xi}(t)$ is the translational/rotational displacement vector, $\mathbf{K}$ is the matrix of restoring coefficients, $\vec{F}(t)$ and $\vec{M}(t)$ are vectors containing the forces and moments from external loads, and $\mathbf{R}(\tau)$ is a matrix with the retardation functions or "memory functions", which is calculated in terms of the radiation damping coefficients $\mathbf{B}(\omega)$ from a cosine Fourier transform, as follows:

$$\mathbf{R}(\tau) = \frac{2}{\pi} \int_0^\infty \mathbf{B}(\omega) \cos(\omega\tau)\mathrm{d}\omega \tag{9.2}$$

In this approach, the frequency domain code is previously executed considering several

wave incidence angles and frequencies, which are used for the construction of a database containing exciting forces, added mass, potential damping and force drift coefficients. Therefore, in order to account for changes in the heading of the floating system in relation to the incoming wave angle, the simulator simply performs a search on the database, updating the exciting and drift forces. An example of a simulator that applies this methodology is the Numerical Offshore Tank (TPN), a code that has been developed at the University of Sao Paulo since 2001, in cooperation with the oil state company Petrobras (see for instance Nishimoto et al. (2003)). In this case, the software WAMIT is used for the hydrodynamic coefficients calculations.

However, in the context of simulations considering the analysis of multi-body systems this approach cannot be extended in a straightforward manner, since the relative positions of the floating bodies may change during the simulations, thus modifying the wave field surrounding them and also the mutual effects caused by each one of the bodies. As frequency domain codes consider only fixed meshes, the aforementioned database had also to consider the changes of the relative positions between the bodies, so as to make the updating of the hydrodynamic coefficients possible during the simulations. Examples of practical operations in which this kind of problem may be observed are: tandem offloading operations in which the direction of wind, waves or current is suddenly changing, or the shuttle is moving due to fishtailing; floatover operations when a barge with topsides is docking between the columns of a semisubmersible unit; and the berthing manoeuver of a LNG carrier towards an offshore LNG terminal, supported by tugboats (BUNNIK, 2014).

Tannuri et al. (2004) developed a numerical scheme that tries to deal with this problem by coupling the frequency domain code WAMIT and the time domain simulator TPN. This version of the code was developed for the analysis of tandem type offloading operations involving a shuttle tanker and an FPSO. The procedure involved monitoring the relative positions of the bodies during the simulations and, when a significant change was detected, the calculations were interrupted and the software WAMIT was executed once again for updating the hydrodynamic coefficients. Analysis of the relevance of such update was done by comparing the mean offsets and the first order motions of the shuttle tanker arising from the simulation using the original procedure, which does not consider the update of relative positions, and the ones computed with the new methodology, which incorporates the WAMIT code in the simulation loop. The authors identified significant differences in the results obtained with the two different approaches, emphasizing the importance of such consideration.

Still with respect to this development in the TPN code, Queiroz Filho and Tannuri (2009) investigated the wave shielding effect induced by the FPSO in the shuttle tanker by analyzing the wave forces experienced by the latter and the consequences in terms of the

power demanded by a dynamic positioning (DP) system designed to perform a station-keeping task. Again, the importance of incorporating the hydrodynamic update was demonstrated, showing that errors up to 27% in the DP power were found if the shadow effects and changes of the relative position were not considered.

More recently, Bunnik (2014) presented results concerning a berthing operation in which an LNG carrier was pushed towards an LNG FPSO in sea waves of different incidence angles. In his work, an approach similar to the one presented by Tannuri et al. (2004) was applied. The results showed that, depending on the wave direction, the effects of the changes in hydrodynamic interaction can be significant, resulting in a considerable change in the time needed to complete the berthing. The author also states that, although the results are apparently logical and realistic, a validation procedure is still required to quantify the accuracy of the developed model.

Although these works present a promising approximation for such a complex problem, some aspects of this approach are still questionable. For example, due to the large computational effort necessary to perform the updating of the hydrodynamic coefficients with a small interval, the numerical scheme needs to consider an arbitrary criterion established in terms of the variation of the relative positions between the bodies. This criterion then determines whether the simulator is interrupted and the coefficients are updated or not. In addition, this procedure may introduce spurious and impulsive hydrodynamic forces as a result of the discrete aspect of the method and, thus, still requires further investigations. Another observation refers to the fact that a frequency domain analysis represents a multi-body system which oscillates steadily at one particular frequency around the mean linearized position. In this sense, as also emphasized by Bunnik (2014), it is quite inconsistent to use the results in a simulation where the relative motions between the bodies are indeed changing. As a consequence, the effects of the flow memory are not treated in a consistent manner, since the retardation functions are convoluted with velocities that are related to a different relative position that occurred in the past.

Aiming at partially overcoming these problems and provide a first step towards the complete solution of such a complex analysis, we propose in this chapter a new development that accounts for large relative displacements between two floating bodies under the action of incoming sea waves by solving the boundary value problems together with a re-meshing scheme that defines new free surface panel meshes as the bodies displace from their original positions. Moreover, an interpolation algorithm used to determine the wave elevation and the velocity potential distribution on the new free surface points is also included. The loop structure of the method is presented in Figure 9.1.

Obviously, the method does only consider linear wave effects, therefore neglecting the

loads induced by wind, current or drift forces. In fact, it is known that in practice these are the forces that may give rise to large horizontal relative displacements between the bodies, but the calculation of these quantities would require other numerical developments that are beyond the main objective of this thesis.

Therefore, in a first assessment, we consider that a large relative displacement occurs somehow and offsets one of the bodies from its initial mean position to another one. In such way, the trajectory of the body is chosen arbitrarily and prior to the beginning of the time domain calculations, being input into the model as a prescribed motion. In addition, we consider that the large body horizontal displacement is slow and, therefore, do not generate waves themselves. As a consequence, we may treat the problem as a quasi-static problem regarding the low frequency displacement.

Upon the considerations aforementioned, we maintain the linear characteristic of our code and so the theoretical basis established in section 3.3 of this text. In this sense, the following sections present the developments carried out for the new method, giving emphasis to the algorithm that performs the re-meshing of the free surface grid and the interpolation schemes used for the determination of the quantities at the new points of the surface after a new mesh is generated.

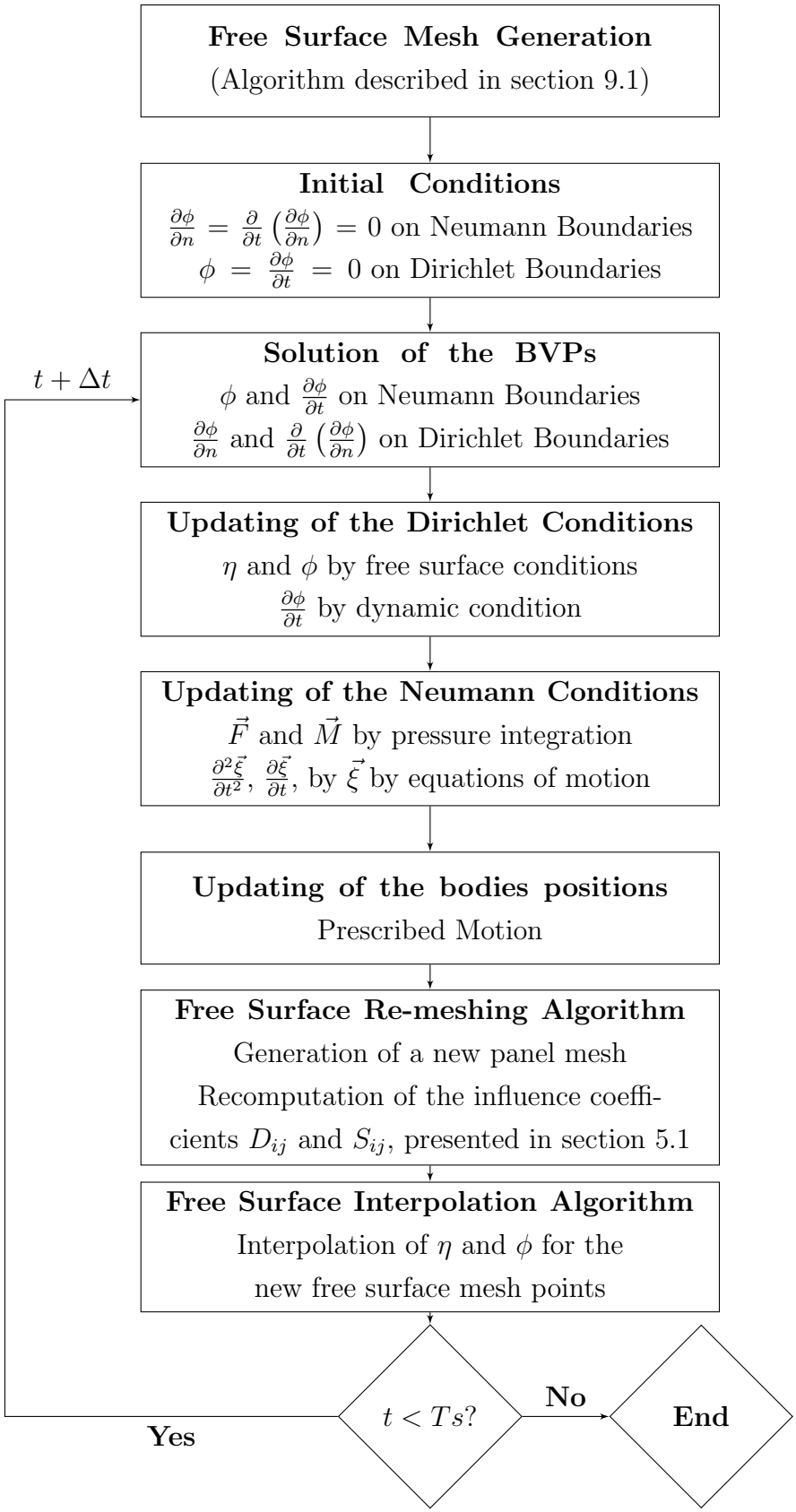

Figure 9.1: Structure of the numerical method including the re-meshing and interpolation algorithms in the time loop

9.1 The free surface re-meshing algorithm

The re-meshing algorithm developed in this work is merely an adaptation of the 2D mesh generator elaborated by Persson (2005), entitled in his work as "A Simple Mesh Generator in MATLAB", for its inclusion in the time domain loop of the boundary elements method presented in this thesis. This method was chosen by its simplicity for being implemented and integrated in our code, as it is explained in a few lines, going in the opposite way of the standard complex meshing softwares that are nearly inaccessible and unfeasible to be coupled in other tools.

The mesh generator algorithm and how it is implemented computationally is fully described in Persson (2005). In this context, and for the sake of completeness, we reproduce here only the theoretical basis necessary for the comprehension of the method.

A simple mechanical analogy between a planar triangular mesh and a 2D truss structure forms the basis of this mesh generator. Accordingly, the triangles edges correspond to bars and the vertexes correspond to joints of the truss, in such a way that each bar has a force-displacement relationship $f(l, l_o)$, which depends on its current l and desired l_0 lengths. From a pre-determined surface defined by the user, there is an external reaction normal force acting at each boundary node, whose magnitude is just large enough to restrain the nodes to move outside this boundary. Therefore, the principal unknowns, which are the x and y coordinates of the joints, are found by solving for a static equilibrium in the structure.

The N_{mp} mesh points may be arranged into a $N_{mp} \times 2$ array p, containing their correspondent x and y coordinates:

$$p = \left[\begin{array}{cc} x & y \end{array} \right]_{N_{mp} \times 2} \tag{9.3}$$

The force vector $F(p)$ acting at each mesh point is decomposed in horizonal and vertical components, containing also the internal forces F_{int} from the bars and the external reaction forces from the boundaries F_{ext}, as follows:

$$F(p) = \left[\begin{array}{cc} F_{int,x}(p) & F_{int,y}(p) \end{array} \right]_{N_{mp} \times 2} + \left[\begin{array}{cc} F_{ext,x}(p) & F_{ext,y}(p) \end{array} \right]_{N_{mp} \times 2} \tag{9.4}$$

As mentioned by Persson (2005), $F(p)$ depends on the current positions of the bars connecting the joints, which by its turn is adjusted by Delaunay triangulation of the mesh points, deciding the edges. Therefore, the force vector $F(p)$ is not a continuous function of p, since the truss topology is changed by the Delaunay triangulation as the points move.

This imposes a complicated problem for solving for a static equilibrium in the structure, represented by the system $F(p) = 0$.

In order to overcome this problem, an artificial time dependence is introduced to the problem, transforming it in a system of Ordinary Differential Equations (ODEs) with non-physical units, in which if a stationary solution is found (within a established criteria), we assume that the system $F(p) = 0$ is satisfied.

$$\frac{\mathrm{d}p}{\mathrm{d}t} = F(p) \quad t \geq 0 \tag{9.5}$$

The system of ODEs is approximated by a simple forward Euler method that in a discretized and artificial time $t_n = n\Delta t$ approximates the current solution $p_n \approx p(t_n)$ by

$$p_{n+1} = p_n + \Delta t F(p_n) \tag{9.6}$$

In this way, when evaluating the force function, the positions p_n are known and also the structure topology of the current step. Furthermore, the external reaction forces enter in the problem by moving back, to the closest boundary point, all the points that went outside the surface boundaries during the update p_n to p_{n+1}.

In these developments, the force function assumes the form $f(l, l_0) = k(l_0 - l)$, considering that only repulsive forces (this ensures that the points spread out across the whole surface) are allowed:

$$f(l, l_0) = \begin{cases} k(l_0 - l) & \text{if } l < l_0 \\ 0 & \text{if } l \geq l_0 \end{cases} \tag{9.7}$$

in which k is included to provide correct units and set to $k = 1$.

The simplified loop structure of the mesh generator is described in the following items:

1. Creation of a uniform distribution of mesh points within a bounding box that covers a pre-specified surface;
2. Removal of all points outside the desired geometry surface;
3. Determination of the truss topology by a Delaunay triangulation and calculation of the structure bars lengths l;
4. Calculation of the force magnitude at the joints of each structure bars by using equation (9.4);

5. Calculation of the force components at the joints of each structure bars;
6. Calculation of $F(p)$ by summing the force vector components from all bars meeting at a node.
7. Updating of the node positions p by using equation (9.6);
8. If a point ends up outside the surface after the update of p, it is moved back to the closest point on the boundary.
9. The last positions p_{n+1} are compared with the previous ones p_n and if non "large movements" are detected (specified criteria) the algorithms is stopped, otherwise the algorithm is restarted in item 3, continuing until the criteria is satisfied.

We exemplify the algorithm by applying it in the generation of a circular mesh of radius $R = 3$ m with a circular aperture of radius $R = 1$ m inside. This surface is equivalent to the free surface meshes presented in chapter 6, but with a smaller diameter. Figures 9.2(a), 9.2(b) and 9.2(c) illustrate the first three steps of the algorithm, whereas Figure 9.2(d) presents the final mesh, it means, when the system $F(p) = 0$ is satisfied.

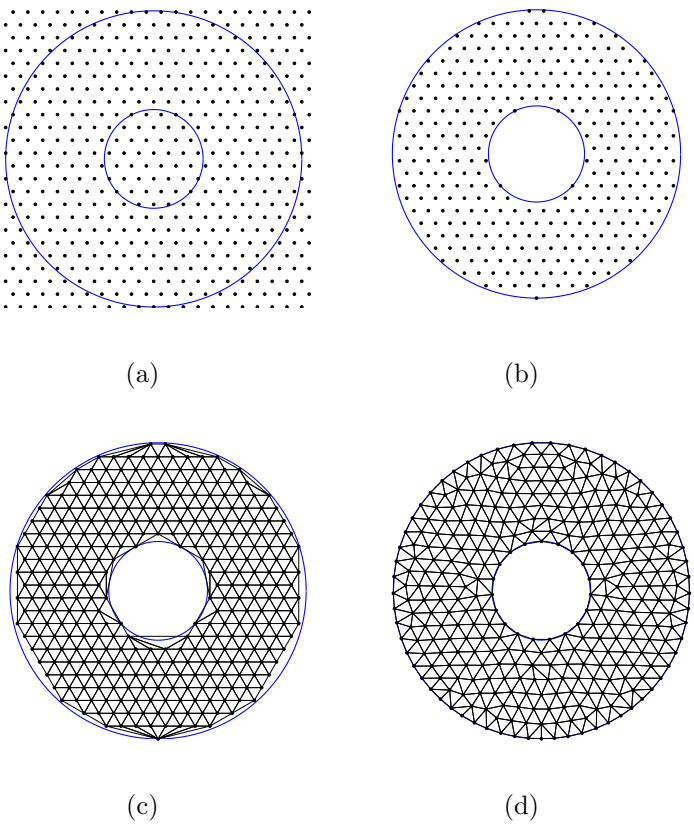

Figure 9.2: Steps of the mesh generation algorithm applied to a circular surface with radius $R = 3$ m with a circular of radius $R = 1$ m inside. Figures (a), (b) and (c) refer to the first three steps of the algorithm loop structure. Figure (d) illustrates the final mesh

We now present, in Figure 9.3, four circular meshes of radius $R = 5$ m with two circular apertures of radius $R = 1$ m in different relative distances, illustrating the algorithm capability to deal with the generation of free surface meshes that may be applied in hydrodynamic problems involving two bodies. These meshes represent four instants of a simulation involving two circular cylinders, in which the trajectory of one of them was prescribed to perform a large horizontal displacement. It is worth mentioning that these meshes are not restricted to cases considering only bodies with circular sections, since ship-shaped vessels, for example, could be surrounded by circular meshes that fit right into the circular apertures.

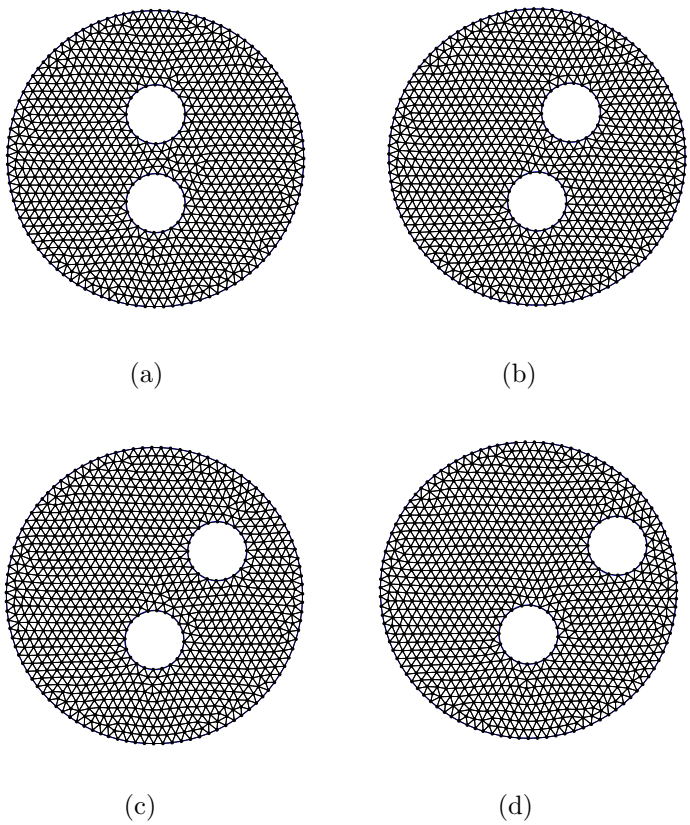

Figure 9.3: Four circular meshes of radius $R = 5$ m with two circular apertures of radius $R = 1$ m in different relative distances

9.2 The free surface interpolation algorithm

A simulation involving relative large displacements between two or more bodies requires the re-generation of the free surface mesh at each time-step. As could be observed in the latter section, as the free surface is re-meshed, new collocation points (centroid of each triangle) are generated, but, unfortunately, neither the free surface elevation nor the

velocity potential are known at these new points, and the simulation cannot continue.

In order to overcome this problem, it becomes necessary to apply an interpolation scheme to link the mesh generator with the flow solver, so as to allow the simulation to be restarted from a previous free surface state. More precisely, after generating a new mesh, the interpolation scheme must recover, as accurately as possible, the previous solution field defined on an old mesh to proceed with the computation.

The choice of the interpolation scheme must be done carefully, since an inadequate selection may be a source of error that, in time-dependent problems, accumulate throughout the simulations. Therefore, linear interpolation methods are normally avoided, in favor of higher order schemes. With this in mind, we have implemented an interpolation scheme that couples a second order polynomial with a weighted moving least-squares method. This method is similar to the one applied by Wang (2005).

In this scheme, the shape of the free surface elevation and the velocity potential distribution is represented by the second order polynomials presented in equations (9.8)

$$\eta = F_\eta(x, y) = a_1 + a_2 x + a_3 y + a_4 x^2 + a_5 xy + a_6 y^2 \tag{9.8a}$$

$$\phi = F_\phi(x, y) = b_1 + b_2 x + b_3 y + b_4 x^2 + b_5 xy + b_6 y^2 \tag{9.8b}$$

in which, fixing to one point in space p_0, the twelve coefficients a_i, b_i, $i = 1, 2, 3..., 6$ of the polynomials are calculated considering only the nearest points within a distance of $2l_0$, where l_0 is the local mesh size. Denote these nearest points as p_k, $k = 1, 2, 3..., N_{np}$, in which N_{np} is the number of points.

Thus, the coefficients are determined by the use of a weighted moving least-squares method with the error function (9.9) given as:

$$\sigma(a_1, a_2, a_3, a_4, a_5, a_6) = \sum_{j=1}^{N_{np}} W_k [F_\eta(x_k, y_k) - \eta_k]^2 \quad N_{np} \geq 6 \tag{9.9a}$$

$$\sigma(b_1, b_2, b_3, b_4, b_5, b_6) = \sum_{j=1}^{N_{np}} W_k [F_\phi(x_k, y_k) - \phi_k]^2 \quad N_{np} \geq 6 \tag{9.9b}$$

in which W_k, see expression (9.10), is the weight function for the nearest points p_k. Notice that the weight function decreases exponentially with the distance between p_k and the point p_0.

$$W_k = e^{-\frac{|p_k - p_0|}{2l_0}} \tag{9.10}$$

In accordance to the least-squares method, let $\partial\sigma/\partial a_j = 0$ and $\partial\sigma/\partial b_j = 0$, obtaining the linear systems of equations (9.11) for a_j and b_j .

$$\sum_{j=1}^{6} A_{\eta_{ij}} a_j = B_{\eta_i} \quad i = 1, 2, 3, ..., 6 \tag{9.11a}$$

$$\sum_{j=1}^{6} A_{\phi_{ij}} b_j = B_{\phi_i} \quad i = 1, 2, 3, ..., 6 \tag{9.11b}$$

in which A_η, A_ϕ, B_η and B_ϕ are defined by the expressions (9.12).

$$A_{\eta_{ij}} = A_{\phi_{ij}} = \sum_{k=1}^{N_{np}} W_k \beta_{kj} \beta_{ki} \tag{9.12a}$$

$$B_{\eta_{ij}} = \sum_{k=1}^{N_{np}} W_k \eta_k \beta_{ki} \tag{9.12b}$$

$$B_{\phi_{ij}} = \sum_{k=1}^{N_{np}} W_k \phi_k \beta_{ki} \tag{9.12c}$$

Finalizing, the coefficients β are calculated by the following expressions:

$$\beta_{k1} = 1 \quad \beta_{k2} = x_k \quad \beta_{k3} = y_k \tag{9.13}$$

$$\beta_{k4} = x_k^2 \quad \beta_{k2} = x_k y_k \quad \beta_{k3} = y_k^2 \tag{9.14}$$

in which $k = 1, 2, 3..., N_{np}$.

The coefficients a and b that result from this interpolation scheme are determined from a mesh, here denoted as current mesh, in which the free surface elevation and the velocity potential distribution are known. Hence, after the positions of the bodies are changed and the re-meshing of the free surface is performed, the polynomials (9.8) are used to determine the desired quantities at the new points of interest.

9.3 Verification of Numerical Computation

Numerical simulations considering two bodies with one of them undergoing large displacements during the time domain calculations are presented in the following sections. The main objective of this study is to evaluate the hydrodynamic interaction between the bodies in a scenario in which the horizontal relative positions of the bodies vary in time. With this approach, the wave shielding effects caused by one of the bodies on the other

is also taken into account and its effects in terms of forces can be quantified.

Once the objectives are established, the study is performed with a set of simulations considering only diffraction effects, it means, the bodies are restrained to oscillate in their six degrees of freedom. In this case, one of the bodies is displaced horizontally from its initial position, performing a slow oscillatory motion with large horizontal amplitude.

However, the verification of the results is not a simple task, since neither numerical nor experimental results considering such scenario could be found in the literature. Moreover, the software WAMIT, which was being used for the verification of the results involving single body simulations, cannot be directly applied for this problem, since it considers only frequency domain calculations that assume, as mentioned before, that the body oscillates an infinite long time around its mean linearised position.

Bearing this in mind, a set of fundamental experimental tests was designed and conducted aiming specifically at verifying the performance of the present numerical method for a multi-body system with bodies undergoing large relative displacements. The tests were carried out at the CH-TPN-USP (main particulars of the basin are described in section 7.2). The main characteristics of the experimental setup are described in the next section.

9.3.1 Experiments

The experimental tests considered a multi-body system comprising two identical aluminium circular cylinders, namely Body 1 and Body 2, which have 0.40 m of diameter, 0.36 m of height and were tested with a draught of 0.20 m. Figures 9.4 and 9.5 present an illustrative sketch and a photograph of the experimental setup, respectively.

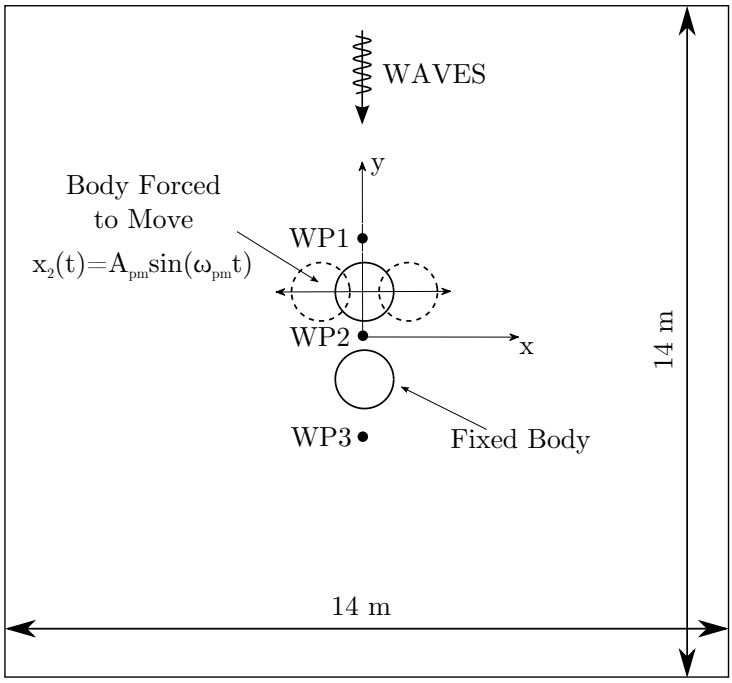

Figure 9.4: Illustrative sketch of the experimental setup

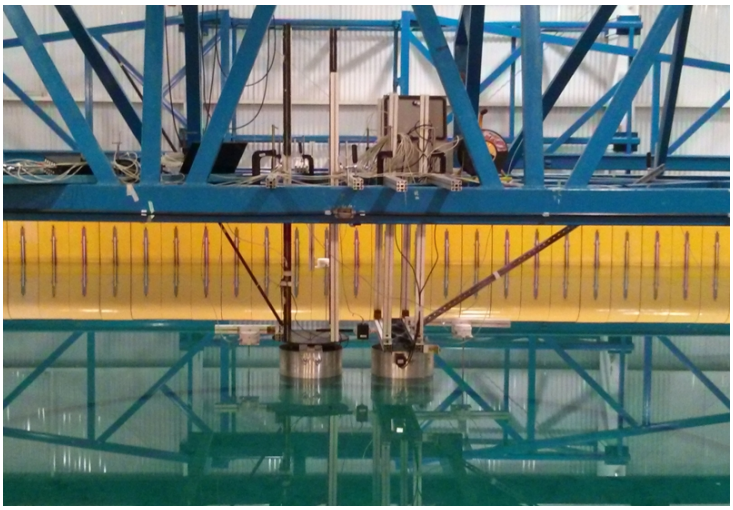

Figure 9.5: Lateral view of the models positioned in the tank

These tests were conceived in a very fundamental configuration with the main goal of providing benchmark data for the present numerical method. Thus, during the tests the Body 1 was kept fixed and connected to a 6 D.O.F load cell (see Figure 9.6), which was used to measure the hydrodynamic forces and moments induced by the waves. In addition, this load cell was properly positioned in the model in order to follow the sign convention of the coordinate system presented in Figure 9.4. The main particulars of the load cell are presented in Table 9.1.

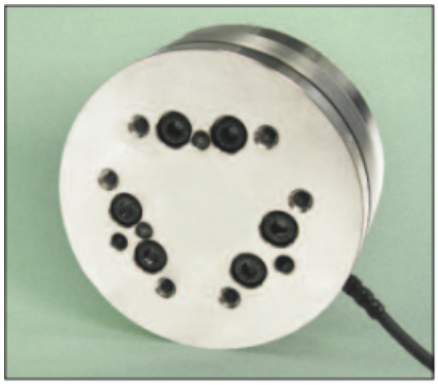

Figure 9.6: ATI MINI85 6 D.O.F Load Cell. Source: ATI Catalog

Table 9.1: Main characteristics of the 6 D.O.F load cell

	Calibration SI-1900-80			
Forces/Moments	F_x, F_y **(N)**	F_z **(N)**	M_x, M_y **(Nm)**	M_z **(Nm)**
Sensing Ranges	1900	3800	80	80
Single-Axis-Overload	13000	27000	500	610

The Body 2 was positioned upstream of Body 1 and was attached to a ball screw shaft driven by a servo motor, this system being used to impose a large prescribed oscillatory motion on the body during the measurements, as illustrated in Figure 9.7. Moreover, this mechanical device was also equipped with a resistive potentiometer, which enabled one to monitor the Body 2 position in a synchronized manner with the forces and moments measured in Body 1. These procedures provided a convenient and controlled multi-body system setup for the sake of the numerical modelling of the problem.

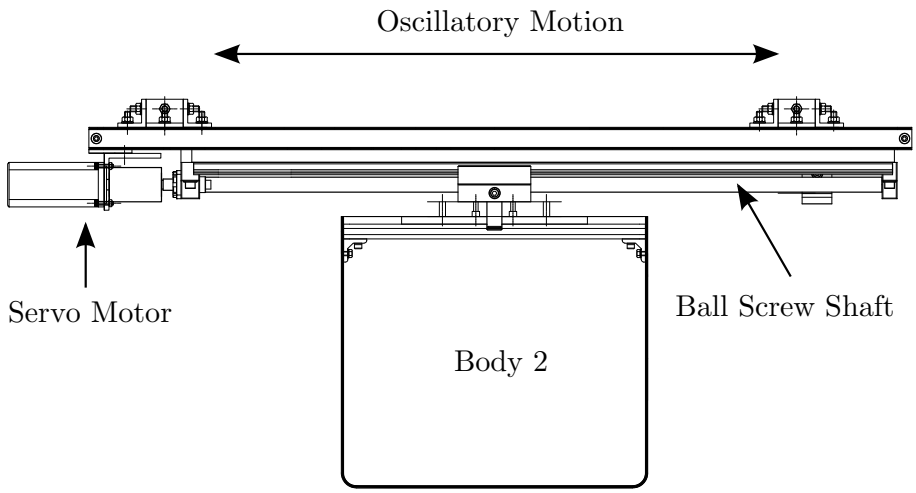

Figure 9.7: Sketch of the mechanical equipment attached to Body 2

Besides the load cell, three wave probes, namely WP1, WP2 and WP3, were used to measure the wave elevations at different locations near the bodies. The WP2 was positioned at the mean position between the bodies and WP1 and WP3 were located upstream and downstream, respectively. The relative distances between the wave probes are presented in Figure 9.8.

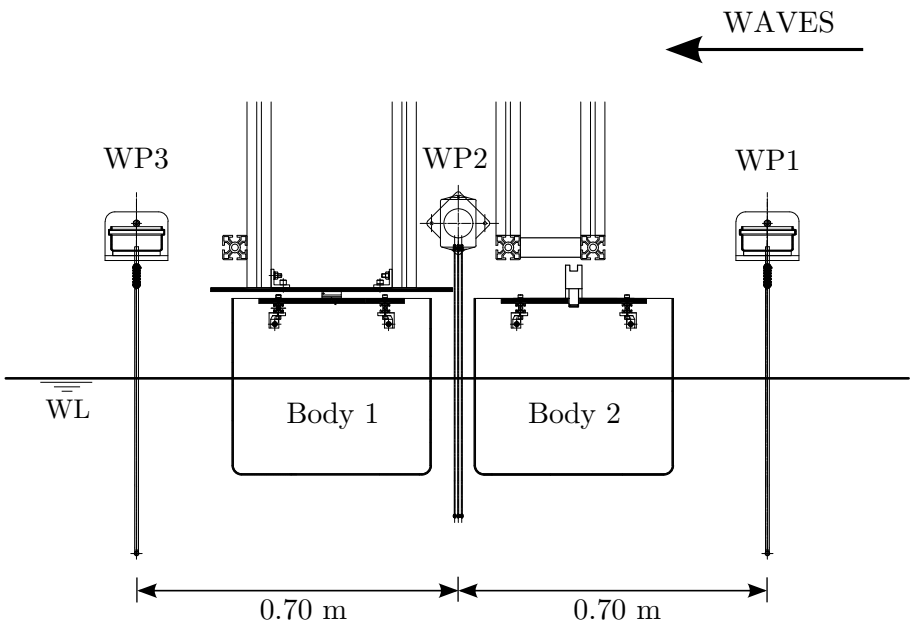

Figure 9.8: Front view sketch of the models and wave probes arrangement

Special care had to be taken into account for the definition of the wave frequencies to be considered in this test. One must keep in mind the difficulties associated with measuring interaction forces induced by waves diffracted from the bodies, which are commonly much lower than those caused by the incident wave itself. Thus, small interferences from reflected waves coming from the tank walls may disturb the results, demanding a good performance of the flaps active control system on absorbing the waves. As presented in Mello et al. (2010), the CH-TPN-USP has a better performance when absorbing waves in the range of frequencies between 3.14 rad/s and 7.5 rad/s and, therefore, the wave frequencies were selected within this range. In addition, since this experimental campaign was conducted focusing on the verification of the present linear numerical method, the tests considered only regular waves of small amplitude and steepness ($H/\lambda \leq 2\%$), which were previously calibrated without the models. Only one wave incident angle was considered ($\theta = 270^o$) due to the restrictions regarding an appropriate space for the positioning of the mechanical device in the tank bridge. In total, 4 regular waves were selected for this test, and their main particulars are presented in Table 9.2.

Table 9.2: Regular waves considered in the tests

ID	ω **(rad/s)**	**T(s)**	**H(m)**
Reg 1	6.400	0.982	0.023
Reg 2	6.800	0.924	0.020
Reg 3	7.000	0.898	0.019
Reg 4	7.200	0.873	0.018

The tests begin with the cylinders aligned with respect to the y axis and with a distance of 0.6 m (center-to-center). Once the wave flaps start to move, the servo motor is also activated and the Body 2 is horizontally displaced from its initial position with a known prescribed oscillatory motion of frequency ω_{pm} and amplitude $A_{pm} = 0.37$ m, this value being the maximum stroke of the ball screw shaft of the mechanical equipment. The oscillation frequency ω_{pm} was defined as a ratio of the incoming wave frequency ω_I. For each regular wave three different oscillation frequencies of Body 2 were considered, being these $\omega_{pm} = \omega_I/15$, $\omega_{pm} = \omega_I/30$ and $\omega_{pm} = \omega_I/60$. Therefore, the test matrix considered 12 different cases, which are described in Table 9.3.

Table 9.3: Test Matrix

		Oscillator Parameters			
Case	**Wave**	ω_I/ω_{pm}	ω_{pm}**(rad/s)**	T_{pm}**(s)**	A_{pm}**(m)**
1	Reg 1	15	0.427	14.73	0.37
2	Reg 1	30	0.213	29.45	0.37
3	Reg 1	60	0.107	58.90	0.37
4	Reg 2	15	0.453	13.86	0.37
5	Reg 2	30	0.227	27.72	0.37
6	Reg 2	60	0.113	55.44	0.37
7	Reg 3	15	0.467	13.46	0.37
8	Reg 3	30	0.233	26.93	0.37
9	Reg 3	60	0.117	53.86	0.37
10	Reg 4	15	0.480	13.09	0.37
11	Reg 4	30	0.240	26.18	0.37
12	Reg 4	60	0.120	52.36	0.37

A better understanding of the experimental setup may be achieved by observing the pictures in Figure 9.9, which displays three video frames recorded during the tests for Case 10. Observe that at instant $t = t_o$ s (Figure 9.9(a)), the two bodies are aligned with respect to the y axis; further on, at $t = t_o + T/4$ s (Figure 9.9(b)), the Body 2 is displaced 0.37 m to right. Finally, at instant $t = t_o + 3T/4$ s (Figure 9.9(c)), the Body 2 is situated 0.37 m left from its initial position. This sequence of events was repeated four times for each case described in Table 9.3.

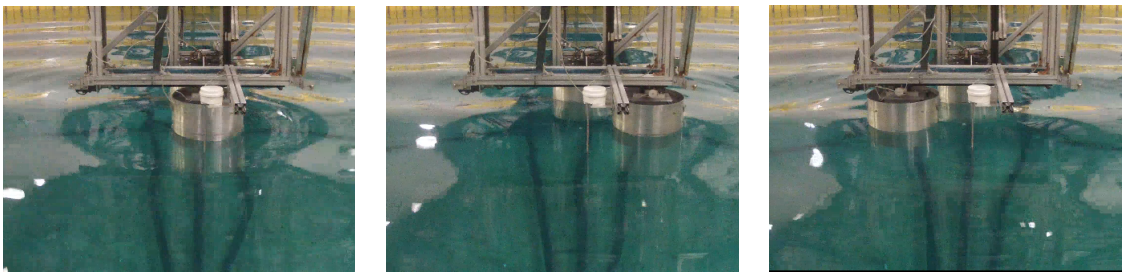

(a) (b) (c)

Figure 9.9: Video frames recorded during the tests with a regular wave of frequency $\omega_I = 7.2$ rad/s and Body 2 oscillation frequency $\omega_{pm} = 0.48$ rad/s. Instants (a) $t = t_o$ s, (b) $t = t_o + T/4$ s and (c) $t = t_o + 3T/4$ s

9.3.2 Numerical Grids for the Case Studies

The simulations are performed with two circular cylinders discretized in 500 quadrilateral panels. These panel meshes follow the same topology and approximate panel resolution of the ones used for the calculations presented before in chapter 6, in which a convergence analysis concerning the verification of the grids was performed.

As in the previous cases, circular free surface meshes were used for the computations shown next. Nevertheless, since the processing times for the present cases are considerably larger in comparison to the simulations involving only fixed meshes, different free surface meshes were applied for each regular wave frequency. As mentioned before, the radius of the free surface has a direct dependence on the wave length and, therefore, a significant number of panels can be saved if the meshes are generated for each specific wave frequency.

For the present calculations, the free surface meshes were constructed with radii of two wave lengths (2λ), in which one wave length was used for damping the waves through the application of a numerical beach zone set with $b = 1.0$ and $a = 1.0$. In this part of the mesh, a stretching factor was also applied so as to decrease the panel resolution at regions far away from the bodies positions. Indeed, this procedure also helped on damping the waves, since the numerical dissipation was intensified by the coarse characteristics of the region. Moreover, this part of the mesh was also kept fixed along the simulations in order to decrease the computational time dedicated to the construction of new meshes at each time step. An example of free surface mesh applied in the computations is presented in Figure 9.10.

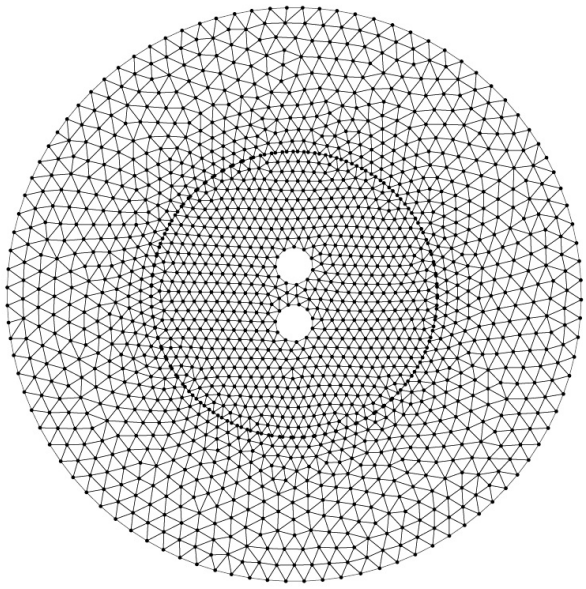

Figure 9.10: Free surface mesh for wave Reg 1. Wave frequency $\omega_I = 6.4$ rad/s

The main characteristics of each free surface mesh used are presented in Table 9.4. It is important to mention that the number of panels represents a reference value, since the total number is not maintained fixed during the simulations, as the meshes are reconstructed at each time step.

Table 9.4: Main particulars of the panel meshes used in the computations

Wave	ω_I **(rad/s)**	r_{fs} **(m)**	**Free Surface Panels**	**Cylinders Panels**	**Total**
Reg 1	6.4	3.01	1581	1000	2581
Reg 2	6.8	2.67	1417	1000	2417
Reg 3	7.0	2.52	1314	1000	2314
Reg 4	7.2	2.38	1246	1000	2246

The coordinate system of the numerical computations follows the same one defined for the experimental tests. For a wave angle of $\theta = 270^o$, the waves propagate in the negative direction of axis y, as presented in Figure 9.11. Once again, a time step of $\Delta t = T/60$ was considered for the simulations.

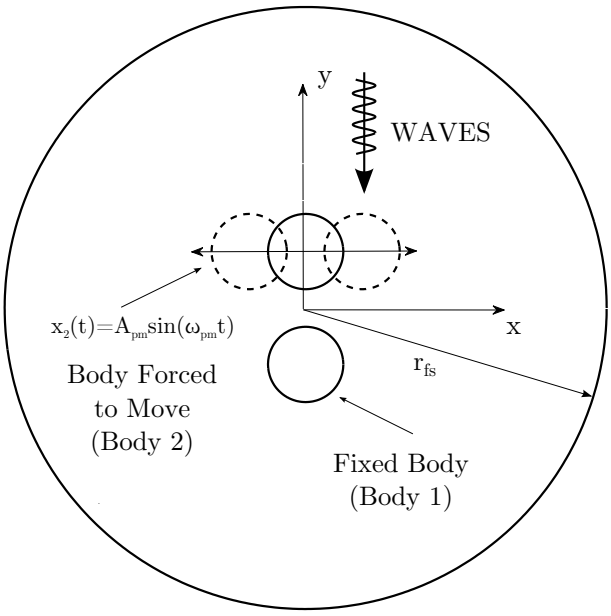

Figure 9.11: Illustrative view of the numerical setup

Similar to the previous calculations, the simulation begins with a ramp time of $T_r = T$ s in order to avoid the generation of spurious waves into the domain as well as non-physical long transient periods in the solution. Moreover, the simulations were run with the amplitudes of the regular waves considered in the experiments.

9.3.3 Comparison between Experiments and Calculations

This section presents the comparison between the numerical computations and the experimental data for the case studies involving a multi-body system with one of the bodies undergoing large horizontal relative displacements. Verification of the numerical results is performed in terms of hydrodynamic forces, moments and wave elevations at three different locations near the bodies. For the sake of conciseness, only the main results, which represents most of the characteristics observed in both experiment and computations is presented in this section. The comparison between numerical and experimental results for all the 12 cases tested (Table 9.3) is presented in Appendix B.

Besides the comparison between the present computations and the experimental measurements, the results presented ahead also include steady-state solutions of several relative positions between the bodies calculated by the frequency domain software WAMIT. This approach does not provide forces and motions time series, but their amplitudes according to the bodies relative positions, which may be used, in its turn, for the construction of envelope curves. In this regard, the time series calculated by the present method may be compared to these envelopes in order to evaluate whether the flow memory and transient

effects, which is not considered by WAMIT, influence the results or not.

Considering Case 1 as an example, Figures 9.12 and 9.13 present the comparisons between the present calculations, experimental data and also the envelope amplitude curves provided by the software WAMIT for the hydrodynamic forces (F_x, F_y and F_z) and moments (M_x and M_y) in Body 1, respectively. This case considers an incident wave frequency of $\omega_I = 6.4$ rad/s and a Body 2 oscillation frequency of $\omega_{pm} = \omega_I/15 = 0.427$ rad/s. These figures also present the position of Body 2 in time, which was used for the synchronization between the numerical and experimental results. The circle markers on the envelope curves indicate the positions of Body 2, for which the WAMIT software was run.

The results show that the hydrodynamic forces and moments F_y, F_z and M_x do not present significant amplitude variations with the change of relative positions between the cylinders. Even though, one may realize that the small modulations observed in the experimental time series were very well captured by the present method. It may also be visualized that the time domain solver provided slightly better results in relation to the software WAMIT, specially for the force F_y, where one may observe that the frequency domain code tend to over-predict the results when Body 2 is located at $x_2 = 0$. This was somewhat expected, since WAMIT considers that the bodies remain at the same relative distance for an infinite time.

Larger modulations of the signals amplitudes are clearly observed for the hydrodynamic force F_x and moment M_y. As expected, WAMIT provides null values for F_x and M_y when the cylinders are in a tandem configuration in $x_2 = 0$ m. This occurs because its solutions neglect the influence of the wave flow arising from the interaction of the incoming wave with Body 2 in its previous positions. As a consequence, the WAMIT envelopes also present a slight shift in time, predicting the minimum and maximum values at different instants than those observed in the measurements. As can also be observed, the present time domain code brought a significant improvement to the results, predicting these instants more accurately, since it considers the flow memory during the computations.

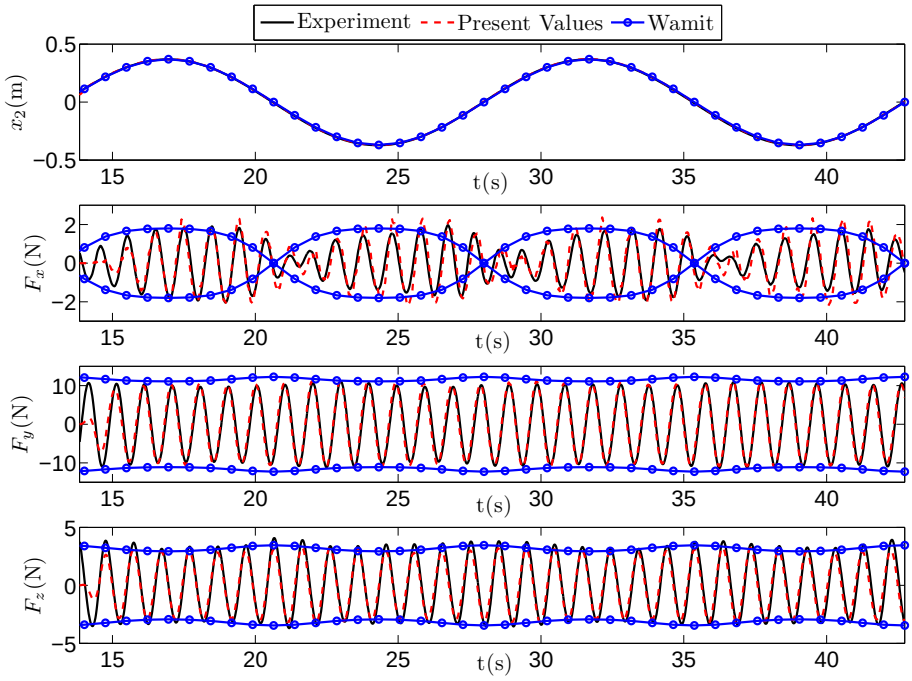

Figure 9.12: Case 1: Comparison of numerical and experimental results in terms of position of body 2 in time and the associated time series of the hydrodynamic forces F_x, F_y and F_z

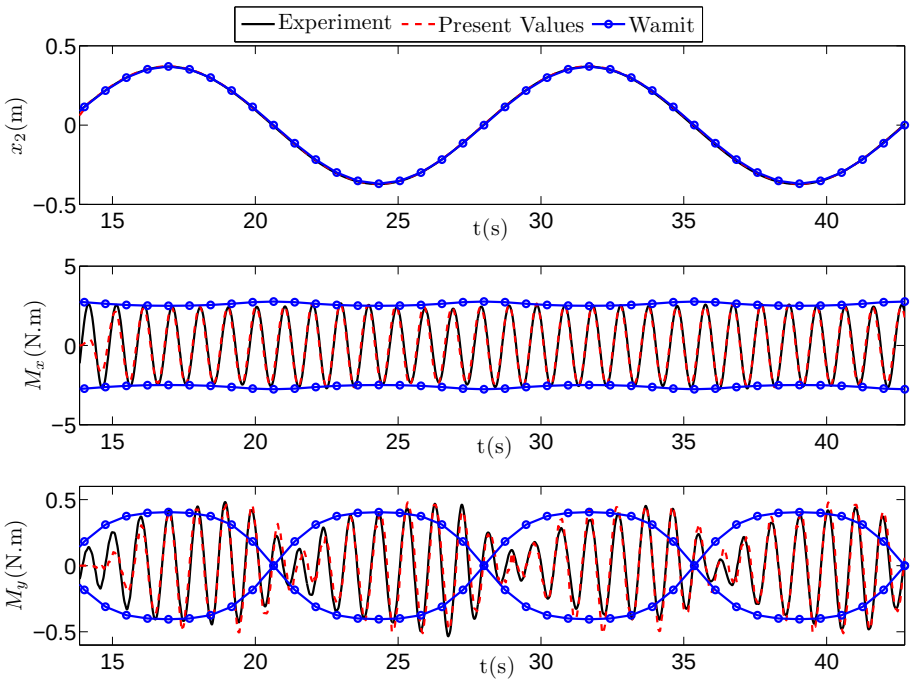

Figure 9.13: Case 1: Comparison of numerical and experimental results in terms of position of body 2 in time and the associated time series of the hydrodynamic moments M_x and M_y

Analogous results for Cases 4, 7 and 10 are presented in figures 9.14 to 9.19. In all these cases, the oscillation frequency of Body 2 was also set with $\omega_{pm} = \omega_I/15$ rad/s. Although in some of these cases the present numerical method and experimental results exhibit small deviations, a good agreement is observed overall. An interesting trend is observed in the time series for F_x and M_y, in which the present method and the experimental measurements show that the signal amplitudes are not the same for equal relative distances. Considering, for instance, the M_y time series presented in Figure 9.13, one should notice that the hydrodynamic moment M_y is larger when Body 2 is approaching Body 1 in comparison to the situation in which the Body 2 is moving away. Again, this behaviour indicates that the flow memory of the wave field, which is not accounted for by frequency domain codes, plays an important role for the proper computations of the hydrodynamic loads, specially when the relative positions of the bodies changes relatively fast along the simulations. For example, if one observes the results for Case 3 (Figures 9.20 and 9.21) and Case 5 (Figures 9.22 and 9.23), in which the oscillation frequencies of Body 2 for Cases 1 and 4 were reduced to $\omega_{pm} = 6.4/60 = 0.107$ rad/s and $\omega_{pm} = 6.8/30 = 0.2267$ rad/s, respectively, it is possible to realize that the signals become more symmetrical with respect to the mean point of each envelope, presenting approximately the same values for the same relative distances between the bodies. In addition, as these scenarios are closer to the one assumed by the software WAMIT, since Body 2 moves more slowly, both numerical results then exhibit a good agreement with the test data.

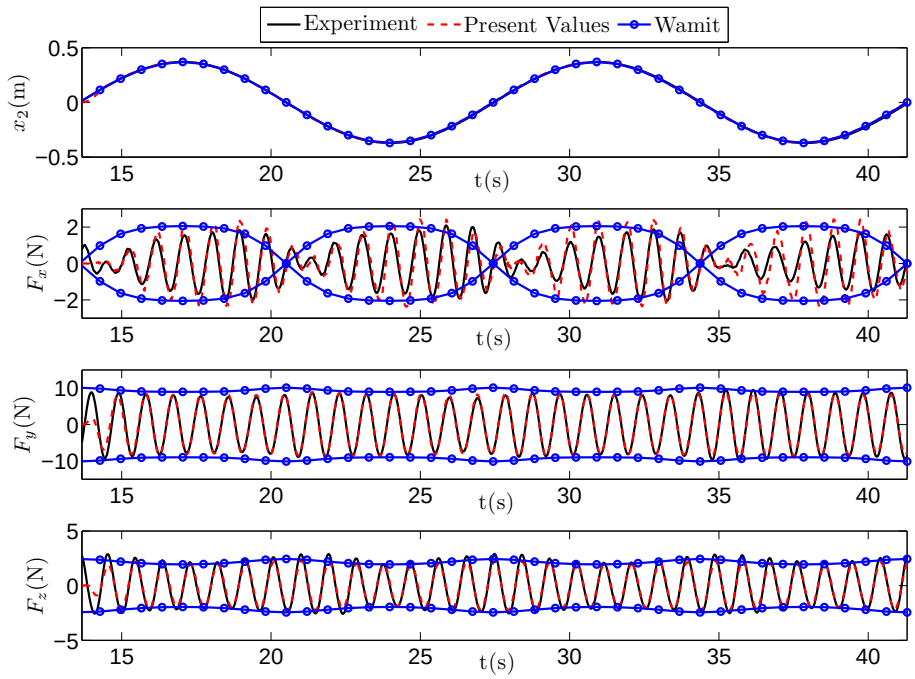

Figure 9.14: Case 4: Comparison of numerical and experimental results in terms of position of body 2 in time and the associated time series of the hydrodynamic forces F_x, F_y and F_z

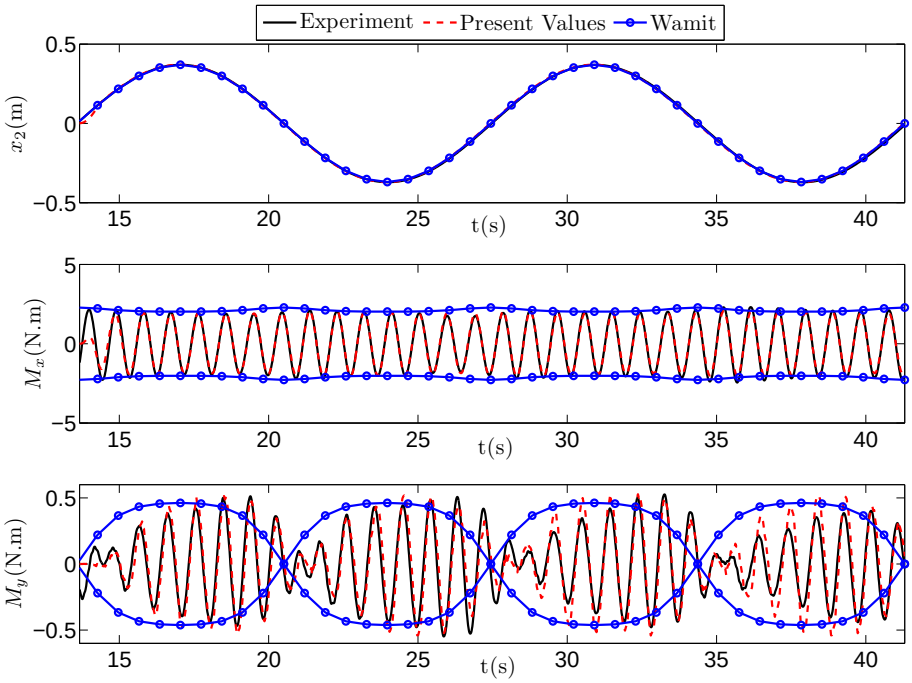

Figure 9.15: Case 4: Comparison of numerical and experimental results in terms of position of body 2 in time and the associated time series of the hydrodynamic moments M_x and M_y

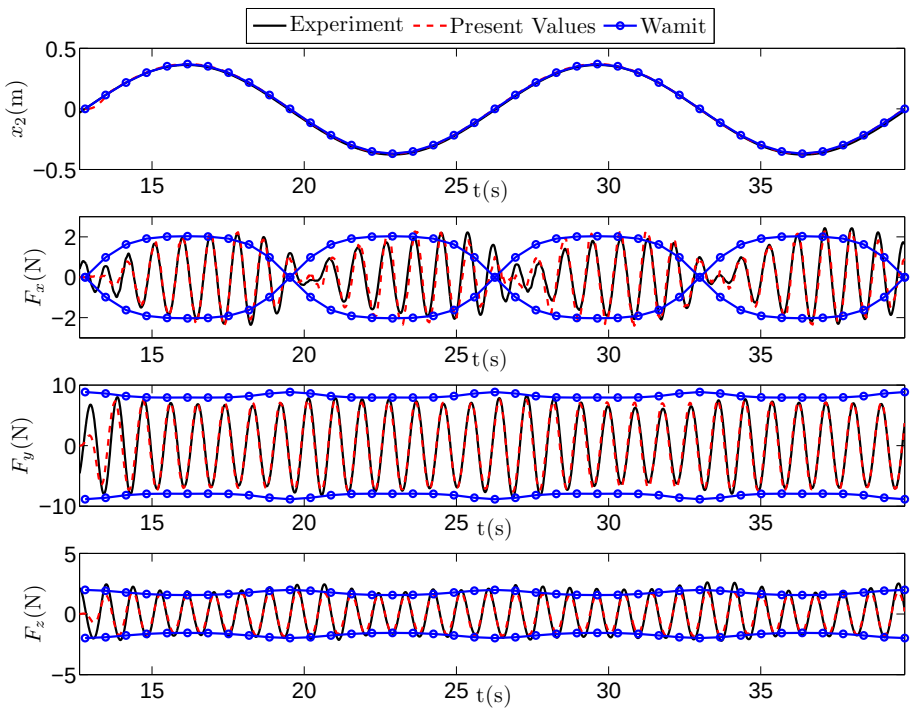

Figure 9.16: Case 7: Comparison of numerical and experimental results in terms of position of body 2 in time and the associated time series of the hydrodynamic forces F_x, F_y and F_z

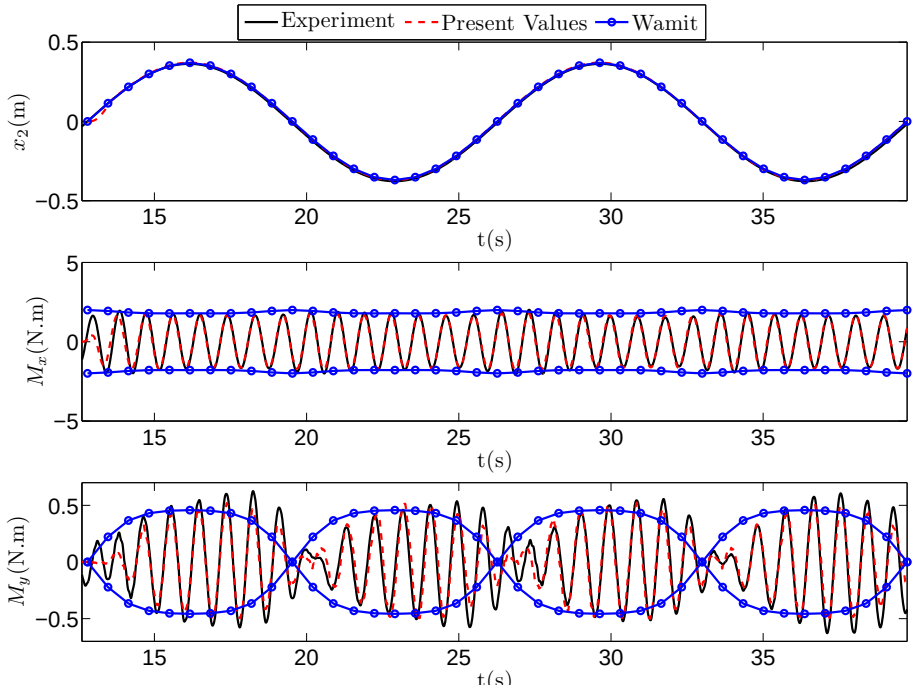

Figure 9.17: Case 7: Comparison of numerical and experimental results in terms of position of body 2 in time and the associated time series of the hydrodynamic moments M_x and M_y

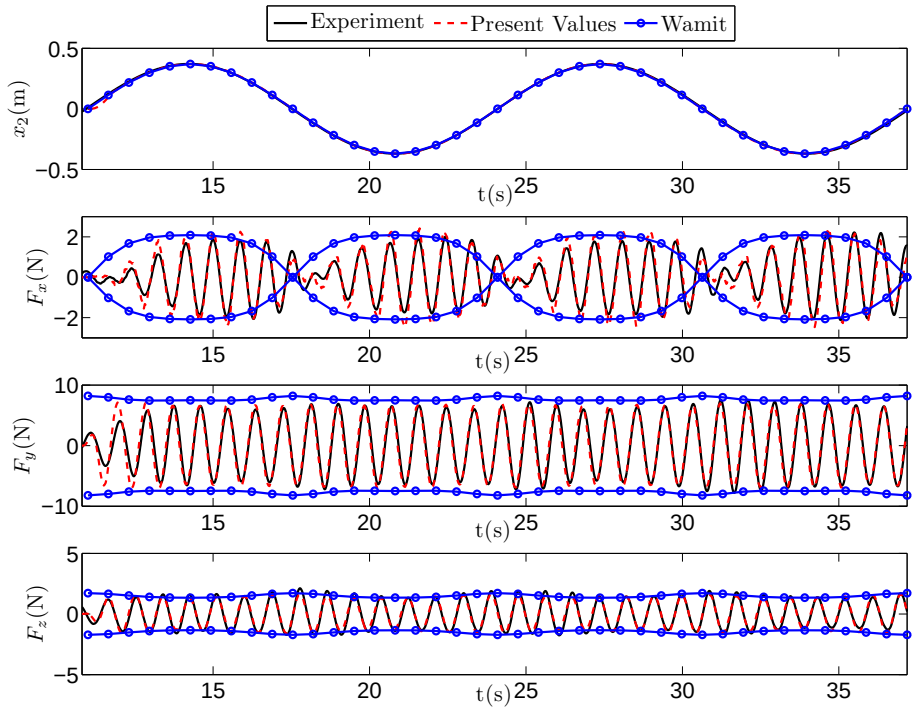

Figure 9.18: Case 10: Comparison of numerical and experimental results in terms of position of body 2 in time and the associated time series of the hydrodynamic forces F_x, F_y and F_z

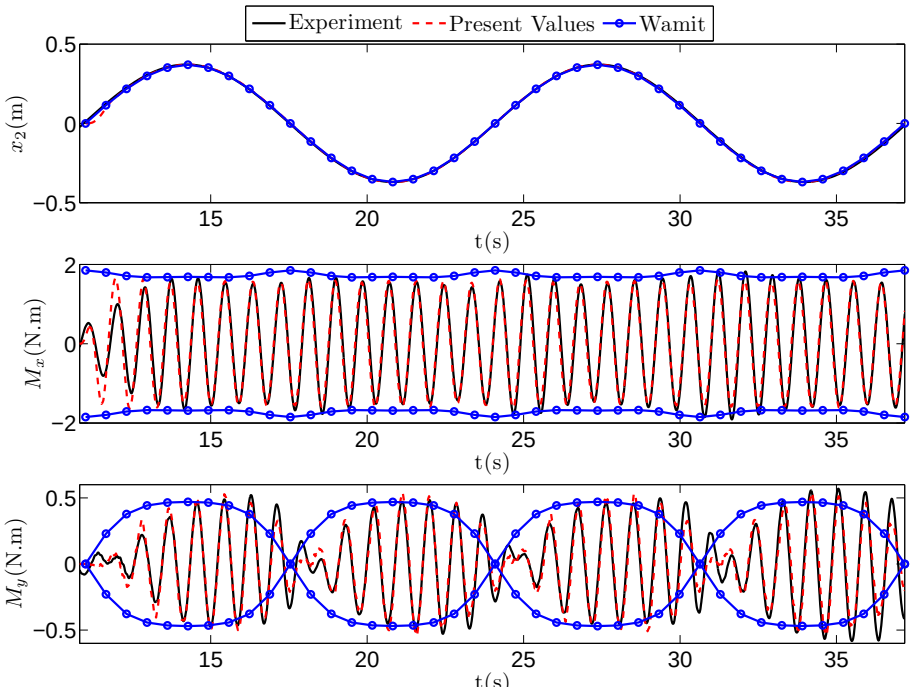

Figure 9.19: Case 10: Comparison of numerical and experimental results in terms of position of body 2 in time and the associated time series of the hydrodynamic moments M_x and M_y

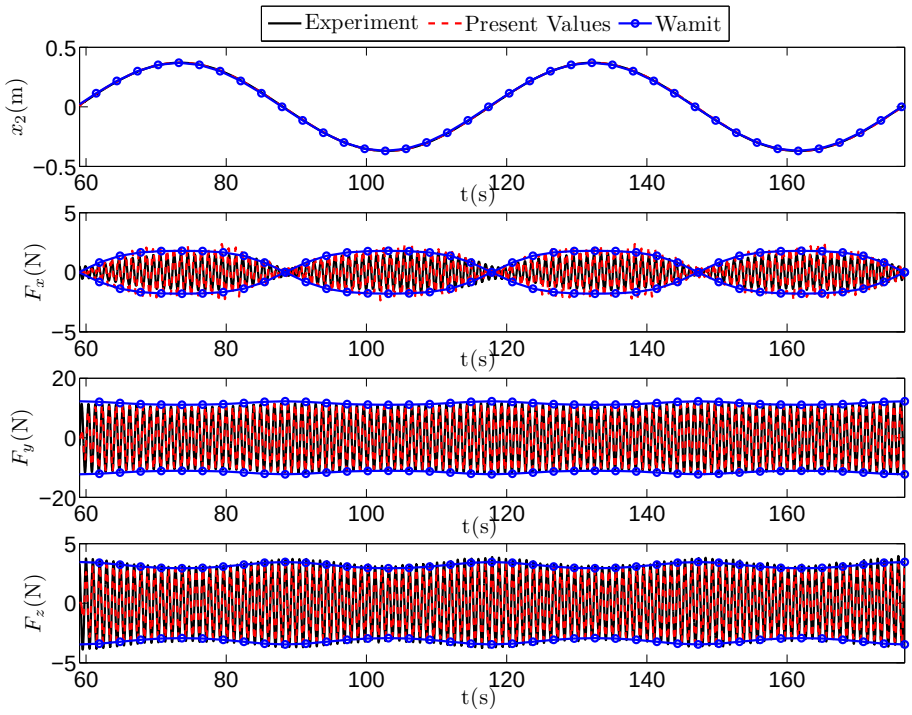

Figure 9.20: Case 3: Comparison of numerical and experimental results in terms of position of body 2 in time and the associated time series of the hydrodynamic forces F_x, F_y and F_z

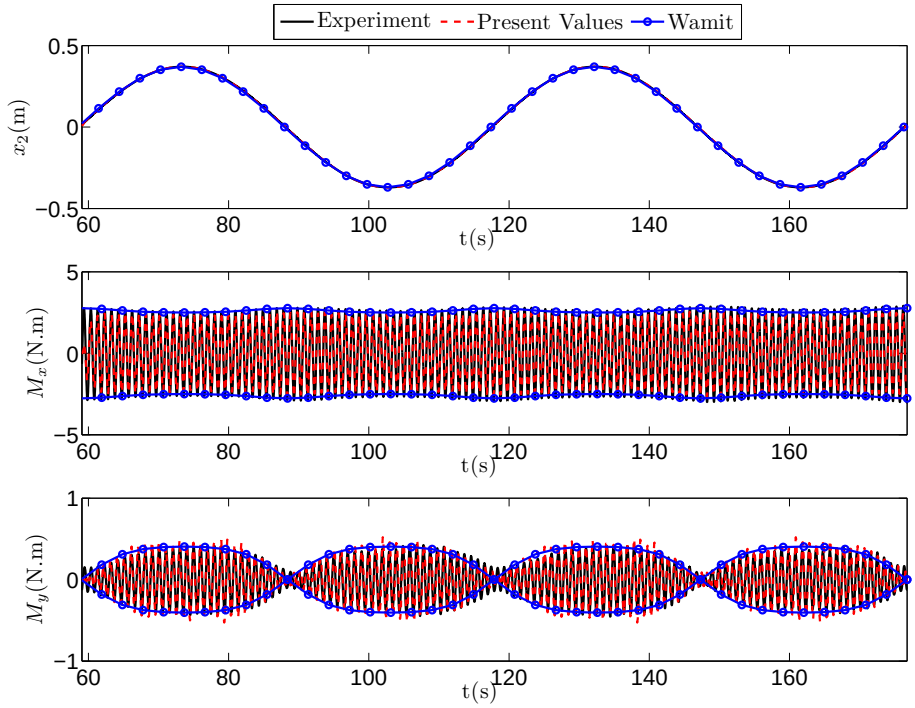

Figure 9.21: Case 3: Comparison of numerical and experimental results in terms of position of body 2 in time and the associated time series of the hydrodynamic moments M_x and M_y

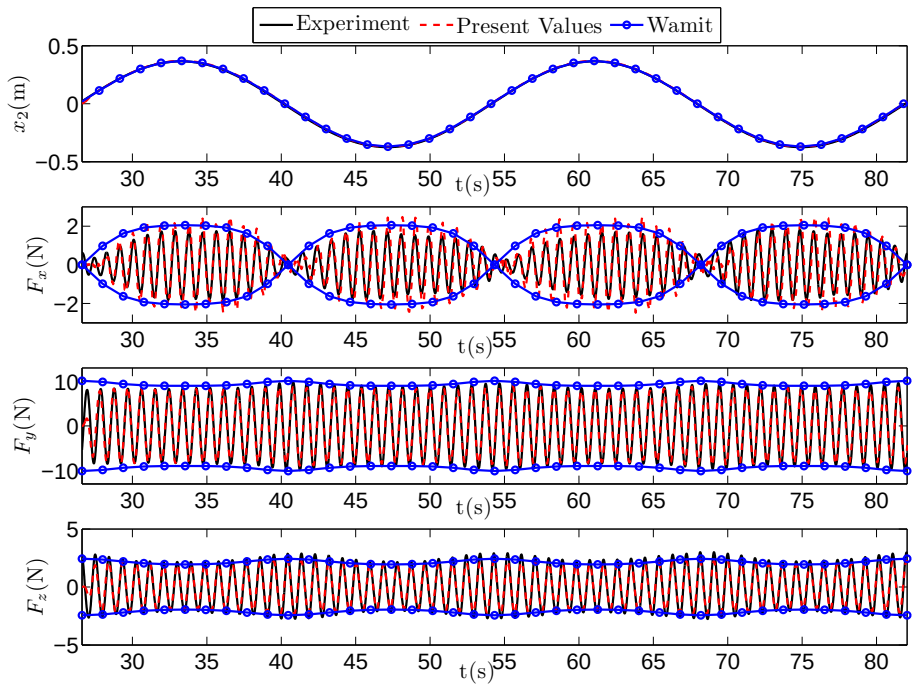

Figure 9.22: Case 5: Comparison of numerical and experimental results in terms of position of body 2 in time and the associated time series of the hydrodynamic forces F_x, F_y and F_z

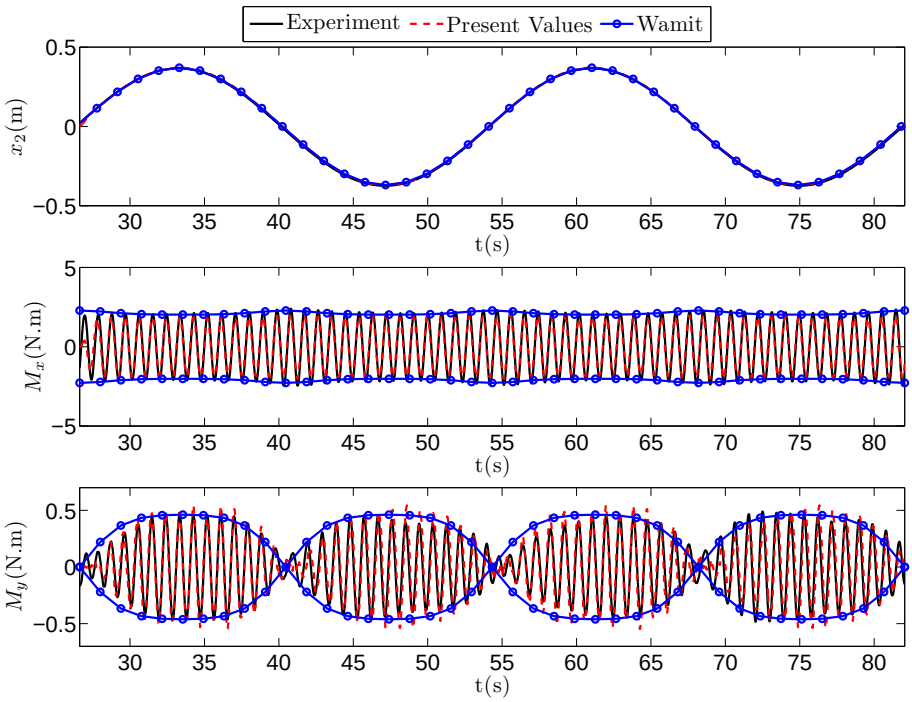

Figure 9.23: Case 5: Comparison of numerical and experimental results in terms of position of body 2 in time and the associated time series of the hydrodynamic moments M_x and M_y

Considering again the results for Case 1, Figure 9.24 presents comparisons in terms of numerical and experimental energy response spectra for F_x and M_y, from which one may realize the presence of energy in two other frequency bands besides the incident wave one. This fact reveals that the oscillatory motion of Body 2 induces a Doppler effect in the Body 1 measured signals, which increases and reduces the wave frequency when Body 2 is approaching and moving away from Body 1, respectively. In fact, since Body 1 is a circular cylinder, the force F_x and moment M_y induced directly by the interaction with the incoming wave tend to vanish, remaining only the force/moment components induced by the waves diffracted from Body 2. Thus, in this problem, Body 2 works as a moving source that emits free surface waves at a constant frequency ω_I. As a result, when Body 2 is approaching Body 1 from negative x coordinates, the wave fronts begin to cluster on the right side and spread further apart on the left side of Body 2, which modifies the wave frequency perceived by Body 1.

As also indicated in Figure 9.24, these frequency components are calculated by the sum and subtraction of ω_{pm} with the incident wave frequency ω_I, which was verified by observing also the F_x and M_y energy spectra for other cases, such as Cases 2 and 3, in which the oscillatory motion frequencies of Body 2 were reduced to $\omega_{pm} = 6.4/30 = 0.213$ rad/s and $\omega_{pm} = 6.4/60 = 0.107$ rad/s, respectively. Once more, the results provided by the present

method recovered very well the experimental data, capturing with reasonable accuracy the physics of the problem. The same behavior was also observed for the other cases.

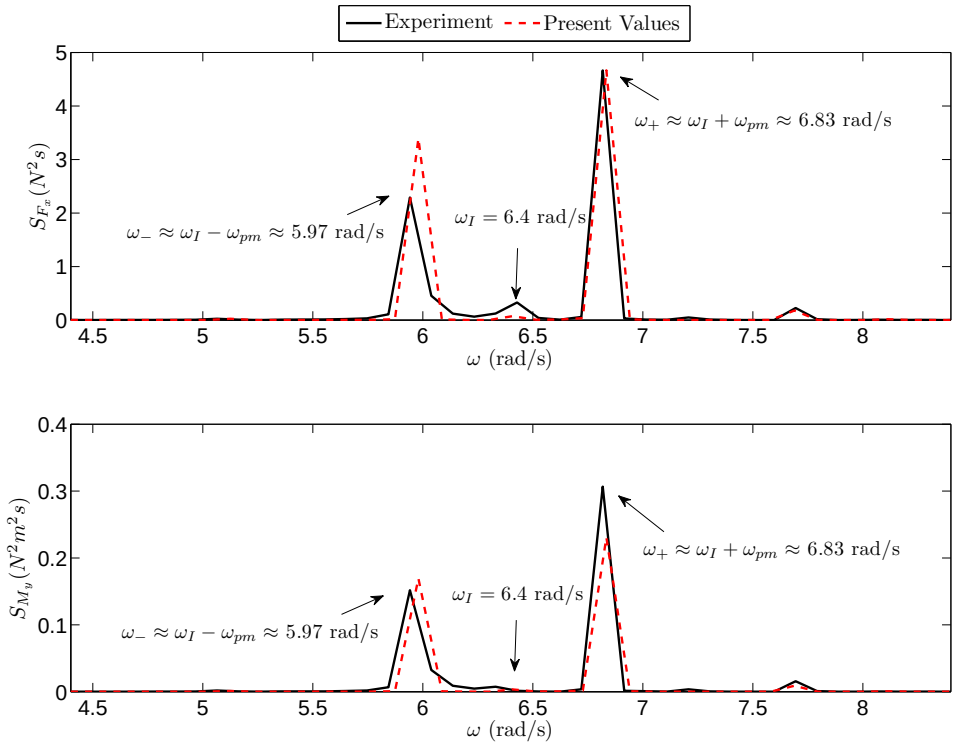

Figure 9.24: Case 1: Comparison between present method and experimental data of F_x and M_y response spectra

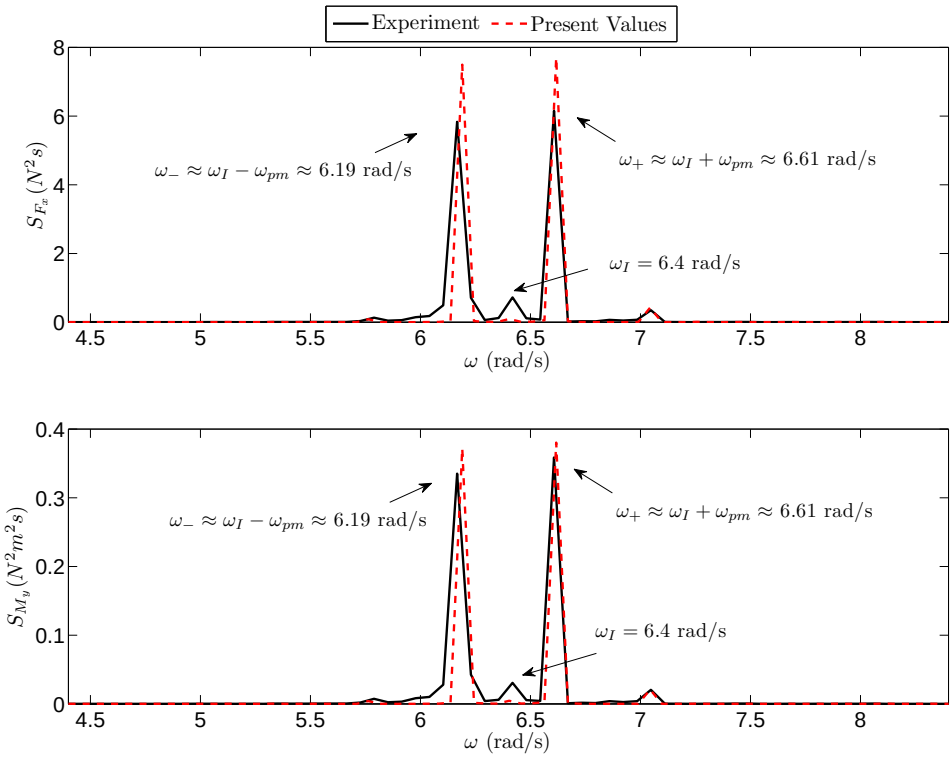

Figure 9.25: Case 2: Comparison between present method and experimental data of F_x and M_y response spectra

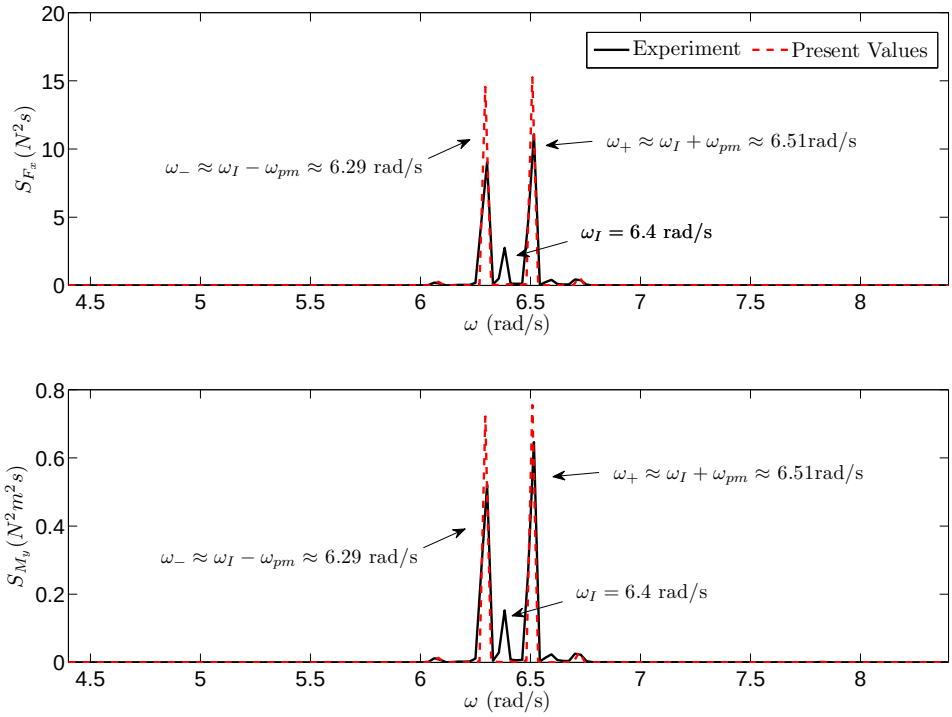

Figure 9.26: Case 3: Comparison between present method and experimental data of F_x and M_y response spectra

Examples of comparisons between numerical and experimental wave elevations for wave probes WP1, WP2 and WP3 (see WPs positions in Figure 9.4 and 9.8) for Cases 1, 4, 7 and 10 are presented in Figures 9.27, 9.28, 9.29 and 9.30, respectively. In all these cases the oscillation frequencies of Body 2 were set to $\omega_{pm} = \omega_I/15$ rad/s. One may realize that the wave elevations measured at the WP positioned behind Body 1 (WP3 - η_{P3}) present a very constant behavior, showing to be independent on the translational movements of Body 2. In fact, this wave probe is located at a sheltered area provided by Body 1, which always results in low wave amplitude values for all cases tested.

On the other hand, small amplitude modulations may be observed for WP1 and WP2, in which again very good agreements are observed between the time series computed by the present method and the experimental results. Indeed, the present method presented a slightly better performance in relation to the WAMIT results, predicting with more accuracy the wave elevations measured by WP2 (η_{P2}). As one may observe, for this wave probe the frequency domain results present higher wave amplitudes in relation to the time domain and experimental measurements when Body 2 is approaching Body 1. Once more, this behaviour tends to be minimized with the increasing of Body 2 oscillation period as exemplified by the wave elevations for Cases 3 and 8 displayed in Figures 9.31 and 9.32, respectively. For these cases the translational oscillation frequencies of Body 2 of cases 1 and 7 were reduced to $\omega_{pm} = 6.0/60 = 0.107$ rad/s and $\omega_{pm} = 7.0/30 = 0.233$ rad/s, respectively.

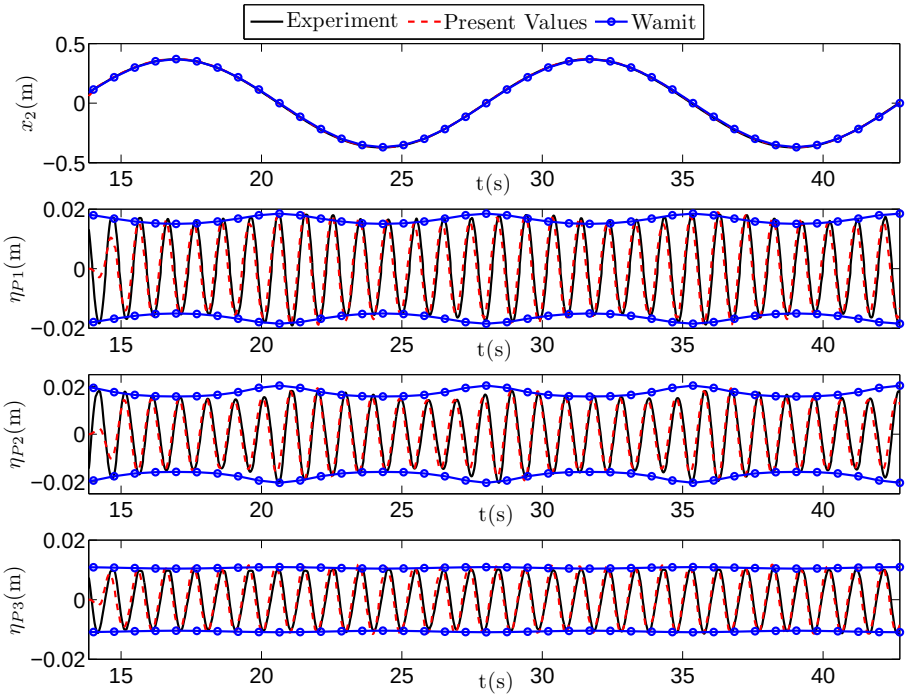

Figure 9.27: Case 1: Comparison of numerical and experimental results in terms of position of body 2 in time and the associated time series of the wave elevations at WP1, WP2 and WP3

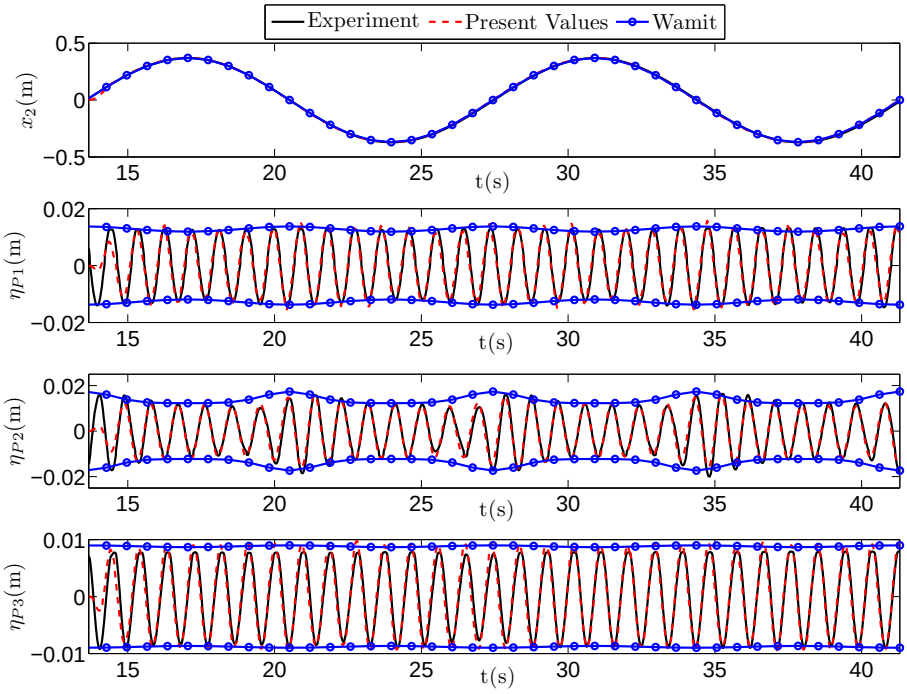

Figure 9.28: Case 4: Comparison of numerical and experimental results in terms of position of body 2 in time and the associated time series of the wave elevations at WP1, WP2 and WP3

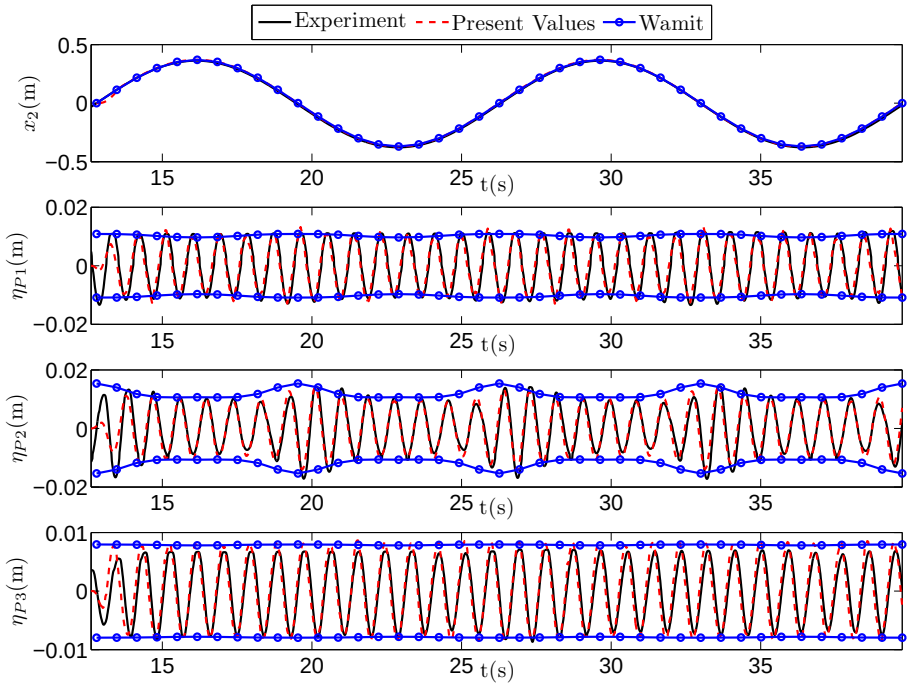

Figure 9.29: Case 7: Comparison of numerical and experimental results in terms of position of body 2 in time and the associated time series of the wave elevations at WP1, WP2 and WP3

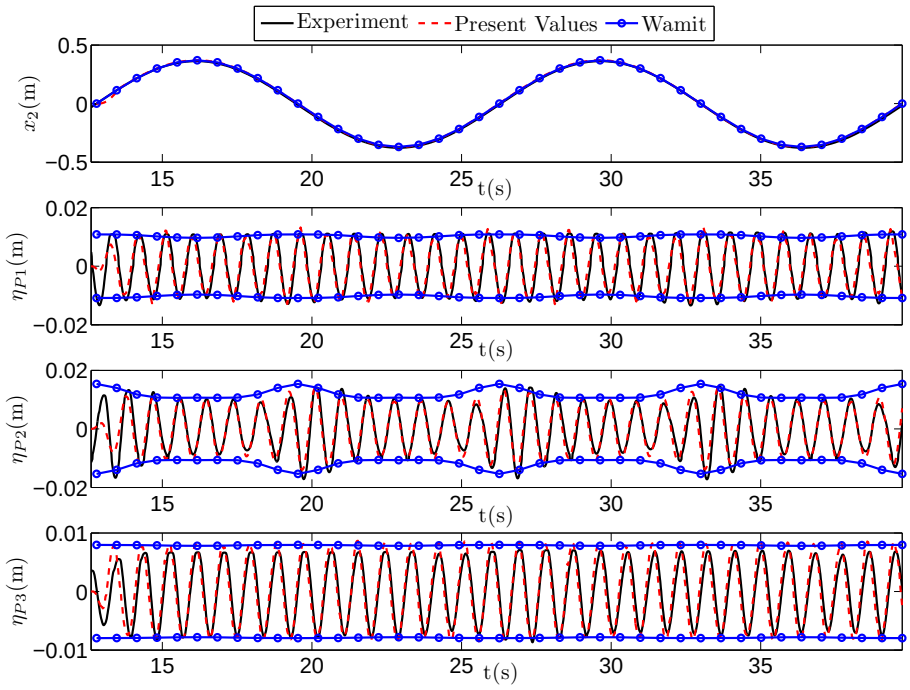

Figure 9.30: Case 10: Comparison of numerical and experimental results in terms of position of body 2 in time and the associated time series of the wave elevations at WP1, WP2 and WP3

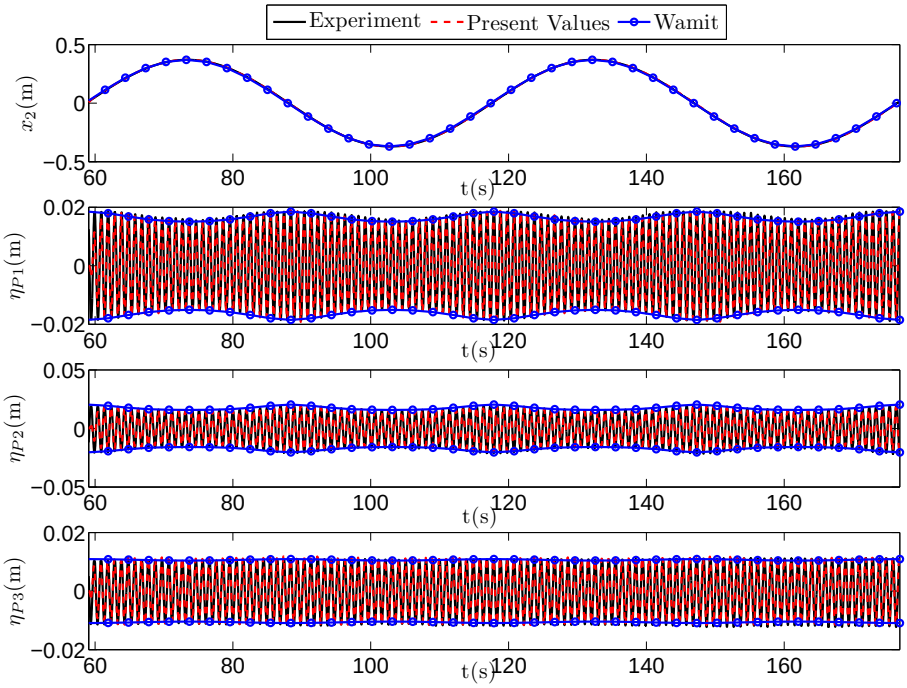

Figure 9.31: Case 3: Comparison of numerical and experimental results in terms of position of body 2 in time and the associated time series of the wave elevations at WP1, WP2 and WP3

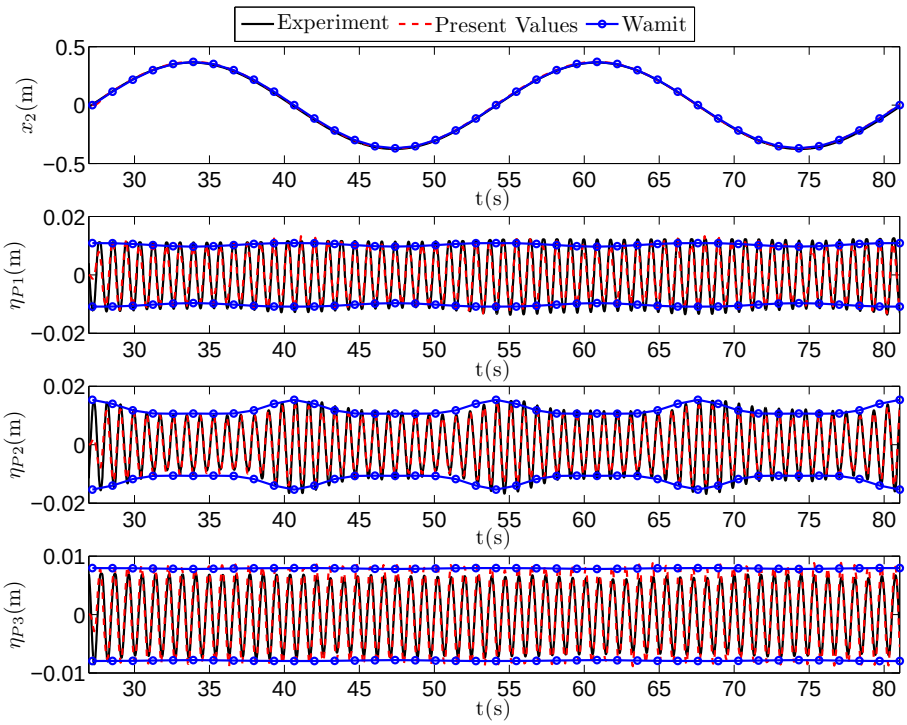

Figure 9.32: Case 8: Comparison of numerical and experimental results in terms of position of body 2 in time and the associated time series of the wave elevations at WP1, WP2 and WP3

Finally, examples of wave elevation patterns for Case 1 at two different instants associated to the maximum wave amplitudes at WP1 and WP2 are illustrated in Figures 9.33 and 9.34, respectively. One should notice that, although the maximum wave heights of these wave probes occur at different instants, in both cases the Body 2 is positioned approximately in front of Body 1.

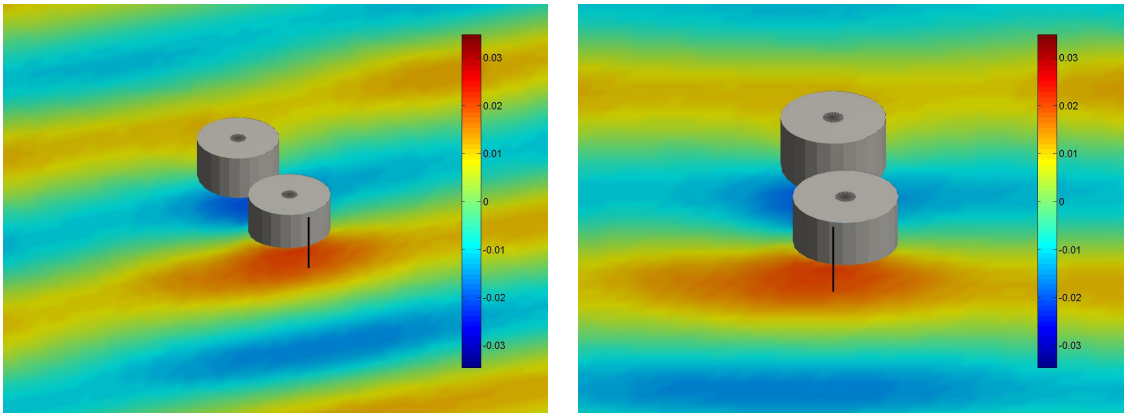

(a) (b)

Figure 9.33: Case 1: Two snapshots of the simulation illustrating the maximum wave elevation calculated at WP1 ($t = 36.23$) s. Perspective (a) and front views (b). Vertical black line refers to the position of the wave probe

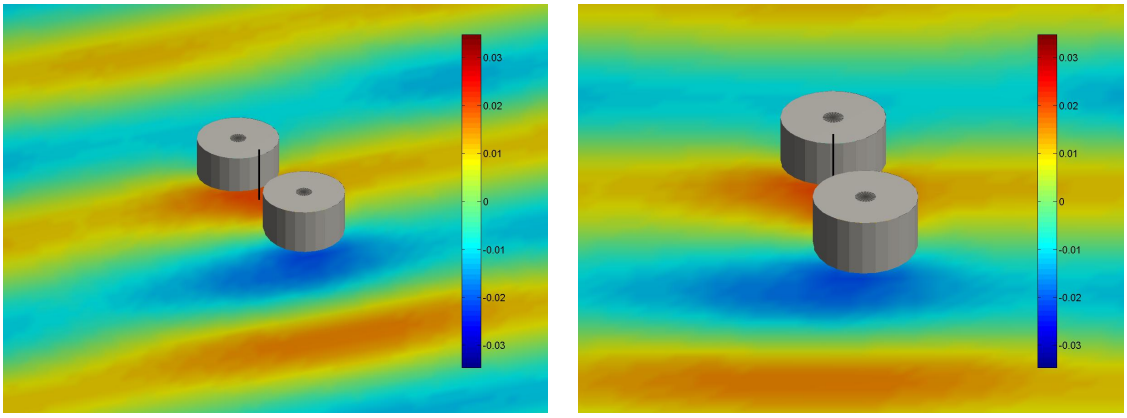

(a) (b)

Figure 9.34: Case 1: Two snapshots of the simulation illustrating the maximum wave elevation calculated at WP2 ($t = 36.72$) s. Perspective (a) and front views (b). Vertical black line refers to the position of the wave probe

Chapter 10

Conclusions

10.1 Conclusions

This work presented the development and verification of a numerical code that deals with wave-body interactions in time domain under the assumption of potential flow theory. The original problem is nonlinear and requires the imposition of boundary conditions on time-dependent surfaces which are not known prior to the problem solution as, for example, the free surface elevation and the position of the floating body surface at each instant of time. These features make the problem very difficult to be solved, being the focus of a vast number of articles which describe methods that deal with this nonlinear problem. Nevertheless, their applicabilities are still restricted to bi-dimensional problems or very simple three-dimensional geometries, which motivated us to apply a linear wave-body formulation as a first stage of the research.

Under the assumption of waves with small amplitude and steepness, and that the bodies do not present large motions around their mean positions, the set of equations were linearized by expansions using Stoke's and Taylor's series. Consequently, the total velocity potential could be decomposed in a sum of a disturbed wave potential and an analytic solution of an incoming wave field, avoiding the necessity of including a numerical wave-maker to generate the waves and making possible to reduce the number of panels by concentrating them around the bodies.

Because of the accuracy required for the calculation of the velocity potential time derivative, the inclusion of a second Initial Boundary Value Problem for the so-called acceleration

potential was made. After a deep research in the literature, we concluded that this method is the most accurate scheme for the calculation of the velocity potential time derivative and consequently for the pressure field which is essential for a consistent formulation in time domain. Although this method is often mentioned in the literature, results with its application in three-dimensional problems are rarely reported.

A Low Order BEM solver formulated in terms of Green's second identity was then developed transforming the original integral equations in two linear systems of algebraic equations. The integration of the influence coefficients received special attention along this topic, illustrating the difficult convergence of the integrals when field and collocation points are close to each other. In order to overcome this problem, a method that split up the quadrilateral panels into triangles was implemented, so as to desingularize the integrand function, transforming it into a smoother function. With this approach, the integrals convergence were reached with a significant reduction of gaussian points in comparison to the direct integration method. The method also holds for triangular panels, treating the problem as a quadrilateral panel with two vertices collapsed.

Additional numerical schemes which are important for the performance of the numerical method were also discussed as, for example, the inclusion of dissipation terms on a portion of the free surface to avoid wave reflections from the domain boundaries and the inclusion of a ramp function that acts in the first seconds of the simulation in order to provide the solution with a gradual increase, to reduce the transient periods and to avoid impulsive responses of the dynamic system. The time scheme and the updating of the boundary conditions were conducted with the widely used RK4 scheme, which provides high accuracy and large stability regions.

The numerical code was first tested by calculating the hydrodynamic loads on a hemisphere and a circular cylinder, solving the well-known problems of diffraction and radiation in waves. In addition, free floating simulations were also conducted in order to verify whether the procedures adopted to couple the fluid and body equations were correctly implemented. Convergence of the results when increasing the number of panels was also verified by performing several simulations with meshes of different panel resolutions. As expected, the larger the number of panels the lower were the relative errors between the present calculations and benchmark values, which were provided by analytic solutions and by the software WAMIT. As could be observed, these comparisons presented very good agreement, attesting that the numerical code is indeed capable of predicting the first-order hydrodynamic loads and motions associated to the wave-body interaction problem.

One step forward, free floating simulations with two different FPSO hull types were also conducted. The present computations were verified through comparisons of motion RAOs

obtained numerically with WAMIT or experimentally in the CH-TPN-USP. In the simulations, the RAOs were obtained considering both monochromatic regular waves and a white-noise spectrum technique that made possible to calculate the RAOs in a very efficient way, performing only one simulation per wave incidence angle. Despite some small deviations, specially concerning resonance peak values, the results presented good agreement with both WAMIT and the experimental data. Moreover, a direct comparison of numerical and experimental time series was also presented, in which not only the amplitudes but also the phases between the motions could be verified.

The performance of the method when dealing with a multi-body problem involving two bodies in side-by-side arrangement, as, for example, in a FLNG offloading operation, was also reported. Aiming at obtaining benchmark data, an experimental campaign was carried out at ETSIN, in Spain. The tests were conceived with a very fundamental setup, considering only regular waves and just one wave direction. In addition, the setup considered one of the bodies fixed (barge) and the other (geosim) restrained in three D.O.F. (sway, roll and yaw) in order to maintain the gap width fixed during the measurements. Results were discussed in terms of the geosim motions and wave amplitudes in the gap. The numerical results presented undesirable overestimations of the experimental values for a range of frequencies, which showed to be dependent on the gap width. In fact, the numerical and experimental results have shown that the resonant frequencies were lower for the system with the largest gap width. Moreover, different resonant frequencies were observed for heave and pitch motions. As demonstrated by the wave envelopes inside the gap, the heave motion is significantly amplified due to the presence of a piston-type mode inside the gap, whereas the pitch motion is influenced by the occurrence of a second longitudinal mode. The same conclusions could be drawn in this respect for both gap widths.

Still concerning the side-by-side problem, it was possible to observe that the numerical model presented numerical convergence problems when simulating wave frequencies near to the gap resonant ones. In these cases, the time series for motions and wave elevations showed a long transient period, attesting the numerical problems to reach the steady-state. This problem was solved by the application of a damping lid method, which incorporates a damping factor in the free surface boundary conditions. By considering this method, the time series reached the steady state much faster. This is indeed a positive indication regarding future applications of the method to the analysis of multi-vessels in irregular wave conditions. In addition, despite the simplicity of the damping model, the use of the damping lid technique has also improved the numerical results, reducing the discrepancies observed with the experimental data. Nevertheless, it should be noticed that the choice of the damping parameter has been done heuristically and for a better insight about the influence of this parameter on the numerical solutions, further analysis is still required.

Finally, the text is concluded with the presentation of a new method to care with multi-body hydrodynamic interactions of bodies undergoing large relative displacements, a problem that cannot be assessed directly with frequency domain codes. As an important part of this development, a generator of unstructured triangular panel meshes that could be integrated in the time-loop of the code was implemented, so as to account for changes of the relative positions between the bodies during the calculations. Moreover, an specific higher order interpolation algorithm had to be considered to proper recover the solutions of a previous time-step and to enable the progressing of the calculations with reasonable accuracy.

Benchmark data was obtained through the conduction of fundamental experimental tests in the CH-TPN-USP dedicated to the evaluation of this specific problem. The tests considered two circular cylinders, being one fixed and attached to a 6 D.O.F load cell, and the other coupled to a mechanical device that was used to impose large and slow horizontal movements on this body. In order to evaluate the influence of the prescribed oscillatory motion frequency on the results, for each regular wave three different oscillation frequencies were considered, these being defined as a ratio of the incident wave frequency.

Despite the fundamental configuration of the tests, the experiments presented a relatively high degree of complexity. Since the main objective was to evaluate the hydrodynamic interaction loads between the bodies, which are indeed very small in relation to the forces induced by the incident wave itself, special care had to be taken in order to minimize the influence of wave reflections from the tank walls. In fact, this was the main difficulty of the experimental campaign, since each test case demanded a long period of acquisition, which, by its turn, increased the possibility of wave reflections effects on the results. For this reason, the tests were conducted considering regular waves in a frequency range, for which the CH-TPN-USP active absorption system presents its best performance.

The new numerical implementation was then verified by reproducing the cases tested experimentally. Results were compared in terms of hydrodynamic loads calculated in the fixed body and wave elevations on three wave probes that were positioned upstream, in between and downstream of the bodies. Through these comparisons, it was possible to verify that when the most rapid prescribed oscillatory motion tested was considered, the time series for transversal forces/moments (in relation to the incident wave angle) were not symmetric, meaning that the signals presented different amplitudes for the same relative distances between the bodies. In fact, the analysis showed that this was occurring due to a Doppler effect induced by the large oscillatory motion of the second body, a physical behaviour that was very well captured by the time domain code. Moreover, this result also emphasized the importance of considering a transient solution of the problem, which cannot be calculated directly by a frequency domain code. In general, as could be

observed, the present method was able to reproduce the experimental data for all cases tested, illustrating that the variation of the relative positions of the bodies in time domain are being correctly modeled.

10.2 Proposed Improvements and Future Work

Based on the conclusions of this thesis, the following tasks are considered as important future works for the improving of the method and its applicability:

- Development of a higher order method, in which both the geometry and the solutions are described in terms of Non-Uniform Rational B-Spline (NURBS) surfaces. With this approach, the study of wave-current interaction effects and the second order problem become more suitable to be tackled, since the spatial derivatives of the velocity potential may be calculated straightforwardly.

- Investigation of other techniques that consider the inclusion of damping coefficients to emulate the viscous effects in the side-by-side problem, as well as different possibilities to calibrate these coefficients. In the method applied in this thesis, a preliminary adjustment of the damping coefficient was performed by matching the numerical results with the experimental data. However, a consistent calibration of these coefficients still demand more investigations of the problem, which may require, for example, the conduction of additional experimental campaigns.

- Implementation of drift forces into the numerical method that deals with multi-body systems with large relative displacements. This development would make possible the simulation of real operations, involving real body geometries, such as FPSOs, Semi-submersible etc. Validation of the results, however, would be a critical task, requiring a very specific and complex experimental test.

- Integration of the present method to a mooring line code in order to perform simulations of moored, single or multi-body, systems situated on deep sea waters, where the inertial and damping effects of mooring lines and risers become nontrivial and the body dynamics can be appreciably affected by them. For instance, this development could be performed in a dynamic simulator, such as the TPN of the University of Sao Paulo, in which, currently, the wave effects are considered decoupled of the equations of motion by using linear hydrodynamic coefficients previously calculated in the frequency domain software WAMIT. As previously discussed in this thesis, this approach brings limitations for solving multi-body transient problems, which

could be partially solved by coupling the hydrodynamic calculations to the bodies equations of motion solved by the dynamic simulator.

- Development of a combined BEM-FEM scheme for the solution of hydroelastic response of flexible seagoing ultra large vessels. As stated by Kim, Kim and Kim (2009), as the sizing of ships is getting larger, their structural natural frequencies generally tends to move down to a smaller frequency range. In addition, forward speed makes the encounter excitation frequency of waves to move much closer to their natural frequency range, leading to higher chance of resonance between the two even under linear wave regime.

References

BAI, W.; TAYLOR, R. E. Fully nonlinear simulation of wave interaction with fixed and floating flared structures. **Ocean Engineering**, v. 36, p. 223–236, 2009.

BATCHELOR, G. K. **An Introduction to Fluid Dynamics**. : Cambridge University Press, 1967.

BECK, R. F.; CAO, Y.; LEE, T.-H. Fully nonlinear water wave computations using the desingularized method. In: **Proceedings of the Sixth International Conference on Numerical Ship Hydrodynamics**. 1994.

BECK, R. F.; REED, A. M. Modern seakeeping computations for ships. In: **Proceedings 23rd ONR Symposium on Naval Hydrodynamics**. 2000.

BERTRAM, V. **Practical Ship Hydrodynamics.** : Butterworth-Heinemann, 2000.

BHATTA, D.; RAHMAN, M. On scattering and radiation problem for a cylinder in water of finite depth. **International Journal of Engineering Science**, v. 41, p. 931–967, 2003.

BOO, S. Y. Linear and nonlinear irregular waves and forces in a numerical wave tank. **Ocean Engineering**, v. 29, p. 475–493, 2002.

BUCHNER, B.; DIJK, A. V.; DE WILDE, . J. J. Numerical multiple-body simulations of side-by-side mooring to a FPSO. In: **In Proceedings of the 21st ISOPE Conference**. p. 343–353, 2011.

BUNNIK, T. A simulation approach for large relative motions of multi-body offshore operations in waves. In: **Proceedings of the ASME 2014 33rd International Conference on Ocean, Offshore and Arctic Engineering, OMAE2014, San Francisco, California, USA**. 2014.

BUNNIK, T.; PAUW, W.; VOOGT, A. Hydrodynamic analysis for side-by-side offloading. In: **In Proceedings of the 19th ISOPE Conference**. 2009.

BUNNIK, T. H. J. **Seakeeping Calculations for Ships, taking into account the Non-linear Steady Waves**. 1999. Thesis (PhD) — Technische Universiteit Delft, 1999.

CAO, Y.; R., B.; SCHULTZ, W. Non-linear motions of floating bodies in incident waves. In: **9th Workshop on Water Waves and Floating Bodies**. 1994.

CHEN, C.-B. Hydrodynamic analysis for offshore LNG terminals. In: **In Proceedings of the 15th ISOPE Conference**. 2005.

CLAUSS, G. F.; DUDEK, M.; TESTA, D. Gap effects at side-by-side LNG-transfer operations. In: **In OMAE 2013-10749, Proceedings of the 32nd International Conference on Ocean, Offshore and Arctic Engineering**. 2013.

CLéMENT, A. Coupling of two absorbing boundary conditions for 2d time-domain simulations of free surface gravity waves. **Journal of Computational Physics**, v. 126, p. 139–151, 1996.

COINTE, R. Nonlinear simulation of transient free surface flows. In: **Fifth International Conference on Numerical Ship Hydrodynamics**. 1990.

COINTE, R.; GEYER, P.; KING, B.; MOLIN, B.; TRAMONI. Nonlinear and linear motions of a rectangular barge in a perfect fluid. In: **Eighteenth Symposium on Naval Hydrodynamics**. 1991.

CUMMINS, W. **The Impulsive Response Function and Ship Motions**. : Department of the Navy David Taylor Model Basin, (1962).

DANMEIER, D. G. **A Higher-Order Panel Method for Large-Amplitude Simulations of Bodies in Waves**. 1999. Thesis (PhD) — Massachusetts Institute of Technology, 1999.

DAWSON, C. W. A practical computer method for solving ship-wave problems. In: **Proceedings of the Second International Conference on Numerical Ship Hydrodynamics**. 1977.

ELIE, B.; RELIQUET, G.; P.-E., G.; THILLEUL, O.; FERRANT, P.; GENTAZ, L.; LEDOUX, A. Simulation of the gap resonance between two rectangular barges in regular waves by a free surface viscous flow solver. In: **Proceedings of the ASME 2013 32nd International Conference on Ocean, Offshore and Artic Engineering, OMAE2013, Nantes, France**. 2013.

FALTINSEN, O. M. **Sea Loads on Ships and Offshore Structures**. : Press Syndicate of the University of Cambridge, 1990.

FERRANT, P. Simulation of strongly nonlinear wave generation and wave-body interactions using a 3-D MEL model. In: **Twenty-First Symposium on Naval Hydrodynamics**. 1997.

FOURNIER, J. R.; NACIRI, M.; CHEN, X. B. Hydrodynamics of two side-by-side vessels. Experiments and numerical simulations. In: **In Proceedings of the 16th ISOPE Conference**. 2006.

GADD, G. E. A method of computing the flow and surface wave pattern around full forms. In: **The Royal Institution of Naval Architects**. 1975.

HESS, J. L.; SMITH, A. M. O. Calculation of potential flow about arbitrary bodies. **Progress in Aerospace Sciences**, p. 1–138, 1967.

HONG, S. Y.; NAM, B. Analysis of 2nd-order wave force on floating bodies using FEM in time domain. **International Journal of Offshore and Polar Engineering**, v. 21, p. 22–28, 2011.

HUANG, Y. **Nonlinear Ship Motions by a Rankine Panel Method**. 1997. Thesis (PhD) — Massachusetts Institute of Technology, 1997.

HUIJSMANS, R. H. M.; PINKSTER, J. A.; DE WILDE, . J. J. Diffraction and radiation of waves around side-by-side moored vessels. In: **In Proceedings of the 11th ISOPE Conference**. p. 406–412, 2001.

HULME, A. The wave forces acting on a floating hemisphere undergoing forced periodic oscillations. **Journal of Fluid Mechanics**, v. 121, p. 443–463, 1982.

ISRAELI, M.; ORSZAG, S. A. Approximation of radiation boundary conditions. **Journal of Computational Physics**, v. 41, p. 115–135, 1981.

JOHN, F. On the motion of floating bodies, I. **Communications on Pure and Applied Mathematics**, v. 2, p. 13–57, 1949.

JOHN, F. On the motion of floating bodies, II. **Communications on Pure and Applied Mathematics**, v. 3, p. 45–101, 1950.

KASHIWAGI, M.; ENDO, K.; YAMAGUCHI, H. Wave drift forces and moments on two ships arranged side by side in waves. **Ocean Engineering**, v. 32, p. 529–555, 2005.

KIM, G.-H.; LEE, C.-S.; KERWIN, J. A B-spline based higher order panel method for analysis of steady flow around marine propellers. **Ocean Engineering**, v. 34, p. 2045–2060, 2007.

KIM, K.-H.; KIM, Y. Time-domain analysis of motion responses of adjacent multiple floating bodies in waves. In: **In Proceedings of the 18th ISOPE Conference**. 2008.

KIM, M. W.; KOO, W.; HONG, S. Y. Numerical analysis of various artificial damping schemes in a three-dimensional numerical wave tank. **Ocean Engineering**, v. 75, p. 165–173, 2014.

KIM, Y.; KIM, K.-H.; KIM, Y. Springing analysis of a seagoing vessel using fully coupled bem-fem in the time domain. **Ocean Engineering**, v. 36, p. 785–796, 2009.

KIM, Y.; KRING, D. C.; SCLAVOUNOS, P. D. Linear and nonlinear interactions of surface waves with bodies by a three-dimensional rankine panel method. **Applied Ocean Research**, v. 19, p. 235 – 249, 1997.

KOO, B.; KIM, M. Hydrodynamic interactions and relative motions of two floating platforms with mooring lines in side-by-side offloading operation. **Applied Ocean Research**, v. 27, p. 292–310, 2005.

KOO, W.; KIM, M.-H. Freely floating-body simulation by a 2D fully nonlinear numerical wave tank. **Ocean Engineering**, v. 31, p. 2011–2046, 2004.

KORSMEYER, F.; BINGHAM, H.; NEWMAN, J. **TiMIT - A Panel Method for Transient Wave-Body Interactions**. : Massachusetts Institute of Technology, (1999).

KRING, D. C. **Time Domain Ship Motions by a Three-Dimensional Rankine Panel Method**. 1994. Thesis (PhD) — Massachusetss Institute of Technology, 1994.

KRISTIANSEN, T.; FALTINSEN, O. M. A two-dimensional numerical and experimental study of resonant coupled ship and piston-mode motion. **Applied Ocean Research**, v. 32, p. 158–176, 2010.

KRISTIANSEN, T.; FALTINSEN, O. M. Gap resonance analyzed by a new domain-decomposition method combining potential and viscous flow draft. **Applied Ocean Research**, v. 34, p. 198–208, 2012.

LAMB, H. **Hydrodynamics**. : Dover, 1945.

LEE, C.-H.; NEWMAN, J. N. Computation of wave effects using the panel method. In: CHAKRABARTI, S. K. (Ed.). **Numerical Models in Fluid-Structure Interaction**. : WIT Press, 2005.

LIU, W.-M.; XUE, M.; YUE, D. K.-P. Computations of fully nonlinear three-dimensional wave-wave and wave-body interactions. Part 2. nonlinear waves and forces on a body. **Journal of Fluid Mechanics**, v. 438, p. 41–66, 2001.

LIU, Y.; XUE, M.; YUE, D. K.-P. Computations of fully nonlinear three-dimensional wave-wave and wave-body interactions. Part 1. dynamics of steep three-dimensional waves. **Journal of Fluid Mechanics**, v. 438, p. 11–39, 2001.

LONGUET-HIGGINS, M. S.; COKELET, E. D. The deformation of steep surface waves on water. I. A numerical method of computation. **Proceedings of the Royal Society of London**, v. 350, p. 1–26, 1976.

MANIAR, H. D. **A three dimensional higher order panel mehod based on B-splines**. 1995. Thesis (PhD) — Massachussetts Institute of Technology, 1995.

MEI, C. C.; STIASSNIE, M.; YUE, D. K.-P. **Theory and Applications of Ocean Surface Waves. Part 1: Linear Aspects**. : World Scientific Publishing Co. Pte. Ltd, 2005.

MEI, C. C.; STIASSNIE, M.; YUE, D. K.-P. **Theory and Applications of Ocean Surface Waves. Part 2: Nonlinear Aspects**. : World Scientific Publishing Co. Pte. Ltd, 2005.

MELLO, P. C.; CARNEIRO, M. L.; TANNURI, E. A.; NISHIMOTO, K. USP active absorption wave basin: From conception to commissioning. In: **Proceedings of the ASME 2010 29th International Conference on Ocean, Offshore and Artic Engineering, OMAE2010, Shangai, China**. 2010.

MOLIN, B. On the piston and sloshing modes in moonpools. **Journal of Fluid Mechanics**, v. 430, p. 27–50, 2001.

MOLIN, B.; REMY, F.; CAMHI, A.; LEDOUX, A. Experimental and numerical study of the gap resonances in-between two rectangular barges. In: **13th Congreess of Intl Maritime Association of Mediterranean IMAM 2009, Instanbul, Turkey**. 2009.

MOLIN, B.; REMY, F.; KIMMOUN, O.; STASSEN, Y. Experimental study on the wave propagation and decay in a channel through a rigid ice-sheet. **Applied Ocean Research**, v. 24, p. 247–260, 2002.

NACIRI, M.; WAALS, O.; DE WILDE, . de J. J. Time domain simulations of side-by-side moored vessels lessons learnt from a benchmark test. In: **Proceedings of the OMAE2007 26th International Conference on Offshore Mechanics and Artic Engineering**. 2007.

NAKOS, D. E. **Ship Wave Patterns and Motions by a Three Dimensional Rankine Panel Method**. 1990. Thesis (PhD) — Massachusetts Institute of Technology, 1990.

NEWMAN, J. N. **Marine Hydrodynamics**. : The MIT Press, 1977.

NEWMAN, J. N. Panel methods in marine hydrodynamics. In: **11th Australian Fluid Mechanics Conference**. 1992.

NEWMAN, J. N. **Application of generalized modes for the simulation of free surface patches in multi body hydrodynamics**. : Wamit Consortium Report, (2003).

NISHIMOTO, K.; FERREIRA, M. D.; MARTINS, M. R.; MASETTI, I. Q.; FILHO, P. D. M.; RUSSO, A. A.; CALDO, J.; SILVEIRA, S. S. Numerical offshore tank: Development

of numerical offshore tank for ultra deep water oil production systems. In: **Proceedings of the 22nd International Conference on Offshore Mechanics Artic Engineering**. 2003.

ORLANSKI, J. A simple boundary condition for unbounded hyperbolic flows. **Journal of Computational Physics**, v. 21, p. 251–269, 1976.

PAUW, W. H.; HUIJSMANS, R. H. M.; VOOGT, A. Advances in the hydrodynamics of side-by-side moored vessels. In: **Proceedings of the 26th International Conference on Offshore Mechanics and Artic Engineering, OMAE 2007, San Diego, California, USA**. 2007.

PERSSON, P.-O. **Mesh Generation for Implicit Geometries**. 2005. Thesis (PhD) — Massachusetts Institute of Technology, 2005.

PINKSTER, J. A. **Low Frequency Second Order Wave Exciting Forces on Floating Structures**. 1980. Thesis (PhD) — Technische Universiteit Delft, 1980.

PRINS, H. **Time-Domain Calculations of Drift Forces and Moments**. 1995. Thesis (PhD) — Tecnische Universiteit Delft, 1995.

QIU, W. **A Panel-Free Method for Time-Domain Analysis of Floating Bodies in Waves**. 2001. Thesis (PhD) — Dalhousie University, 2001.

QUEIROZ FILHO, . A.; TANNURI, E. DP offloading operation: A numerical evaluation of wave shielding effect. In: **8th Conference on Manouvering and Control Marine Craft (MCMC2009)**. 2009.

ROMATE, J. E. The numerical simulation of nonlinear gravity waves. **Engineering Analysis with Boundary Elements**, v. 7, p. 156–166, 1990.

ROMATE, J. E. Absorbing boundary conditions for free surface waves. **Journal of Computational Physics**, v. 99, p. 135–145, 1992.

SARPKAYA, T.; ISAACSON, M. **Mechanical of Waves Forces on Offshore Structures**. : Van Nostrand Reinhold Company, 1981.

SCLAVOUNOS, P. D.; NAKOS, D. E. Stability analysis of panel methods for free-surface flows with forward speed. In: **17th Symposiumn on Naval Hydrodynamics**. 1993.

SERVÁN-CAMAS, B.; GARCíA-ESPINOSA, J. Accelerated 3d multi-body seakeeping simulations using unstructured finite elements. **Journal of Computational Physics**, v. 252, p. 382–403, 2013.

SHAO, Y.-L. **Numerical Potential-Flow Studies on Weakly-Nonlinear Wave-Body Interactions with/without small Forwar Speeds**. 2010. Thesis (PhD) — Norwegian University of Science and Technology, 2010.

SINGH, S. P.; SEN, D. A comparative linear and nonlinear ship motion study using a 3-D time domain methods. **Ocean Engineering**, v. 34, p. 1863–1881, 2007.

STOKER, J. J. **Water Waves**. : Interscience Publishers, 1957.

STOKES, G. On the theory of oscillatory waves. **Mathematical and Physical Papers - Reprinted from the Original Journals and Transactions**, v. 8, p. 441–455, 1847.

SUN, L.; TAYLOR, R. E.; TAYLOR, P. First and second-order analysis of resonant waves between adjacent barges. **Journal of Fluid Strucutures**, v. 26, p. 954–978, 2010.

TANIZAWA, K. A nonlinear simulation method of 3-D body motions in waves. **Journal of the Society of Naval Architects of Japan**, 1995.

TANIZAWA, K. The state of the art on numerical wave tank. In: **Proceeding of 4th Osaka Colloquium on Seakeeping Performance of Ships**. p. 95–114, 2000.

TANNURI, E. A.; BRAVIN, T. T.; SIMOS, A. N.; ALVES, K. H.; NISHIMOTO, K.; FERREIRA, M. D. Dynamic simulation of offloading operation considering wave interactions between vessels. In: **Proceedings of OMAE04 23nd International Conference on Offshore Mechanics and Artic Engineering**. 2004.

TAYLOR, R. E.; WU, G. Transient motion of a floating body in steep water waves. In: **Proceedings of the 11th International Workshop on Water Waves and Floating Bodies**. 1996.

THOMSON, L. N. M. **Theoretical Hydrodynamics**. : The Macmillan and Company, 1968.

VAN DAALEN, . E. F. G. **Numerical and Theoretical Studies of Water Waves and Floating Bodies**. 1993. Thesis (PhD) — University of Twente, 1993.

WANG, Q. X. Unstructured MEL modelling of nonlinear unsteady ship waves. **Journal of Computational Physics**, v. 210, p. 368–385, 2005.

WEHAUSEN, J. V. The motion of floating bodies. **Annual Review of Fluid Mechanics**, v. 3, p. 237–268, 1971.

WEHAUSEN, J. V.; LAITONE, E. V. Surface waves. **Handbuch der Physics**, v. 9, p. 446–815, 1960.

YAN, S.; MA, Q. W.; CHENG, X. Fully nonlinear hydrodynamic interaction between two 3D floating structures in close proximity. In: **In Proceedings of the 19th ISOPE Conference**. 2009.

YANG, C.; NOBLESSE, F.; LöHNER, R. Comparison of classical and simple free-surface green functions. In: **Proceedings of The Fourteenth International Offshore and Polar Engineering Conference**. 2004.

YANG, M.; TENG, B.; NING, D.; SHI, Z. Coupled dynamic analysis for wave interaction with truss spar and its mooring line/riser system in time domain. **Ocean Engineering**, v. 39, p. 72–87, 2012.

ZHAO, W.; YANG, J.; HU, Z.; TAO, L. Prediction of hydrodynamic performance of an FLNG system in side-by-side offloading operation. **Journal of Fluid and Structures**, v. 46, p. 89–110, 2013.

ZHAO, W. H.; YANG, J. M.; HU, Z. Q.; WEI, Y. F. Recent developments on the hydrodynamics of floating liquid natural gas (FLNG). **Ocean Engineering**, v. 38, p. 1555–1567, 2011.

ZHEN, L.; BIN, T.; DE-ZHI, N.; YING, G. Wave-current interactions with three-dimensional floating bodies. **Journal of Hydrodynamics**, v. 22, p. 229–240, 2010.

APPENDIX

Appendix A

Damping Zone Analysis

This section presents an empirical study concerning the performance of the damping zone on absorbing the waves, varying its parameters b and a. The study considers an hemisphere body and a circular free surface discretized with 800 and 1225 quadrilateral panels, respectively. The details of the meshes may be observed in section 6.1. The comparison of the damping zone performance for different parameter values (b and a) is performed in terms of the hydrodynamic vertical force F_3 induced by a imposed vertical oscillatory motion of unitary amplitude $A_3 = 1.0$ m and an arbitrary frequency $\omega = 2.426$ rad/s. The time-step applied on the simulations is $\Delta t = T/60$ s, being T the oscillatory motion period.

Figures A.1, A.2, A.3 and A.4 present the comparisons of hydrodynamic vertical forces F_3 for damping zones of lengths $b = 2$, $b = 1.0$, $b = 1.5$ and $b = 2.0$, respectively. Notice that each figure presents five forces time series, which are associated to different a values ($a = 0.0$, $a = 0.5$, $a = 1.0$, $a = 1.5$ and $a = 2.0$. Among these time series, the one for $a = 0.0$ represents the case, in which no damping zone was applied in the simulations. One may observe that the parameter b presents a larger influence on the results then parameter a. In fact, for damping zone lengths lower than one generated wave length ($b < 1.0$), significant amplitude modulations, induced by wave reflections, on the signals are observed, irrespective of the damping zone intensity value a (Figure A.1). In addition, the results demonstrate that as the damping zone length is increased, these modulations tend to vanish even considering the smallest tested value of a.

Figures A.5 and A.6 present the wave field patterns resulted from a simulation disregarding the damping zone and one considering $b = 2.0\lambda$ and $a = 1.0$, respectively. Notice that the case without the damping zone present a constructive and destructive pattern, resulted from reflections on the domain boundaries, whereas the case with damping zone present a regular progressive wave pattern field.

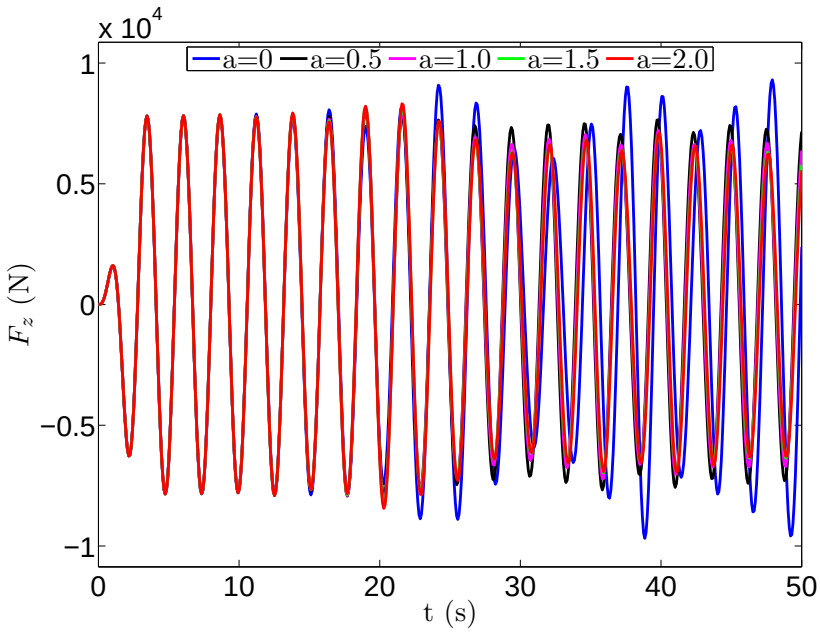

Figure A.1: Comparison of hydrodynamic vertical force F_3 on a hemisphere induced by a forced vertical oscillatory motion of amplitude $A_3 = 1.0$ m, considering a damping zone length of half generated wave length $b = \lambda/2$ and different values of dissipation intensity a

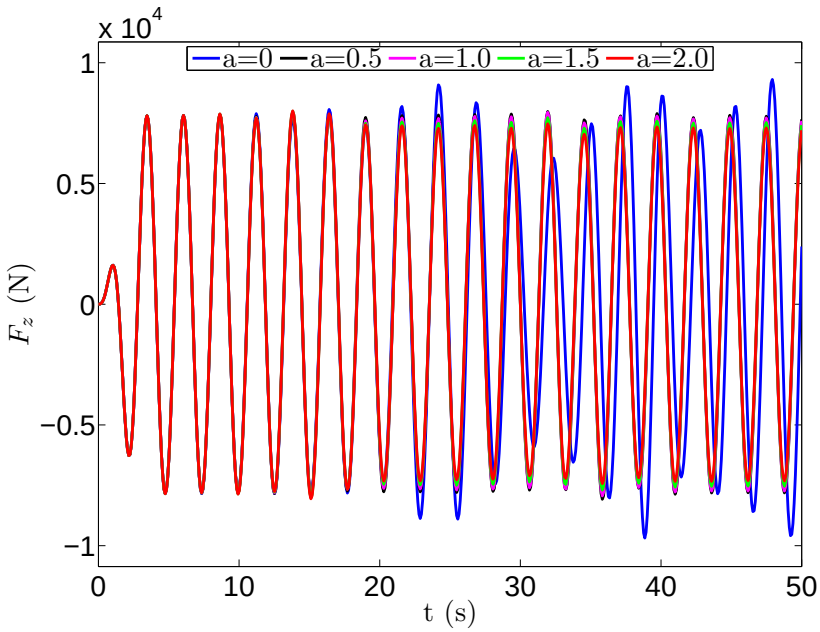

Figure A.2: Comparison of hydrodynamic vertical force F_3 on a hemisphere induced by a forced vertical oscillatory motion of amplitude $A_3 = 1$ m, considering a damping zone length of one generated wave length $b = \lambda$ and different values of dissipation intensity a

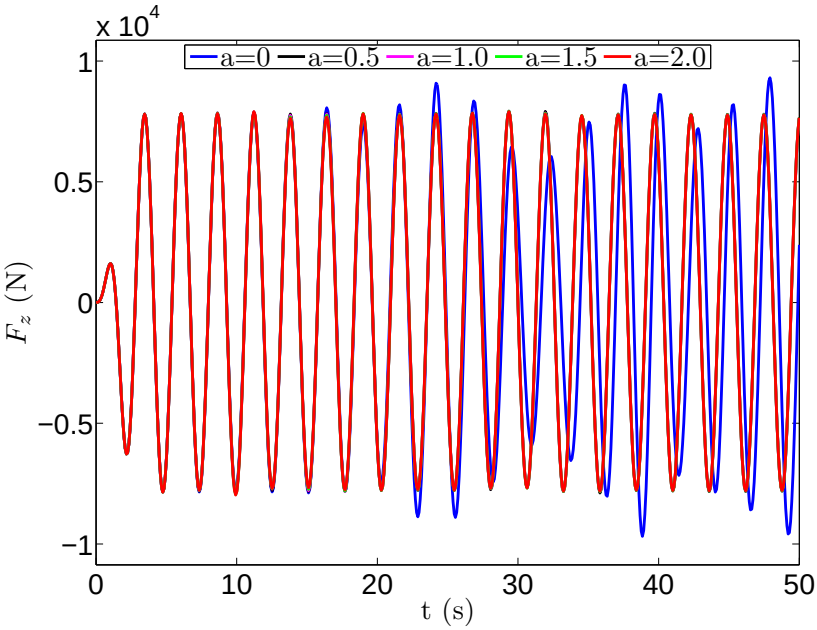

Figure A.3: Comparison of hydrodynamic vertical force F_3 on a hemisphere induced by a forced vertical oscillatory motion of amplitude $A_3 = 1$ m, considering a damping zone length of one and a half generated wave length $b = 1.5\lambda$ and different values of dissipation intensity a

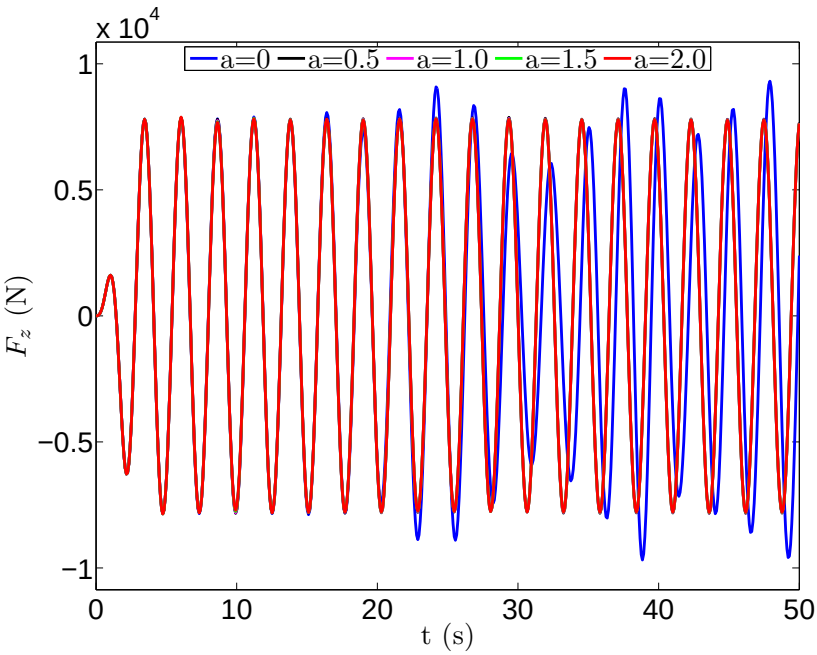

Figure A.4: Comparison of hydrodynamic vertical force F_3 on a hemisphere induced by a forced vertical oscillatory motion of amplitude $A_3 = 1$ m, considering a damping zone length of two generated wave lengths $b = 2.0\lambda$ and different values of dissipation intensity a

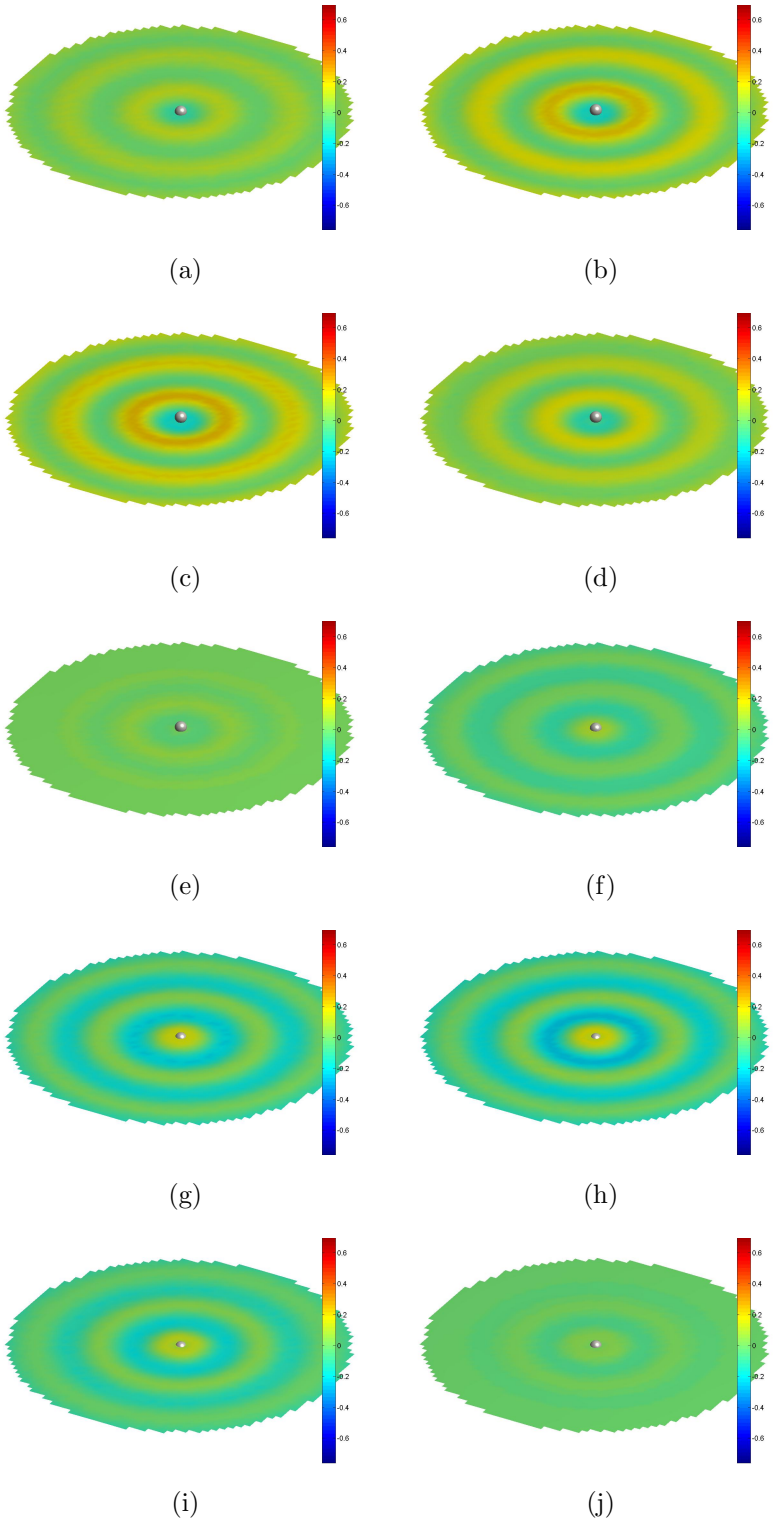

Figure A.5: Snapshots of the simulation without damping zone at 10 different instants of time within one period. Vertical oscillatory motion amplitude $A_3 = 0.5$ m (a) $t = 56.98$ s, (b) $t = 57.24$ s,(c) $t = 57.50$ s, (d) $t = 57.76$ s, (e) $t = 58.01$ s, (f) $t = 58.27$ s, (g) $t = 58.53$ s, (h) $t = 58.79$ s, (i) $t = 59.05$ s and (j) $t = 59.31$ s

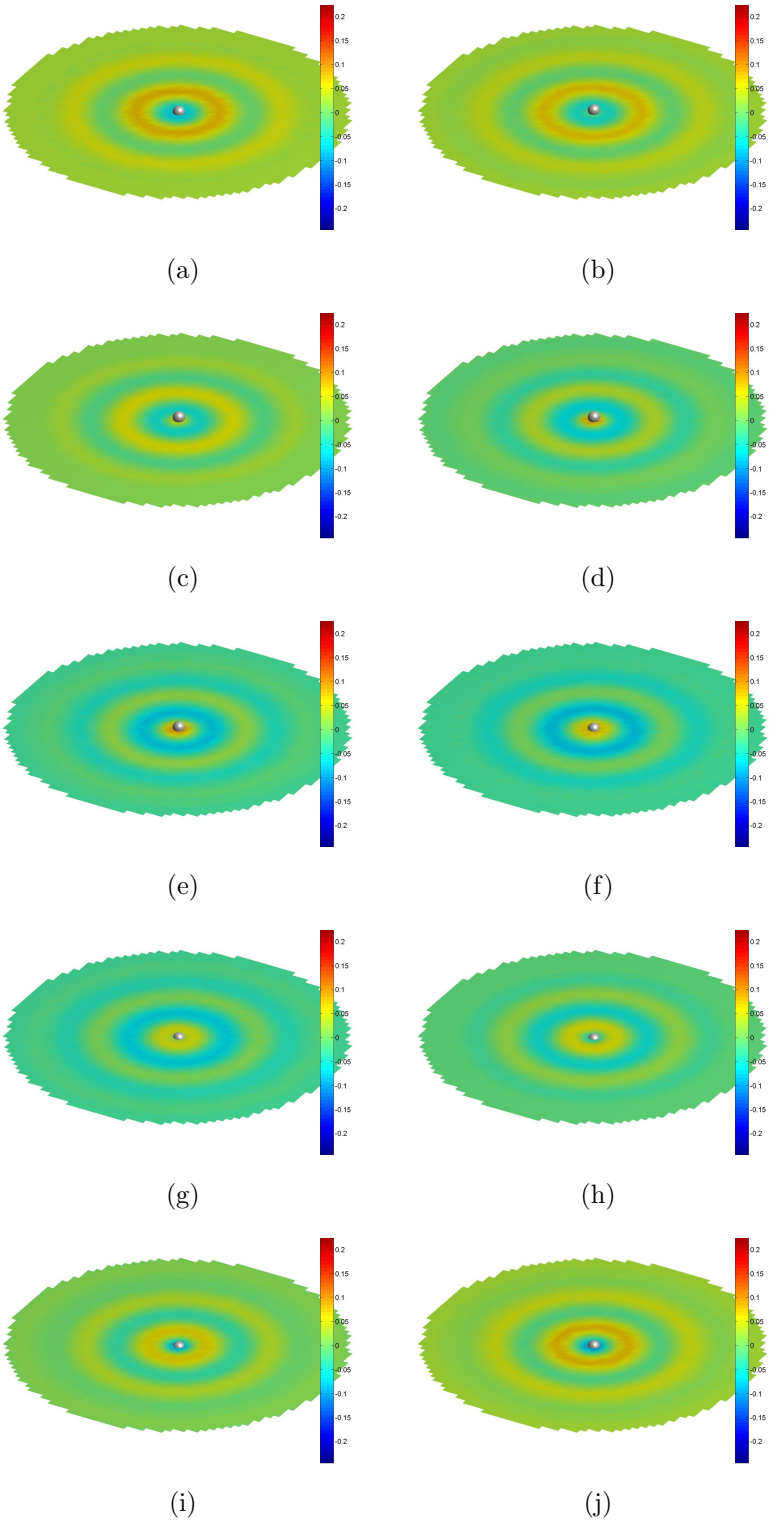

Figure A.6: Snapshots of the simulation with damping zone parameters $b = 2.0$ and $a = 1.0$ at 10 different instants of time within one period. Vertical oscillatory motion amplitude $A_3 = 0.5$ m (a) $t = 56.98$ s, (b) $t = 57.24$ s,(c) $t = 57.50$ s, (d) $t = 57.76$ s, (e) $t = 58.01$ s, (f) $t = 58.27$ s, (g) $t = 58.53$ s, (h) $t = 58.79$ s, (i) $t = 59.05$ s and (j) $t = 59.31$ s

Appendix B

Multi-Body Simulations with Large Relative Displacements

B.1 Comparison between Experiments and Computations

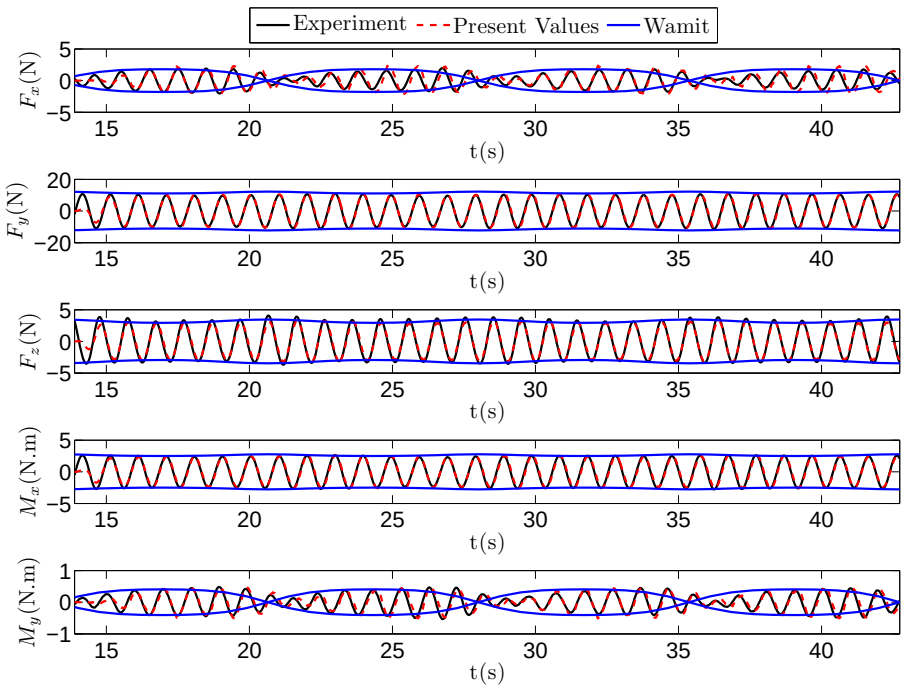

Figure B.1: Case 1 Comparison of numerical and experimental results in terms of position of Body 2 in time and the associated time series of the hydrodynamic loads F_x, F_y, F_z, M_x and M_y

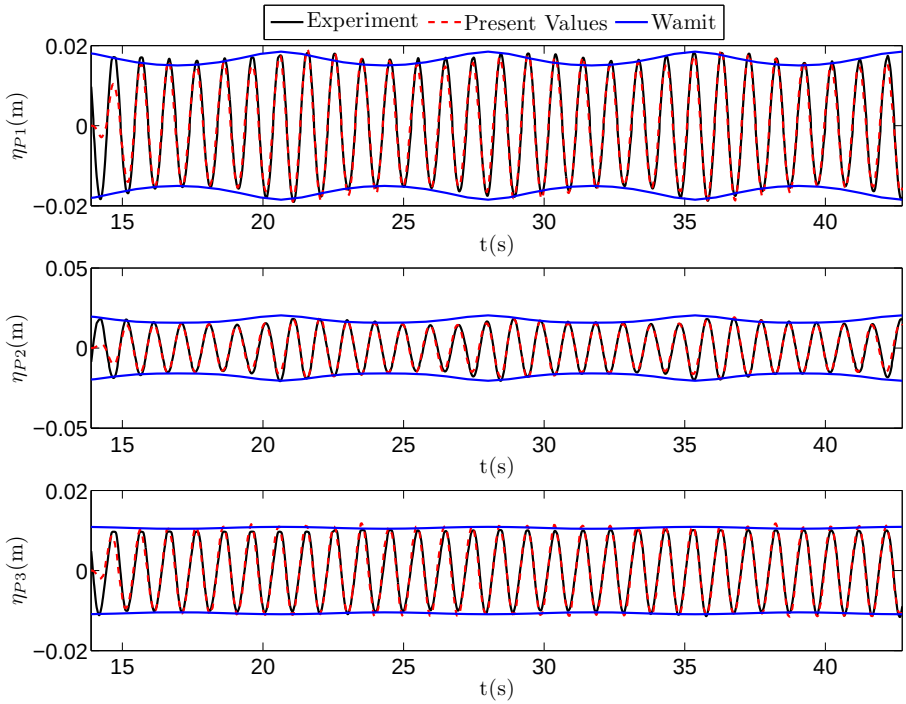

Figure B.2: Case 1: Comparison between numerical and experimental results in terms of position of Body 2 in time and the associated time series of the wave elevations at WP1, WP2 and WP3

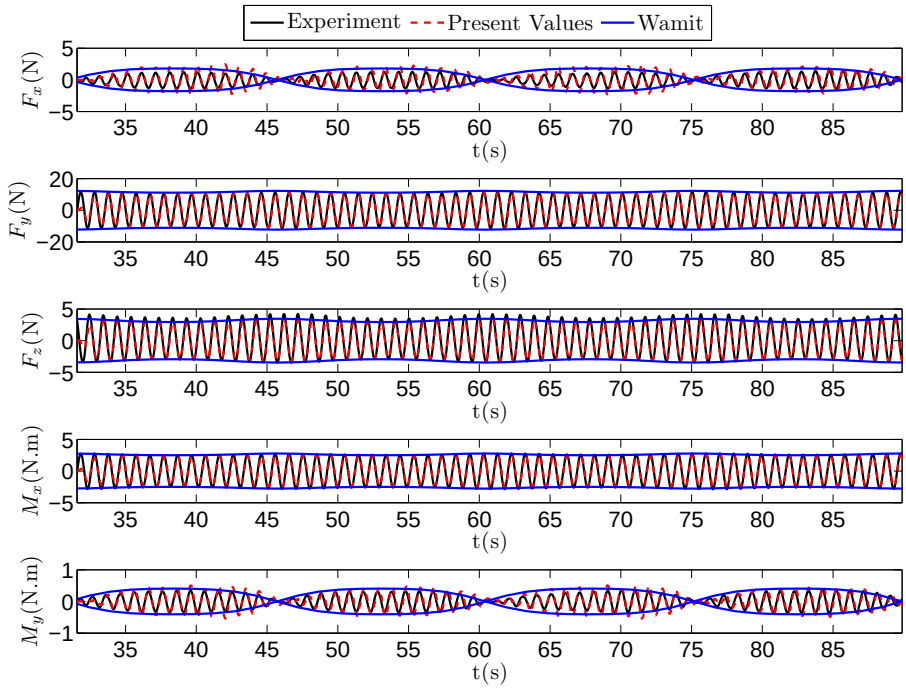

Figure B.3: Case 2 Comparison of numerical and experimental results in terms of position of Body 2 in time and the associated time series of the hydrodynamic loads F_x, F_y, F_z, M_x and M_y

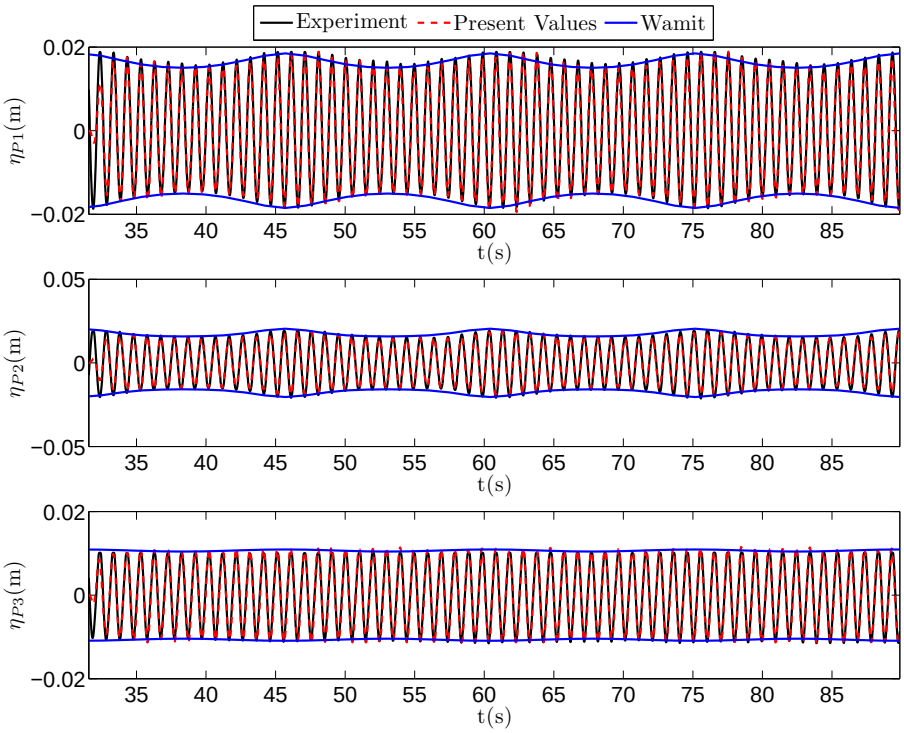

Figure B.4: Case 2: Comparison between numerical and experimental results in terms of position of Body 2 in time and the associated time series of the wave elevations at WP1, WP2 and WP3

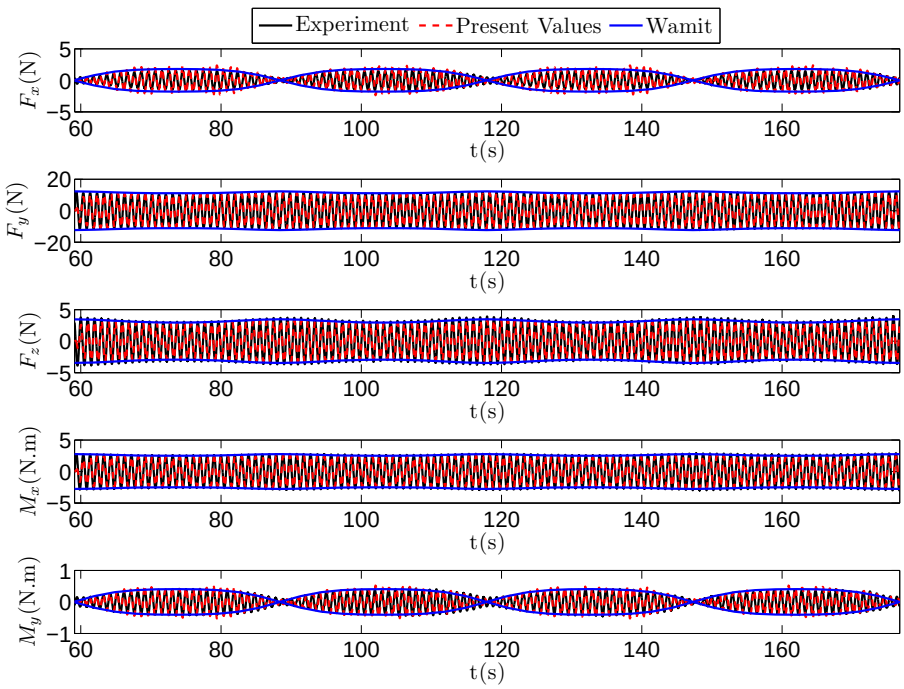

Figure B.5: Case 3 Comparison of numerical and experimental results in terms of position of Body 2 in time and the associated time series of the hydrodynamic loads F_x, F_y, F_z, M_x and M_y

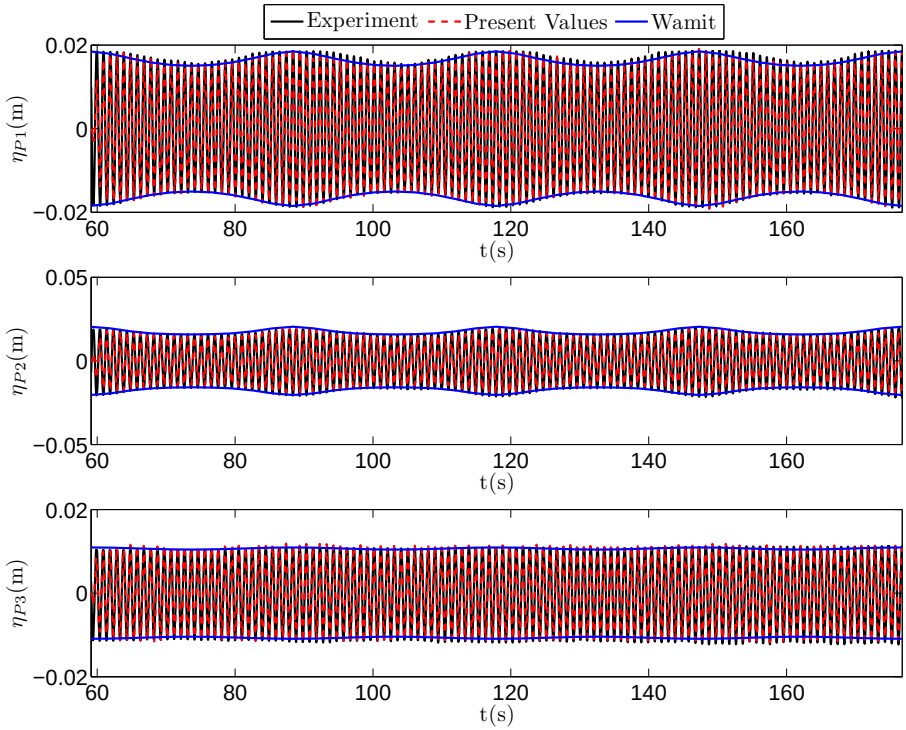

Figure B.6: Case 3: Comparison between numerical and experimental results in terms of position of Body 2 in time and the associated time series of the wave elevations at WP1, WP2 and WP3

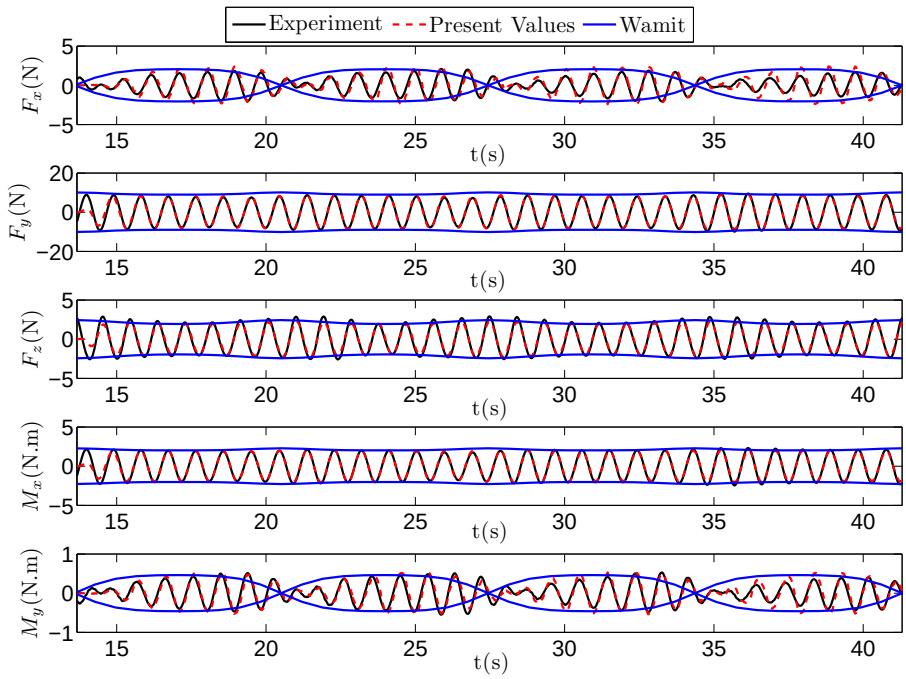

Figure B.7: Case 4 Comparison of numerical and experimental results in terms of position of Body 2 in time and the associated time series of the hydrodynamic loads F_x, F_y, F_z, M_x and M_y

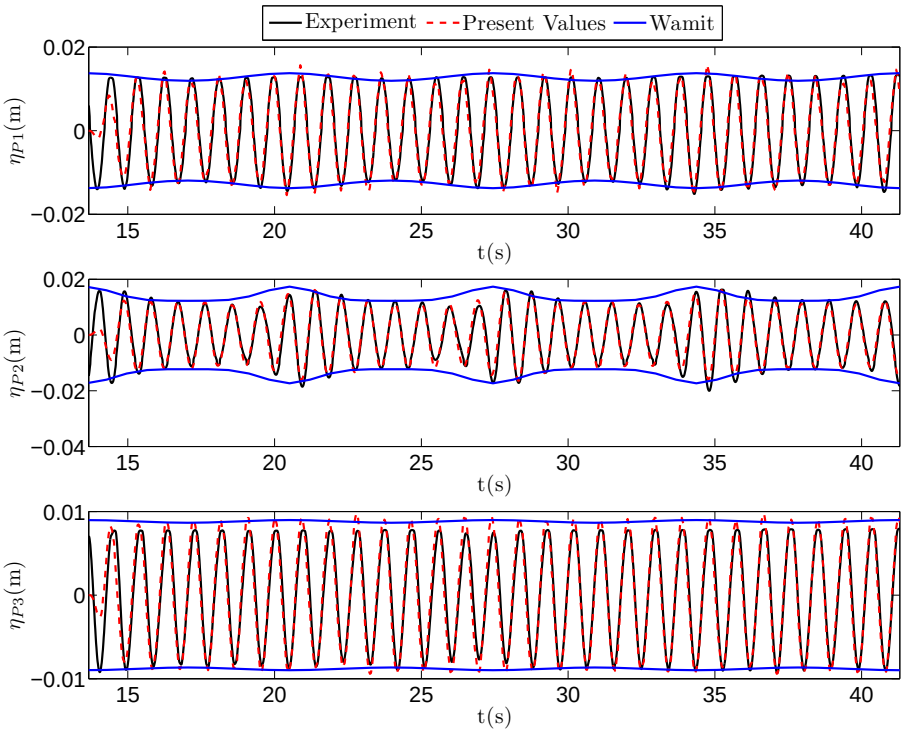

Figure B.8: Case 4: Comparison between numerical and experimental results in terms of position of Body 2 in time and the associated time series of the wave elevations at WP1, WP2 and WP3

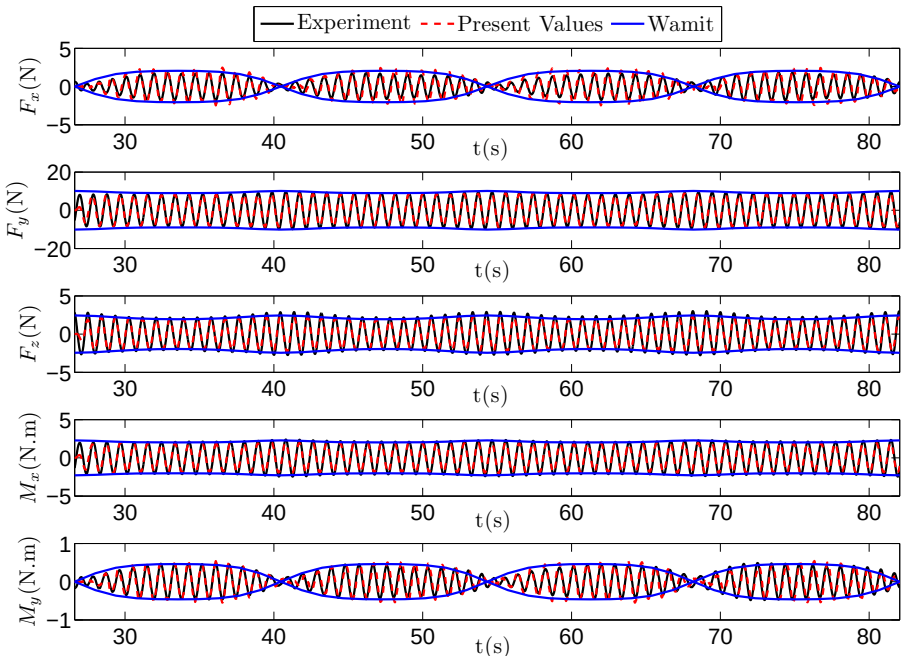

Figure B.9: Case 5 Comparison of numerical and experimental results in terms of position of Body 2 in time and the associated time series of the hydrodynamic loads F_x, F_y, F_z, M_x and M_y

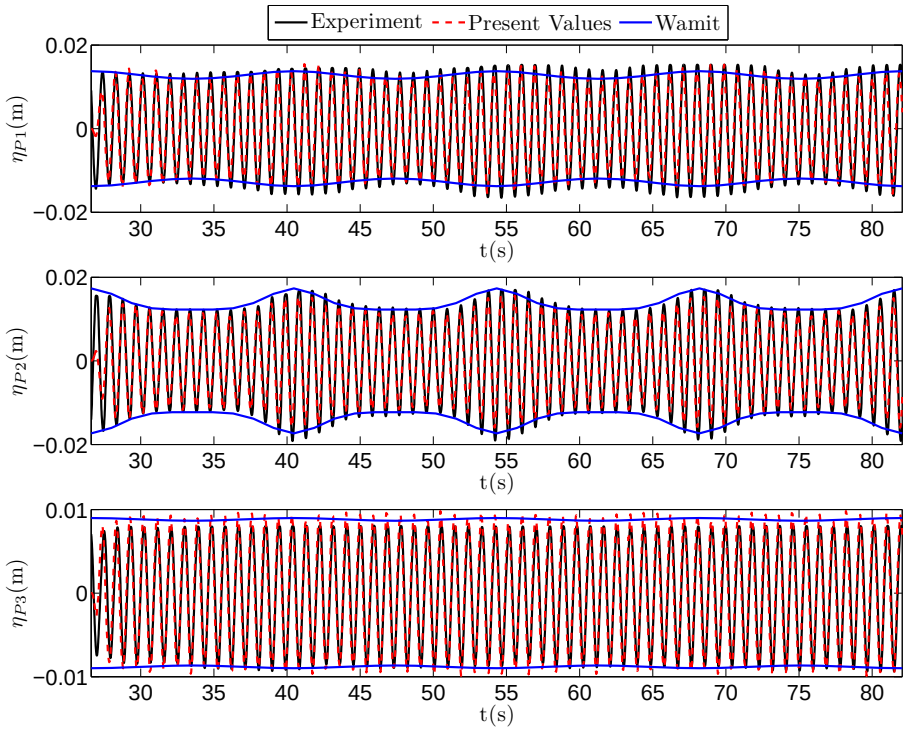

Figure B.10: Case 5: Comparison between numerical and experimental results in terms of position of Body 2 in time and the associated time series of the wave elevations at WP1, WP2 and WP3

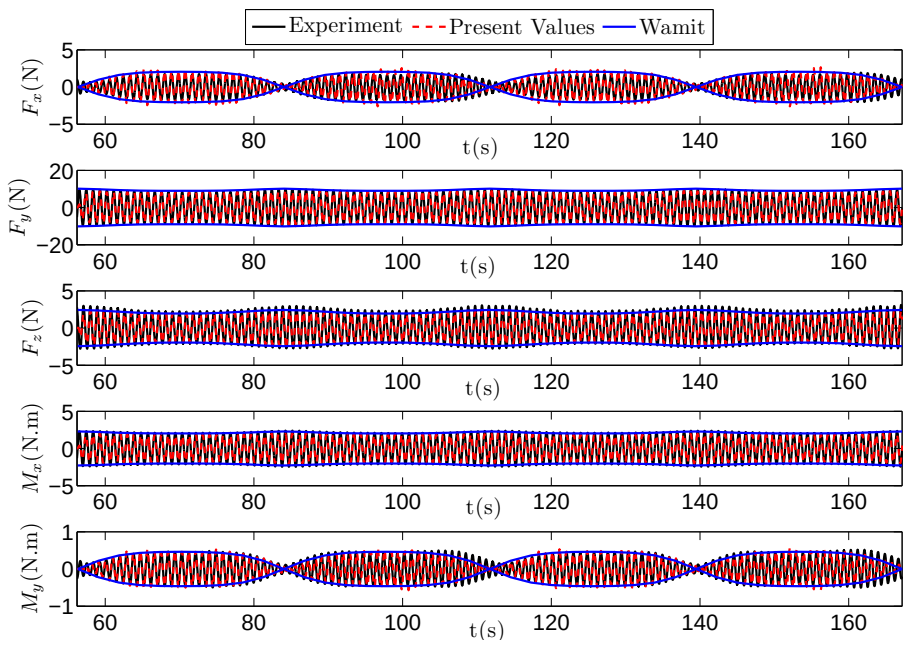

Figure B.11: Case 6 Comparison of numerical and experimental results in terms of position of Body 2 in time and the associated time series of the hydrodynamic loads F_x, F_y, F_z, M_x and M_y

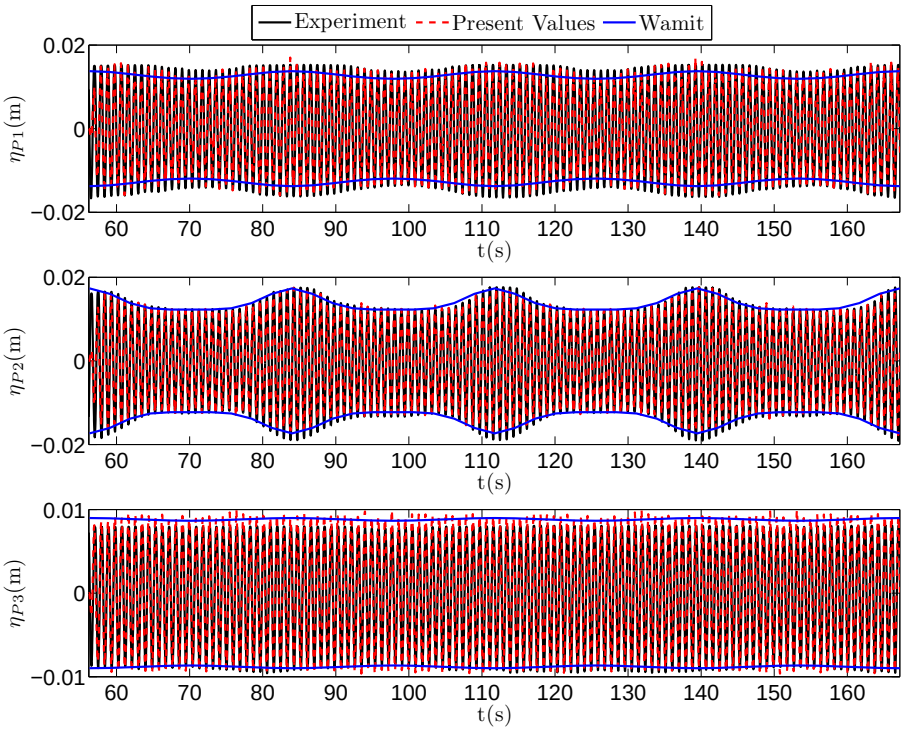

Figure B.12: Case 6: Comparison between numerical and experimental results in terms of position of Body 2 in time and the associated time series of the wave elevations at WP1, WP2 and WP3

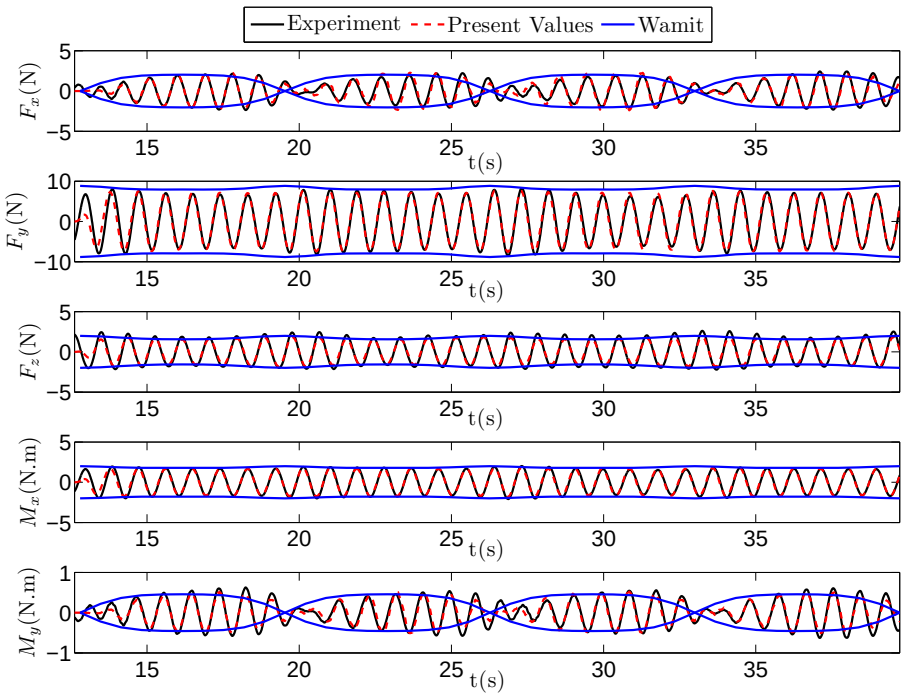

Figure B.13: Case 7 Comparison of numerical and experimental results in terms of position of Body 2 in time and the associated time series of the hydrodynamic loads F_x, F_y, F_z, M_x and M_y

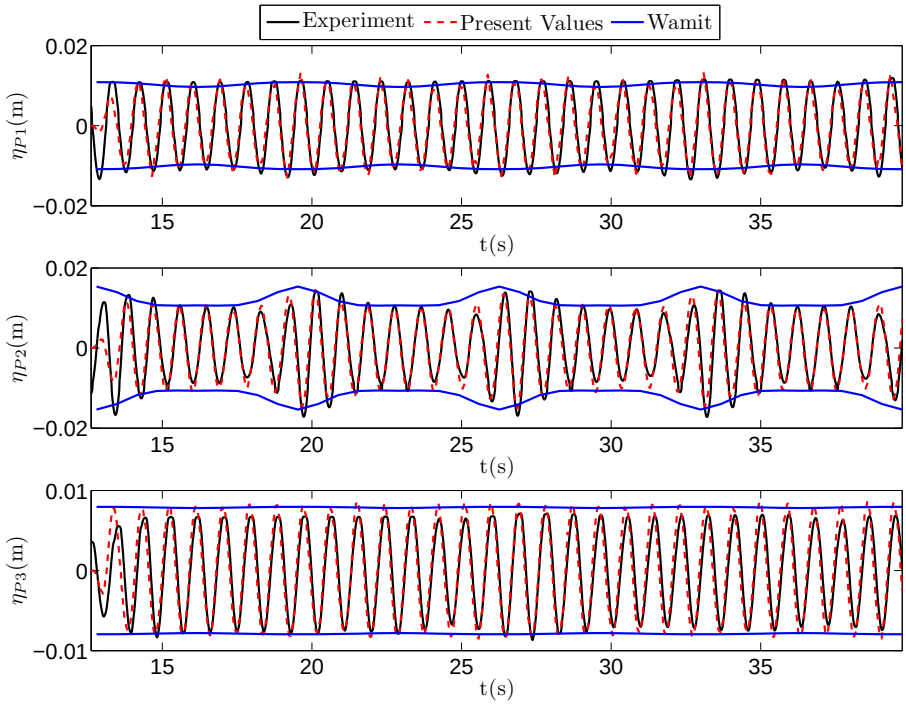

Figure B.14: Case 7: Comparison between numerical and experimental results in terms of position of Body 2 in time and the associated time series of the wave elevations at WP1, WP2 and WP3

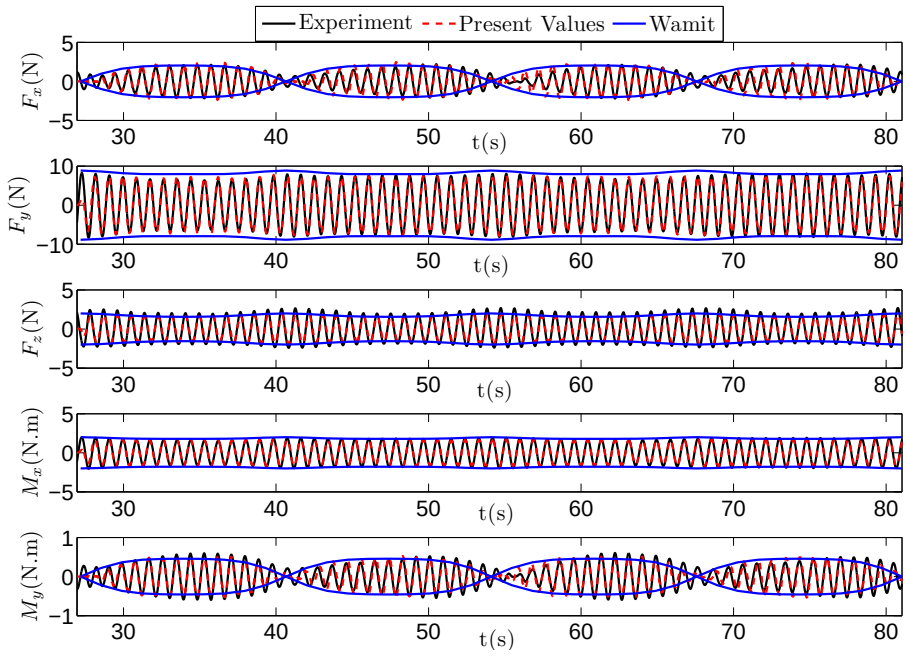

Figure B.15: Case 8 Comparison of numerical and experimental results in terms of position of Body 2 in time and the associated time series of the hydrodynamic loads F_x, F_y, F_z, M_x and M_y

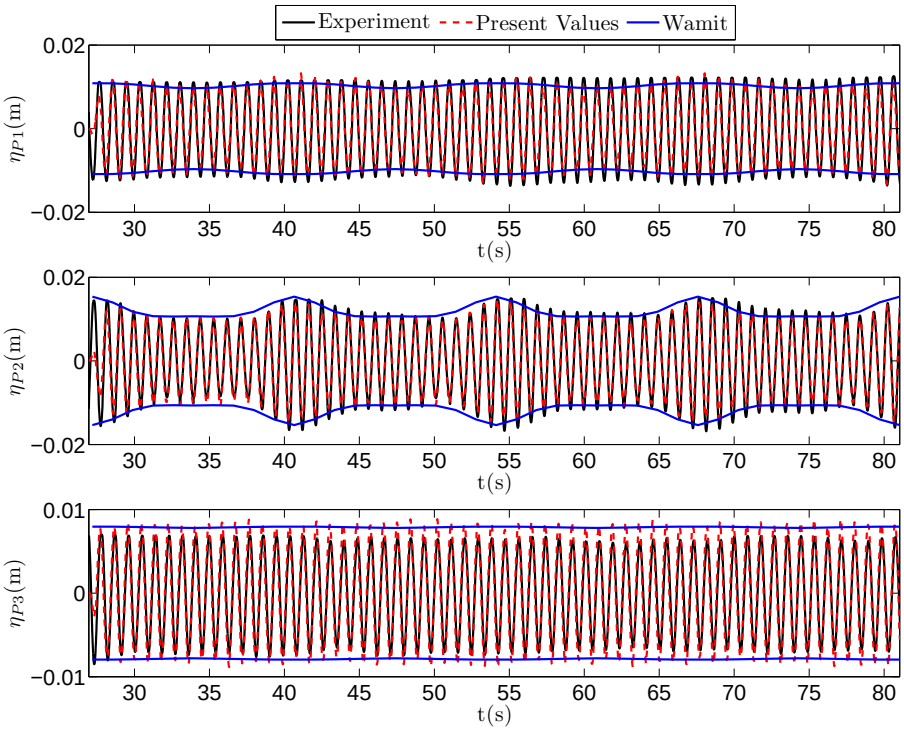

Figure B.16: Case 8: Comparison between numerical and experimental results in terms of position of Body 2 in time and the associated time series of the wave elevations at WP1, WP2 and WP3

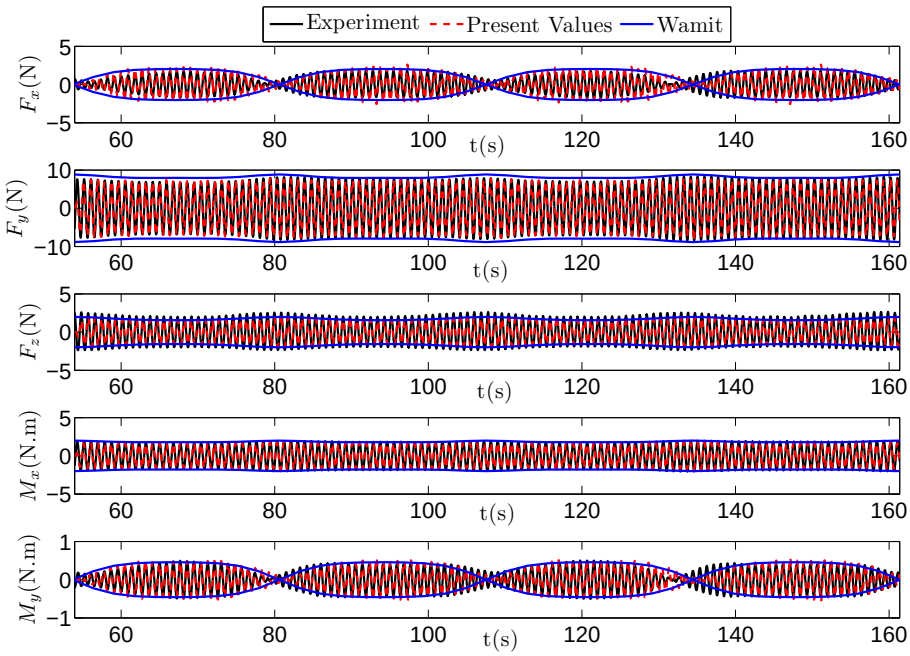

Figure B.17: Case 9 Comparison of numerical and experimental results in terms of position of Body 2 in time and the associated time series of the hydrodynamic loads F_x, F_y, F_z, M_x and M_y

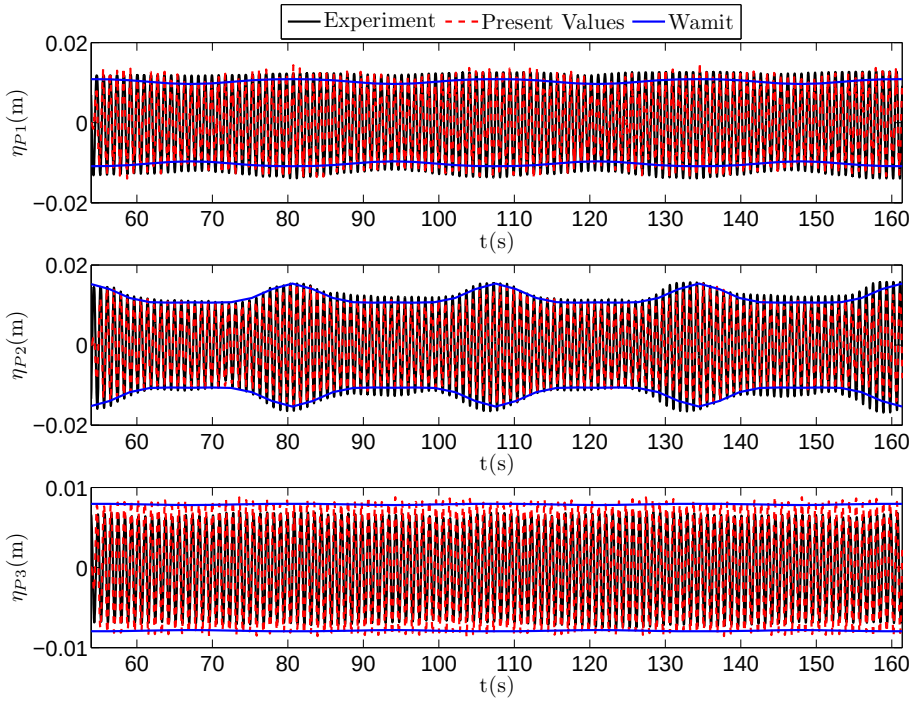

Figure B.18: Case 9: Comparison between numerical and experimental results in terms of position of Body 2 in time and the associated time series of the wave elevations at WP1, WP2 and WP3

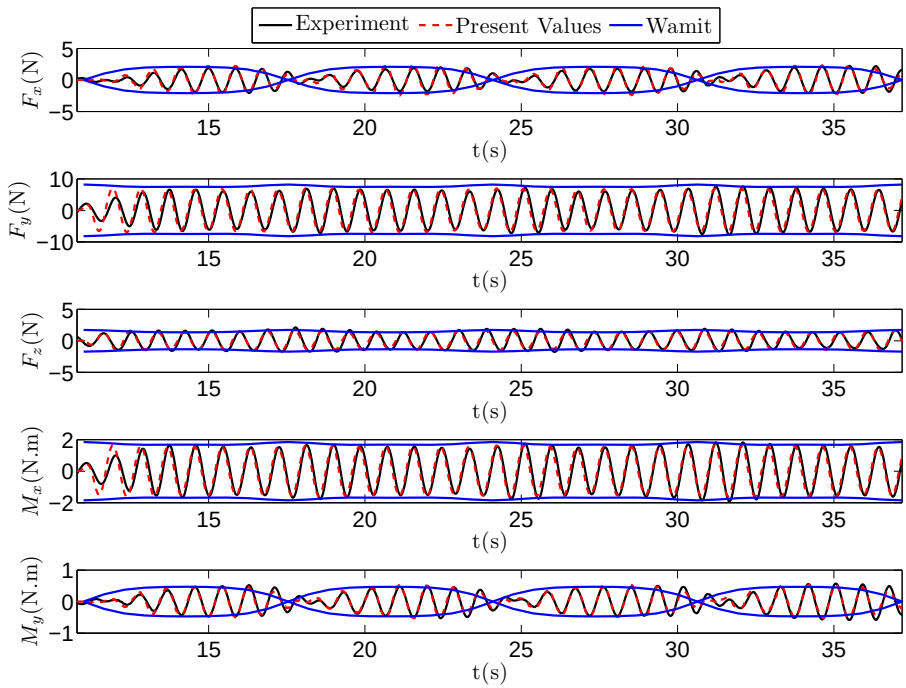

Figure B.19: Case 10 Comparison of numerical and experimental results in terms of position of Body 2 in time and the associated time series of the hydrodynamic loads F_x, F_y, F_z, M_x and M_y

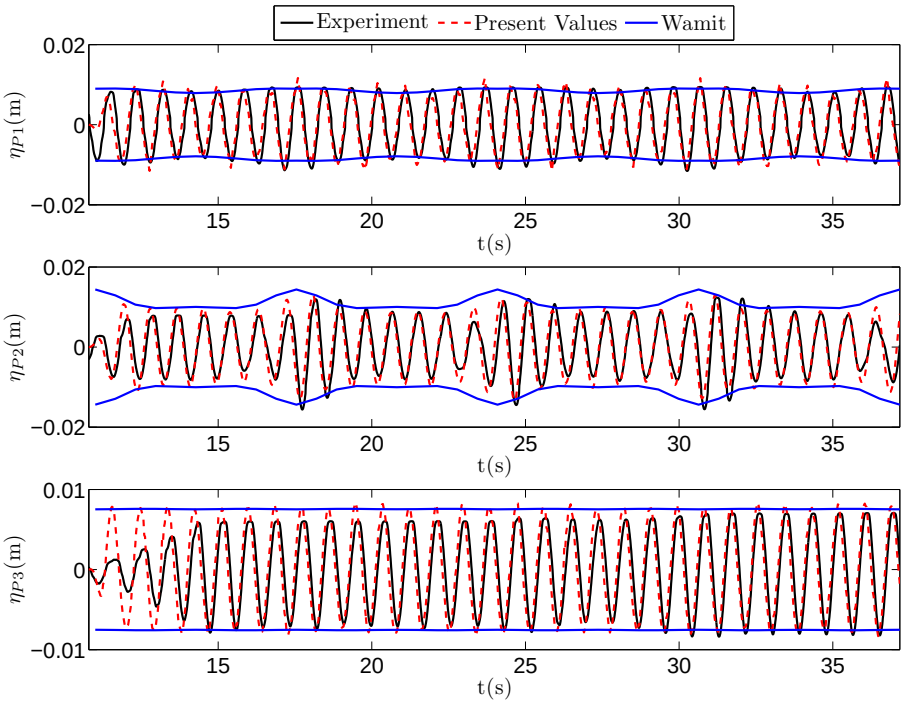

Figure B.20: Case 10: Comparison between numerical and experimental results in terms of position of Body 2 in time and the associated time series of the wave elevations at WP1, WP2 and WP3

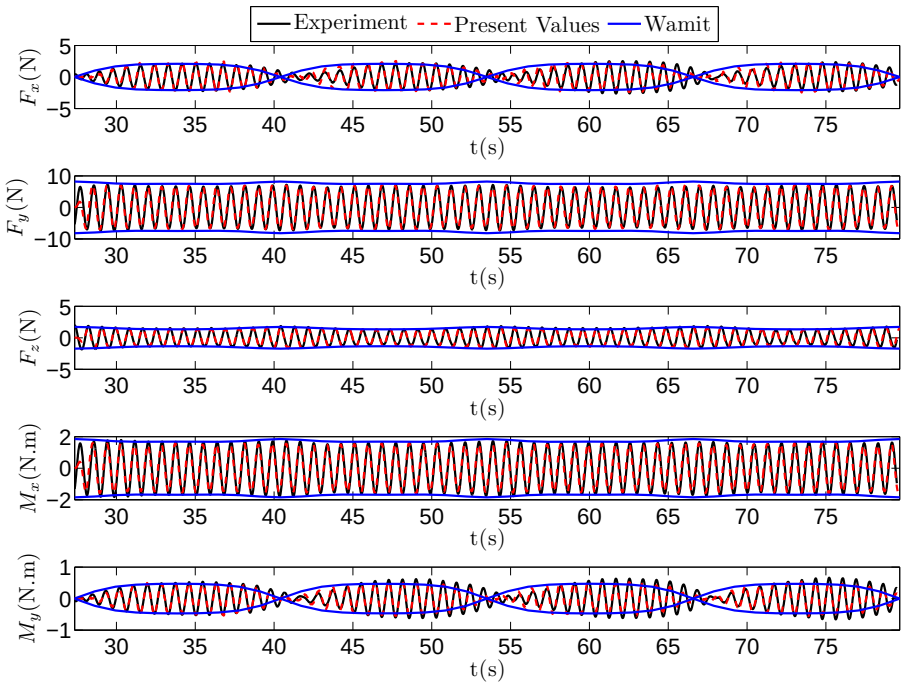

Figure B.21: Case 11 Comparison of numerical and experimental results in terms of position of Body 2 in time and the associated time series of the hydrodynamic loads F_x, F_y, F_z, M_x and M_y

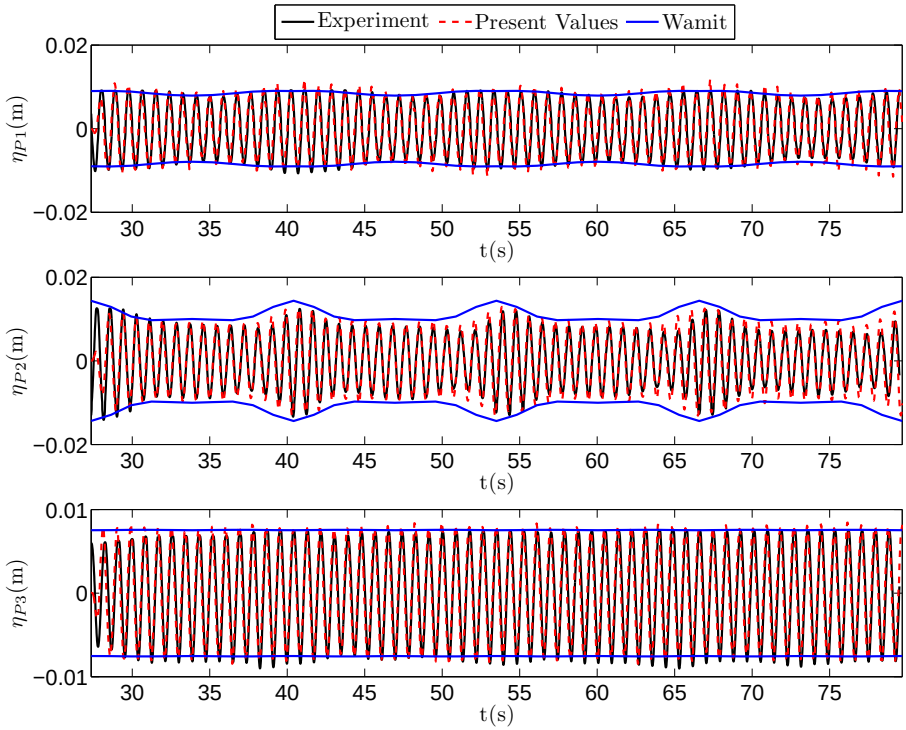

Figure B.22: Case 11: Comparison between numerical and experimental results in terms of position of Body 2 in time and the associated time series of the wave elevations at WP1, WP2 and WP3

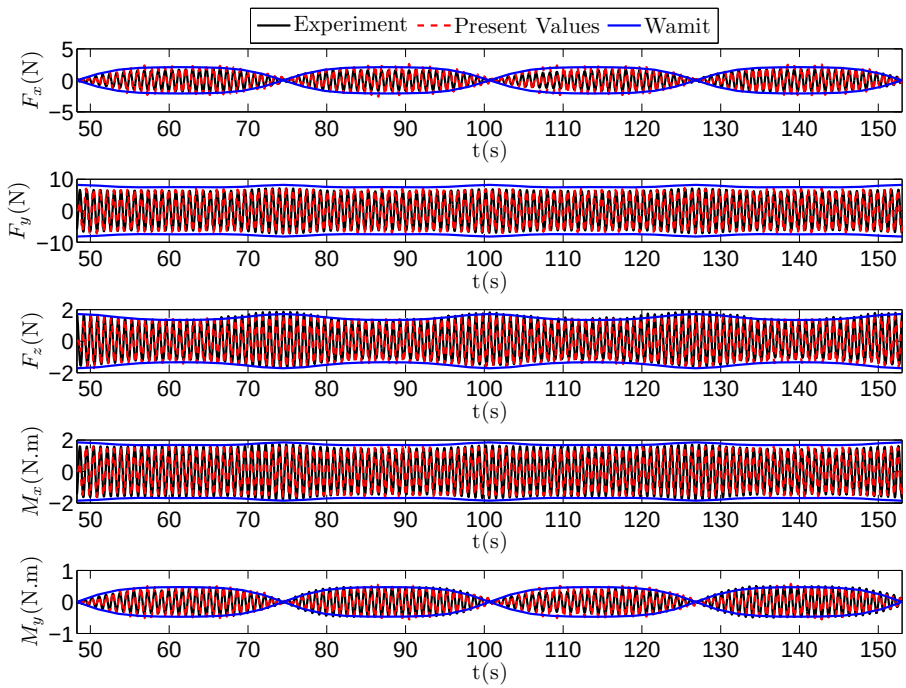

Figure B.23: Case 12 Comparison of numerical and experimental results in terms of position of Body 2 in time and the associated time series of the hydrodynamic loads F_x, F_y, F_z, M_x and M_y

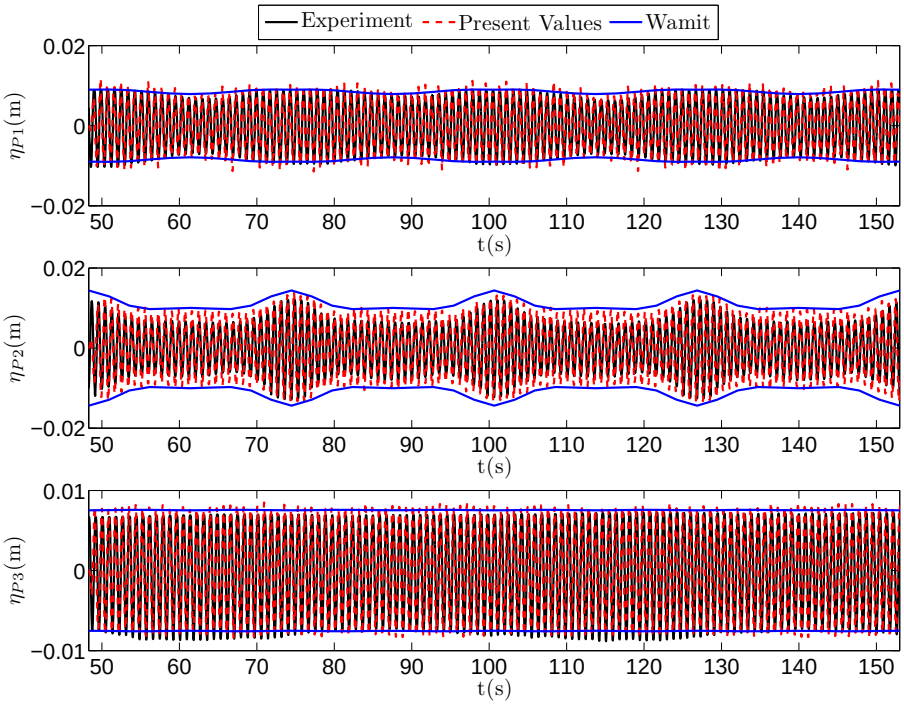

Figure B.24: Case 12: Comparison between numerical and experimental results in terms of position of Body 2 in time and the associated time series of the wave elevations at WP1, WP2 and WP3